Development of Titanium Dioxide Metasurfaces and Nanosoupbowls for Optically Enhancing Silicon Photocathodes

Dissertation

zur Erlangung des akademischen Grades

DOCTOR RERUM NATURALIUM

(Dr. rer. nat.)

im Fach Physik

eingereicht an der

Mathematisch-Naturwissenschaftlichen Fakultät
der Humboldt-Universität zu Berlin

von
MSc. Gauri Mukund Mangalgiri

Präsident der Humboldt-Universität zu Berlin
Prof. Dr.-Ing. Dr. Sabine Kunst

Dekan der Mathematisch-Naturwissenschaftlichen Fakultät
Prof. Dr. Elmar Kulke

Gutachter: 1. Prof. Dr. Martina Schmid
2. Prof. Dr. Oliver Benson
3. Prof. Dr. Isabelle Staude

Tag der mündlichen Prüfung: 28.02.2019

"To daddy's love for problem solving symbolised by the aluminium foil reflector we made together"

for MBM

Zusammenfassung

Der rapide Anstieg der Bevölkerung führt zu einer dramatischen Zunahme des Brennstoff- und Energiebedarfs. Längerfristig kann die nachhaltige Energieversorgung der Menschheit nur durch erneuerbare Energiequellen gewährleistet werden. Dies motiviert die Bemühungen um alternative, sauberere Brennstofftechnologien wie z.B. die Erzeugung von Wasserstoff.

Diese Arbeit untersucht die Verbesserung der optoelektronischen Eigenschaften von Silizium Photokathoden, durch optische Nanostrukturen, die die Reflexion mittels optischer Resonanzen reduzieren. Wir konzentrieren uns dabei auf die Entwicklung von Nanostrukturen , die optische Konzepte wie Mie-Resonanzen und periodische Indexprofilierung nutzen. Um diese optischen Nanostrukturen zu realisieren, verwenden wir zwei Herstellungsverfahren. Die Verfahren werden durch einen iterativen Ansatz optimiert, um zu den Nanostrukturen mit den gewünschten optischen Eigenschaften zu gelangen. Die erste Art von Nanostrukturen gehört zur Klasse der Meta-Oberflächen (Metasurfaces) und wird durch Elektronenstrahl-Lithographie und Top-Down-Herstellung implementiert. Die optischen Spektren dieser Strukturen werden dann mit Hilfe von Simulation und Experimenten eingehend untersucht. Die zweite Art von Nanostrukturen basiert auf Änderungen des Brechzahlprofils von dielektrischen periodischen Nanostrukturen. Diese Strukturen werden durch Maskenlithographie mittels Polystyrol-Kugeln hergestellt. Auch bei diesen Strukturen werden die optischen Eigenschaften vermessen und ihre physikalischen Bedeutung mit Hilfe von numerischen Simulationen analysiert.

Um den Einfluss dieser Strukturen auf die Kurzschlussstromdichten von Silizium Photokathoden zu demonstrieren, charakterisieren wir den Photostrom, der über einen Silizium-Elektrolyt-pn-Übergang mit und ohne Nanostrukturen gemessen wird. Zusammenfassend stellen wir einen Vergleich der Antireflexionseigenschaften der beiden entwickelten Strukturen sowie eine Verbesserung der photoelektrochemischen Funktionalität vor. Daraus leiten wir Ideen für zukünftige Oberflächendesigns ab, welche die noch bestehenden Nachteile beider Strukturen überwinden.

Abstract

Global fuel and energy demands continue to increase due to the rapid rise in population and the dependence of this increasing population on exisiting energy resources for its sustainance. This has led to efforts in developing cleaner fuel sources such as hydrogen generation. This thesis focuses on demonstrating the optical benefit of nanostructures to improve the optoelectronic functioning of silicon photocathodes which aid in hydrogen generation via nanostructured antireflection.

We lay our focus on the development of nanostructures which utilise optical concepts such as Mie type resonances based on metasurfaces and periodic index profiling. Computational design is used to obtain structure parameters for achieving desired effects. To implement these optical effects we take aid of two methods of fabrication. These fabrication methods are optimised via iterative trials to arrive at nanostructures of high quality. The first type of nanostructures belong to the metasurface class. These are implemented by e-beam lithography and top down processing. The optical spectra are then comapred with aid of simulation and experiments. The second type of nanostructures belong to the class of gradually varying periodic nanostructures. We obtain these via iterative fabrication using colloidal mask lithography. In a subsequent step we analyse experimentally their optical spectra and with aid of simulations analyse their physical implication.

To demonstrate an optical benefit of these structures on enhancing the short circuit current densities of silicon photocathodes, we characterise the photocurrent measured across the silicon-electrolyte pn-junction with and without nanostructures and evaluate this increase. In conclusion, we provide a comparison of the antireflection properties offered by the two developed structures as well as in terms of improving photoelectrochemical environment. As an outlook, we propose ideas to overcome the existing drawbacks of both structures.

Contents

Chapter 1

Introduction

"There is a crack in everything, that's how the light gets in". This is a popular Leonard Cohen song line which could be used to describe the combined efforts of engineers, physicists and material scientists to use nanotechnology to crack through material limitations to achieve desired control in manipulating light. This often requires structuring of the materials at the nanoscale. These nanoscale materials possess unique light controlling properties which can be exploited to address challenges observed in the field of clean fuel generation, medicine and communication. In this thesis, we focus our attention on demonstrating an enhancement in hydrogen generation via efficient optical design of nanostructures. A clear design ideology defining the desired optical effects and its implementation via fabrication is the first step in demonstrating the benefit of nanostructure integration into fuel generation with the aid of solar energy.

General Motivation

Humankind, right from its inception has looked at the sun among other natural resources as an aid for sustainance for light, energy and food to foster innovation. Sunlight controls crop cycles and drives the operation of green energy technologies. Sunlight can be converted into electricity using photovoltaics (solar cells) or used to drive chemical reactions and produce solar fuels such as hydrogen with photoelectrochemical cells.[77, 26] These methods of energy production have the added benefit of being pure and renewable sources of energy. While a lot of effort has been put into optical optimisation of photovoltaic devices but not so much effort has been seen to improve hydrogen generation with photoelectrochemical cells.[72, 16] Since hydrogen is a valueable fuel for environment friendly applications such as hydrogen driven electric cars, it is important to optimise the solar hydrogen evolution reaction wherever it occurs. Our efforts are focussed towards optically optimising the hydrogen evolution reaction

which occurs at the photoelectrochemical interface of a semiconductor and an electrolyte. Our approach involves conceptualisation of nanophotonic structures along with their implementation to enhance semiconductor light absorption for hydrogen generation. Light enhancement in the semiconductor implies generation of higher number of photogenerated charge carriers.

Such an absorption enhancement requires the nanostructure to improve light coupling into the semiconductor. This requires the optical performance of the nanostructure to efficiently transfer light into the semiconductor. This light transfer requires optical effects that increase semiconductor light absorption. Nanostructuring materials to spectrally and directionally control light requires careful selection of material properties. These material advantages need to be complimented with suitable fabrication technology in order to get desired optical properties.

Moreover, optical effects such as resonances, non resonant light transfer or optical impedance matching need to be be conceptualised for the operational design. Design implementation of these phenomena should directly result in efficient light transfer into the semiconductor. This results in the formulation of a multivariable design problem. A qualitative design conceptualisation can be tested via numerical simulation via iterative parameter sweeps. Parameters obtained via these simulation values can be implemented via a suitable fabrication process. Another approach is to fabricate trial structures and optimise them depending upon outcome of measured optical spectra. Numerical simulation can then be sought to interprete the observed behavior. The utility and simplicity of the simulation is dependent on the efficiency with which the adopted design and fabrication sequence implements the envisioned optical design problem. This is determined by material selection and fabrication routine for nanostructuring.

Prelude

As an interesting prelude to the main content of this thesis, we briefly describe our first attempt to synthesise a nanostructure for optimising light control and efforts to use it in combination with a photoelectrochemical interface. Our attempt was based on nanostructuring of so called zinc oxide grass.

Electrodeposited zinc oxide is popularly referred to as zinc oxide grass and has been shown to exhibit promising optical and optoelectronic properties.[81] Owing to its grass like morphology, optically it functions as an effective medium consisting of zinc oxide and air. In order to add further degrees of design parameters related to nanostructuring, we started off

investigations for this doctoral thesis with an extra colloidal lithography masking step to electrodepositing zinc oxide.[85] Since these colloidal spheres are commercially avaiblable, we utilise two sizes i.e 300 and 900 nm, fairly near to the extreme ends of the visible spectrum (400-800 nm). Transparent conducting oxide substrates were patterned with colloidal masks of different sizes followed by electrodeposition. The obtained nanostructures are shown in figure 1.1. The structure was investigated for optical spectra in the visible range (300-800

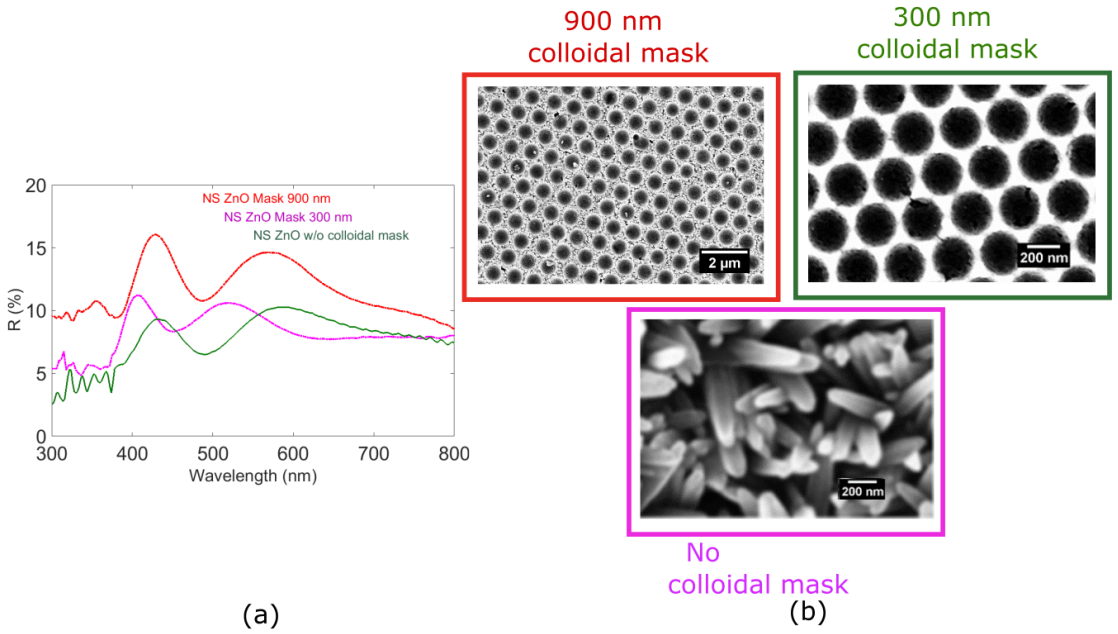

FIGURE 1.1: (a) Spectral reflection characteristics of electrodeposited zinc oxide with and without colloidal masks. (b) Morphological overview of different colloidal masks and bare electrodeposited zinc oxide.

nm) and compared with the spectra of the non-lithographically electrodeposited counterpart. For both normal and angular incidence, spectral signatures characteristic to the nanooptical effects as a result of the lithographic step were not observed. As an example we show the reflection spectra of electrodeposited zinc oxide and that of the lithographically deposited zinc oxide in figure 1.1(a). All three spectra indicate similar spectral trend but appear to be slightly shifted on the wavelength axis. While the mask size is significantly varied from 300 nm to 900 nm, the observed difference in optical spectra is not as significant. The patterened electrodeposited structure merely functions as an effective optical medium just like the electrodeposited zinc oxide grass. The step of patterning electrodeposited zinc oxide and creating hexagonal arrays of circular patterns seen in the figure above therefore did not add new features peculiarly characteristic to the variation of the lithographic mask. Moreover the combination of patterned zinc oxide grass on transparent conducting oxide does not offer optical effects such as antireflection or near field enhancement or nanostructured diffraction in the visible frequency range. Further attempts to utilise this nanostructure in photoelectrochemical measurements using metal oxide semiconductors such as copper bismuth oxide

($CuBi_2O_4$) for hydrogen evolution did not yield improved results. This can be attributed to the poor stability of zinc oxide in electrohydrolic environments. This entire analysis proved the heavy dependence of the process sequence and materials adopted for nanostructuring to effectively enhance the optical performance on one hand and to also seek for optoelectronic compatbility on the other.

These obtained results called for reconsidering the nanostructures in terms of material, fabrication methods and their optical response in order to prove optoelectronically benefical to solar energy applications.

Choice of materials and specific approaches

Titanium dioxide has gained tremendous popularity in the visible frequencies in the domain of nanostructured devices owing to its excellent optical properties. From structured flat lenses over to metasurfaces to resonant antireflection systems, nanostructures made out of high quality titanium dioxide have shown novel spectral properties in terms of engineering light.[64] It has a moderately high refractive index in the visible spectrum and zero optical loss. Planar layers of titanium dioxide can be easily deposited with processes yielding high material quality such as sputtering.[71] This establishes the material superiority of titanium dioxide and its ease of fabrication.

Gustav Mie showed that spheres and cylinders having dimensions same as the light wavelength, exhibit special scattering resonances.[89] Other nanoshapes such as blocks and columns also show similar behaviour.[41] These are referred to as Mie type resonances.[79].Two dimensional arrangements of nanostructures which exhibit novel optical properties as a result of nanostructured resonances are called metasurfaces.[114] With the aid of these metasurfaces it is possible to obtain complete transmission or reflection of light at different spectral positions.[79] Such metasurfaces based on Mie type resonances have proved to be of significant benefit in semiconductors such as gallium arsenide or silicon to trigger resonant peaks in the near and mid infrared frequency ranges.[41, 78] These frequency ranges correspond to the electromagentic spectrum where the material optical constants are all dielectric. Similar Mie type resonances can be triggered in the visible range by choice of adopting appropriate methods and all dielectric materials such as titanium dioxide. Such pronounced resonant effects are implemented due to combination of the lithographic method adopted as well as deep physical insight to carefully implement Mie resonances.[123] Mie resonances engineered via metasurfaces therefore are a good design approach to engineer novel light transfer properties.

One of the most abundant elements on earth, silicon is a common light absorbing semiconductor material in photovoltaics and photoelectrochemical devices. However, crystalline silicon reflects more than 30 percent of the incident light from the sun and suffers from relatively low optical absorption in the near infrared spectrum. Maximising light coupling into silicon, and thereby overcoming its highly reflective behavior has lead to several innovations in antireflection optics.[16]

In the view of unfavourable results obtained for the combination of dielectric oxides and semiconductor metal oxides and the strong potential which titanium dioxide holds in terms of material stability and optical tunability, we base the rest of this thesis on using titanium dioxide nanostructures to control silicon reflection. This two layer stack is used as an optically optimised photocathode in a three electrode system (photocathode, anode and counter-electrode) with an electrolyte to form the p-n junction between the electrolyte and the optically optimised photocathode. In the presence of visible sunlight i.e (sun), the photocathode absorbs light and releases two electrons into the electrolyte which results in the reduction of the hydrogen ions of the electrolyte to hydrogen gas. This reaction is the principal step of the hydrogen evolution reaction.

Antireflection with the help of nanooptical phenomenon is a well explored area and with the advent of modern fabrication technologies, different physical effects can be excited by employing lithographic patterning and subsequent processing.[93, 111, 55] In this thesis, we use two lithographic processes: e-beam lithography and colloidal lithography in combination with material growth and etching. E-beam lithography based process sequence is adapted to the outcome of the iterative parameteric sweeps from computational simulations to generate Mie type resonances in the visible spectrum for titanium dioxide. The colloidal mask based process sequence is optimised experimentally. The idea behind demonstrating two lithographic techniques is to investigate their different degree of tunability and impact in terms of exciting nanostructure optical response. The e-beam is highly precise and tunable to parameters suggested by simulation but expensive and ineffective in terms of scalability. This precision helps in implementing novel optical properties characteristic to metasurfaces. Contararily the colloidal masking is largely scalable but has limitations in terms of tunability. **The key approach of this thesis is demonstrating two nanostructures functioning on distinct optical effects. Optical measurements are used to characterise spectral response. Simulations are used to design the structures as well as provide an explantion for the measured spectra**

We now proceed to introduce the contents of thesis as distributed in the folllowing chapters.

Outline of thesis

In chapter 2 titled - **Fundamentals** we focus on all relevant concepts necessary to understand the working principle of optical nanostructures. These include the optical material constants of dielectric materials and the method used to measure them. We also describe standard optical phenomenon relevant to thin film optics such as Fresnel coefficients, interferences before describing basic antireflection theory. We elaborate on the theory of Maxwell equations which describe the light matter interactions. We also provide an overview of scattering and Mie type resonances in close connection with Mie theory. To describe the periodic arrangement of the nanostructures, we look at diffraction theory of nanostructured arrangements. We describe the numerical methods used for simulation and specifically focus on the finite element method and describe the solver used - JCMsuite. Towards the end of this chapter, we elaborate upon the hydrogen evolution reaction and indicate on the pn- junction formation between the photocathode and electrolyte interface.

In chapter 3 titled - **Antireflection - A review**, we describe different approaches of antireflection as found in the literature. We divide the examples in terms of the physical concepts used such as effective medium theory, dielectric resonances, plasmonics or multilayer films in order to couple light into the active optoelectronic material. We also describe the complementary approach of nanostructuring the active optoelectronic material to control reflection.

In chapter 4 titled - **Fabrication of nanostructures** we focus on the methods used to fabricate the two structures. We discuss the top down approach involving sputtering, e-beam lithography and reactive ion etching. Metasurfaces are obtained out of this fabrication method. The second approach discussed here is the iterative bottom up method involving sputtering and utilising collodial etch masks and results in the soupbowl structure. We describe the key parameters and show the morphological images via an electron microscope.

In chapter 5 titled - **Computationally Analysing Building Blocks of the Metasurface** we analyse with aid of simulating singulated nanostructures, the scattering properties of nanocylinders and nanofrustums. In this chapter, we highlight the importance of aspect ratio for obtaining good light scattering tendencies into silicon for different incident angles. We provide the demonstration of introducing a taper on the scattering cross section. Qualitative analysis from these simulations are performed.

In chapter 6 titled - **Comprehensive Analysis of Nanofrustum Metasurfaces** we carry out systematic numerical simulations to construct a well functioning antireflective nanostructured surface by analysing the spectral properties of the spectra for different material interfaces. The influence of the pitch of the nanostructure array in terms of controlling reflection is investigated. This approach gives parameters of the system. In order to get the reflection values to below 5 percent even at long wavelengths, we introduce a planar film between the silicon and the nanostructure. With this analysis, we provide optimisation guidelines at both short and long wavelengths. These measurements are compared with the simulations and a detailed overview of the performance at angular incidence is provided with the aid of numerical simulations. The structures are then characterised for photoelectrochemical performance.

In chapter 7 titled - **Comprehensive analysis of the bottom up fabrication approach** the fabricated of the so called soupbowl structure is optically characterised for normal and angular incidence. We also simulate the ideal structure with the obtained morphological dimensions. We give a detailed account about the differences observed and analyse the limitations of the existing fabrication method. Finally we conclude with demonstrating photoelectrochemical benefit of the structure.

In chapter 8 titled - **Evaluating struture functionality** we compare the antireflection performance of the two structures with respect to each other. We also compare the structures with respect to planar layers of titanium dioxide on silicon in order to prove the optical benefit of the employed techniques. Additionally we provide a brief comparison of the two structures with the heavily cited work by Spinelli et al. in [111] which focusses on titanium dioxide cylinders. Finally we show the difference in photoelectrochemical properties of the structures.

In **Conclusions and outlook** we provide a holistic overview of the most important conclusions that can be drawn from the investigations from this thesis. We also provide a qualitative outlook on how the performance of these structures can be improved on the optical and optoelectronic front.

Chapter 2

Fundamentals

The goal of designing an effective antireflection system requires understanding the interaction between light and matter. In this section, we elaborate upon the theory of different optical phenomena which occurs at material interfaces. We start with the basic principle of antireflection and extend the discussion to optics of thin films. This includes discussing optical interferences and their spectral dependance. We further introduce Maxwell equations as a starting step to account for nanostructured resonances. The discussion also includes the specific resonant properties of the nanostructures as described by Mie theory. The design goal is to make efficient use of the optical properties of nanostructures in terms of antireflection. This often results in periodic arrangement of nanostructures. Such a periodic arrangement has characteristic optical properties which is described by the theory of photonic crystals and diffraction. We also describe metasurfaces a special class of periodic nanostructures. No analytical solutions exist to combine the myriad optical phenomena in a given nanostructured material at optical interfaces with a certain geometry. However numerical techniques have been developed to solve the parametric formulation of the Maxwell equations over a domain. We briefly summarise numerical methods used to simulate electromagnetic fields in photonics. The results described in this thesis are obtained with the aid of the finite element technique implemented by the commerical software package - JCMsuite. We conclude this section by describing the intended photoelectrochemical action and corresponding properties.

2.1 Light propagation in matter

2.1.1 Optical material properties

Light propagation in any given medium is governed by its instrinsic optical material properties. These are described via relative permittivity and relative permeability with reference to vacuum. In common formulation, the optical constant is given by the square root of the

dielectric permittivity and permeability of the material. For non-magentic materials this is equivalent to the square root of the dielectric permittivity. It consists of a real and an imaginary part. The real part is referred to as the refractive index. The imaginary part is called the absorption loss coefficient. Both these values play an important role in controlling the electromagnetic response of the material.[4] In this thesis we confine our study to dielectrics and semiconductors in the visible wavelengths of light between 400-800 nm. We mainly confine ourselves to titanium dioxide as the dielectric. Titanium dioxide has excellent optical properties - a high to moderate refractive index value as well as no losses in the aforementioned bandwidth.[121] We discuss in this thesis reflection control for p - type silicon to use it as photocathodes. The equations describing the relative dielectric permittivity [51] are as follows

$$\tilde{n}(\lambda) = n(\lambda) + ik(\lambda) \tag{2.1}$$

$$\epsilon_r(\lambda) = (\tilde{n}(\lambda))^2 \tag{2.2}$$

Here $\tilde{n}$ is the optical dielectric constant with real and imaginary parts n and k which vary with the wavelength λ. ϵ_r is the relative permittivity. The relative dielectric permittivity of a given material is always described relative to the permittivity of free space ϵ_0. Titanium dioxide in this thesis is synthesised via sputtering. The resulting dispersive properties of the processed film are obtained via ellipsometric measurements.[38] Ellipsometry derives optical material constants by measuring the change in amplitude and phase of p and s components of light upon reflection or transmission.[43] A reference beam is the integral part of the measurement. The schematic of the measurement system used is shown in figure 2.1 based on [46]. Linearly polarised light with s and p components is incident on the sample. The

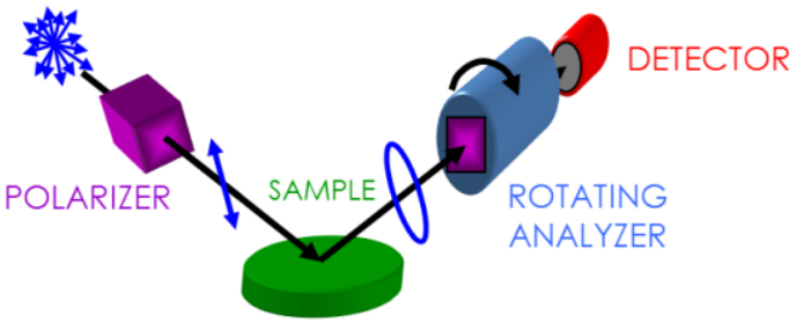

FIGURE 2.1: Schematic of the ellipsometric measurements to extract optical constants of titanium dioxide adapted from [37]

linearly polarised light reflects from the sample surface and travels through a continously rotating polariser referred to as the analyser. The amount of light that passes across the analyser depends on the polariser orientation relative to the elliptical electric field generated after light incidence from the sample. This light is then converted into electronic signal by the detector. This information is compared to the known input polarisation to determine the

polarisation change caused by the sample polarisation. These measurements are referred to as ψ and δ.[46] ψ is the reduction in amplitude upon reflection and δ is the phase difference induced by the reflection.

After having measured the changes in polarisation due to reflection from the given sample, the next step is to analyse the data. The aim of the ellipsometeric measurement is to measure the changes in light polarisation to determine the sample's properties such as film thickness and optical constants. In the case of homogenous thin films, the equations derived for a single reflection are reversed to provide the dielectric constants from the ellipsometry measurement.[35] However most of these measurements involve multi layer stacks which necessitates regression analysis between the measured data and the assumed model till a perfect fit is achieved. A starting set of optical constants are used to start the fit with the measured data. A regression analysis involving considerations for material properties such as material bandgap, free charge carrier density and roughness models and the dispersive trends observed in optical constants, results in obtaining the right fit between the measured data and the model and thereby the right optical constants.

The Lorentz oscillator model formulates electromagentic interaction of matter at the microscopic level. It describes all electromagnetic forces as a function of the electric fields acting on a charged particle in a material.[42] An applied electric field interacts with the charge of an electron causing equivalent stretching or compression observed in a spring mass system in accordance to Hooke's law, which results in an oscillatory motion of the electron. The total force acting on the electron is equated to the spring force. Other forces such as material damping γ are also included in the model. The Lorentz oscillator model is thus equivalent to a classical damped driven oscillator: where P being the polarisation, ω_0 the natural frequency, N is the density of charged particle e - electrons, m - electronic mass and E_y is the electric field component

$$\frac{d^2P}{dt^2} + \gamma\frac{dP}{dt} + \omega_0^2 P = \frac{Nq^2}{m}E_y \tag{2.3}$$

Derivation of the solution of this equation in the time domain is fairly cumbersome. This is overcome by taking the Fourier transformation of the above equation. This replaces all time derivatives with a proportional $j\omega$ factor. This provides a final solution to the polarisation as a function of the frequency (wavelength) and the applied electric field E_{oy}.

$$\tilde{P}(\omega) = \frac{\epsilon_0\omega_p^2}{(\omega_0^2 - \omega^2 + j\gamma\omega)}E_{oy} \tag{2.4}$$

As the constitutive equations between the electric field and polarisations also involve the material constants such as relative permittivity and susceptitibility, (explained in section

2.1.3) [51] this results in the following

$$\tilde{\epsilon}(\epsilon_0) = 1 + \frac{\omega_p^2}{(\omega_0^2 - \omega^2 + j\gamma\omega)} \tag{2.5}$$

The equation above shows a dispersive relation between the material constants and the wavelength. Here ω_p is the referred to the plasma frequency of the material and is expressed by $\frac{Nq^2}{m}$. This dispersion relation is fitted to ellipsometric measurements. The obtained data for titanium dioxide obtained via ellipsometeric measurements and subsequent calculations form the basis of all design approaches described in this thesis. Moreover it also helps in comparing the measured optical spectra to the simulated counterparts. Proper minimisation of the difference between measured and modeled spectra and subsequent scientific interpretations requires generation of accurate optical data from such measurements.

There are several models which describe the dispersive trend of the optical constants. These models correspond to dispersive trend of permittivity as derived by the harmonic oscillator treatment. These models are solutions in the form of polynomial expansions to the harmonic oscillator model valid for free charge carriers expressing the dielectric constant as a function of wavelength and other numerical values.[32] Common models for dielectric materials such as oxides are the Cody-Lorentz and Cauchy Lorentz models.[76]

2.1.2 Fresnel coefficients and basic antireflection theory

Fresnel equations describe the light propagation at an planar interface formed between materials with different optical properties. They quantify the amount of light reflected and transmitted at each material interface as a function of the refractive indices as well as incident angle and light polarisation.[90] Boundary conditions are defined for the electric or magnetic field for the tangential and longitudinal components. These tangential and longitudinal components are defined with respect to the plane of the interface. p- polarised (parallel) light by convention is referred to the case when the electric field lies in the plane of propagation and the magnetic field is in the tangential plane. s- polarised (senkrecht) light by convention is referred to the case when the magnetic field lies in the plane of propagation and the electric field is in the tangential plane. For s-(senkrecht) polarised light, the total magnetic field in the plane of the interface is continous. For p-(parallel) polarised light, the total electric field in the plane of the interface is continous. The distribution of fields is shown in figure 2.2 for both polarisations. **E**, **B** and **k** in the figure are the electric, magnetic and propagation vector. The indices i, t, r represent the relevant quantities with regards to the incident, transmitted and reflected light fields. The continuity conditions in the fields for both longitudnal and tangential components across the interface give rise to equations for

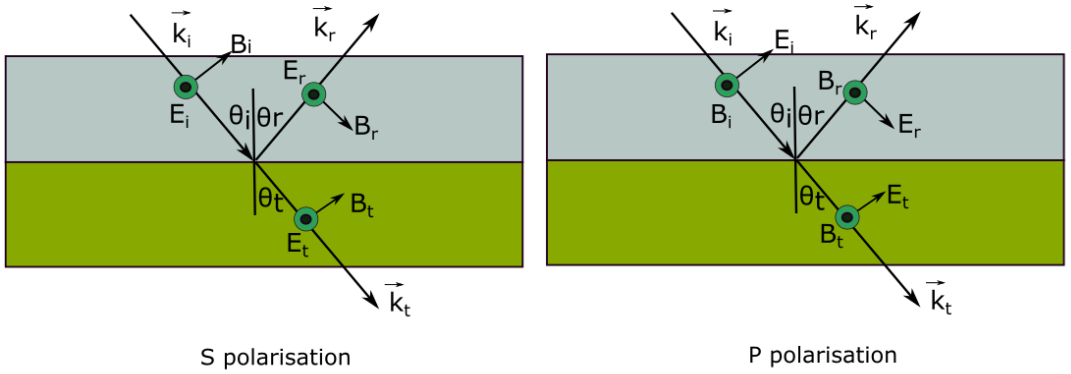

FIGURE 2.2: Electric and magnetic fields across an interface for s- and p- polarised light which sets up conditions for Fresnel coefficients. The explicit directions of the fields are indicated in both scenarios to indicate the compenents at each interface used to calculate the fresnel coefficients.

the reflected fields in terms of the incident fields. The ratio of the magnitude of the reflected electric field to that of the incident electric field magnitude is referred to as the reflection coefficient. Since we mainly focus on controlling reflection in this thesis, we provide the value of reflection coefficient derived from the continuity conditions for both s- and p- polarised light.[47]

$$r_s = \frac{n_i \cos(\theta_i) - n_t \cos(\theta_t)}{n_i \cos(\theta_i) + n_t \cos(\theta_t)} \tag{2.6}$$

$$r_p = \frac{n_t \cos(\theta_i) - n_i \cos(\theta_t)}{n_i \cos(\theta_t) + n_t \cos(\theta_i)} \tag{2.7}$$

Here r_s and r_p represent the reflection coefficients for s- and p- polarised light. These coefficients are derived using field equations. In presence of optically absorbing materials, these coefficients become complex.

Reflectance is obtained from the ratio of the power or intensity of the wave that is reflected to the power or intensity of the incident wave. This translates to the ratio of the square of the magnitude of the reflected electric field to the square of the magnitude of the incident electric field as shown in the equation 2.8.

$$R = \frac{\left\|\vec{E}_r^2\right\|}{\left\|\vec{E}_i^2\right\|} \tag{2.8}$$

where $\vec{E}_r$ is the reflected electric field and $\vec{E}_i$ is the incident electric field. Similar approach is followed to obtain the transmittance of the system. For a non absorbing system, the sum of reflectance and transmittance should be equal to one. In presence of optical loss, reflectance, transmittance and absorptance should add to one. Conventionally these quantities are

referred to the reflection, transmission and absorption while respecting their mathematical significance.

Interference is an important phenomemon in optics and gives rise to peculiar spectral responses which find applications from lithography to hologoraphy. Optical interference is based on the superposition principle.[94] Two light waves qualitatively superimpose with each other and generate a wave with characteristic properties. Significantly strong spectral contributions arise in the form of interference spectra upon light interaction with material features including planar films having comparable thickness as the incident light. In terms of designing nanostructured antireflection, interference control is important in spectral regions where the nanostructure is not resonant or does not exhibit specially configured optical modes. In these spectral areas, the nanostructure should ensure destructive interference of the reflected waves at the air - nanostructure and nanostructure-substrate interface. This is one of the design guidelines in designing the nanostructured system. Such a destructive interference can be achieved by deploying nanostructures of shapes which allow gradual variation of refractive index profiles.

One of the optical design goals of this thesis is to minimise reflection at the air-silicon interface. Most of this reflection is a result of the high refractive index of silicon in comparison to air. Its average value is 4 in the visible spectrum. In order to minimise this reflection, a material with suitable refractive index is used to couple light into silicon. The thickness and optical properties of this material should minimise the reflection which occurs as a result of the interference between rays reflected at the air-antireflection material interface (A) and the silicon - antireflection material interface (C). In order to cancel out this interference, the two waves (A) and (C) need to destructively interfere. From figure 2.3, for perpendicular light incidence, it can be deduced that the path difference between the two waves is expressed in equation 2.9.

$$\Delta path_{A,C} = 2t_{film} \tag{2.9}$$

The difference in number of waves between A and C is given by

$$\Delta waves_{A,C} = \frac{2t_{film}}{\frac{\lambda}{n_{AR}}} \tag{2.10}$$

where n_{AR} is the refractive index of the antireflection material. A destructive interference between A and C can only occur if the phase difference between the waves from the two interfaces is an odd multiple of 180°.[82] Equivalently, this refers to the fact that the number

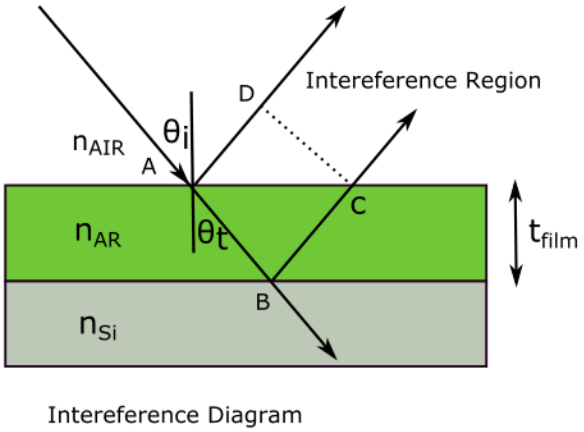

FIGURE 2.3: Sketched schematic indicating interferences arising on account of a thin film

of waves between A and C is 0.5 or odd multiples of 0.5.

$$\frac{2t_{film}}{\frac{\lambda}{n_{AR}}} = 0.5(m + \frac{1}{2}) \tag{2.11}$$

where m = 0,1,2,3 ... The resulting expression for the thickness of the film is then given by

$$t_{film} = (m + \frac{1}{2})\frac{\lambda}{4n_{AR}} \tag{2.12}$$

This condition in equation 2.12, known as the phase condition, sets up the condition for the thickness of the film.[65] In order to minimise the amplitude of the destructive interference and thereby achieve significant gain in antireflective properties we go back to the reflection amplitudes of the two waves at the two described material interfaces predicted by Fresnel's theory. For a planar interface, the ratio of the reflected to incident power is reduced to the square of the Fresnel reflection coefficient. We use this to calculate the reflection R_1 in equation 2.13 which corresponds to the reflection which occurs at the air (n_{air}) - antireflection film (n_{AR}) interface. The reflection at the interface at the anti reflection film n_{AR} and silicon is given by R_2 in equation 2.15.

$$R_1 = (\frac{n_{AR} - n_{air}}{n_{AR} + n_{air}})^2 \tag{2.13}$$

$$R_2 = (\frac{n_{silicon} - n_{AR}}{n_{silicon} + n_{AR}})^2 \tag{2.14}$$

For the out of phase condition to hold true, the difference

$$R_1 - R_2 = 0 \tag{2.15}$$

$$n_{AR} = \sqrt{n_{Si} n_{air}} \tag{2.16}$$

This bound on the refractive index of the antireflection film is called as the amplitude condition. The amplitude and the phase condition together decide the design of the antireflection layer. The obvious drawbacks of such a film is that optical properties of standard optical materials do not satisfy the conditions desribed by the above equations for all wavelengths owing to dispersive properties unique to all materials. This calls for rendering new optical properties with the aid of nanostructures at material interfaces. Such nanostructures result in spatial and phase variations across different material interfaces.[55] This requires simultaneous solutions to all electric and magentic fields.

The above conditions were derived for normal incidence, for oblique incidence one needs to separate the Fresnel coefficients for both s- and p- polarisations. It is relatively easier to derive this condition based on an admittance theory approach taking aid of fields at the interface.[83] The optical admittance at the interface between air and the antireflection material as a result of the antireflection material can be defined in terms of the complete electric and magnetic fields at the point as following

$$Y = \frac{H_A}{E_A} \tag{2.17}$$

Considering the relationship between the fields at interfaces A,B and the phase factor (δ) from A to B, this admittance is derived as the following

$$Y_{AR} = \frac{\eta_{si} cos(\delta) + i\eta_{AR} sin(\delta)}{cos(\delta) + i(\frac{\eta_{si}}{\eta_{AR}}) sin(\delta)} \tag{2.18}$$

Here η_x is the optical admittance of each medium and is given by the ratio of the magnetic field to electric field. The generalised phase factor (δ) is given by $\delta = \frac{2\pi N_{AR} t_{film} cos(\nu)}{\lambda}$, where ν could be complex. The reflectance of such a system can be given by

$$R = \frac{\eta_{air} - Y}{\eta_{air} + Y} \left(\overline{\frac{\eta_{air} - Y}{\eta_{air} + Y}} \right) \tag{2.19}$$

To arrive at the zero reflection condition, the complex conjugate product in 2.19 must be set to zero. This will then lead to constitutional relations for the thickness t_{film} and the refractive index N_{AR}. Another approach to tackle antireflection is analogous to the smith chart of impedance matching in electronic circuits. It involves generalised treatment for optical impedance matching can be found in [65, 83], where the impedance between two dielectric interfaces is expressed as a function of the amplitudes of the electric fields and

Poynting flux. Such a treatment can be used to derive parameters for more multivariable systems such as material profiles and multilayer systems.

2.1.3 Propagating fields

Propagation of electromagnetic energy such as light through matter is described by Maxwell's equations. This set of equations describes with the electromagentic fields at any given point in three dimensional real space at a given instant of time.[51] This is defined by four real valued vector fields which describe the electromagnetic response of the system: the electric field strength **E**, the magnetic field strength **H**, the electric flux density **D** and the magentic flux density **B**. The sources of the electric and magnetic fields consist of a scalar quantity- the macroscopic charge distribution ρ - and macroscopic electric current density **j**.[51, 116] The Maxwell equations along with their characteristic names are enlisted below.

Faraday's law of induction

$$\frac{\partial \mathbf{B}}{\partial t} + \nabla \times \mathbf{E} = 0 \tag{2.20}$$

Columb's law

$$\nabla \cdot \mathbf{D} = \rho \tag{2.21}$$

Ampere's law

$$\frac{\partial \mathbf{D}}{\partial t} - \nabla \times \mathbf{H} = -\mathbf{j} \tag{2.22}$$

Absence of magnetic monopoles

$$\nabla \cdot \mathbf{B} = 0 \tag{2.23}$$

Faradays law and Ampere's law together are referred to as the time dependent Maxwell equations and are utilised in laying the framework of numerical methods in electromagnetics. Boundary conditions imposed on the Maxwell equations for a given material system result in scattered, propagating or resonant solutions. The electric and magnetic field vectors are connected via the following constitutive equations.

$$\mathbf{D} = \epsilon_o \mathbf{E} + \mathbf{P} \tag{2.24}$$

$$\mathbf{B} = \mu_o \mathbf{H} + \mathbf{M} \tag{2.25}$$

The constants ϵ_o and μ_o are called vacuum permittivity and permeability and are connected to the speed of light. Their ratio defines the vacuum impedance. The polarisation **P** and magnetisation **M** correspond to the electric and magnetic dipole moments in a unit volume of a material. For a material showing linear non-dispersive susceptibility they can be defined as

$$\mathbf{D} = \epsilon_o \epsilon \mathbf{E} \tag{2.26}$$

$$\mathbf{B} = \mu_o \mu \mathbf{H} \tag{2.27}$$

The Maxwell equations along with the material constitutive relations are capable of accounting for all electromagnetic phenomenona. For ease of handling of electromagnetic problems each of these four equations and the material constitutents are converted from time domain to frequency domain. On combining Faraday's law with the Ampere's law in the frequency domain, we get the following equation consisting of only one field vector, either electric or magnetic. We show below the above set of equations derived into a single second order equation for the electric field and the impressed current density j_i .

$$\nabla \times \mu(r,\omega)^{-1} \nabla \times \mathbf{E(r)} - \omega^2 \epsilon \mathbf{E(r)} = i\omega j_i \tag{2.28}$$

Equation 2.28 is referred to as the electromagnetic wave equation and it is the starting step to investigate all light propagation.[115] Solutions to this equation consist of electric and magentic fields. These fields provide an overview of the spectral distribution of the the total electromagnetic energy. This is conventionally quantified by the Poynting vector. In the course of the thesis, the Poynting vector is useful to decribe the energy flux after scattering at resonant structures. The analytical formula of the Poynting vector is given by

$$S = \frac{1}{\mu_0} \mathbf{E} \times \mathbf{B} \tag{2.29}$$

For spherical and cylindrical resonator shapes analytical solutions for the scattered field are derived by Mie theory. However for all other shapes, aid of numerical simulations is necessary. These simulations first solve for the scattered electric and magnetic fields. These are then used to calculate the outgoing Poynting flux. The ratio of the outgoing Poynting field from a light scatter flux to the input incident field flux normalised by its cross sectional surface area is called the scattering cross section.

2.1.4 Scattering and Mie resonances

The total electromagnetic response of a system consists of the sum of the absorbed, the scattered field and the incident fields.[89] The classically defined electromagnetic scattering problem considers this full response of a particle upon light incidence. This light matter interaction has been studied by Gustav Mie in the formulation of Mie theory. Mie derived an analytical solution for the plane wave incidence on a spherical or cylindrical particle. The incident plane wave is expanded into an infinite series of vector speherical harmonics and the boundary conditions are fullfilled.[15] This section is based on the direction of many abridged versions of this analytical treatment which have been used in many design applications based on Mie theory.[87] Mie coefficients a_m and b_n are associated with the electric and magnetic fields which result in the scattering cross section. These vector spherical harmonics are special

vector functions which are solutions to the vector wave equation. The vector wave equation is generated from scalar functions which solve the scalar wave equation. We assume a plane wave traveling parallel to the z axis with the E field pointing along the y direction. Similar treatment could be given to a plane wave traveling along a given direction.

$$\mathbf{E}_{inc} = E_0 e^{ik_z z} \hat{\mathbf{e}}_y. \tag{2.30}$$

Where E_0 is the incident field amplitude, i is the imaginary constant, k_z is the z component of the propagation wave vector, z is the distance along the z axis and $\hat{\mathbf{e}}_x$ is the unit vector of the x axis. The scalar wave equation in the general form is given by

$$\nabla^2 \psi + k^2 \psi = 0. \tag{2.31}$$

The solution to this equation in spherical coordinates by using the variable separation method results in the following equations,

$$\psi_{emn} = \cos(m\phi) P_n^m(\cos\theta) z_n(kr), \tag{2.32}$$

$$\psi_{omn} = \sin(m\phi) P_n^m(\cos\theta) z_n(kr). \tag{2.33}$$

where r is the radial coordinate, θ is the polar angle and ϕ is the azimuthal angle. The integer indices m, n, k indicate all possible solutions to ψ values. The subscript e and o distinguish the solutions in terms of symmetry of the function which explictly maps to the azimuthal angle. The Legendre polynomials determine the explicit dependence with the polar angle θ. The radial dependence is given by the Bessel functions of the first, second, third and fourth kind. Based on these solutions, vector functions are generated. They are orthogonal to each other and given by

$$\mathbf{M} = \nabla \times (c\psi), \tag{2.34}$$

$$\mathbf{N} = \frac{\nabla \times \mathbf{M}}{k}, \tag{2.35}$$

where c is a constant, k is the wavenumber and ψ is the solution to the scalar wave equation. These vector functions represent the different field modes possible. The M type electric modes correspond to modes which do not contain a radial magnetic field and are refered to as the electric type modes. The magnetic field in these types of modes is only present in the transverse plane. The N type fields describe magnetic modes with no radial electric field. The electric field is present in the form of transverse components. Both functions, M and N have an explicit dependence on ψ. ψ in turn is dependent on the odd and even radial, polar and azimuthal functions. This gives a combination of 8 different functions to specify the vector fields.[89, 15] The objective of Mie theory is to solve for scattered fields. We first express the incident field with the aid of the above established vector functions, this is given

by,

$$\mathbf{E}_{inc} = E_0 \sum_{n=1}^{\infty} i^n \frac{2n+1}{n(n+1)} (\mathbf{M}^1_{o1n} - i\mathbf{N}^1_{e1n}), \tag{2.36}$$

$$\mathbf{H}_{inc} = \frac{-k}{\omega\mu} E_0 \sum_{n=1}^{\infty} i^n \frac{2n+1}{n(n+1)} (\mathbf{M}^1_{e1n} + i\mathbf{N}^1_{o1n}), \tag{2.37}$$

The superscript 1 refers to the type 1 bessel function used to determine the radial dependence. The scattered electric and magnetic field is expressed in terms of the incident field in the following equations,

$$\mathbf{E}_s = \sum_{n=1}^{\infty} E_n (ia_n \mathbf{N}^3_{e1n} - b_n \mathbf{M}^3_{o1n}), \tag{2.38}$$

$$\mathbf{H}_s = \frac{k}{\omega\mu} \sum_{n=1}^{\infty} E_n (ib_n \mathbf{N}^3_{o1n} - a_n \mathbf{M}^3_{e1n}). \tag{2.39}$$

Here, E_n and H_n are the n^{th} coefficients of the expansion for the incident field. The expression of this field is given by $i^n E_o \frac{2n+1}{n(n+1)}$ The superscript 3 refers here to the type 3 Bessel function used to express radial dependence. a_n and b_n are called the Mie coefficients and their values are determined by boundary conditions at the interface of the sphere. A similar set of expansions has been derived by Mie for cylindrical coordinates. The electric and magentic fields in the interior of the sphere is given by

$$\mathbf{E}_i = \sum_{n=1}^{\infty} E_n (c_n \mathbf{M}^1_{o1n} - id_n \mathbf{N}^1_{e1n}), \tag{2.40}$$

$$\mathbf{H}_i = \frac{-k_i}{\omega\mu_i} \sum_{n=1}^{\infty} E_n (d_n \mathbf{M}^1_{e1n} + ic_n \mathbf{N}^1_{o1n}), \tag{2.41}$$

where k_i and μ_i are the wave number and permeability inside the sphere, respectively. In order to solve for the coefficients a, b, c, d we introduce the Riccati-Bessel functions and assume that magnetic permeability of the sphere and the outside is equal to 1. This is assumption is true for non magentic materials.

$$\psi_n(x) = x j^1_n(x), \tag{2.42}$$

$$\xi_n(x) = x h^1_n(x). \tag{2.43}$$

This simplifies the intimidating mathematics of the above equations and results in the coefficients to give the following values

$$a_n = \frac{m\psi_n(mx)\psi_n^{'}(x) - \psi_n(x)\psi_n^{'}(mx)}{m\psi_n(mx)\xi_n^{'}(x) - \xi_n(x)\psi_n^{'}(mx)}, \tag{2.44}$$

$$b_n = \frac{\psi_n(mx)\psi_n^{'}(x) - m\psi_n(x)\psi_n^{'}(mx)}{\psi_n(mx)\xi_n^{'}(x) - m\xi_n(x)\psi_n^{'}(mx)}, \tag{2.45}$$

$$c_n = \frac{m\psi_n(x)\xi_n^{'}(x) - m\xi_n(x)\psi_n^{'}(x)}{\psi_n(mx)\xi_n^{'}(x) - m\xi_n(x)\psi_n^{'}(mx)}, \tag{2.46}$$

$$d_n = \frac{m\psi_n(x)\xi_n^{'}(x) - m\xi_n(x)\psi_n^{'}(x)}{m\psi_n(mx)\xi_n^{'}(x) - \xi_n(x)\psi_n^{'}(mx)}. \tag{2.47}$$

The important parameters in these coefficients are the size x and the relative refractive index m which are defined as

$$x = kr, \tag{2.48}$$

$$m = \frac{n_p}{n}, \tag{2.49}$$

where r is the sphere radius and n_p and n are the refractive index of inside and outside the sphere, respectively. Returning to the previous definition of n as the summation subscript for the expansion, we see that as the value of n increases, the value of all of these coefficients will eventually become negligible, meaning that the infinite sums for the fields can be evaluated since above a cutoff value for n, all the coefficients are negligible. With the aid of these vector spherical harmonics, a complete expression of the scattered field solution is available. For a comparison to far field measurements, the cross sections in the far field are needed. We now have the complete description of the fields inside and outside of the sphere. These fields can be used to derive the definitions of the scattering and extinction cross section. These cross sectii are calculated as a ratio of the Poynting vector definitions inside and outside the sphere with the aid of E and H fields and the input incident power. They are then normalised to the cross sectional area of the sphere. This results in the following equations

$$Q_{sca} = \frac{2}{x^2}\sum_{n=1}^{\infty}(2n+1)(|a_n|^2 + |b_n|^2), \tag{2.50}$$

$$Q_{ext} = \frac{2}{x^2}\sum_{n=1}^{\infty}(2n+1)\,\mathrm{Re}(a_n + b_n). \tag{2.51}$$

These scattering cross sectii also determine the order terms of the electric or magnetic multipolar response and are the basis to calculate cross sections. The most fundamental effect harnessed to give different optical properties consist of effects based on Mie theory. For dielectric materials owing to negligible loss, most of the incident light is converted into scattering on account of dipolar magnetic and electric type of resonances depending upon the incident frequency and material refractive index. For the spherical shape, the fundamental

order mode is the magnetic dipole. The next higher order mode is the electric dipole. Other easily excitable modes are the quadruple and octapolar modes. In the visible spectrum, with most dielectric spheres and cylinders, dipolar resonances are commonly observed. Due to low loss in this frequency range, barely any light is absorbed and most of the light is scattered. We show in figure 2.4, the electric field distributions in a sphere in the plane of polarisation

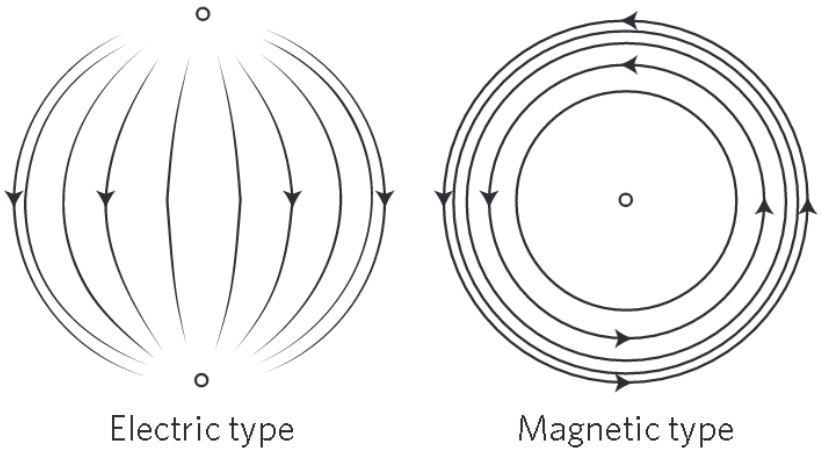

FIGURE 2.4: Electric field lines of the electric and magnetic coefficients of dipolar Mie modes of a spherical particle as derived by Mie [15]

for an electric and magnetic dipole. These distributions are obtained for the most simple case described in equations in 2.31-2.34. Most of these modes are seen as peaks in the scattering cross section spectra.[78] While these field expansions and modes are strictly derived for spherical coordinates, they can also be extended to other geometries where the aspect ratios are similar to those of a sphere. This includes blocks, cubes and other geometrical shapes where the lateral and longitudnal dimensions are not too different from each other.[41] These modes in literature are referred to as the Mie type modes and have been popularly extended to nanostructures to achieve different properties.

These Mie type resonances, have played an important role in inducing in peculiar spectral properties which are otherwise not found in common dielectrics. However, these spherical systems are hard to implement with the aid of standard lithographic techniques. The important criteria of extending classical Mie resonances to other geometries is identifying the electromagnetic distribution in the plane of polarisation. The electric and magnetic field distributions in these alternate geometrical shapes should directly correspond to the field distributions as calculated by Mie theory. Only when the fields in the nanostructures correspond to those of a sphere, the structure is said to have Mie type resonance.[114] The scattering cross section of non spherical geometries in this thesis is numerically calculated with the aid of numerical simulation programs.[45] We essentially maintain the scattering cross section formulation and calculate with the aid of numerical simulations the ratio of the power flux on account of the scatterer to the input incident area.

2.1.5 Periodic nanostructures

Nanostructured antireflection often involves periodic arrangements of nanostructures. These arrangements typically result in regular spatial variation of the dielectric constant across the material. The electric field satisfies the Bloch periodic boundary condition

$$\mathbf{E}(\mathbf{x}+\mathbf{a}_i) = \mathbf{E}(\mathbf{x})e^{(i\mathbf{k}_B\mathbf{a}_i)} \tag{2.52}$$

Where k_B is the given Bloch vector for one or more lattice vectors a_i located in the xy plane. The z propagating field has upward and downward directional components. These directional components are written in terms of their transverse and longitudinal coordinates.

$$\mathbf{E}(\mathbf{x}_\perp, z) = E_\uparrow(\mathbf{x}_\perp, z) + E_\downarrow(\mathbf{x}_\perp, z) \tag{2.53}$$

The intensity of these field components is determined by the nanostructure scattering and resonant properties. Moreover as a result of the periodic arrangement, the propagating k-vector of the electromagnetic light field is given by[19]

$$\vec{k} = \vec{k}_0 + G_{m_1,m_2} \tag{2.54}$$

where G_{m_1,m_2}

$$G_{m_1,m_2} = m_1\frac{2\pi}{p}\vec{x} + m_2\frac{2\pi}{p}\vec{y} \tag{2.55}$$

Here G_{m_1,m_2} is the reciprocal lattice vector which is the numerical inverse of of the nanostructure pitch -p. m_1 and m_2 are integer values. This could result in two types of k vectors, real and complex. Depending upon the value, the electric field could be propagating or evanescent. Diffraction orders contain all k vectors corresponding to a propagating field. Solutions to all possible k vectors are obtained by solving the Maxwell equation expressed in the form in the frequency domain. The following equation essentially combines the two time dependent Maxwell equations.

$$\boldsymbol{\nabla} \times \epsilon(\mathbf{r})^{-1}\boldsymbol{\nabla} \times \mathbf{H} = \frac{\omega^2}{c^2}\mathbf{H} \tag{2.56}$$

This process requires splitting the wave propagating vector in different directions. We elaborate this process for a one dimensional periodic system, with periodicity assumed along the x direction and a wave travelling along the z direction.[20] We assume light travelling from air ($n_1 = 1$) via a medium with index n_2 to a periodic system with index n_3 in figure 2.5. This results in the following equations for the k vector in each of the media 1, 2, 3

$$(k_x + G_n)^2 + (k_z^{1,n})^2 = \frac{\omega^2}{c^2} \tag{2.57}$$

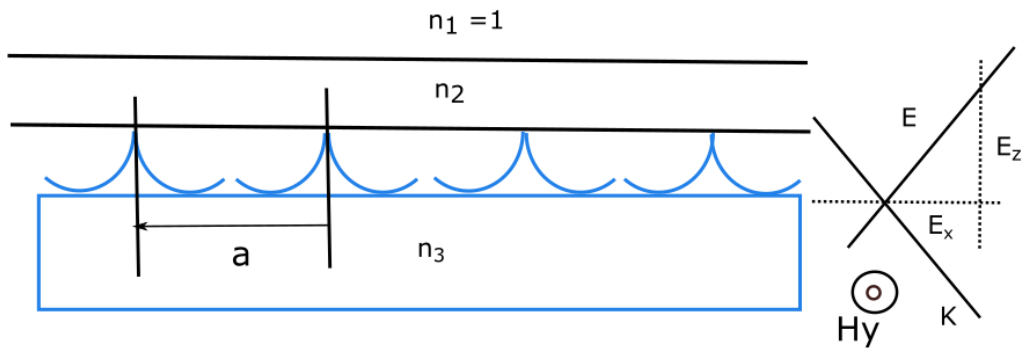

FIGURE 2.5: An illustration of a system peroidic in the x direction with orientations of the electric and magnetic fields. We illustrate in the subsequent equations trends of electric and magnetic fields as a result of periodic lattice propagation

$$(k_x + G_n)^2 + (k_z^{2,n})^2 = \frac{\omega^2}{c^2} n_2^2 \tag{2.58}$$

$$(k_x + G_n)^2 + (k_z^{3,n})^2 = \frac{\omega^2}{c^2} n_3^2 \tag{2.59}$$

Here $G_n = 2\frac{n\pi}{p}$ for all integer values of n. Electric and magnetic fields in each of the regions are expanded to give rise to the following equations. The fields in air contain the electric and magnetic components of the incident field as well as the reflected diffracted orders. For a representational purpose, we elaborate field equations for the transverse magnetic polarisation. This implies that the magnetic field is along the y direction and the electric field is in the x-z plane.

$$\mathbf{H} = H_y^0 e^{ik_x x} e^{-ik_z^{(1,0)} z} + \sum_n (r_y^n) e^{i(k_x + G_n)x} e^{ik_z^{(1,n)z}} \tag{2.60}$$

The first term corresponds to the incident plane wave in air. The second term in the summation corresponds to the reflected diffracted orders in air where r_y^n is the reflection coefficient.[20] The electric field in medium 1 consists of the incident electric field as well as diffracted reflected component. The incident field is given by

$$E_{inc} = E_x^0 e^{ik_x x} e^{-ik_z^{(1,0)} z} + E_z^0 e^{ik_x x} e^{-ik_z^{(1,0)} z} \tag{2.61}$$

Here the quantity $k_z^{i,n}$ refers to z component of the n^{th} order k vector component in different mediums n_1, n_2 and n_3. The reflected field is given by

$$E_{reflected} = r_x^n e^{i(k_x + G_n)x} e^{ik_z^{(1,n)z}} + r_z^n e^{i(k_x + G_n)x} e^{ik_z^{(1,n)z}} \tag{2.62}$$

Similar expressions can be obtained for the electric and magnetic fields in the the transmitted direction in the medium with refractive index n_3. These fields arise as a result of the

diffraction of the periodic structure into the transmission direction. These fields are given by

$$H = \sum_n t_y^n e^{i(k_x+G_n)x} e^{-ik_z^{(3,n)z}} \tag{2.63}$$

The transmitted electric field is give by

$$E = \sum_n t_x^n e^{i(k_x+G_n)x} e^{-ik_z^{(3,n)z}} + \sum_n t_z^n e^{i(k_x+G_n)x} e^{-ik_z^{(3,n)z}} \tag{2.64}$$

Solutions to all k include the propagating diffraction order in the reflected and transmitted direction as well as and evanescent terms. These solutions are obtained via staircasing approximation and using the transfer matrix approximation between each step. Solutions for waves propagating in periodic media also include certain wavelength bands where all k might be strictly evanescent, resulting in no light transfer. These regions are called photonic bandgaps of the lattice. On the other hand, some of these solutions might result in strong k-vector bands in region (1) - reflected diffraction or region (2) - transmitted diffraction. In terms of looking at nanostructured antireflection, we are more interested in the propagating diffraction orders in both directions from the nanostructure than the evanescent modes. These diffraction orders are obtained by calculating the propagating vector. Analytical solutions are available for simple arrangements such as arrays of holes and pillars.[61] However for geometries with nanostructures with finite thickness, numerical methods need to be adopted to calculate all components of the k-vector. Another important quantity is to find the diffraction orders. These are defined by the reciprocal grid vectors. These diffraction orders are analogous to the diffraction of light acrosss multiple slits. The nanostructure periodicity replaces the slit. The fundamental order is always present at all wavelengths.

Depending upon incident light conditions and geometry, other diffraction orders arise. These diffraction orders numerically quantify the number of k vectors present in different directions as a result of the periodic arrangement. Thus in such a lattice, propagation vectors are present in different angular directions including the fundamental incident direction. Such an angular distribution of diffractive components is expected to be present both in reflection and transmission. The number of orders in reflection can be reduced by maintaining a pitch of subwavelength dimensions. This rule is derived from the reciprocal space of propagation vectors.[61] Modes which propagate in air and the high index medium are bounded by circles in the reciprocal space with radii $\frac{2\pi}{\lambda}$ and $n\frac{2\pi}{\lambda}$ respectively, where n is the optical refractive index of the high index medium, i.e in our case silicon.[128] If the pitch is less than the wavelength then the propagation vectors in the reciprocal spaces in air are smaller than those in the high index. This can be deduced from the equations 2.52-2.64. This varying intensity is illustrated via the two different circles shown in 2.6. All points in the interior of the circle are the allowed wavevectors for the propagating wave modes to which the incident

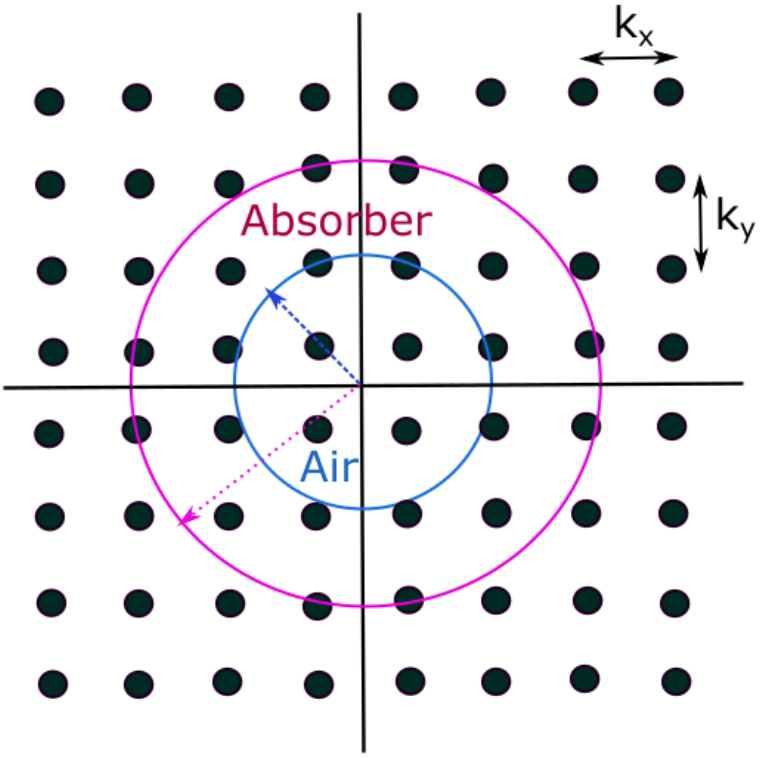

FIGURE 2.6: Representation of k space as well as propagation vectors

plane waves can couple. If the pitch is smaller than the wavelength, only the fundamental reflection mode is present in air.[126] On the other hand, multiple number of modes are available for the excitation in the high index silicon. Such a regular arrangement therefore results in high number of modes being coupled into silicon. The radius of the circles in k space is representative of the effective mode confinement across the interface.[91]

This set of equations is valid for systems where most of the diffractional properties arise as a result of the periodic lattice.

2.1.6 Metamaterials and metasurfaces

Resonant behaviors of metallic nanostructures such as spheres, antennas or split ring resonators in the optical frequency range are accompanied by heavy intrinsic absorption losses. This problem is overcome by utilising dielectric materials which possess low to zero optical loss. The resonant effects are obtained via triggering the circular displacement of the currents inside the dielectric material.[52, 114] Changing from metallic to dielectric materials helps in eliminating optical loss however one is still restricted to the inherent optical dispersion of dielectric materials. Depending upon the class of materials - metallic oxides (titanium dioxide) or III-V group semiconductors, these materials have zero optical loss in the visible

or near infrared spectrum. This is accompanied by high values of refractive indices (real component greater than 2). While these properties are conducive for optical applications, they are not sufficient to engineer novel optical effects involving high quality factor resonances with tunable dynamic frequency ranges.

This demands for additional degrees of freedom taking aid of nanostructuring. The design space now consists of optical materials constants as well as of geometrical parameters. This can be utilised to arrive at structures which have effective dielectric permittivity and magnetic susceptibility as a result of phase and amplitude manipulations via the structural arrangement. Recently such structures have been widely investigated in vast depths and the resulting optical spectra can be classified into transparent all dielectric perfect reflectors, negative index materials, all dielectric magnetic mirrors.[52, 114] This results in a four quadrant space defined by the material permeability and permittivity.[52, 114] In this space both electric permittivity and permeability can be designed to have combinations of positive and negative values. This class of structured materials with design influenced optical constants is referred to as metamaterials on a broad scale.[52, 114, 106] Common examples of such engineered nanostructures include hyperbolic and chiral dispersive structures.[52] This implies that the effective permittivity of these structures is a hyperbolic function of wavelength.

Metamaterials synthesised via basic dielectric materials are referred to as all dielectric metamaterials. We focus our attention on describing the physics of dielectric metamaterials. Depending upon the optical response and physical phenomena implemented these can be exclusively distinguished into high index aperiodic nanoresonator arrays, metasurfaces, fanostructures.[52] These high index nanoresonators are made up of nanostructures such as cubes, spheres among others. When light below the optical absorption bandgap of the material is incident on a nanosphere for example, then based on Mie theory electric and magnetic dipole resonances are excited. The magnetic dipole is referred to as the first Mie resonance and the electric dipole is refered to as the second Mie resonance.[114, 78] In dielectric materials, the circular displacement of the dielectric current enhances the magnetic fields at frequencies corresponding to the magnetic resonance. By implementing an ensemblic arrangement of such spheres or cubes with aspect ratios close to one, desired optical spectra can be obtained.[53] Such arrangements make it possible to have complete transmission or reflection of light across a significant bandwidth range. Arrays of semiconductor materials such as silicon give rise to such selective spectra in the near infrared range as a result of conducive optical properties. The collective interaction of each resonant structure with light results in phase and directional changes in the incident light. This interaction can also be used to achieve polarisation control of light via the near fields of such nanostructures.

A special class of dielectric nanoresonator ensembles is a metasurface. As the name suggests, these metasurfaces utilise novel (meta) properties of periodic optical arrangements (surface). The vertical thickness of these arrangements is restricted to the low aspect ratio of nanoresonators. This periodic arrangement might appear similar to the periodic photonic nanostructures discussed in the previous section however they differ in operation. As previously discussed, on account of the periodic arrangement such as grating structures, different orders of reflected and transmitted modes are possible depending upon angle of incidence and other structural parameters. Metasurfaces however restrict such modes to the fundamental order and provide directional control of light. The direction of this fundamental order may be in different directions as compared to direction of incoming light. Such directional control is derived via near field interactions as well as selective scattering of resonant nanostructures. Silicon metasurfaces consisting of disks arrangements operate on Mie type resonances occuring beyond the wavelengths at which the periodic diffraction occurs. This results in manipulation of incident light fields either in the reflected or transmitted direction. In equations 2.52-2.58 we desrcibe the expressions of electromagentic fields as a function of different diffracted orders parameterised by n. At the operating Mie frequencies of the aforementioned resonator, these fields in all dimensions are characterised by the single mode fundamental order. The fields arising out of the interaction of light at the resonant interface dominate the effective reflective or transmittive behavior.

The close relationship between periodic diffractive structures and metasurface stems from the similar building blocks and the arrangement between them. This makes it possible to analyse the boundary conditions and parameters which result in the spectral transition from photonic crystals to metasurfaces. This is extensively studied by [106]. This work differentiates between propagation of light influenced by diffractions arising out of the entire periodic structure and propagation influenced by each single element or building block of the periodic structure. The system under investigation is a cartesian array of rods with radius r at a periodicity a and permittivity epsilon. At a given radius and lattice constant, with increasing permittivity of the rods, the photonic crystal response of such a structure translates to a metamaterial like behavior. This can be explained via the dominant light interaction of the high index nanostructured resonator. For a given dielectric permittivity, varying the ratio between the radius and lattice constant, transitions from metasurface to photonic crystals and vice versa can be obtained. An example of such a transition is shown in [106] and we indicate it in figure 2.7. Thus by adapting the material contstants and the ratio between the lattice constant we can change the spectral positions of the Mie type modes and the diffractive modes with respect to each other. The two main ways of going from a photonic lattice structure to a metasurface is either increasing the permittivity of the material or decreasing the lattice constant.

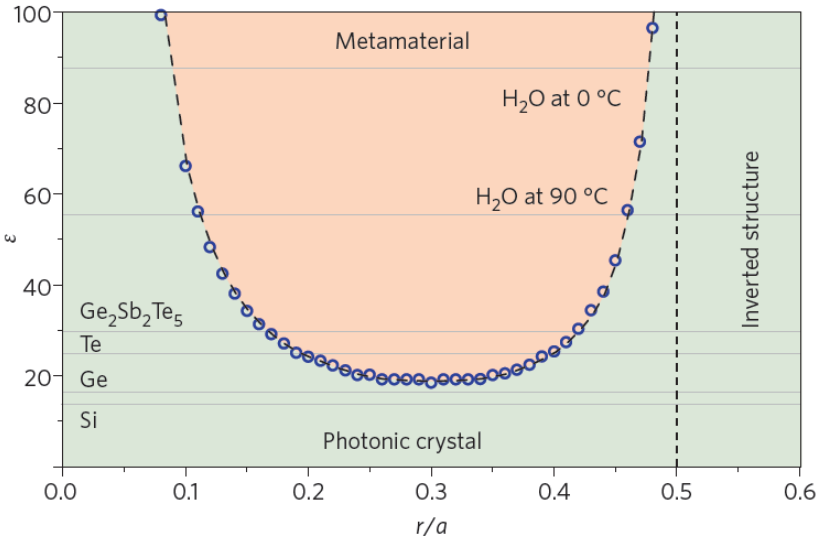

FIGURE 2.7: Transitions between metasurfaces and photonic diffractive structures as a function of material parameters and geometrical parameters- a is the lattice constant and radius is the radius of the nanostructure as studied in [106]. [Reprinted] with permission from [106].

2.2 Numerical methods

In the discussion above, we explained several phenomenona involving the light interaction of thin films and nanostructures which are necessary for designining an effective and functional antireflection system. This involves controlling the design space to get the desired spectral trend from multiple effects such as interferences, diffraction orders and nanostructured resonances. Analytical solutions are not available to compute the simultaneous interaction of these effects. Utilising numerical solvers is therefore necessary to obtain fullwave solutions to the light interactions of nanostructures on a material interface problem. Application of numerical methods in photonics is a pivotal tool in bridging the gap between existing analytical solutions and optical effects shown by popularly investigated optical devices such as resonator arrangements or waveguide bends.

These methods help in understanding the essence of electromagnetic properties of such devices and aid in the design and optimisation process. These numerical methods in photonics solve the time dependent Maxwell's equations. In this section, we will provide a brief overview of some of the methods used in the scientific community including the finite element method. We then focus specifically on the finite element based solver JCMsuite which is used to simulate the structures discussed in this thesis.

The most common methods in the community include *Finite Differences (FD)*, *Finite Difference Time Domain Method* (FDTD), *the Fourier Modal Method (FMM)*, the *Finite*

Element Method (FEM) and the *Discontinous Galerkin* (DG) method.[96, 101, 18] Other methods include the beam propagation method for axially propagating beams, boundary integral methods as well as plane wave expansions for simulating band structures. All of these methods involve certain physical considerations which simplify the compexity of the problem involved. The most generalised photonics problem consist of nonlinear dispersive media which requires a time dependent solution. This problem can be handled by FDTD and DG to arrive at general solutions. For linear and non-dispersive problems it is benefical to follow the time harmonic approach. Subject to the requirements of the system under analysis, it is then beneficial to combine the obtained time harmonic solutions via fourier transform with different frequencies to obtain time dependent behavior. Considering a time dependent approach involves usage of high computational power and is not required for systems where no energy level transition is involved, like the ones investigated in this thesis.

Another method of simplifying the problem is approximating full vector field equations to their scalar equivalents. Some of these approximations are utilised to simplify equations in terms of polarisation dependence.[101] In that regard, for paraxial waveguide problems, the beam propagation method approximates paraxial propagation in tapered waveguides into a two dimensional problem where the field solution in the cross section is propagation along the direction of the axis. This significantly reduces computational power.[101] We now proceed to describe briefly different methods.

2.2.1 The Finite Difference Time Domain Method (FDTD)and the Discrete Galerkin (DG) Method

The finite difference time domain method is directly based on the time dependent Maxwell's equation. It offers solutions to nonlinear, nonlocal and dispersive responses due to close proximity of this method's implementation with Maxwell equation. It is based on a Yee lattice implementation which implements the topology of the Maxwell equations. This is shown in figure 2.8. This is then plugged into the time dependent equation, expressed here in the one dimensional case [101]

$$\frac{\partial H_y}{\partial t} = \mu^{-1}\frac{\partial E_z}{\partial x} - \sigma^* H_y \tag{2.65}$$

$$\frac{\partial E_z}{\partial t} = \epsilon^{-1}\frac{\partial H_z}{\partial x} - \sigma E_z \tag{2.66}$$

Here σ and σ^* are the electric and equivalent magnetic conductivities. The curl of the magnetic field is centered on an out of plane electric field which induces a propagating electric field. This requires for the field to be staggered in space. The propagation from one end of the plane to another needs to be accounted which results in the field being staggered in

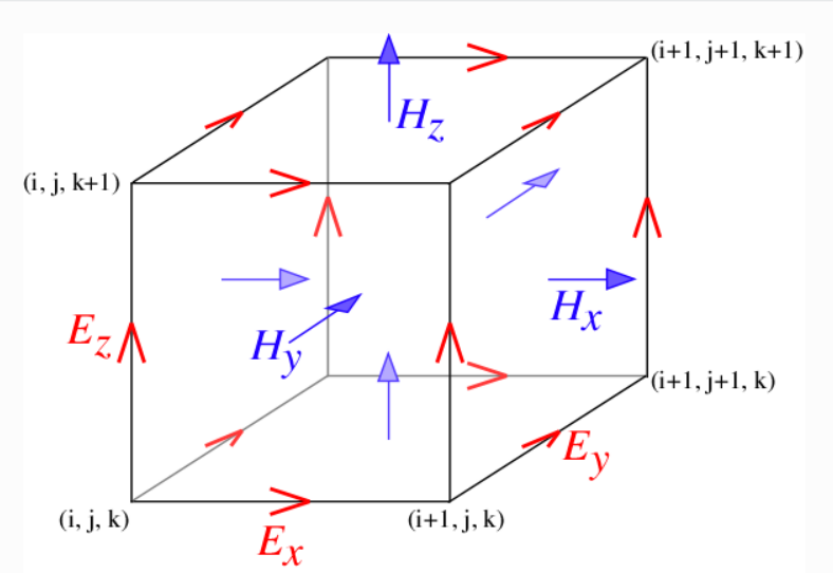

FIGURE 2.8: Conventional representation of time dependent Maxwell's equations in the form of a staggered grid of electric and magnetic fields in time and space from the MEEP documentation [96]

time. In a homogenous material this results in the time dependent Maxwell equations being formulated into a second order update scheme taking into account discretisations in time and space. This discretisation approach is not so straightforward along material boundaries and requires special considerations. Overall this method is simple to implement and quite fast in computational performance.[20] Since this method is based on a cartesian grid, it restricts adaptation to complex geometries. The second order accuracy in space and time makes it difficult for large domains to be investigated with the aid of the finite difference time domain method.[96, 101]

The nanofrustum metasurface presented in chapter 6 can be investigated using FDTD however the soupbowl structure presented in chapter 7 would require more computational resources as a result of the curved surface.

The FDTD is a popular method used to investigate time depenendent response of systems. However due to cartesian staggering of fields it is difficult to effectively deal with complex geometries. Another drawback of the FDTD is the second order accuracy in space and time. The **Discontinous Galerkin method** overcomes these problems.[18] This method is based on combining the adaptive spatial discretisations which the finite element method (FEM) uses along with time treatment in finite volume methods.[101] The principle used here is to localise most of all spatial discrete elements indepentently and connect the field in each of them via continuity conditions. The principle of time evolution is implemented in each of

these discretised elements which results in an explicit scheme. This method combines time treatment with a high order spatial discretisation.

2.2.2 The Fourier Modal Method

In the Fourier Modal Method, the geometry under investigation is subdivided into a sequence of waveguide type sections. In each waveguide like section, the field is represented by up and down propagating modes as well as evanescent modes. The interaction of the individual sections is realised by posing proper continuity conditions at the interfaces with the aid of scattering matrix or transfer matrix formulations.[101] In the transfer matrix approach, the electric field is decomposed into the upward and downward propagating parts with respect to the z direction with the aid of transfer matrix coefficients. The scattering matrix approach uses a similar ideology but the order of coefficients is reordered. This reordering follows from the fact that constitutional relation is established between the field coefficients incident to boundary and the field coefficients scattered away from the boundary. Both these approaches are then evaluated for an n-layer system. The Fourier Modal Method is rather suitable for systems where the field distribution in the transverse plane propagates along a longitudanal direction. A curved structure like the soup bowl structure investigated in chapter 7 requires discretisations into many sub domains and fields in each of those need to be represented by many modes. This increases the computational complexity of the problem.

2.2.3 The Finite Element Method (FEM) and JCMsuite

The Finite Element Method implements Maxwell equations in the variational form via integral expressions on the computational domain of interest. It implements the complete set of Maxwell equations without any approximations but discretises the geometry. FEM solutions are obtained by providing a number of polynomials on each discretised element of the geometry. These discretised elements with the polynomials are called finite elements. The most common examples of finite elements in a two dimensional calculation consist of triangles and rectangles.[101] An example of two and three dimensional meshes utilsed in the computational investigations performed in this is shown in figure 2.9. In three dimensional problems cubes and tetrahedrons are used as discretisation elements. These are colloquially refered to as meshes. Most polynomials consist of constant, linear, quadratic and cubic polynomials. The formulation of these polynomial spaces need to ensure tangential continuity of magnetic and electric fields across boundaries of each patch. Post definition of these conditions, the poynomials are inserted into the variational equation. This results in a linear system, solution of which is a piecewise polynomial approximation.

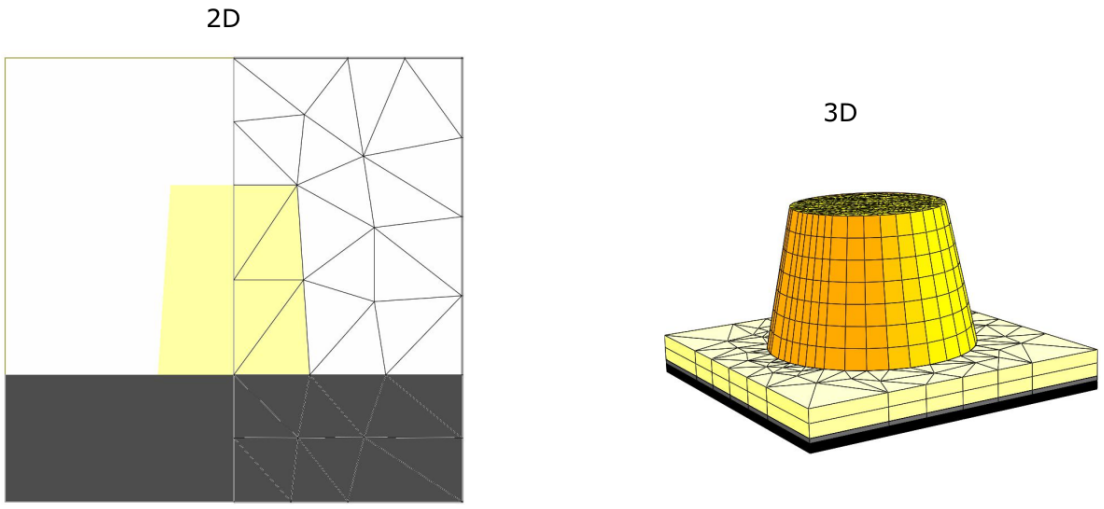

FIGURE 2.9: Illustration describing two dimensional and three dimensional mesh elements of structures used in this thesis.

We illustrate the finite element concept in one dimensional formulation with the aid of one dimensional wave equation in 1D in equation 2.67 The length of this computational domain is assumed to be L.

$$\partial_x^2 u(x) + k^2 u(x) = 0 \tag{2.67}$$

where

$$u(x) = e^{ikx} \tag{2.68}$$

Over the length L, 2.67 is multiplied with the complex conjugate of a test function, v(x) and integrated over the domain to arrive at

$$\int_0^L v^*(x)(\partial_x^2 u(x) + k^2 u(x))dx = 0 \tag{2.69}$$

The restriction on the function v(x) is that it should allow meaningful computation of the integral. This generates a space of functions referred to as the test space. The space of functions containing solutions to u(x) is called the trial space. The convergence theory of each of the elements defines the test and trial case.[101] For the solution to converge, the integral value should be less than infinity. This gives a class of square integral functions for the function v(x). The equation 2.69 is integrated in by parts to give rise to

$$\int_0^L v^*(x)(\partial_x^2 u(x)) + k^2 u(x))dx = \int_0^L (\partial_x v^*(x)\partial_x u(x) + k^2 v^*(x)u(x)dx + v^*(x)\partial_x u(x)|_0^L \tag{2.70}$$

The integral in 2.70 is called a sesquilinear because it contains linear and non-linear terms in its expression. This integral defines the variational formulation of the finite element problem. This is then solved with aid of localised matrices and assembly processes. As a result of such

discretisation, complex geometries can be treated without geometrical approximation. The finite element mesh can be numerically adapted to the behavior of the solution including sharp corners in geometries.

Salient features of FEM include error estimation which leads to adaptibility of the problem as well as the possibility to increase the degrees of freedom.[118] One of the methods of increasing the degree of freedom is increasing the polynomial degree of the functions on each of the discretised elements. Another way is to increase the number of elements, this is called refinement. The numerical accuracy of the solution can be increased after analysing the necessity, i.e cases where the estimated error is high. Increasing the degrees of freedom allows for relatively fast convergence tests. This implies testing the numerical solution for a case where the analytical solution is available.

Having described the introductory math behind the finite element method, we describe about our computational investigations, performed using JCMwave, the finite element based solver. JCMsuite has features which solves optical and microwave problems involving scattering, propopagation and resonant modes. This is largely governed by the boundary conditions applied and the solutions required in a given frequency range.[104] The input to each calculation consists of the structure geometry and material parameters for a given wavelength bandwidth. Additionally, suitable boundary conditions are defined to arrive at the desired solution. Depending upon the type of the problem solved, i.e scattering or propagation these boundary conditions can be periodic or transparent. Periodic boundary conditions ensure continuity of fields in relation with Bloch-Floquet vector. Transparent boundary conditions are used when the problem requires that no fields are reflected backwards from the boundaries of the computational domain.[60] This is implemented with a perfectly matched layer. This layer is numerically implemented to heavily and rapidly damp the outgoing field from the computational boundaries. It is also numerically implemented to prevent reflections at the computational domain boundary, thereby avoid interaction between reflections and the incident wave. The geometry forms the computational domain. Each part of the computational domain is discretised into small triangles in two dimensions and tetrahedrons in three dimensions referred to as the mesh. This mesh enables discretisation of the given geometry consisting of nanostructures and into relatively smooth small number of elements. Maxwell's equations are then defined over each element of the geometry. These are then solved across each element across the computational domain. Solutions to these equations consist of variable degree polynomials which exist on each discretised element.

2.2.4 JCMSuite operational execution

In this section, we provide salient remarks on the operational execution of JCMsuite solver to solve the computational problems described in this thesis. We use the solver to obtain spectral electromagnetic responses in the frequency domain. The major quantities of our interest include reflection, transmission and absorption for problems involving periodic boundary conditions. For isolated boundary conditions we investigate the scattering response by computing the scattering cross section. While calculating these quantities numerically using solvers based on numerical methods including JCMsuite, the accuracy and reliable repeatibility of this accuracy are particularly important. This reliable repeatibility is referred to as the convergence of the computational problem. JCMsuite is a robust solver in the domain of computational photonics so the regular intracacies need not be rigorously analysed. For the problems discussed in this thesis, accuracy and convergence have been assured by appropriate choice of mesh sizes and geometric parameters, degree of polynomial as well as the adaptability of these parameters sensitive to material optical properties and electromagnetic wavelength.

Any computational problem is associated with a target value of the precision to extract out of the computation, the desired electromagentic quantities. This attainability of this target precision is determined by the numerical error of the problem. The numerical error of the computational problem is governed by the following equation.

$$\text{error} \propto (\frac{nh}{\lambda})^p \tag{2.71}$$

Here λ is the wavelength of the excitation source, n is the refractive index of the material, h is the mesh size and p is the polynomial degree. The error therefore can be reduced to minimum by increasing the polynomial degree, reducing mesh size adequately for given material and wavelength values while maintaining reasonable computational effort. The mesh size is defined in the problem by a so called side length constraint (slc). For modelling air spaces, we use a side length constraint of 25 nm. For higher indices such as titanium dioxide and silicon we use one fourth of this side length. In the spectrum of interest between 400-500 nm, between 500-800 nm we use a polynomial degree of 3 and between 500-800 nm we use a polynomial degree of 4. This helps in reducing the error at wavelengths where the refractive index is high and helps to obtain the target precision of 1e-3.

For three dimensional calculations, the shape of the mesh is tetrahedron which is extruded in the three dimensional plane. These features are adapted to ensure ensure sufficient number of mesh elements at steep slopes, material interfaces, circular interfaces, curves of the metasurface and soupbowls structures desribed in this thesis. Ensuring a sufficiently fine mesh

structure results in thorough coverage of polynomial formulation of the Maxwell equation across the entire computation domain.

To compute the quantities of interest, i.e. reflection, transmission and absorption, we 'post process' the calculated eletromagentic field. This involves that the calculated field is expressed in the form of plane waves. This gives rise to a discrete set of propagation vectors and electromagentic fields for a periodic simulation. By notation these sets are referred as the propagating Fourier coefficients. These are used to calculate all spectral characteristics of the metasurface and soupbowls. These fields and vectors can be used to calculate reflection as follows in equation 2.72.

$$R = \frac{1}{k_0 \left\| \vec{E}_0^2 \right\|} \sum_{n=1}^{N} |k_i . \vec{e}_n| \left\| \vec{E}_i^2 \right\| \tag{2.72}$$

In this equation the space (E_i, k_i) corresponds to each of the N diffractive modes present in the outgoing plane wave. The upper half space of the computation domain is used to tap the upward propagating wave (E_i, k_i). E_0 is the input electric field, and k_0, the incoming propagation vector. The transmission is calculated using a similar ideology in lower space of the domain. Except in this case we utilise the downward propagating wave. Here another important quantity is the refractive index contrast between the incoming wave (n_{down}/n_{up}) propagating in the downward direction (down) and the medium in which it initially propagates (n_{up}). This gives the following equation for the value of the transmission in equation 2.73.

$$T = \frac{n_{down}}{n_{up}} \frac{1}{k_0 \left\| \vec{E}_0^2 \right\|} \sum_{n=1}^{N} |k_i . \vec{e}_n| \left\| \vec{E}_i^2 \right\| \tag{2.73}$$

Absorption is calculated by taking the density integral of the electric field in each absorbing region of the geometry and corresponds to the imaginary part of the total energy. This is expressed in equation 2.74 where P_{in} corresponds to the the input power expressed as $P_{in} = \frac{n_{up}}{Z_o A_{CD}} \left\| \vec{E}_0^2 \right\|$ where Z_o is characteristic vacuum impedance and A_{CD} is area of the computational domain in the two dimensional plane.

$$A = \frac{2\omega}{P_{in}} \sum_{\text{domains i}} \int_V Im(\left\| \vec{E}_i^2 \right\|) dV \tag{2.74}$$

The calculated reflection, transmission and absorption are then summed to arrive at unity values.

For isolated calculations for scattering cross section ratios, the set (E_i, k_i) is continous and cannot be differntiated into individual values, therefore we evaluate the outgoing flux in each

direction and normalise with incident energy. The formula used to derive the normalised scattering cross section is the following, where S is the electromagnetic flux integral.

$$Q_{scat} = K \int SdA \tag{2.75}$$

where

$$K = \frac{1}{P_{in} \times \frac{A_{res}}{A_{CD}}} \tag{2.76}$$

In an isolated calculation, energy balance to establish physical relevance of the computational simulation is done by monitoring if all boundary fluxes add up to the input power for the lossless case assumed. These equations form the basis of the simulation results presented in this thesis. Other specific investigations have been explained together with the results they generate.

2.3 Photoelectrochemistry for hydrogen generation

2.3.1 General processes and photoelectrochemical cell

Photoelectrochemistry for hydrogen generation is a branch of science which utilises light sources such as sunlight to trigger electrochemical reactions including the splitting of water. Optimal water splitting into hydrogen then can be utilised as a very clean fuel source. This has been under investigation with the aid of stable semiconductors which are designed to split water at their surface. A big advantage of this method is the ease at which an electric field can be created at a semiconductor/liquid junction. Hydrogen generation by splitting water requires 237.2 kJ/mol which translates to 1.23 V per electron transferred.[127] It takes two electron hole pairs per molecule to split water. This implies that the semiconductor splitting water at its interface must absorb light greater than 1.23 eV. Ideally this should come directly from the semiconductor bandgap.[127, 12] This can also be implemented with the aid of tandem semiconductor configurations where the energy band levels of different semiconductors align with each other to form a complete band gap of 1.23 eV. This results in the following reactions at the interface between the electrolyte and the semiconductor.

$$4H^+ + 4e^- \rightleftharpoons 2H_2 \; E^o_{red} = 0.000 \; Vvs \; NHE \tag{2.77}$$

$$2H_2O + 4h^+ \rightleftharpoons 4H^+ + O_2 \; E^o_{ox} = 1.23 \; Vvs \; NHE \tag{2.78}$$

Equation 2.77 involves 4 electrons being utilised by hydrogen ions to give rise to hydrogen gas. In standard electrochemistry formulation, this is referred to as a reduction reaction. In the

electrochemical formulation this reaction is referred to the reversible hydrogen reaction(RHE) and rendered as a reference for all potenial levels of other electrochemical oxidation-reduction reactions. The electrochemical potenial which facilitates this reaction is called the reduction potenial, E^o_{red}. Equation 2.77 involves generation of hydrogen ions. This ion generation reaction is called oxidation reaction as a result of proton exchange. The electrochemical potenial which results in this reaction is called oxidation potential, E^o_{ox}. Proton reduction involves 2 electrons for every H_2 molecule (4 electrons for two H_2 molecules) so it is much easier than the water oxidation reaction which is 4 electrons (or 4 holes for every O_2 molecule). Both levels are measured with reference to the normal hydrogen electrode potenial (NHE). The normal hydrogren electrode is a reference standard used in electrochemistry to reference all oxidation reduction reactions against the hydrogen reduction reaction shown in equation 2.78. The energy levels of these reactions is shown in figure 2.10. The first reaction is called hydrogen reduction and the second reaction is called water oxidation reaction. The energy difference between these reactions is 1.23 eV. This figure also shows the position of the silicon bandgap with respect to the energy level of the reactions. For p - type silicon, the fermi level lies near the valence band. The reported fermi level for p-type silicon is 0.67 V vs the NHE. In order to trigger the water splitting reaction which occurs at 1.23 eV. As shown in figure 2.10 to hole transfer from the electrolyte into silicon. This hole (positive) charge is required for the splitting of water molecule to hydrogen ions. These reactions occur at the interface of the semiconductor liquid interface. Depending upon p - type or n - type semiconductor, different energy band transitions occur at the interface. For a p - type semiconductor, under illumination, electrons (minority) charge carriers are generated. These electrons are then driven to the semiconductor electrolyte interface as a result of the electric field formed. These photogenerated electrons drive the hydrogen reduction reaction shown in equation 2.77. This electron flow is governed by the physics of the semiconductor liquid contact.

We describe this for a p - type semiconductor and a complementary electrolyte. When a semiconductor is immersed in an electrolyte, charge transfer occurs at the interface because of the difference in electron affinition levels. This results in an electric field being formed across the space charge region as a result of the charge carrier exchange. A p - type semiconductor contains excess negative charge from the dopant atoms while the electrolyte contains excess positive charge. A space charge region conducive to facilitate electronic charge transfer only occurs when the bangap of the material (p-type silicon, BG = 1.1 eV) is close to the redox couple of the electrolytic solution (1.23 eV). Electron flow occurs from the p- type semiconductor into the electrolyte containing positively charged acceptor species at the interface. This results in bending of energy levels of the conduction band and valence band.[95] This band bending is seen in figure 2.11. Moreover under illumination, the fermi level splits into

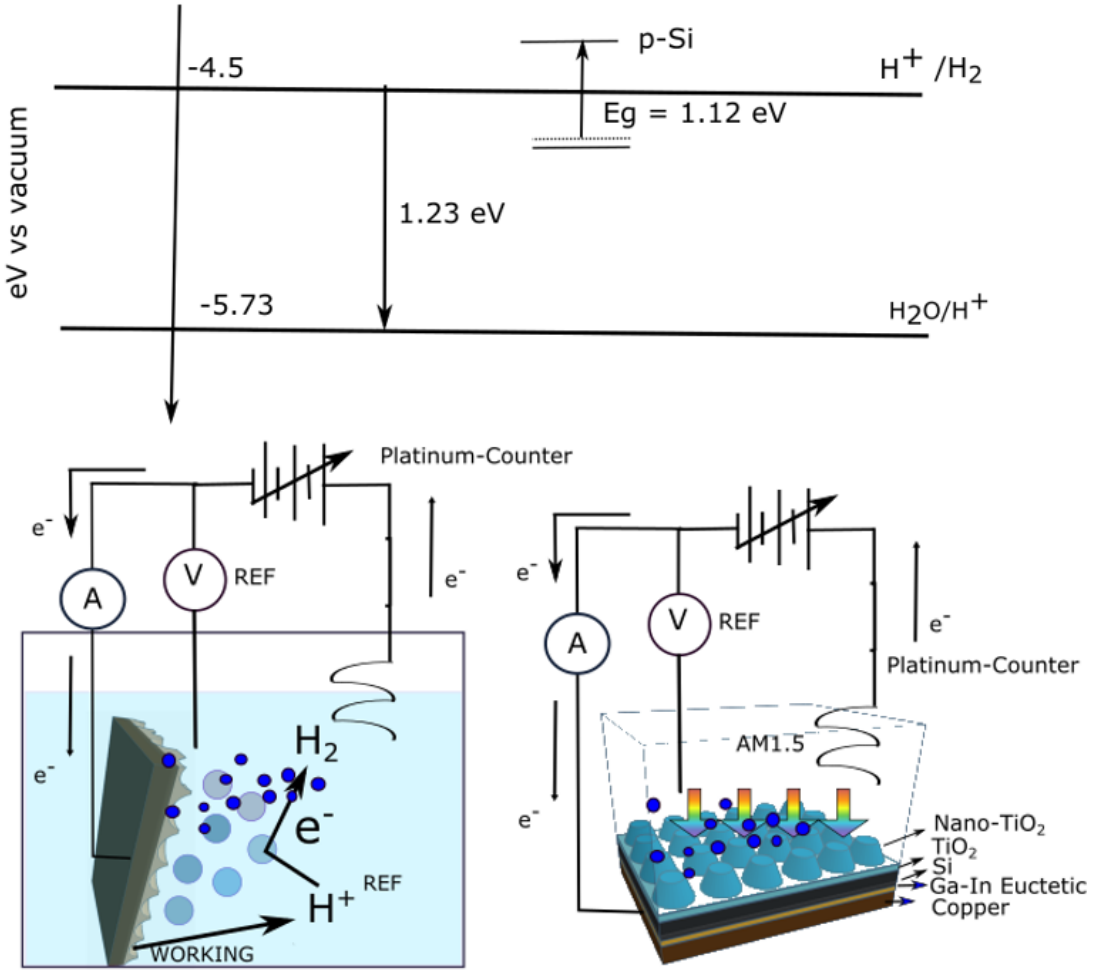

FIGURE 2.10: Energy levels of the two reactions : hydrogen reduction and water oxidation plotted against the silicon bandgap. The figure also shows band levels of silicon indicating that bandgap of silicon shows a deficit of 0.13 eV against the required energy level. The actual required overpotenial is indicated in the subsequent section. For the structures shown in this thesis, we indicate how the deficit in silicon bandgap is compensated with an additional bias voltage

two levels $E_{F,n}$ and $E_{F,p}$ due to the generation of photogenerated electron hole pairs. Photogenerated electron transitions from the valence to the conduction band into the electrolyte to drive the hydrogen reduction reaction shown in equation 2.77. Photogenerated holes move to the interior of the semiconductor with the aid of the additional bias applied. This additional bias ensures to bridge the gap between the redox potenial voltage of 1.23 eV and the fermi level of p-type silicon which is reported to be 0.67eV.

In a photoelectrochemical cell, the p - type semiconductor acts like a photoelectrode - i.e the photocathode. Charge transfer occurs through the photoelectrodes across the photoelectrode-electrolyte interface, and through the electrolyte.[102] It provides negative charge into the

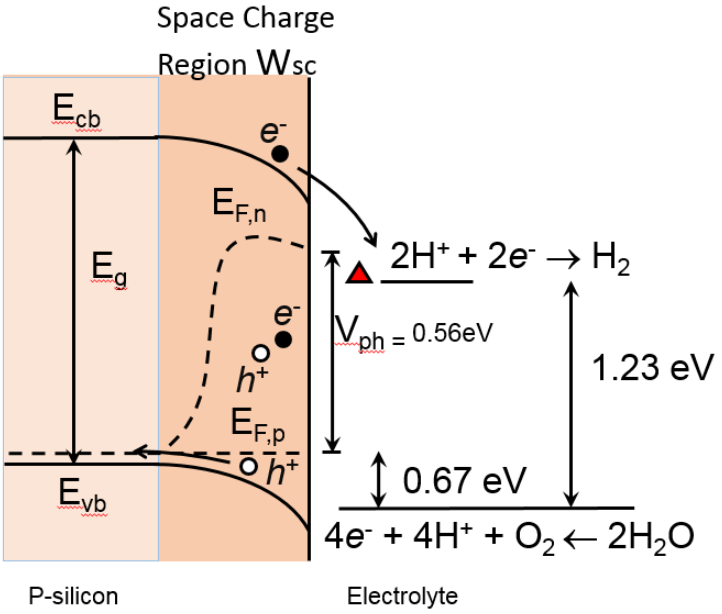

FIGURE 2.11: Band bending of energy levels observed as a result of junction formation between semiconductor and electrolyte as explained in[95, 12]. The figure shows fermi level in p-type silicon to be near the valence band. Reported energy value of this level is 0.67 eV vs RHE. Upon light incidence, electron transfer occurs from the valence to conduction band. Hole transfer occurs from the solution to silicon. For this hole to reach the water splitting voltage (1.23eV) an over potential of 1.23-0.67 eV = 0.56eV needs to applied

electrolyte. Another component of this system is the counter-electrode. It collects charges of opposite polarity as compared to those collected by the photoelectrode. In a three electrode photoelectrochemical setup a reference electrode is also used to measure the electrochemical potenials. The photoelectrode is required to satisfy the following properties. It should have strong light absorption as well as be able to facilitate the charge seperation of the electron hole pairs at its interface. Additionally to successfully achieve water splitting at its surface, it should allow evolution of oxygen or hydrogen at its surface depending upon its intended function as a photocathode or photoanode respectively. Other material requirements include stability under acqeous environments and low cost.[26] This material should also have a band gap which straddles the water oxidation and proton reduction potenials. A material satisfying this critieria forms a pn- junction with the electrolyte. It converts the incident photons to electron-hole pairs. These electrons and holes are spatially separated from each other due to the presence of an electric field inside the semiconductor. Light absorption by the photoelectrode results in generation of electric current into the solution.

This electron transfer current is determined by the photocathode light absorption and charge transfer ability.[56] The hydrogen evolution reaction occurs at the cathode/photocathode and the oxygen evolution reaction occurs at the anode/photocathode.[127] In this thesis,

we focus our attention towards photocathodes which release electrons and lead to the hydrogen generation reaction.[57] At the counter electrode, which is often made of platinum for analytical systems, the second reaction involving oxygen evolution occurs.[26] We use p type silicon as the photocathode as a result of its stability in the acidic environment.

2.3.2 Silicon photocathode and semiconductor electrolyte interface

Having understood the band bending between the semiconductor electrolyte interface we now describe the functioning of the system under illumination.[26] The band structure of the system consisting of p- type silicon, electrolyte and counter electrode is shown in figure 2.12. E_{cb} is the conduction band, E_F is the fermi level ($E_{F,n}$ corresponds to the fermi level of the n- type carriers and $E_{F,p}$ corresponds to the fermi level of p- type carriers), e^- is the negative electronic charge,h^+ is positive electronic charge, W_{sc} is the width of the space charge region formed as a result of the pn- junction formed between the electrolyte and the semiconductor. Clear bending of the silicon bands occur towards the direction of the band levels of the

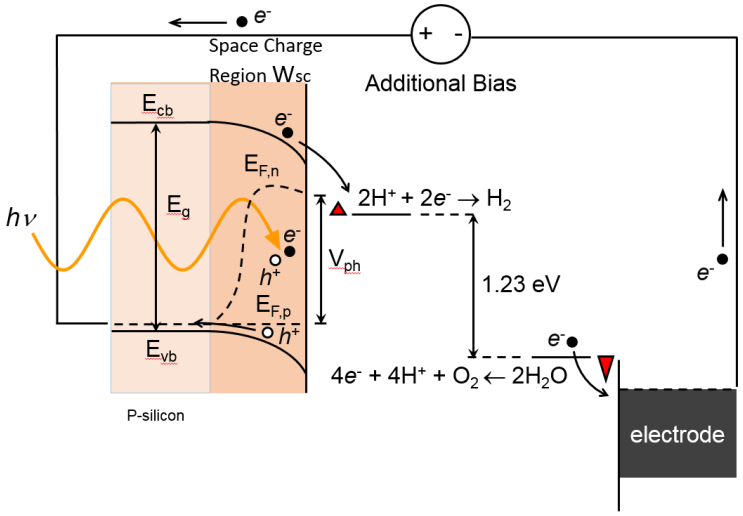

FIGURE 2.12: Energy band diagram (adapted from [12, 26]) of the semiconductor electrolyte indicating the entire setup of the photoelectrochemical cell. Under illumination, electrons flow from the semiconductor to the electrolyte. The additional bias helps in compensating the deficit in silicon bandgap and facilitating hole transfer Absorption of solar intensity and generation of charge carriers results in shifting of the fermi level. This vertical magnitude of this shift corresponds to photovoltage

electrolyte as a result of the formation of the space charge region W_{sc} With the abosrbed photons, electrons from the valence band from silicon migrate towards the conduction band. As a result of the band bending, these electrons find their way into the electrolyte. These two electrons drive the hydrogen evolution reaction at the photocathode. The amount of hydrogen released is directly proportional to the photocurrent generated as a result given the fact that two electrons are required for hydrogen generation.

Chapter 3

Review of approaches for Antireflection

In this chapter, we provide an overview of different concepts, methods and materials described in literature to solve the conventional problem of reflection. We describe these works in terms of the physical approaches namely index profiles as well as nanostructured antireflection involving subwavelength optics and optical resonances. The focus of this thesis is to implement nanostructured solutions for controlling silicon reflection. However in this chapter we mainly focus on briefly elaborating different effects to supress reflection for variety materials including silicon and glass.

3.1 Nanostructuring active optoelectronic materials

Innovations in nanotechnology have made it possible to realise high quality nanostructures of common semiconductor materials. This has resulted in nanostructuring silicon into dense nanowire/nanorod arrays using different dry etching properties. Hung et al. in [49] proposed silicon nanowires of different tapers and aspect ratios to shrink silicon reflection from 50 to 10 percent in the visible and near infrared ranges. This method is based on implementing different transitions in the refractive index between air and silicon with the aid of the silicon nanostructure. This effect is therefore purley longitudinal in nature and does not include optical phenomenona in cross sectional plane of the nanostructure. This theory stems from the so called Moth eye effect discovered by Bernhard in the late 1960s.[13, 105] He discovered that the corneas of moth eyes have a structured surface that dramatically supresses reflection of light. Exemplary morphological images from the work of Hung et al. [49] are shown in figure 3.1. An example of the popularly used moth eye structuring of the active optoelectronic material is nanostructuring of silicon as shown by Lalane et al.[73] These structures

are designed by minimising the amplitude of the first order reflection and obtaining the corresponding geometric parameters. We show the morphology of this structure in figure 3.2.

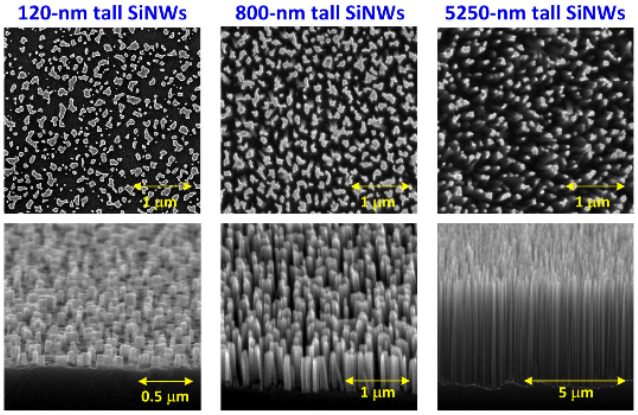

FIGURE 3.1: Silicon nanowires of different heights as produced in [49] via etching. [Reprinted] with permission from [49] © The Optical Society

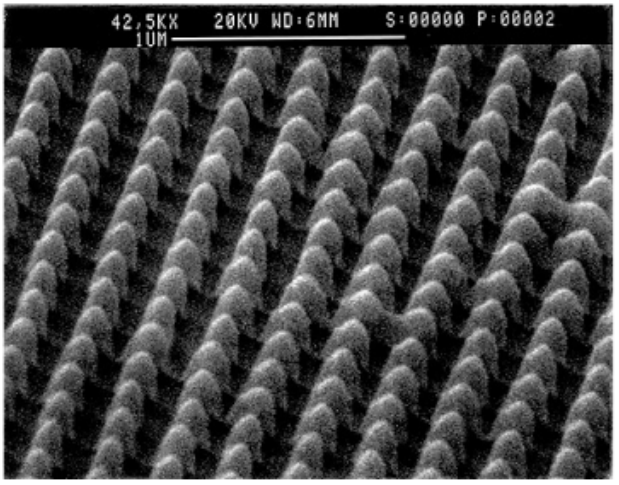

FIGURE 3.2: Morphological image of silicon nanopillars etched into silicon as shown in [73].[Reprinted] with permission from [73].

Other geometries investigated based on this effect consist of silicon nanotips, nanocones, nanowires, nanopillars and domes.[112] The geometrical parameters such as height, base diameter and aspect ratio of these nanostructures have been optimised to provide broadband supression of reflection for even higher incident angles. These investigations reveal that for silicon, high aspect ratio structures, ensure good antireflection behavior whereas structures with lower aspect ratios ensure more light scattering into silicon itself. Another popular geometry investigated is based on the traditional theory of sinusoidal gratings. Additionally,

Yu et al. in [133] devised techniques for forming very regular silicon nanocones by nanoimprinting a pattern on a tri-layer resist, multistep reactive ion etching to transfer the pattern through the resist and further reactive ion etching to arrive at the nanocones. Köppel et al. in [68] have demonstrated the overall increase in the optoelectronic performance via a hexagonal sinusoidal arrays. Figure 3.3 shows a detailed schematic of this system. This approach has

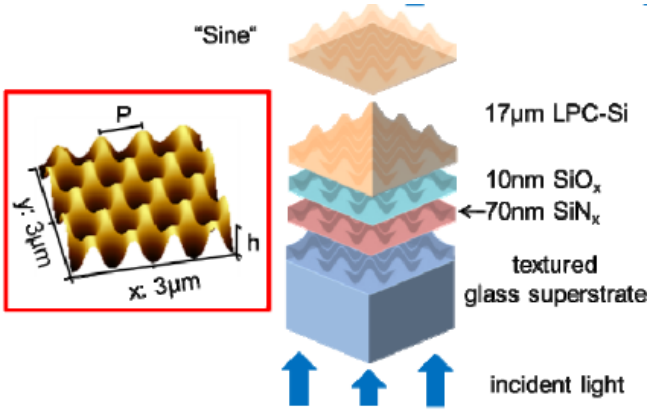

FIGURE 3.3: AFM image and schematic of sinusoidally textured silicon used to couple more light into silicon as shown in [68].[Reprinted] with permission from [68]

also been used for other active optoelectronic materials such as gallium phosphide.[40]

In addition to periodic structures made from silicon, efforts also include random textures in silicon. This is popularly referred to as black silicon.[80, 97] It visibly appears black in comparison with the highly reflective silicon. It is obtained via dry and wet etching of silicon without using a patterned mask. Another variation of antireflective nanostructures include continous structures which result in rough surfaces with random hillocks ranging from 10-100 nm. This is done by sputtering metal layers on silicon and performing wet chemical etching to arrive at randomised structures.[70] We show this example in figure 3.4. Depending upon the type of etching agents used (hydroflouric acid and hydrogen peroxide) and the corresponding etch time, the reflection spectra can be optimised to get a good antireflection performance.

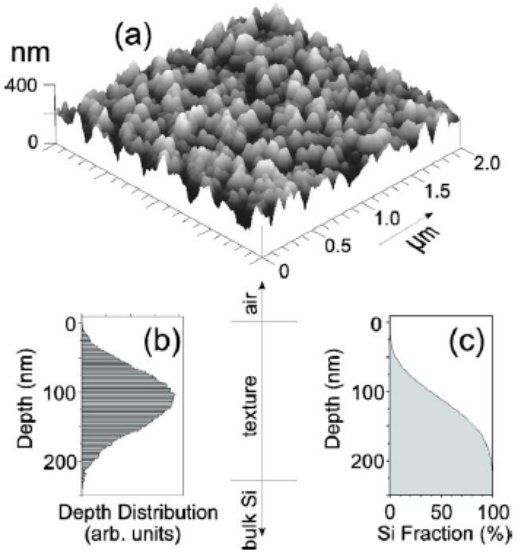

FIGURE 3.4: (a)Random profile etched into silicon from wet chemical etching (b) Distribution of depth of the structure (c) Numerical value of the depth of the structure as shown in [70]. [Reprinted] with permission from [70].

3.2 Nanostructured dielectrics

Existing attempts with respect to nanostructured dielectrics in terms of controlling reflection are based on two optical effects. Some nanostructures utilise their geometric depth to enable a gradual transition of refractive index between the incident medium to the targeted material. This technique is referred to as the gradient index nanostructures. The wavelength of the light must be on the same scale as the depth of the graded index layer. This is essentially referred to as index matching across the interface. Theoretical investigations show that this principle works best when the functional form of the gradient profile has multiple continous derivatives at material interfaces which form the profile. These include quintic profiles described in [110] and half period of the exponential sine function in [103]. We show the graphical representation in figure 3.6 as shown in [103]. However these profiles are difficult to fabricate in practice. Examples of more feasible profiles include linear gradients implemented via single and multilayer structures.

Achieving an effective medium via a graded index profile taking aid of nanostructuring entails use of sizes which are much smaller than the wavelength of light to vary the density of the material above the active semiconductor layer. With variation of this density, the effective refractive index of the material varies. A popular approach of this kind has been the use of multilayer nanostructures from silica and titanium dioxide. Such nanostructures are implemented by using oblique angle deposition to yield high aspect ratio nanorod arrays. The group of Schubert et al. in [129] reduced reflection to 0.2 percent on aluminium nitride

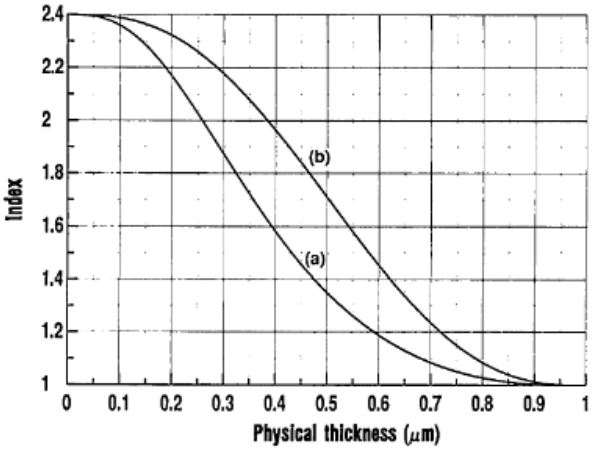

FIGURE 3.5: Refractive index profiles as a function of thickness of the material for (a) polynomial profile in refractive index as a function of thickness (b) quintic profile in refractive index as a function of thickness as shown in [103]. [Reprinted] with permission from [103]. © The Optical Society

substrate at a single wavelength by implementing a 5 layer system consisting of alternate layers of titanium dioxide and silicon dioxide arrays. The representative image is shown in figure 3.6. Such a 5 layer system implements a quintic profile and shrinks reflection at localised

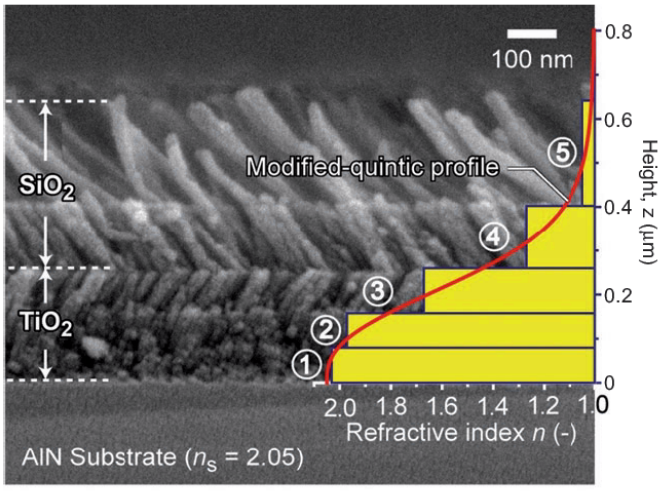

FIGURE 3.6: 5 layer system of isolated dielectric nanostructures which result in gradual variation of refractive index above the optoelectronic material as shown in [129]. [Reprinted] with permission from [129]

.

wavelengths. However having 5 layers of dielectric materials may not be conducive for charge transfer along the optoelectronic interface. As shown in figure 3.6, these nanostructures are isolated from each other.

Using electrodeposition to create a dense fraction of zinc oxide nanorod arrays results in an effective medium layer whose refractive index varies with the density of nanorod arrays. Such arrays are used as antireflection layers on top of solar cells. This has been shown in the work of Ludwig et al [81] indicated in 3.7 The process parameters used for depositing

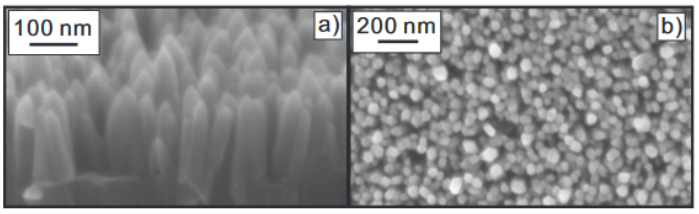

FIGURE 3.7: Morphological images of electrodeposited zinc oxide used as an effective medium as shown in [81]. [Reprinted] with permission from [81]

the electrodeposition determine the packing fraction of nanorods and thereby the reflection value. Planar zinc oxide is also used as a window layer to result in improved index matching. This is shown in the work of B. Hussain et al. [50] which reports using planar zinc oxide on a thin film solar cell made out of crystaline silicon. On account of the antireflection effect, the optoelectronic performance increases.

A highly cited work based on resonant nanostructures using titanium dioxide consists of close packed titanium dioxide nanostructures based on Mie scatterers on planar layers of titanium dioxide and aluminium oxide.[111] We show this in figure 3.8 This work uses substrate conformal implant lithography to lay out the pattern of the nanostructure on an electron beam evaporated titanium dioxide. This structure shows tremendous supression of silicon reflection in the wavelength range between 400-900 nm. The reported average reflection as a result of the nanostructures is 2.8 percent shown in figure 3.8. Combination

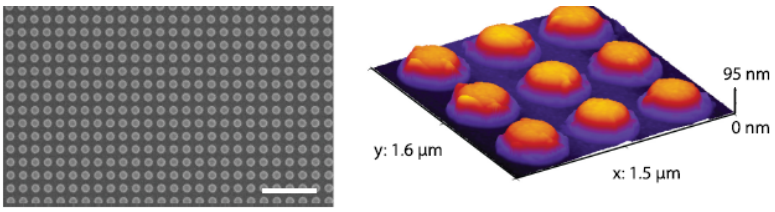

FIGURE 3.8: Morphological images of titanium dioxide nanostructures based on mie resonances on multilayer thin films of aluminium dioxide and titanium dioxide to control silicon antireflection as shown in [111]. [Reprinted] with permission from [111].

of nanostructured silicon nitride and planar titanium dioxide is used to control the high reflection of a bilayer stack of aluminium indium phosphide and gallium indium phosphide in the work of Buencuerpo et al. in [17]. We illustrate this in figure 3.9. This work uses a diffraction grating of silicon nitride. Together with the diffraction grating and the planar

layer of titanium dioxide, index matching with the high index substrate (aluminium indium phosphide) and (galium indium phosphide) is achieved. Using a closed packed arrangement of

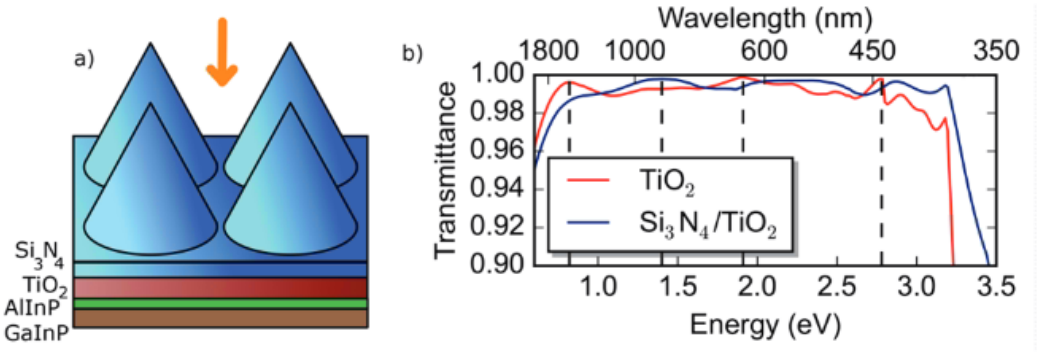

FIGURE 3.9: Silicon nitride nanostructures in combination with a planar titanium dioxide layer to reduce reflection of bilayer of GaInP and AlGaInP in [17]. [Reprinted] with permission from [17]. © The Optical Society

colloidal dielectric nanospheres on top of window layers of solar cells results in antireflection performance as shown by Yin et al. in [132]. A modified version to add more degrees of spectral freedom to this problem is to use a multi sized sphere arrangement. In addition to antireflection, such an arrangement performs the function of light trapping into the active optoelectronic layer.

For a low index substrate such as quartz, self-assembled lithography of colloidal spheres is used to create a hexagonal pattern following chromium deposition to obtain a metallic hard mask. Dry etching on this mask is used to create nanopillars made up of quartz which shows good reflection control over angular incidences.[120] This approach shows that depending upon the nature of the etch, sufficient control can be obtained in terms of geometry of the pillars to obtain cones and tapers. Utilising the appropriate geometric parameters therefore ensures high transmission into quartz for angles of incidence as high as 60°.

3.3 Plasmonics for antireflection

Using a combination of metals and nanostructured dielectrics antireflection performance can be improved. As shown in figure 3.10, a conformal thin film of aluminium is used in combination with a commerical antireflection substrate (Omrocomp,[23]) as shown in the work of Christiansen et al. in [23]. This structure truncates reflection in the wavelength range of 500-600 nm. This effect arises as a result of the surface plasmon polariton propogation at the interface of the nanostructure and metal. This effect is shown to have tailoring capacities by altering the thickness of aluminium.

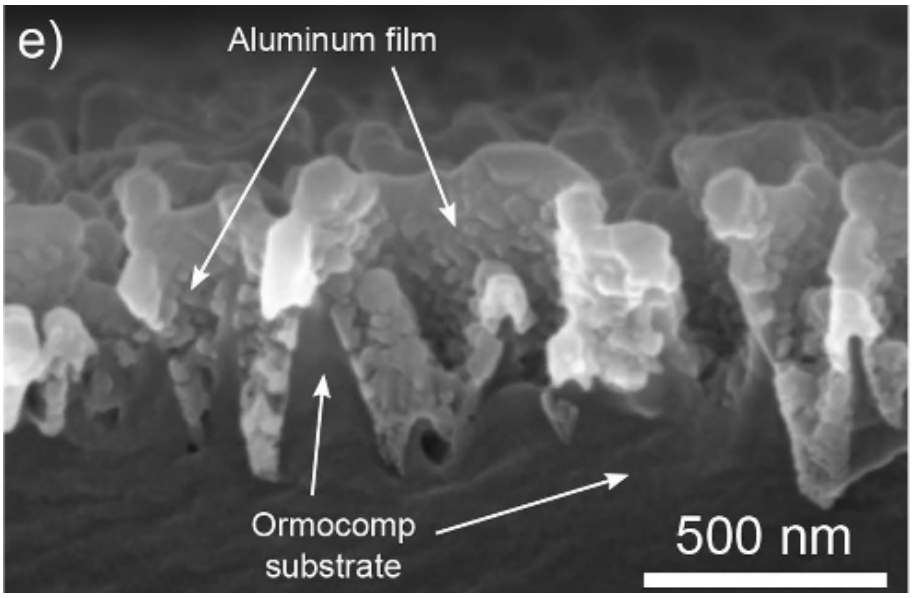

FIGURE 3.10: Metallic aluminium film deposited on a nanostructured dielectric film as shown in [23]. [Reprinted] with permission from [23].

Another approach of using plasmonics, is to use metallic silver particles in the window layers of solar cells. In [113], silver nanoparticles are embedded in a planar window layer of titanium dioxde as shown in figure 3.12. As a result of the antireflective performance, the net optoelectronic performance of the system improves. Forward scattering of the metallic particle layer results in increased light transfer into the solar cell thereby increasing absorption.

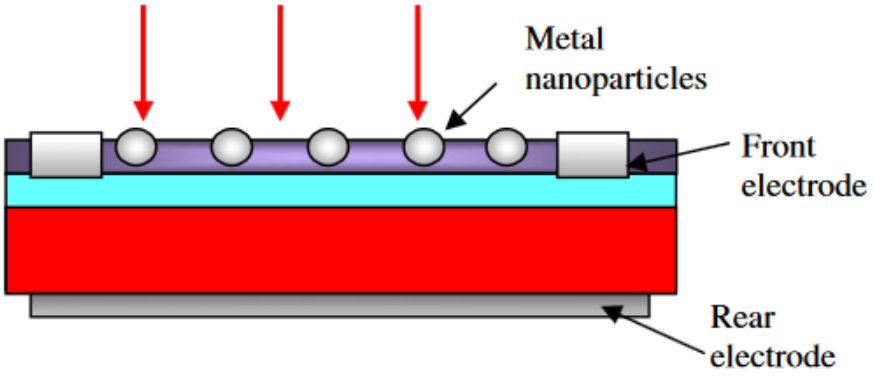

FIGURE 3.11: Metallic nanoparticles in dielectric window layer in order to direct more light into the absorber layer via forward scattering mechanisms as shown in [113]. [Reprinted] with permission from [113].

Another combination of metallic and dielectric particle combination, is the broadband antireflection system described in [62]. In this approach a thin film of silicon dioxide is deposited between gold particles on a bilayer of silicon dioxide and gold on a silicon wafer.

This combined system helps in reducing the silicon reflection to below 5 percent values in the wavelength range between 500-750 nm.

Mie resonances are easily excitable in spherical particle systems. This behavior is exploited in the work of Baryshnikova et al. in [10] which discusses modelling of spherical particles made out of either silver or silicon. This work utilises Kerker effect which describes the leaking/forward transfer of particle resonances on substrates.[7] Mie resonances leak into a high index material (substrate) when the particle is present on the substrate. This phenomenon helps in shrinking of silicon reflection to moderately low values depending upon the type of particles used. This approach is particularly successful in tuning the spectral response to have near zero reflection at localised wavelengths. This behavior is shown in figure 3.12.

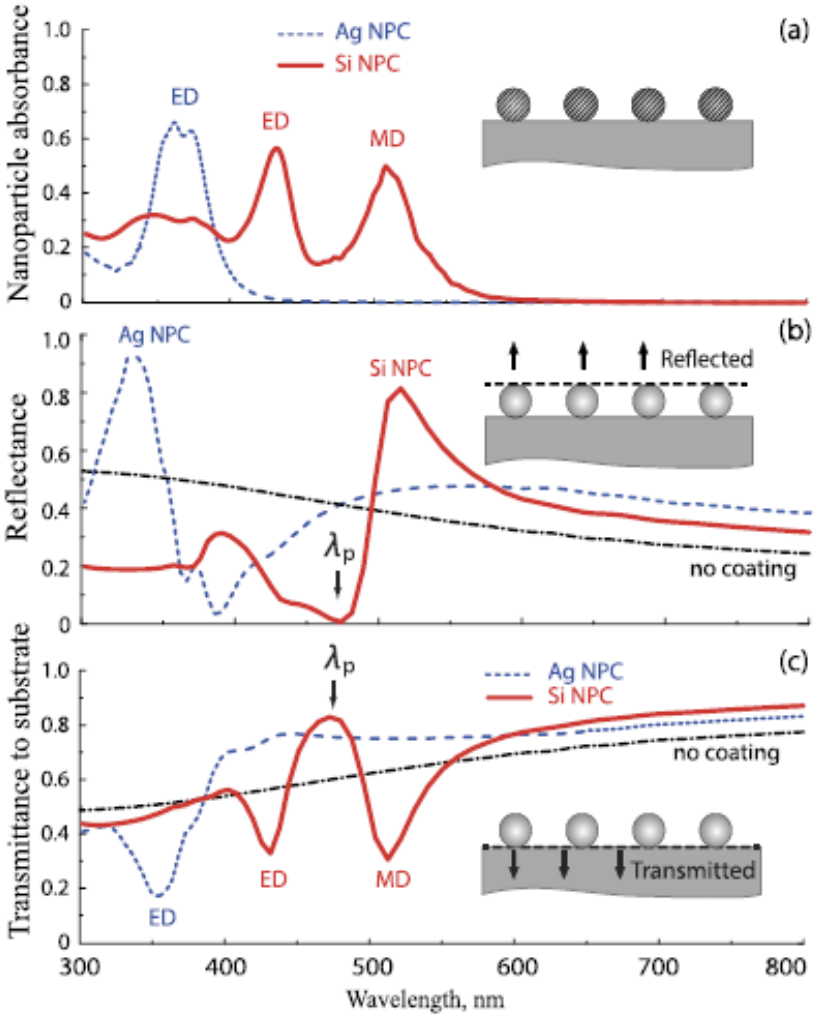

FIGURE 3.12: Silver or silicon nanoparticles on silicon substrates which have been demonstrated to reduce silicon reflection as shown in [7]. This shows particle resonances such as electric dipole (ED) or magnetic dipole (MD) influencing transmission into a high index substrate.[Reprinted] with permission from [7].

These examples display the spectrum of approaches utilised to solve the problem of anti-reflection based on a variety of optical principles.

Chapter 4

Fabrication of Nanostructures

In this chapter, we systematically describe the two fabrication approaches for the metasurface and the so called soup bowl nanostructure. E-beam lithography forms the backbone behind the patterning of titanium dioxide into a periodic arrangement to obtain metasurfaces. Self organised polystyrene spheres form the deterministic step to the initial mask to arrive at the soup bowl structure. These fabrication sequences play an important role in imparting optical properties to the nanostructures. Each step in the fabrication process ensures this optical goal. We first begin with describing the fabrication sequence of nanofrustum surfaces and then describe the iterative approach of the soupbowl structure.

4.1 Fabrication sequence of the nanofrustum metasurface

The fabrication sequence used to fabricate metasurfaces consists of material deposition via sputtering, electron beam lithography for patterning and material etching to get to the final nanostructure. We summarise the described process steps graphically in figure 4.1 and then describe each step elaborately. Individually each of these steps are established generic nanofabrication procedures. However here we describe them in connection with our efforts to tailor them specifically to fabricate the metasurfaces we have designed via numerical simulations. Every minor detail of the physical functioning of these processes contributes to the reasonable agreement between measured and simulated spectra we show in the subsequent chapter 6. Without these steps it would be extremely difficult to implement the desired optical effects to form.

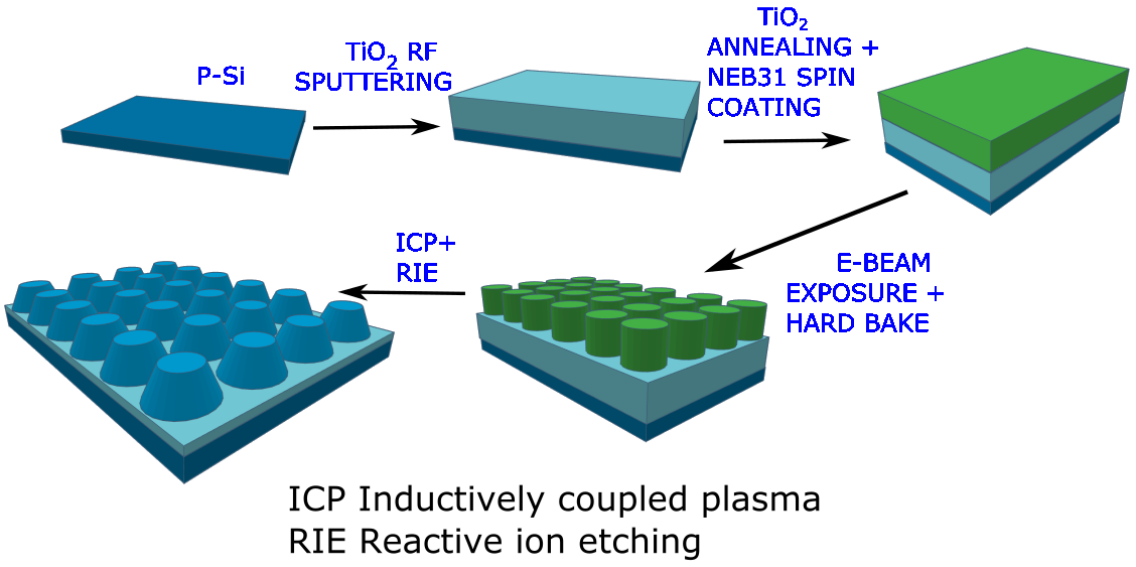

FIGURE 4.1: Overview of the fabrication sequence adopted to obtain the nanofrustum metasurface,using material deposition (RF sputtering), E-beam deposition to create the mask on the pattern and etching the mask with inductively coupled reactive ion etching (ICP)

4.1.1 RF sputtering for titanium dioxide deposition

The geometrical parameters of the metasurfaces are derived from the comprehensive simulation to be presented in chapter 5 and 6. One of the starting parameters of utmost importance is the material quality of the titanium dioxide used. This material quality influences the optical constants as well as the surface characteristics to obtain a good nanostructure post etch. This calls for deploying a well optimised deposition process which results in a good quality material deposition without using extended duration processes such as atomic layer deposition. The other alternative is to use electron gun depositon. However considering the dielectric nature of titanium dioxide, this process is time consuming and requires tremendous optimisation.[54] A favorable option is to use RF magnetron sputtering. Although the sputter rate of titanium dioxide is significantly low, it can be optimised by carefully varying the process parameters.[71] The important parameter is the RF power which excites the plasma. The Argon gas concentration treats the newly formed film. Supply of other gases which help in improving the material quality of the deposited titanium dioxide include oxygen. The sample distance from the target also helps in determining the solid angle which the plasma makes with the substrate. The material source is compact solid titanium dioxide. This is placed on high field magnet to which the RF power is supplied. The combination of an RF source in presence of a high field magnet results in the titanium dioxide from the target ionising. The applied RF power also sets up a bias between the target (anode) and the sample (cathode).[36] This results in the upward transfer of titanium dioxide ions from the target to the sample. In order to increase the sputtering rate as well as to ensure that high quality

plasma is incident on the sample, we maintain a close sputtering distance of 9 cm. Material scientists and chemists have proved that introducing oxygen gas during sputter deposition helps in improving the quality of the sputtered layer.

Our observations during sputtering trials indicated that having oxygen in the process results in a decrease in the rate of deposition.[28] Therefore we decided to keep the oxygen supply on for only the first 15 mins of the process. Argon is supplied into the chamber for the entire duration. This helps in maintaining a good surface quality of the film. We maintain an RF power of 180 W with the help of a well controlled impedance matching network to compensate for the changes in chamber impedance as a result of gas and ion flow. Over iterative trials, we observe that to obtain a planar film of 200 nm, a total process time of 90 minutes is required.

In order to further improve the quality of the deposited layer, post deposition, we anneal the obtained film in the presence of oxygen in an oven. This annealing is performed by raising the temperature of the film with a peculiar time distribtuion. Such a distribution helps in the gradual heating and cooling of the film. We maintain the maximum temperature in this annealing curve to be less than the crystallisation temperature of titanium dioxide. The used heating curve is shown in figure 4.2. The slow gradients in the annealing process in presence of oxygen result in obtaining good material quality.

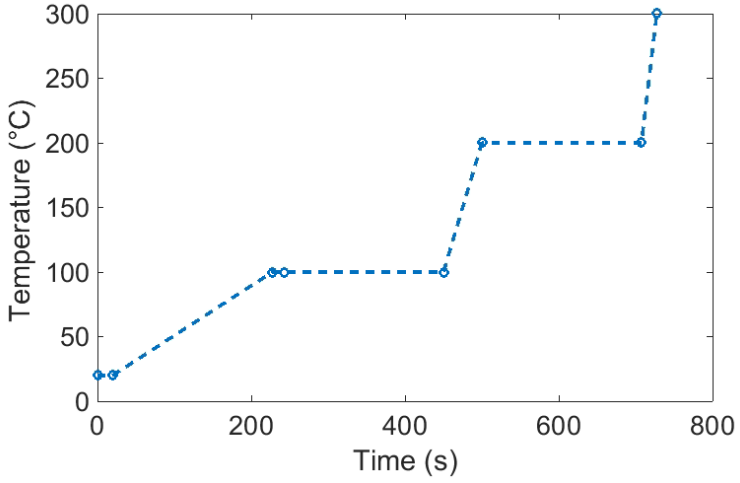

FIGURE 4.2: Temperature distribution of the annealing process against time

In order to characterise the film for optical constants, we perform ellipsometric measurements on the planar film. The measured data is fitted against analytical models to arrive at the refractive index value. From figure 4.3 the refractive index of titanium dioxide is at par with the best case values reported in literature. The imaginary part of the refractive

index is zero starting from 360 nm. This is of tremendous benefit for the intended application of antireflection. The obtained optical constants are used to model the reflection of a planar film of a known thickness. The measured reflection of this film is compared with the modeled reflection obtained from the measured optical constants. A good fit between the measured and modeled reflection confirms the validity of the obtained optical constants and their dispersive trend.

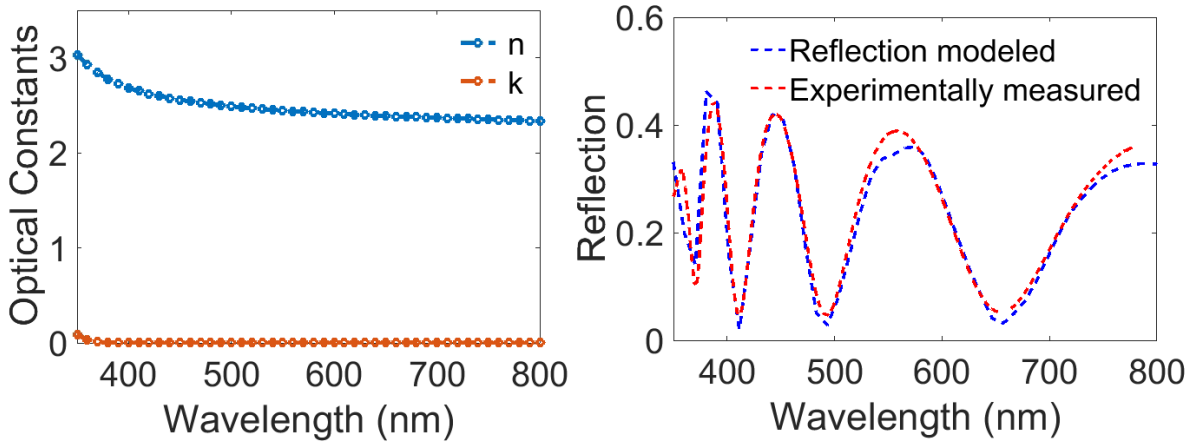

FIGURE 4.3: Obtained optical constants from the process and comparison between calculated and measured reflection. The optical constants (n,k) are obtained by performing ellipsometric measurements. These are then confirmed by the reasonable agreement obtained with the modeled reflection of titanium dioxide on silicon using measured optical constants and the actual measured silicon reflection

4.1.2 E-beam lithography

We use electron beam lithography to precisely arrive at the subwavelength lattice pattern obtained out of iterative simulations. Electron beam lithography functions by precisely focussing a beam of high kinetic energy electrons on easily transformable organic resist. This high kinetic energy is achieved with aid of high acceleration voltage. Most organic resists are polymers which are susceptible to transformation upon exposure of an electron beam. The choice of this resist depends upon two factors. The feature density in the desired mask pattern determines the choice of the resist. The second and the most important consideration of the choice of the resist is the strong ability to withstand the extreme chemical and physical environments of the etch process used to arrive at the final nanostructure. Taking overview from various databases we use the organic resist NEB31. This resist is negative, i.e it is sacrificed during exposure from a planar film to the pattern which is intended to be developed. It forms cylinders which protect the integrity of the material below it. These cylinders are used as etch masks in the subsequent etch process to etch away titanium dioxide

to to obtain the final structure. Post exposure with the E-beam, the resist is developed with a developer solution and unexposed resist is washed off.

In combination with the appropriate resist, the physical parameters of the electron beam, such as the beam current and beam voltage determine the total spot size. An high electron beam acceleration voltage and very low beam current results in an extremely small spot size. Such a low spot size is required in order to effectively arrive at feature dimensions of the order of few 100 nanometers placed at a subwavelength spacing. Typical values of beam voltage is 30 KV and beam current are in the range of 1-2 pA. In order to successfully arrive at the mask pattern of the desired dimensions, the flux per unit area which is incident on the resist film needs to be iteratively optimised. This flux is commonly referred to as the electron beam dose. The unit of this dose is nC/cm and is a function of the susbtrate used, the thickness of the resist and the polarisation sensitivity of the resist for the desired pattern feature linewidth and density. The resist thickness is decided by the targeted etch depth of the desired nanostructure. For physically and chemically harsh etching environments, the resist thickness should be much higher than the desired etch depth. This prevents mask erosion and helps in fabricating high quality structures. After feedbacks from substanial etch trials we maintain a resist thickness of 450 nm. We spin coat the resist with the help of a calibrated motorised spin coater. The target thickness is obtained by gradually stepping up the speed of the motor. After several iterative dose trials, we arrive at the appropriate mask for a dose value of 45 nC/cm on the JEOL e-beam system and 12.5 nC/cm on the Nabity e-beam system. The two systems are electron beam lithography systems which difffer in terms of speed of implementing the pattern. The nabity e-beam system is used to generate masks as trial masks to arrive at the correct parameters of inductively coupled plasma etch process. The final 1 mm $\times$ 1 mm samples are prepared by the JEOL e-beam system for optical characterisation as well as application as photocathodes.

Post patterning with e-beam, the obtained mask needs to be developed with the help of a compatible solution. The compatible developer for the resist used is MF321. In the next step, this is baked on a hot plate to a temperature of 90° C. In principle, the resist is ready for etching at this stage. After feedback from the etch trials, in order to improve the sustainance of the resist against the resist erosion, we introduce the hard baking step. In this step, we bake the resist up to a temperature of 90°C on a hot plate for a time duration of 15 minutes. This hardens the resist without altering the morphology of the mask since the temperature is lower than the repolymerisation of the resist. Such a hard bake resist shows impeccable integrity in withstanding harsh etching environments.

4.1.3 Inductively coupled plasma etching

After obtaining a well exposed and developed resist, the next step is to etch the titanium dioxide not covered by the mask. Titanium dioxide as a result of its dielectric nature is quite resistant to etch tendencies. This calls for extreme physical and chemical etch environments.[2] The physical environment helps in improving the physical quality of the etch. The chemical environment decides the etch rate of the titanium dioxide. The etch consists of a combination of an inductively coupled plasma(ICP) component and a reactive ion component. The inductively coupled plasma generates a high power Argon plasma. This forms the physical environment of the etch. The power of the so called ICP source determines the kinetic energy of the Argon plasma. The Argon (Ar) plasma is responsible in maintaining clean surface energies post the reactive component. This results in extremely smooth surfaces. It plays a pivotal role in eliminating biproducts of the chemical etch reaction from the lateral surface of etched nanostructure. It is important to not have too high a value for the inductively coupled plasma source to avoid physical etching of the resist mask as a result of the high ion bombardment.

The chemical environment of the etch results in titanium dioxide reactively etched with the help of a reactive flourine rich gas. Carbon tetraflouride CF_4 is the gas used in this case. The extent of this etch is decided by the operating temperature, gas flow ratio, pressure as well as kinetic energy of CF_4. The kinetic energy of CF_4 is determined by the RF power which maintains a potential bias between the sample to be etched and the etch chamber (gas inlet). This bias potential results in the gas flow from the source to the sample. The bias potential decides, the kinetic energy of the CF_4 ions which react with titanium dioxide. This value also determines the directionality of the etch. A high bias results in a highly directional etch resulting in perpendicular side walls. By gradually tuning the values of this bias generating power, we can arrive at the right side wall angle desired. The desired etch depth and the accompanying side wall angle need to be achieved by maintaining the right balance of the gas flow (CF_4/Ar) and the RF power which forms the accelerating bias to the system. Both these values should be such that the resist is not eroded substantially.

Another important parameter is the time duration for which the etch is performed. This is iteratively tried till satisfactory values are obtained in terms of the structure height and taper angle. The temperature inside the etch chamber plays an important role in determining the reaction dynamics and the final etched shape obtained. A high temperature increases the rate of the reaction, this tends to hinder the surface quality of the side walls. In addition to the chamber temperature, localised heating can arise as a result of the high energy bombardment of electrons. This causes localised heating into the substrate. This results in inconsistent

variation in the etch rate. To prevent this, we insulate the sample from the chamber by mounting it on a silicon carrier wafer which is spin coated by a standard organic resist. The resist helps in protecting the sample from external temperature fluxes.

The gas flow ratio, decides the volume mix of the gases inside the etch chamber. The operating pressure does determine the gas flow in the system as well as the ionic energy. In accordance to the volume of the chamber this value is set to 10 mT. The last and most important etch parameter is good and reliable stability of the RF phase matching network which controls the power levels of the inductively coupled plasma and the plasma of the reactive ions. The phase matching network needs to be configured in a way that it is able to match itself with respect to the chamber impedance. In such a situation, almost no power is reflected away from the chamber through the network but rather transmitted into the chamber. In this situation, we have maximum etch yield.

It is evident from the discussion above that each parameter of the etch process holds tremendous physical significance in influencing the final outcome. After spending considerable effort in iteratively varying each etch parameter and observing the difference we arrive at the following process parameters summarised in table 4.1. Post etch, the sample is plasma

Etch Parameters- Titanium Dioxide (Etch rate 1nm/sec)- Etch Time 150 secs				
Inductively Coupled Plasma	Reactive Ion Plasma	Argon Flow	CF_4 Flow	Pressure
400 W	25 W	50%	40%	10mT

TABLE 4.1: Final etch parameters used to obtain the desired structures after iterative process development

cleaned with the aid of an oxygen plasma for about two hours to clean the surfaces of the resist residue as well as any remaining biproducts of the etch process. Post this step the samples are ready for morphological and optical characterisation.

Post successful implementation of the above described process sequence, we characterise the obtained structures with the aid of a scanning electron microscope and a focused ion beam. Figure 4.4 show top view, cross section images (FIB), and images under a tilt when viewed under an electron microscope. These images indicate the outcome of a well defined grid of structures with extremely good quality material properties. The careful implementation of each stage of the process step results in good structures. The uniformity of these structures in terms of obtained cross sections as well as side wall tapers is a result of the iteratively optimised etch process. The flat tops of the frustum indicate that the resist mask did not get

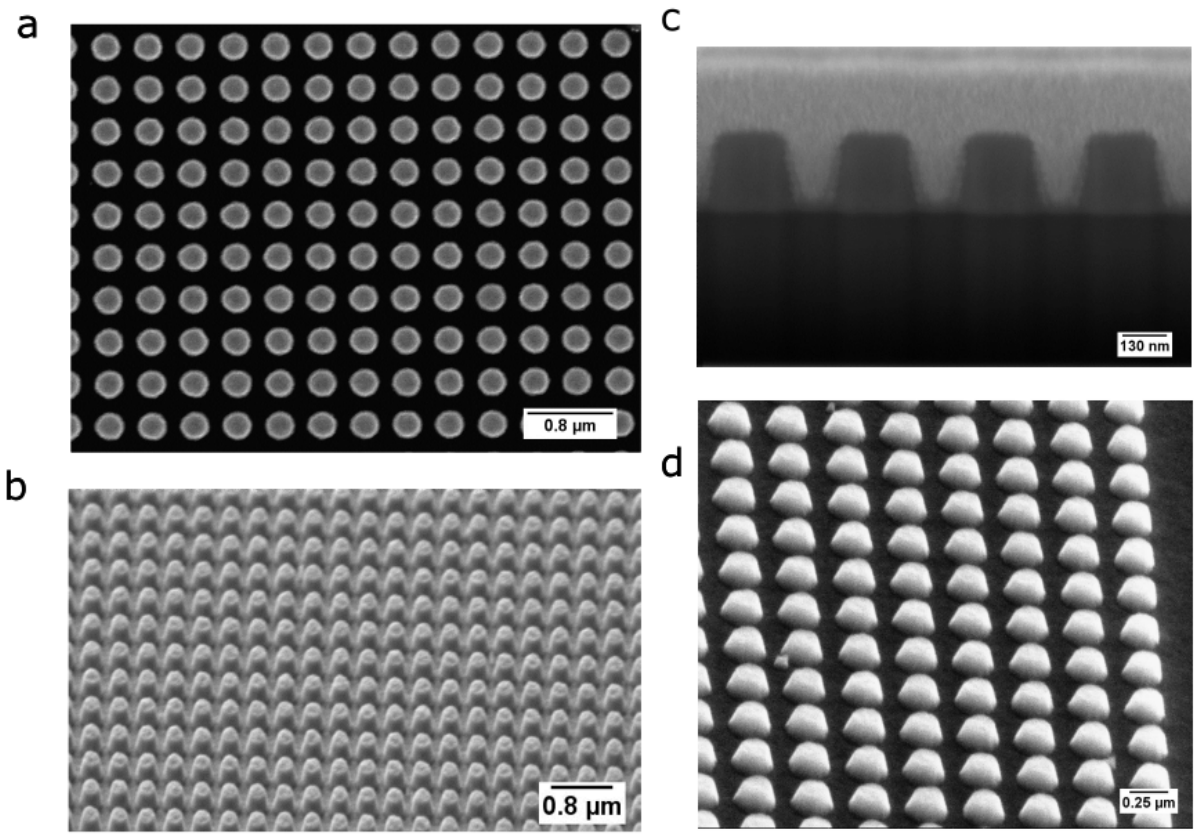

FIGURE 4.4: Morphology output of the obtained metasurface: (a) Top view (b) Tilted view (36°) (c) FIB cross section (d) Tilted view(45°) focussing on the smooth side walls

depleted during the etch process. This leads to extremely uniform frustum geometry. The dimensions of these structures are shown in table 4.2. These dimensions are obtained with the aid of the reference scale of the electron microscope visualiser and are associated with the tolerances involved. This relative error is expected to be very small compared to the overall sizes reported and maybe ignored.

Dimensions of the Titanium Dioxide Nanofrustums				
Frustum Height	Radius Top	Radius Bottom	Height of Planar Film	Pitch
150 nm	100 nm	120 nm	50 nm	360 nm

TABLE 4.2: Dimensions of the frustums obtained out of the process sequence

4.2 Fabrication sequence of the soupbowl nanostructure

In order to exploit the full potential of nanostructures to be commercially viable candidates over planar anti-reflection layers, the pattern generation process defining the structure should be easy to scale up. This calls for the selection of a pattern which offers enough selectivity in terms of geometric parameters as well as having the potenial to pattern over large areas. Colloidal nanosphere lithography offers both these features. We use colloidal lithography as a part of an iteratively developed process sequence. This sequence is shown in figure 4.5. In the subsequent text, we describe the development of this sequence in terms of masking via colloidal lithography, etch aided mask modification and material deposition. The detailed

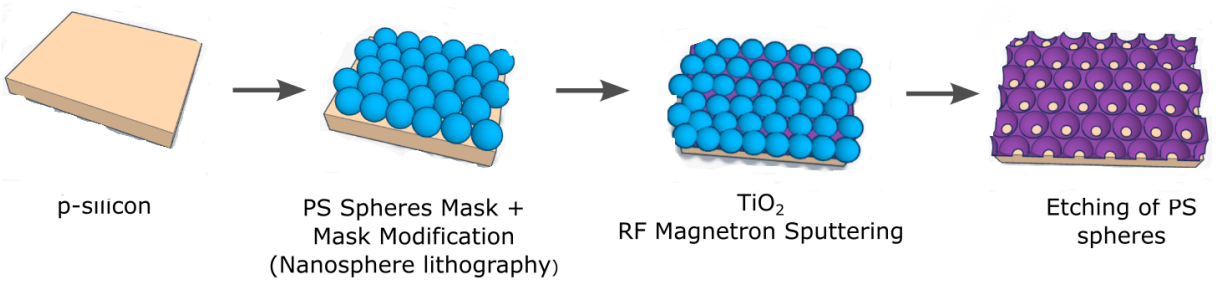

FIGURE 4.5: Process sequence to obtain titanium Dioxide soup bowls on Silicon

optical characterisation of these structures and inferences from computational analysis is shown in chapter 7. Due to the concave shape of the formed nanostructures as a result of the nanosphere mask, we refer to the structures as soupbowls.

We use nanosphere lithography as a starting step to lay out a mask.[29, 24, 44] A commercially available colloidal solution of polystyrene nanospheres is used to pattern a piece cut out of a p- type silicon wafer. In order to achieve a closed pack arrangement of spheres, the colloidal solution is mixed with a solution of polystyrene in ethanol. For ease of visibility and handling, we start with a sphere diameter of 900 nm. This size later needs to be tailored in order to obtain a geometry which is attainable with the process sequence and furthermore offers significant anti-reflection properties.[8] Polystyrene enables good bonding between the spheres in order to achieve a targeted mask arrangement which resembles a hexagonally packed lattice structure.

The mask is developed on a clean water surface by using the well known Langmuir-Blodgett method in wet chemistry. De-ionised water is filled in a thoroughly cleaned palm sized petri dish. A glass pipette is given an angular bend at its outlet with the help of a Bunsen flame in order to enable constant laminar flow of the collodial solution. A constant laminar flow of the solution from the pipette results in a shimmering surface on the water surface. Figure 4.6(a)

describes the flow of the collodial mixture to form a monolayer on the water surface.[98] It is essential to provide gentle nudges to the petri dish in order to create ripples on the water surface. These ripples result in the mask centering itself on the petri-dish and forming a closed packed layer.

Cleaned double sided polished silicon substrates are then immersed at the bottom of the petri dish. Additional water is gradually drained with the help of a small suction syringe without disturbing the mask areas. The water surface eventually reaches close to the substrate top surface such that the mask starts cornering around the substrate edge. At this point the mask settled on the silicon subsrtrate can be left to dry. The masking procedure as well as a fully masked silicon sample are shown in figure 4.6(a)

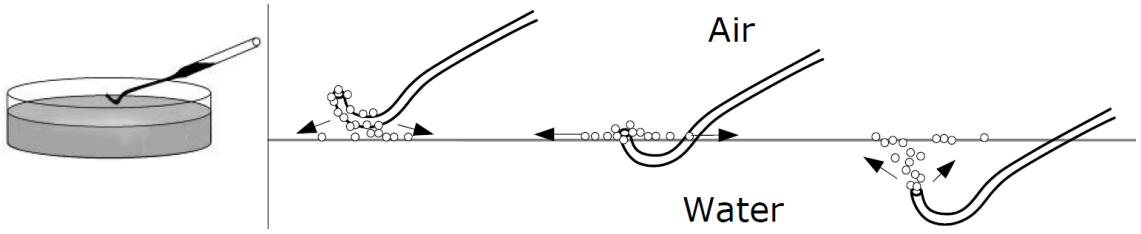

(a) Langmuir Blodgett procedure

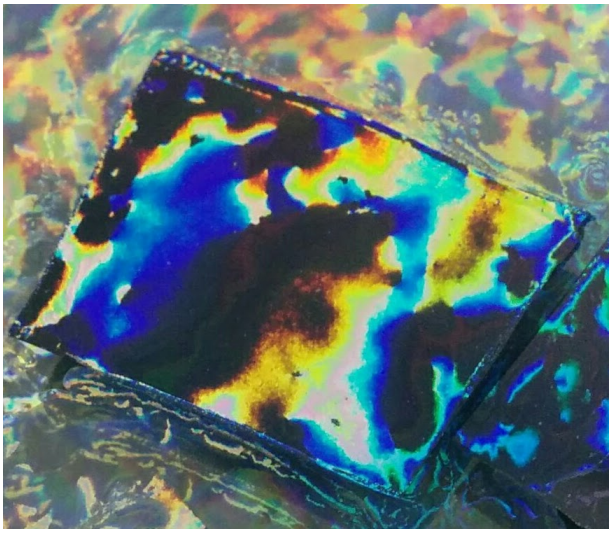

(b) Patterned mask on a 2 cm X 1 cm piece of silicon

FIGURE 4.6: (a) Langmuir Blodgett procedure [98] and (b) corresponding developed colloidal mask on silicon on a 2 cm x 1 cm piece of silicon

Aiming to directly sputter titanium dioxide between the already exisiting minor openings of the mask did not yield a viable structure. This called for strategies to loosen the close packed nature of the mask while maintaining its spherical integrity. This spherical integrity is important in order to have the material growth conform to the mask. A subsequent sputter

deposition of titanium dioxide should follow this step. This can be achieved with modifying the mask via suitable chemical or physical means. Such a mask modification should facilitate the opening of spaces between the spheres by shrinking them in size without disrupting their arrangement. Any organic solution based approach tends to be strongly chemically reactive which often results in damaging the spherical surface of the spheres. This calls for a mild chemical approach (gas interaction) in a systematically regulated physical environment (pressure and flow regulation) such as plasma etching.[31] A low vacuum, low power etcher with oxygen inlet is sufficient for this purpose. The samples to be etched are placed across a potential bias with respect to the ion inlet, which directs the ion flow to the sample. Oxygen gas ions are then directed towards the sample as a result of the bias.[134] The oxygen ions react with the mask and etch the spheres in size. This reduction in the sphere size is hereby referred to as the etch rate. This etch rate is influenced by the physical conditions such as the applied etch power and gas pressure. Additionally it is also a function of the sphere diameter and substrate material. It has been proved that the etch rate increases with high power and increased oxygen concentration. Subsequently this etch rate also paves the way for the titanium dioxide to be deposited in between the gaps of the nanostructure. It eventually also determines to what extent the sputtered titanium oxide shall follow the spherical contour of the spherical mask.

It thereby becomes inevitable to systematically vary the most important process variables particularly - diameter of the masking spheres, sphere etch time and sputter process time. The standard parameters involved with the sputter process only influence the refractive index of titanium dioxide. Starting with a sphere diameter of 900 nm we vary the etch times to 3 min, 5 min and 7 mins and calculate the resulting etch rate of the spheres. The spheres etch at an average rate of 35-50 nm/min. Each of the three samples, hereby named as 900a, 900b and 900c corresponding to the etch times, respectively. The overview of these increased gaps are shown in figures 4.7(a), 4.7(b) and 4.7(c).

Obtaining samples with a loosely packed ordered arrangement in the mask, allowed for increasing the sputtering time to enable nanostructure growth conformed to the mask pattern. It is with this aim, that the sputtering time is set to 2 hours. Oxygen is purged in for the first one hour along with argon. For the second hour, the oxygen supply is turned off. Following a sputter deposition, the mask is etched with toluene and the obtained morphology is obtained for all three cases. This is shown in the subsequent images. We observe a good growth

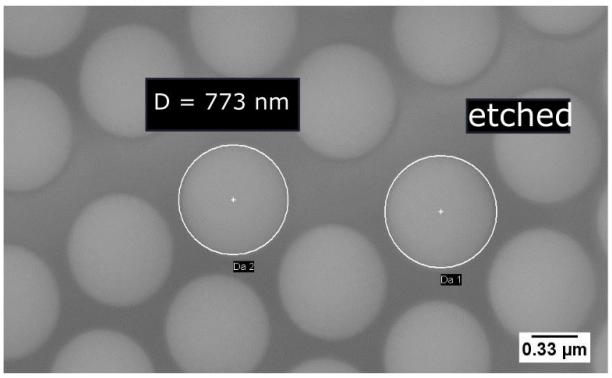

(a) 900a- 3 min Etch time

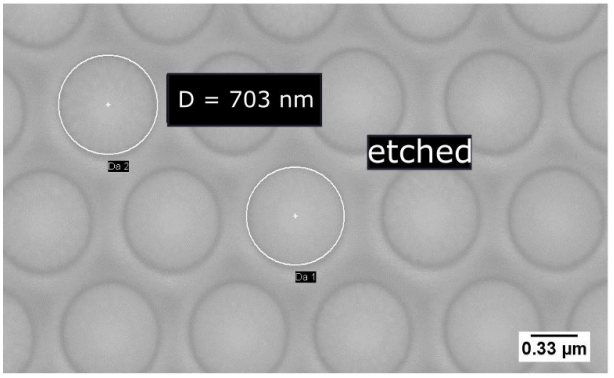

(b) 900b-5 min Etch time

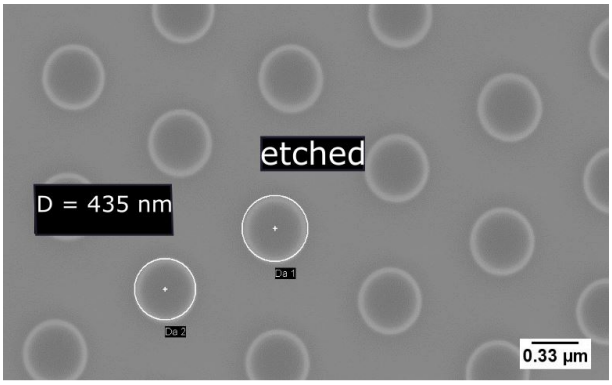

(c) 900c- 7 min Etch time

FIGURE 4.7: SEM top views of substrates with colloidal masks etched at different etch times

conformity to the spherical contour of the mask in the case where the spheres are etched for 3 mins in figure 4.8(a). For the other two etch times, however, owing to excessive shrinkage of the mask, the deposited layer almost traps the mask, resulting in a non-viable nanostructure. These SEM images clearly indicate excessive titanium dioxide growth on the surface of the mask which prohibits its complete separation as seen in figure 4.8(c) and figure 4.8(b). After this trial of the etch time, we now have the complete set of parameters for the sequence using the 900 nm mask.

In order to evaluate this structure optically, we take the aid of optical spectral measurements to check for anti-reflection performance. These measurements are used as a feedback for the fabrication process and decide the next fabrication steps to be tried. Using a well calibrated spectrometer setup in combination with an integrating sphere, we measure the total and diffuse reflection. The diffuse spectra of the nanostructure are obtained via eliminating the specular light from the total light collected in the integrating sphere during the measurement. In an integrating sphere, light is incident at an angle of 8°, the specular reflected light corresponds to the light reflected at 8°. The specular reflection is then obtained by

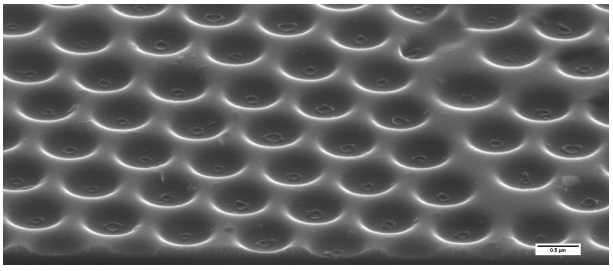

(a) 900a- 3 min Etch time- Post Process

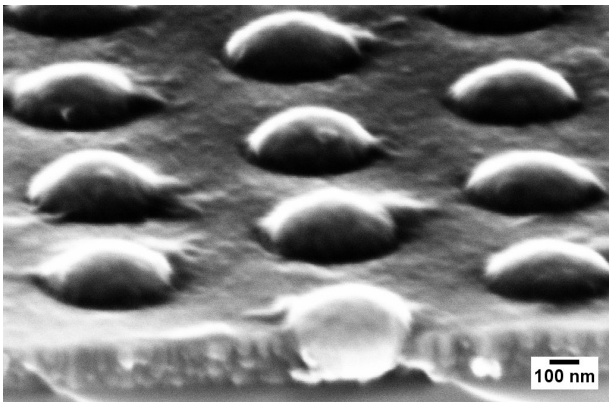

(b) 900b- 5 min Etch time- Post Process

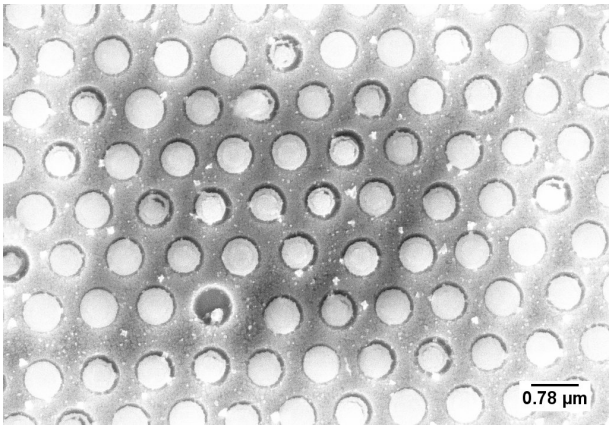

(c) 900c- 7 min Etch time-Post Process

FIGURE 4.8: SEM images of titanium dioxide deposited on substrates with masks etched for different times

subtracting the diffuse reflection from the total reflection. All the three curves are measured between 300-800 nm as shown in figure 4.9.

In order to evaluate the optical properties as a result of the adopted process sequence, we compare the measured reflection of the nanostructures on silicon to that of measured bare silicon reflection. The nanostructure on silicon sample offers significantly less total reflection in comparison with the bare silicon. This decrease in reflection is reasonably uniform across the entire measurement bandwidth. We observe that in the wavelength bandwidth between 400-700 nm, the total reflection value is around 20 percent with minor fluctuations. A silicon wafer being smooth and planar has almost no diffuse reflection, therefore the obtained reflection is entirely specular. If we look at the diffuse reflection spectra of the nanostructure then it significantly contributes to the measured total reflection. A high diffuse reflection normally arises from morphological properties such as the lattice like pattern of the spherical bowls and material texture in the nanostructure. The interface between the nanostructure and silicon is also of particular significance. In figure 4.8(a), we clearly observe rough circular

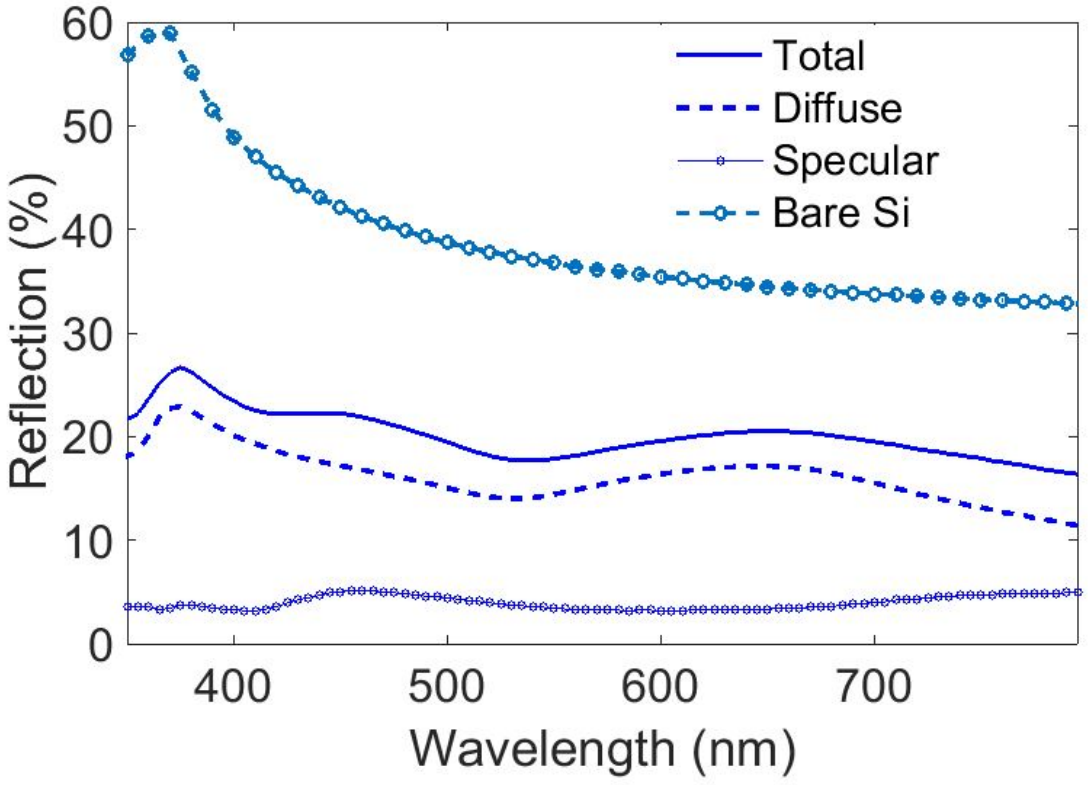

FIGURE 4.9: Spectral reflection properties result of the structures formed by the 900 nm colloidal mask

shape patches at the bottom of the holes where the soup bowl touches the silicon. The circular shape here is an effect of the material growth around the spherical mask. The measured specular reflection, which is the difference between the total and the diffuse reflection is rather low. The adopted process therefore is useful to significantly reduce reflection. However the average value of reflection is still high and the process parameters could be optimised in order to reduce this further.

At this juncture, a viable argument would be to take aid of electromagnetic simulations and get the correct model which appropriately simulates the obtained structure. This would then pave the way to find via rigourous simulations geometric parameters which minimise reflection. However this is not straightforward as it seems as a result of the predefined parameters of the commerically available colloidal lithography mask. The parameter space of the simulations could be reduced to obtaining the correct height for a given mask size but the challenge still remains to obtain the right process parameters to obtain that height for the given mask. We therefore adopt to experimentally improve the antireflection performance. The material sputter growth on such a masked sample is highly subject to the shape and spacing of the mask. This implies that the growth rate would not remain the same for two different mask sizes. Furthermore, as shown above there might be cases where the

growth results in trapping of the mask in the grown layer. This mask trapping results in no homogenous titanium dioxide nanostructure formed. It therefore is more appropriate to optimise the structure experimentally first and then simulate it.

In order to experimentally optimise the structure with the aid of the process parameters, we keep the time and parameters of the sputter growth constant and focus on varying the mask size. In order to try and achieve low reflection, we start with reducing the mask diameter to 600 nm. Reducing the mask size, effectively reduces the spacing between the individual nanostructures. In accordance with the theory of periodic nanostructured lattices, it is expected that reducing the spacing between the nanostructures, reduces if present, the higher orders of reflection. It is an attempt to try and possibly restrict the reflection only to the fundamental order, i.e the specular reflection and reduce the amplitude of this order. The goal is to reduce the overall reflection by the nanostructure. Additionally, it will play a significant role in determining the curvature of the grown bowls. For the next process step, i.e. the mask etching step, we use 2 times, 1 min and 3 mins owing to the slightly reduced size of the starting colloidal mask. After this step, we use the same sputter routine and etch away the spheres obtained. On examining the structure under an electron microscope,

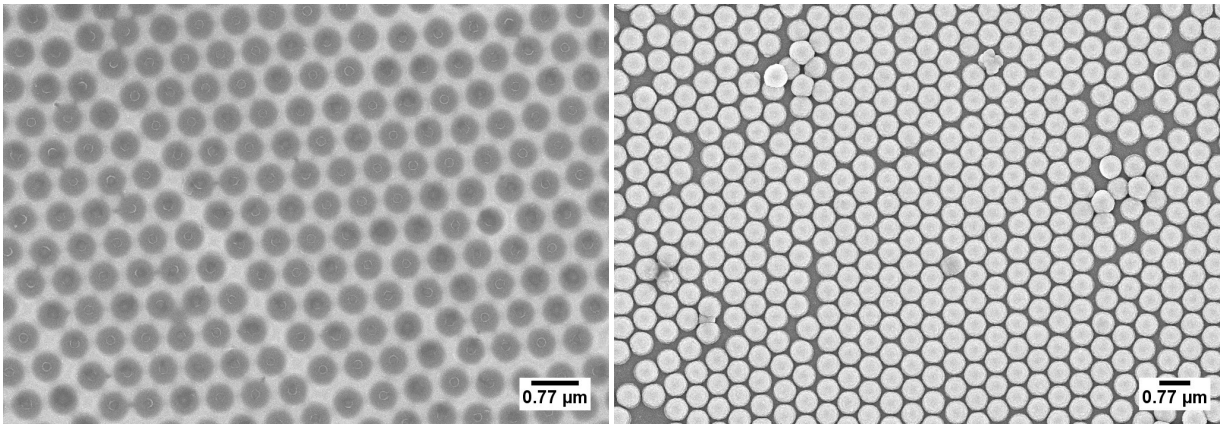

(a) 600 nm mask - 1 min etch time- Post Process (b) 600 nm mask - 3 min etch time-Post Process

FIGURE 4.10: SEM images indicating the outcome of the complete process sequence using 600 nm mask for different etch times

as seen in figure 4.10(a) and figure 4.10(b), for the 1 min etch time, the structure has a good spherical contour. For the three min mask etch time, the spherical mask, is trapped in the layer grown as a result of the overgrowth of the film in comparison of the mask size. Subsequently we characterise the obtained structure, for spectral optical properties as previously described. Figure 4.11 shows the total reflection of the nanostructure. We observe that the total reflection in this case is lower than the nanostructure developed using the 900 nm mask. This process iteration shows that by reducing the size of the mask as well as in proportion with the mask etch time, we can significantly reduce the observed total

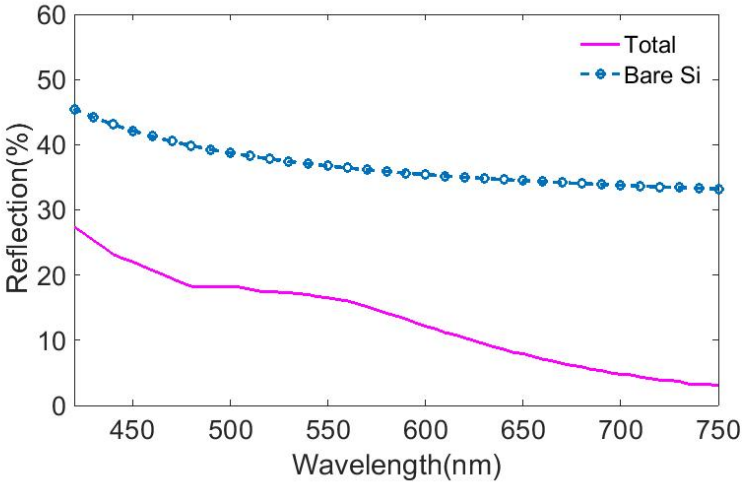

FIGURE 4.11: Reflection spectra of the nanostructure obtained using the 600 nm mask. We also compare this spectra to the bare silicon reflection.

reflection. Reflection begins to decrease at 420 nm, at a very strong rate. Across a bandwidth of 200 nm, in the wavelength range 400 - 600 nm the total reflection drops by almost by 50 percent. Moreover between 600 - 750 nm, the reflection goes down to 5 percent which is quite a remarkable broadband effect for silicon considering its high refractive index and the relatively simple lithography based process sequence used.

With this process sequence, we achieve a suppression above 480 nm wavelength by at least 50 percent. Much of the measurement bandwidth is absorption free for titanium dioxide, thereby ensuring that the light quantified by '1-Reflection' is directed to silicon as a result of the nanostructure. This light corresponds to non-reflected light for the bilayer stack. Owing to zero optical loss in titanium dioxide in this wavelength range, this light is then entirely available for silicon absorption. Therefore by simply changing the initial mask size we can drastically influence the reflection to more desired values.

In order to try and further exploit this effect, we decrease the mask size to 300 nm in order to target even sub-wavelength dimensions for the far U-V and early visible wavelengths [48] We use two mask etch times of 30 and 60 secs. Processing via the same sputter routine, in the morphological views, we obtain a non-viable nanostructure as a result of colloidal mask spheres being trapped in the sputtered layer. In order to counteract this action, in subsequent trials, we reduce the sputtering time to one hour but it did not change the yield. Reducing the time even further may intutively be the solution to a viable structure. However the reflection spectra of such a structure would not lie in the category of high performing

antireflection across a large bandwidth. Various trials such as reducing the combined oxygen argon purge time in the sputter process or skipping it entirely leads to no avail. The relevant information to be drawn from this trials is that packing density of the mask after etching is still much dense for the 300 nm collodial mask size. In the sputtering step, this closed packed density leads to profound vertical sputter growth. In effect, it makes it difficult to obtain a viable nanostructure with similar geometrical properties as described above. If suitable process modifications are obtained which allows homogenous structure growth with sphere diameters less than 600 nm, then this would be of significant advantage to enhance antireflection performance.

Nonetheless, through iterative process development, we have managed to get a partially optimised well performing nanostructure. The feedback between optical spectra and process parameters helped in establishing the process parameters for a well performing nanostructure. With a 600 nm colloidal sphere mask size and mask etch time of 1 min with the pre-established sputtering routine, we obtain a high performing nanostructure with good anti-reflective properties. The obtained dimensions of this structure are summarised in table 4.3 Subsequently we also show the microscope images using a tilt in figure 4.13 and figure

Dimensions of the titanium dioxide soupbowls		
Height	Lattice Length	Diameter hole
240 nm	290 nm	480 nm

TABLE 4.3: Dimensions of the spherical soupbowl obtained out of the iterative fabrication process. The lattice length is calculated from the diagonals of the hexagonal lattice formed by the spherical holes. The dimensions are extracted from the SEM images and entailing geometrical calculations

4.12 the cross section images obtained using focussed ion beam to give a complete overview of the morphology of the structure.

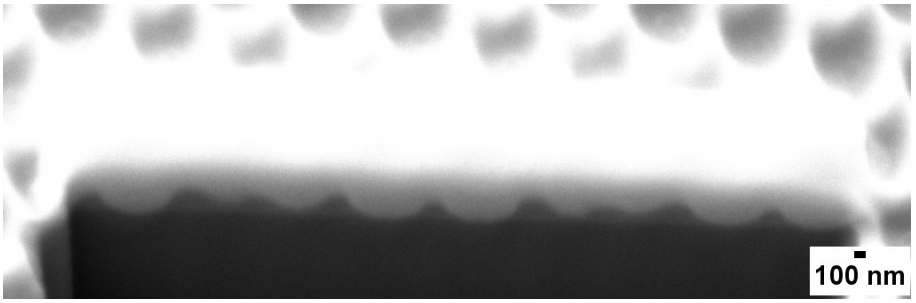

FIGURE 4.12: Morphogical image of the fabricated spherical bowl structure in the cross section

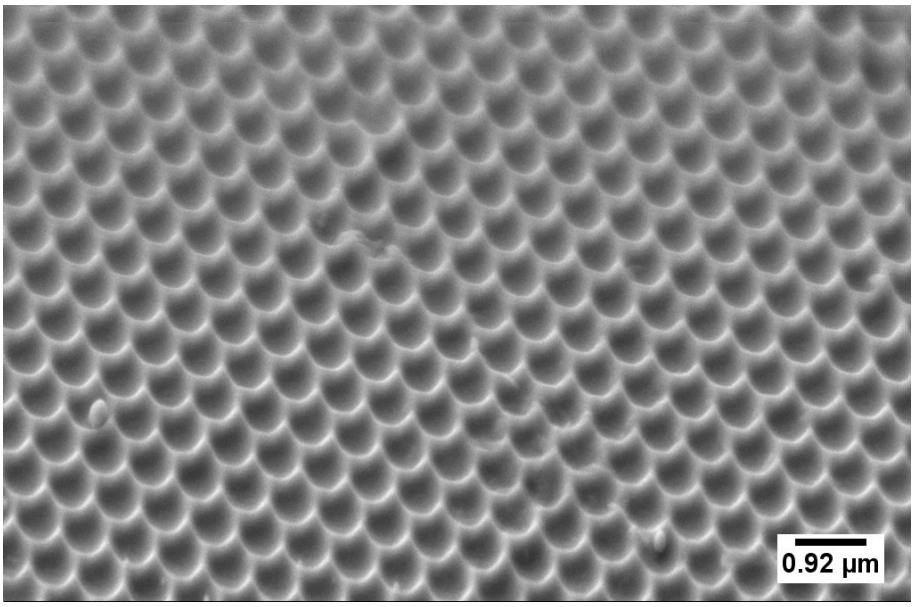

FIGURE 4.13: Morphological image of the fabricated spherical bowl structure under a tilt

Chapter 5

Computationally Analysing Building Blocks of the Metasurface

In this chapter, we take aid of computational simulations to design the basic building blocks of the metasurface. The spectral scattering of these nanostructures play a predominant role in influencing the antireflection performance. We perform a detailed analysis of the nanostructure light interaction with focus on light scattering into silicon. This involves deep physical insights obtained with the aid of numerical simulations to excite desirable resonant properties. Part of the results on scattering on a material interface are based on those results presented in [86]. These investigations form a part of the first simulation approach to arrive at the parameters of nanofrustum metasurfaces.

We focus on understanding the influence of the geometrical features of the building blocks which direct light into silicon. The goal is to obtain an overview of the dependencies of the building block geometries on the spectral scattering characteristics at the air-silicon interface. We further iteratively optimise the geometry in order to achieve high forward scattering into silicon for even higher angles of incidence. With these investigations we demonstrate the design approach to arrive at building blocks which aid in maximising light transfer into silicon.

5.1 Approach

The effective design should include the study of all possible resonant features which can be enabled in a high quality optical material to gain full extent of nanostructuring. This calls for systematic parameter studies and understanding the impact on resonant properties. The scattering cross section is derived via the Poynting vectors computed out of numerical calculations. The nanostructure parameters and the electromagnetic fluxes obtained out

of computational calculations are adapted to this definition of the Poynting vector as specified chapter 2 in equation 2.75 and 2.76 to generate scattering cross section plots.[51] The scattering cross section is given by

$$Q_{scat} = K \int SdA \tag{5.1}$$

where

$$K = \frac{1}{P_{in} \frac{A_{res}}{A_{CD}}} \tag{5.2}$$

In equation 5.2, A_{CD} is the area of the two dimensional face of the computational domain on which the electromagnetic flux integral is calculated. In order to keep the influence of the parameter sweeps independent of the size of the computational domain, the overall Poynting flux to power ratio is normalised by the area of the computational domain, A_{CD}. This integral is normalised by the input excitation power (P_{in}) and the cross sectional area of the resonator A_{res}. This Poynting vector is an output of finite element based numerical simulations. The quantity Q_{scat} in 5.1 is referred to as the scattering cross section of resonator/nanostructure. It compares the actual area seen by light in comparison with geometric cross sectional area of the nanostructure. For both the nanofrustum and the nanocolumn, we normalise with the first cross sectional area where the light is incident, i.e. the area of the top surface. These investigations described in the following sections are performed by using the software JCMsuite.[104] Such a calculation is based on defining a unit cell model. This unit cell model consists of the nanostructure geometry as well as of the surrounding environment. We provide an overview about the unit cell in figure 5.1

Since the considered features are symmetric about the vertical axis, we use mirror symmetry in the two dimensional plane to reduce the computational effort.[130] This restricts the light interaction confined to the two dimensional plane. As seen in figure 5.1 only half of the unit cell is meshed and given as an input to the computational solver. For the other three boundaries we define an infinite space numerically with the aid of a perfectly matched layer. A perfectly matched layer prevents reflections from the computational boundaries and gradually decays the energy propagating into the layer.[135] This establishes conditions of an infinite half space without having a large computational domain, thus saving computational effort. The Poynting vector is calculated by the power flux integrals on all the relevant boundaries. Normalising the sum of these integrals with the input power flux and the geometric cross section of the resonator gives rise to the scattering cross section.[88] It refers to the effective cross section area seen by the light. The source of light in the simulation is a

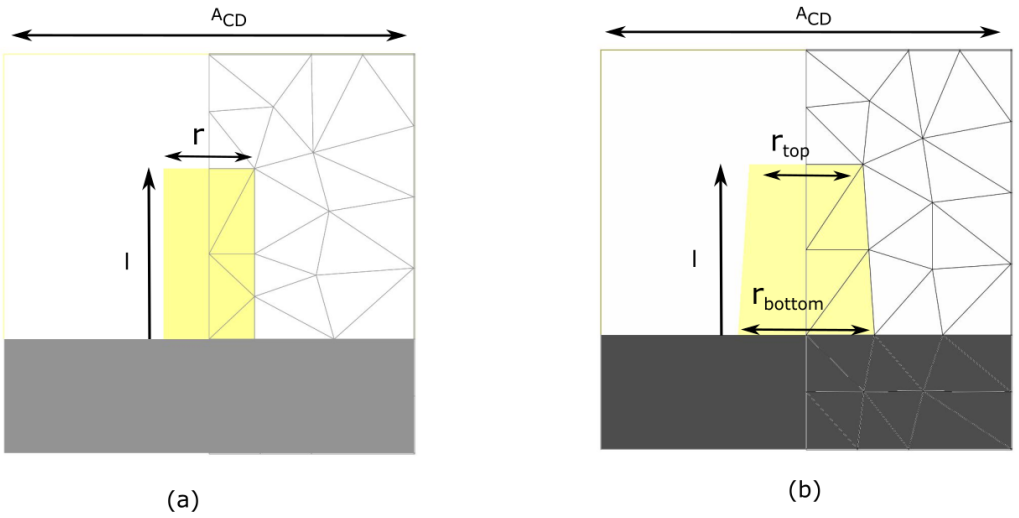

FIGURE 5.1: Simulation cell describing the unit cells used to computationally analyse building blocks - (a) nanocolumn and (b) nanofrustums

linearly polarised plane wave. For angular incidence, solutions to both polarisations, s and p are shown. In the first step, we obtain via rigorous simulations, the dependance of the scattering cross section of a column on an air-silicon interface. Part of these results are based on the work shown by the author in [85].

5.2 Scattering trend of titanium dioxide nanocolumns on silicon for angular incidence

The goal of this section is to obtain an overview of scattering tendencies of the nanocolumns into silicon. We examine this in terms of peaks observed in the scattering cross section spectra. Since these columns form the building blocks of the nanostructured metasurface for funtional antireflection, we characterise these qualities for different incident angles. A uniformly high scattering cross section across a wide angle range helps in determining ideal design parameters for the building block itself. In the starting investigation, we start with column geometries of three different heights and observe the scattering cross section spectra for different angles. We start with a height of 600 nm and a radius of 120 nm. This corresponds to a high aspect ratio. The idea is to verify the functioning of scattering into silicon between the incident angles of $5° - 75°$ for different aspect ratios. The air-silicon interface defines two half spaces in the computational problem. The upper half space is referred to as the air half space. The lower half space is referred to as the silicon half space.

The forward scattering cross section corresponds to the effective light propagated into silicon for both polarisations. In the air half space, we calculate a similar quantity called the backward scattering cross section. For the calculation of scattering cross sections, the silicon

absorption is considered zero, to entirely focus on the light propagation into silicon via the nanostructure. Disabling silicon absorption thus prevents damping of the scattering of the nanostructure into silicon. The surface map of the scattering cross section as a function of incident angle for the given dimensions is shown in the figure 5.2(i). For p- polarised light,

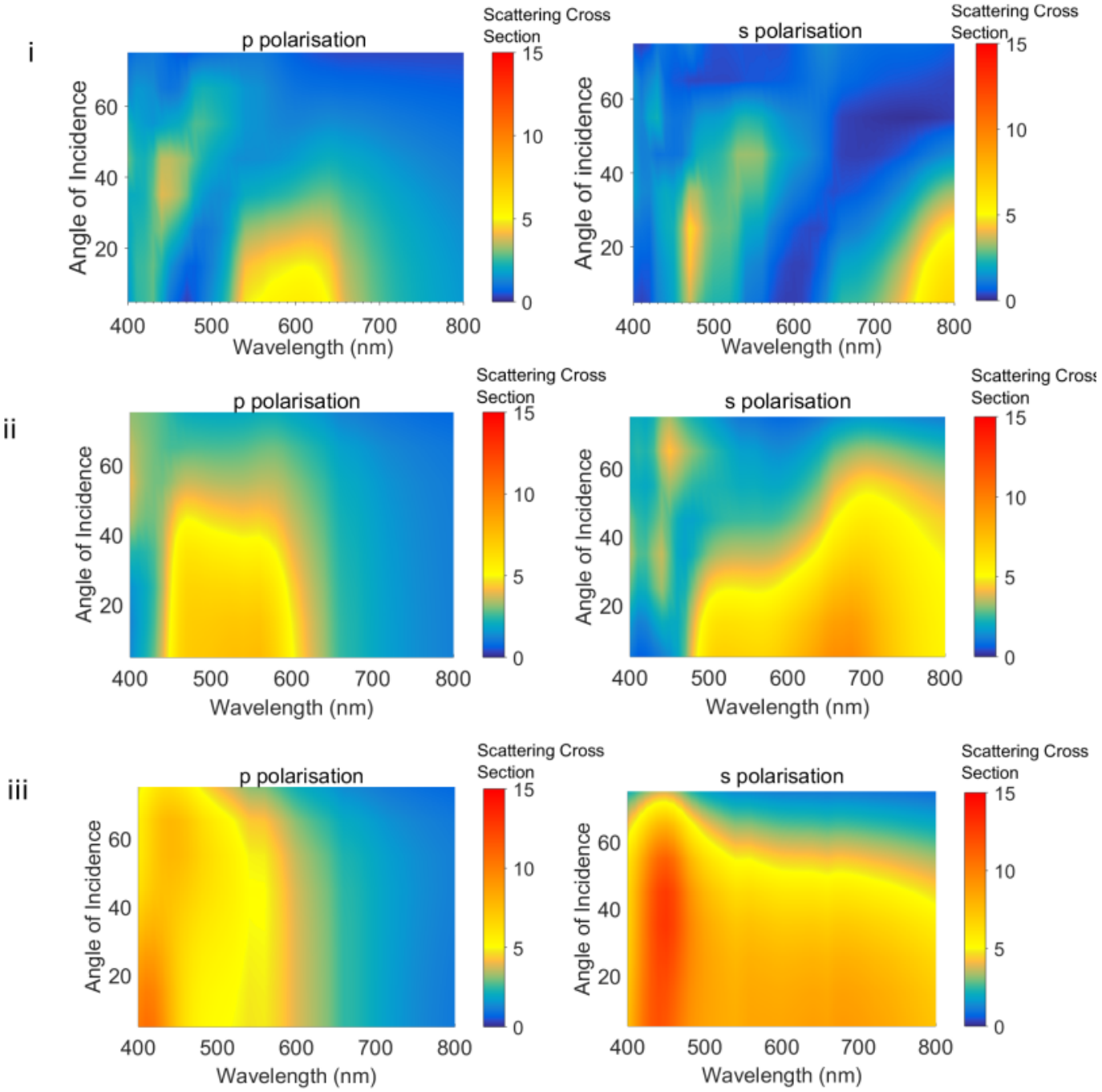

FIGURE 5.2: Forward scattering cross section for s- and p- polarised light for incident light for nanocolumn with radius = 120 nm and (i) l = 600 nm, (ii) l = 300 nm, (iii) l = 150 nm

two distinct forward scattering maxima are observed centered around 420 and 600 nm. In the

short wavelength range this narrow band maxima is sustained up to 65°. For the maximum centered at 600 nm, the angular sustainance is limited only up to 40°. Both these scattering intensities have a low amplitude and lack the required character for a broadband antireflection system as shown in figure 5.2(i). For s- polarised light, the two localised maxima bands in amplitude present in 5.2(i) slightly red shifted as compared to the p- polarised light with similar spectral trends.

This calls for some change in the geometry. In order to understand the influence of the aspect ratio, we keep the radius constant and reduce the height to 300 nm and repeat the above calculation. In figure 5.2(ii), the forward scattering cross section, has a local maxima at 500 nm which decreases in magnitude in both directions along the wavelength axis from 480 to 600 nm. The amplitude remains high up to 60°. For s- polarised light, the spectral spread of the forward scattering is red shifted as compared to p and broadly extends up to 800 nm. The forward scattering amplitude for higher angles is quite poor in the wavelength ranges between 500-600 nm, however it improves between 600-800 nm. For p- polarised light, between 600-800 nm, the forward scattering amplitude is weak. The polarisation selectivity in the long wavelength range is an influence of the superposition of the interface properties and the nanostructure dipolar resonances.[6] Under an incident angle, these dipolar resonances, tend to have different directional intensities across the spectra. The amplitude of the forward scattering is improved for both polarisations as compared to the 600 nm height shown in figure 5.2(i). Reducing the aspect ratio, therefore helps in increasing light scattered into silicon. It also broadens the wavelength range for which high intensities are observed in the silicon scattering cross section.

In order to further improve the directional propagation into silicon, we reduce the height of the structure down to 150 nm. The relevant properties are shown in figure 5.2(iii). For p-polarised light, the forward scattering is uniformly high (10-12) for all angles of incidence in the wavelengths between 400-500 nm. Uniform and moderately high amplitude of 8 is also observed between the wavelengths 500-600 nm across all incident angles. This is the effect of enhanced forward scattering which is present for all angles of incidence. For s- polarised light, the forward scattering spectra, broadens across the incident angles while maintaining a reasonably high amplitude across the visible spectrum. Reducing the length to 150 nm therefore improves the forward scattering behavior as indicated in 5.2(iii).

It is also important to minimise the backward scattering cross section in order to prevent the nanostructure scattering to add to reflection occuring at the air silicon interface. This in turn ensures that the forward scattering cross section has a high magnitude. The backward scattering spectra is also governed by the basic interferences arising out of the air silicon

interface. For s- polarised light as shown in figure 5.3(i), this amplitude increases with increasing incident angle. This therefore results in proportionate high magnitude of backward scattering for s- polarised light as shown in figure 5.3(i). For p- polarised light, reflection also increases with increase in angle of incidence, so the high amplitude observed between angles $20° - 70°$ is an evidence of the high backward scattering arising from the nanocolumn itself.

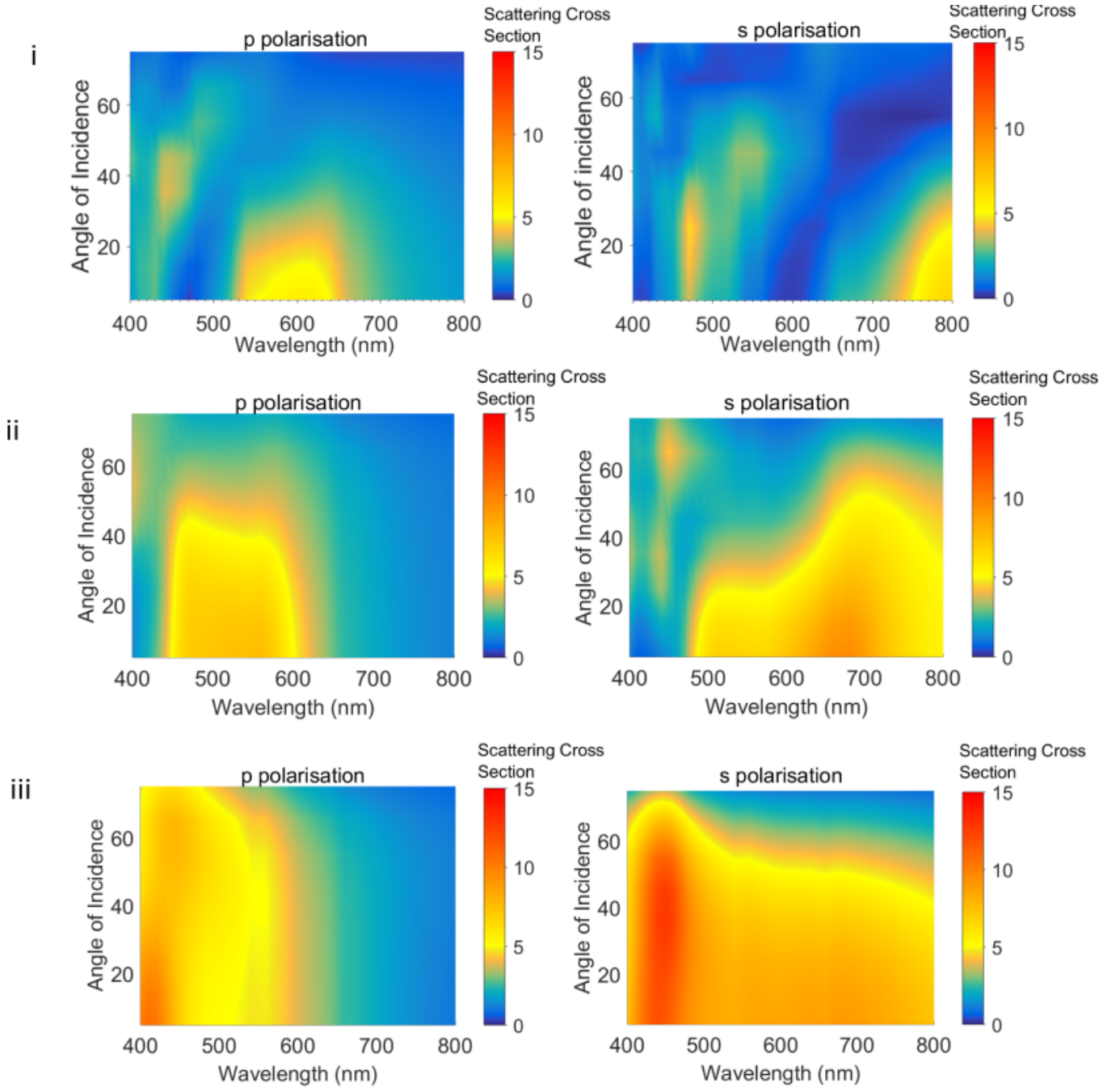

FIGURE 5.3: Backward scattering cross section for s- and p- polarised light for incident light for nanocolumn of radius = 120 nm and (i) l = 600 nm, (ii) l = 300 nm, (iii) l = 150 nm

For a height of 300 nm, the backward scattering in figure 5.3(ii) has a higher amplitude for both polarisations. This amplitude is high only for higher angles of incidence. Morever the spectral spread is restricted only up to 450 nm for incident angles up to 50° and up to 600 nm for incident angles above 75°. In the case of backward scattered light for s- polarisation a high amplitude is seen which is proof of the fact that the geometry needs improvement. This proves that the improved light interaction of the nanocolumn results in predominant backward scattering for a column height of 300 nm

For a 150 nm column, the backward scattering is shown in figure 5.3(iii). The amplitude of p- polarised light is significantly reduced as compared to the column with 300 nm height. The spectral spread of the backward scattering is significantly restricted only to the short wavelengths and incident angles more than 50°. For p- polarised light, high intensity is confined in a narrow angular band only to the short wavelengths. For s- polarised light, this amplitude is much larger in comparison for p- polarised light but this behavior stems from the basic trend of the air silicon interface for s- polarised light as evident in figure 5.3(iii). The amplitude of the back scattered light in this case is on an average lower than the previously considered geometries. Comparing 5.3 and 5.2 proves that an aspect ratio close to one leads to preferential forward scattering properties into silicon for both polarisations across a wideband of incident angles.

The pronounced variation of the backward scattering is a strong reason to further checking the influence of the length of the nanostructure and we reduce the length to a bare 50 nm and evaluate the scattering cross section for both polarisations. For p- polarisation, the forward scattering slightly reduces in amplitude for the 400-450 nm wavelength band. The amplitude significantly weakens over the 500-600 nm range. In figure 5.4, for s- polarised light in the forward scattering cross section, a high amplitude i.e. 14 is seen between 400-450 nm. However beyond this wavelength, the intensity in the scattering cross section reduces significantly. For the 50 nm height, the backward scattering cross section, is low and has a very limited spectral spread. However the weak forward scattering cross section renders it undesirable to be deployed as a part of a nanostructured antireflection system. This proves that merely reducing the height doesn't result in an enhanced forward scattering but rather the aspect ratio needs to be appropriate in order to result in maximum light transfer into silicon. The backward scattering cross section doesnt particularly indicate extreme reduction in the interface properties. The forward scattering cross section in figure 5.4 is fairly high across all angles across the considered bandwidth for the nanocolumn with a height of 150 nm. However the backward scattering cross section is still signficantly high for the column to be implemented as a building block of a nanostructured antireflection system. Additionally the spectral spread of the observed high magnitude forward scattering needs to be improved

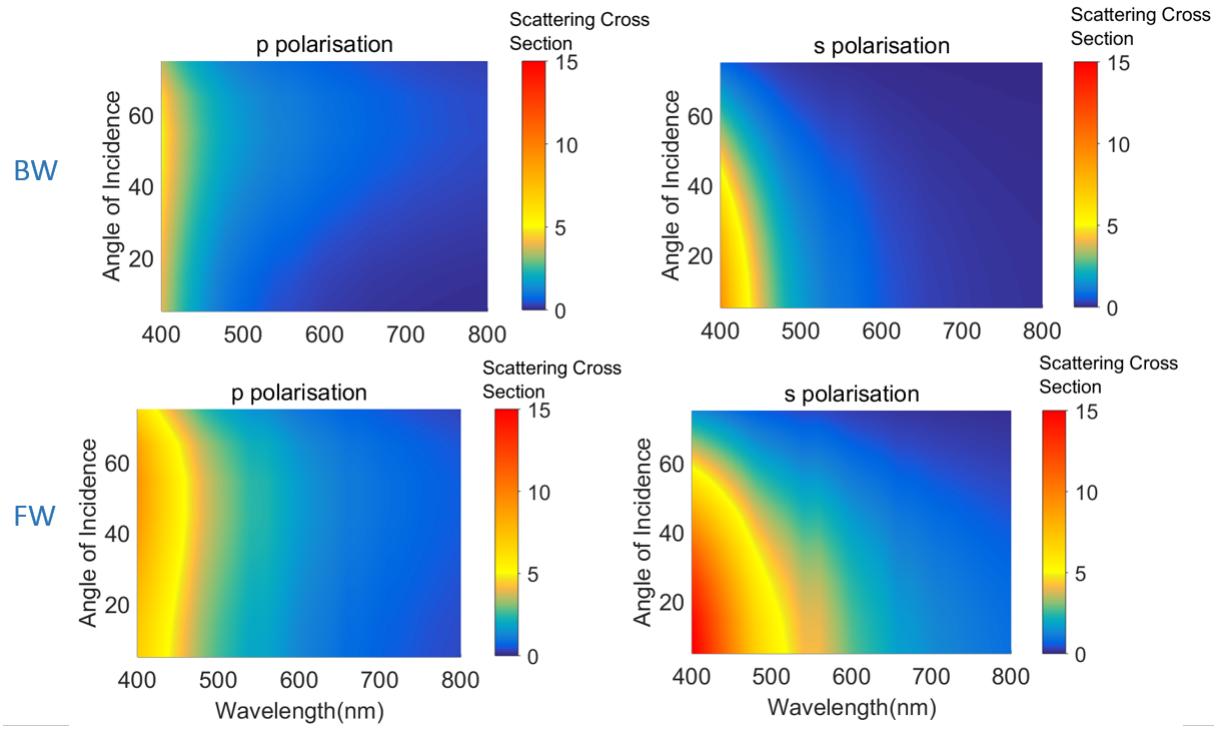

FIGURE 5.4: Backward (BW) and Forward (FW) scattering cross section for s- and p-polarised light for a low aspect ratio nanocolumn (l = 50 nm, radius = 120 nm)

across several incident angles. This calls for a change in the resonator geometry. In order to allow for the implementation of standard top down fabrication techniques, the change should not be drastic. Moreover the change in geometry should exploit a physical effect which shrinks the backward scattering cross section on the air-silicon interface. The simplest idea in this direction is to change the radial profile of the cylinder to give way to a frustum like geometry. The main influence of such a taper is to increase light confinement into the frustum shaped resonator. This increased light confinement is theoretically referred to as the mode confinement.[92] The mode confinement refers to the peculiar electric and magnetic responses of the resonator with light.[109] In the next section, we provide an overview of the forward scattering behavior of a nanofrustum.

5.3 Scattering trend of titanium dioxide nanofrustums on silicon for angular incidence

In this section, we describe the light interaction properties of nanofrustums in order to improve forward scattering for angular light incidence. We already proved in the previous section, that having an aspect ratio close to one results in good forwards scattering into silicon. In order to study the influence of scattering properties of the nanofrustum we keep a height of 150 nm and a bottom radius of 120 nm. We introduce a taper in the vertical profile by changing the top radius of the nanofrustum and perform similar calculations. Altering the top radius of the nanofrustum therefore significantly changes the scattering properties into silicon. We chose a top radius of 100 nm in order to analyse the scattering for angular incidence of the resulting taper profile. The forward scattering spectra for p- polarised light, remains unchanged but for s- polarised light, the angular performance improves between the wavelengths of 500-600 nm for higher angles. This improvement comes at the cost of an increased backward cross section for both polarisations. For p- polarisation, the backward cross section has now a stronger amplitude with respect to the previous case between 400-500 nm even for the low angles of incidence. For s- polarised light, this increase is uniformly spread across all angles of incidence. This demonstration proves that strong forward scattering cross section can be tuned by changing the geometry of the building block. These changes need to be in line with the adopted fabrication sequence and should facilitate with the functional operation of the envisioned metasurface.

The forward scattering cross sections for both polarisations have high values across the wavelength range. The angular spread of the forward scattering is particularly improved for s- polarised light, with high scattering intensity observed till 600 nm. The backward scattering cross section shows significant magnitude reduction between the wavelength range of 600-700 nm for higher angles of incidence. This demonstrates that a small taper angle is necessary to improve the forward scattering properties. Once the forward scattering cross section is maximised of the nanofrustum, the periodic arrangement of the nanofrustums can be designed into an effective metasurface to minimise silicon reflection. This is discussed in chapter 6.

5.4 Discussions from isolated calculations

These investigations may occur to the reader as an extreme deployment of parameteric computational simulations. There aren't exact analytical solutions which depict the scattering problem of a finite nanoresonator on an interface.[11] The outcome of these simulations help in analysing the light interaction subject to incident angles for the associated polarisations.

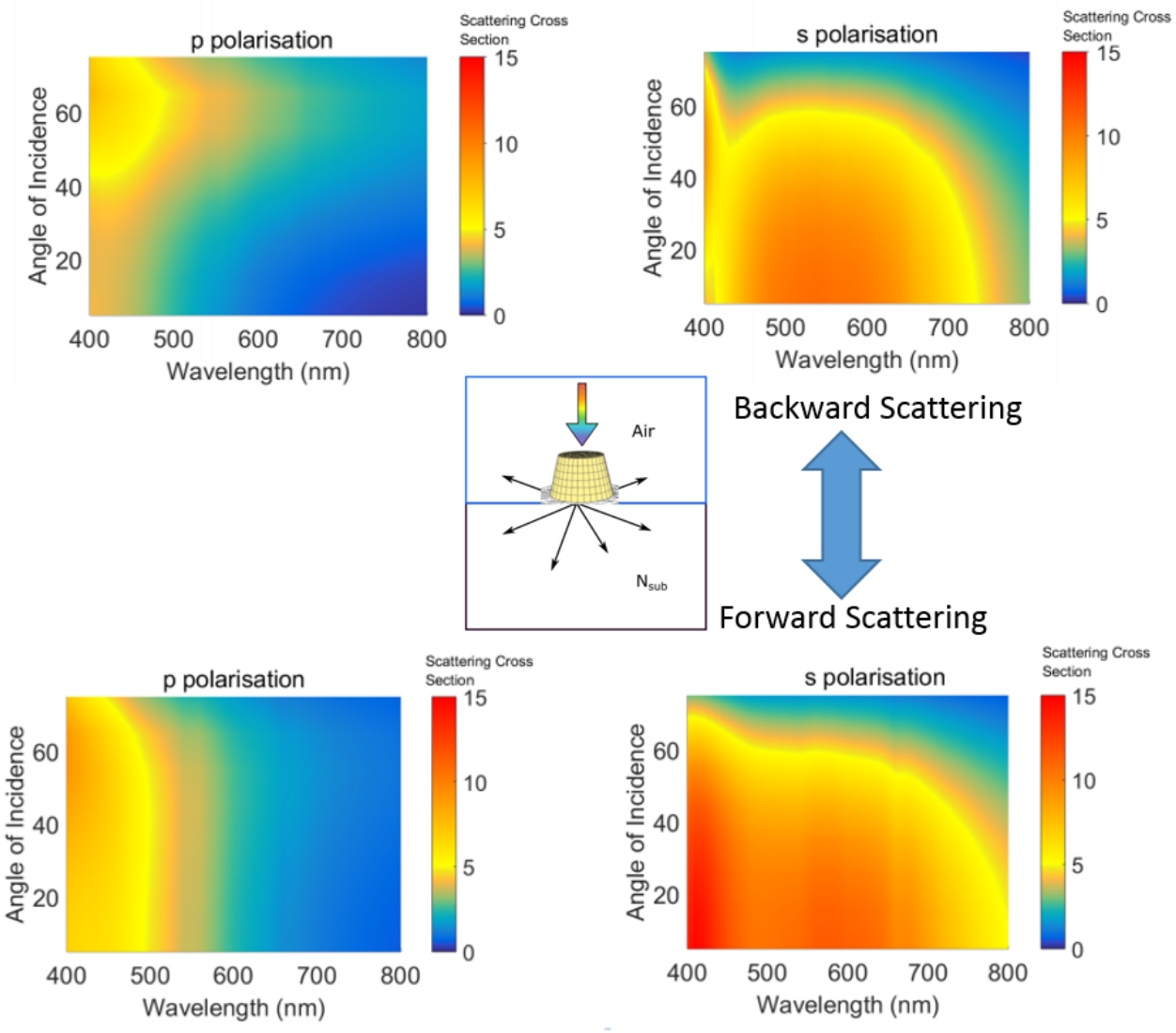

FIGURE 5.5: Forward scattering cross section for s- and p- polarised light for incident light for a low aspect ratio nanofrustum((l = 150nm, $\text{radius}_{\text{top}}$ = 100 nm, $\text{radius}_{\text{bottom}}$ = 120nm). The inset indicates the calculation spaces of the backward and forward cross sections to be air and hypothetically assumed lossless silicon respectively

The differences seen for different aspect ratios on the interface helps in proving the sensitivity of the resonator to influence scattering into silicon. This is evident from the improved forward scattering as the height of the nanocolumn is reduced. Reducing the height not only reduces the backward scattering but improves the overall spread of the forward scattering as seen in figures 5.2(i), (ii) and (iii). The inherent reason for the high forward scattering into silicon is based on two phenomenona. The first is the inherent resonance of the nanocolumn itself.[99] The aspect ratio of this nanocolumn determines the resonant properties. For a high aspect ratio (length/diameter >> 10) dielectric nanocolumns, nanorods, theoritical investigations are well established to describe a waveguide like behavior.[34] For moderate aspect ratios, no analytical description is possible due to the discontinuities in the electric field propagation

vector which occur at the interface of the nanostructure. In a low aspect ratio nanostructure (length/diameter ~ 1), the geometrical dimensions allow the approximation of the structure to have equal lengths in the vertical and horizontal dimensions. This assumptions allows for a good physical correlation of the modal characteristics of the structure to those of a sphere.[117] These are predicted by Mie theory as electric and magnetic responses to an incoming plane wave excitation. The most easily excitable responses of these structures are the so called electric and magnetic dipole resonances.[125] These occur at wavelengths depending upon the structure dimensions for a given material.[124] These resonances tend to preferably couple light into the high index material such as silicon. This effect in theory is referred to as the Kerker effect.[3] Based on this effect, it is possible to have close to perfect transmission of light into the substrate. This perfect transmission is achieved by minimising the backward scattering on account of design of the nanostructure.[79] Such a carefully considered design results in the electric and magnetic dipoles which after few oscillations within the structure geometry result in the light being coupled into silicon.[21] The objective function is to maximise the total forward scattering and at the same time minimise the total backward scattering. Observing this trend for different polarisations, helps in understanding the impact of geometry for different angles of incidence.

Introducing a tapered profile helps in limiting the spectral spread and amplitude of the backward cross section. Additionally it also helps in broadening the spectral spread of the forward cross section. Such a taper is more effective in simultaneously reducing the backward cross section and increasing the forward cross section. This is evident from figure 5.5. The nanofrustum geometry is of physical significance with respect to obtaining good scattering behavior for larger angles of incidence. For a nanocolumn and nanofrustum with the same height and base radius, the forward scattering properties of the frustum with top radius of 100 nm tend to be better than that of the column. The column has a slightly higher maximum value, but the frustum has a broader spread of high amplitude across all angles for both s- and p- polarisations. Moreover the backward cross section amplitude also remains low for angles as high as 60°.

This proves that in order to optimise the forward scattering into silicon, careful optimisation of the scattering cross section needs to be considered in combination with effects such as interferences and nanostructure resonances occuring at angular incidences. For a thin film, interference at the interface is governed by the material data, thickness and light incidence factors. For a nanostructure, this is a additionally a function of the geometry and is easier to be analysed from the effect (influence on backward scattering cross section) rather than the cause. Introducing a taper, changes the vertical profile of the column in the plane of polarisation thereby directly influencing the field distribution inside the dielectric volume

of the building block. This improved field interaction is seen to prove beneficial especially for higher angles of incidence. These simulations reveal the variation in the scattering on silicon of the indivdual building blocks for different angles of incident light. This provides an overview of the role the nanofrustum scattering in controlling reflection. The extent of reflection reduction control depends on the interaction of the periodic arrangement and will be discussed systematically in the subsequent chapter.

Chapter 6

Comprehensive Analysis of Nanofrustum Metasurfaces

In this chapter we elaborate on a full circle approach of the fabricated metasurfaces involving design ideology, characterisation and optoelectronic application. We start with design startegies to utilise the power of metasurfaces to achieve good antireflection. A simultaneous interplay of the optical phenomenona is modeled via numerical simulations to give way to the final parameters. We elaborate on the intrinsic properties of the metasurfaces for the selected dimensions first entirely independent of the air-silicon interface to demonstrate the intrinsic optical properties exhibited by the structure. Via a sequence of computational analysis we investigate the behavior of a periodic two dimensional arrangement of nanofrustums on different optical interfaces. After considering overlap of optical effects such as resonances, diffraction and interference with the aid of finite element based simulations we arrive at an optimised structure parameters for antireflection. In the near infrared and infrared spectrum the dielectric nature of semiconductors has been utilised to trigger Mie type resonances. These Mie type resonances operate in the fundamental diffraction order in a two dimensional arrangement of periodic nanostructures. Mie theory has been analytically derived for spherical and cylindrical systems. Other nanoshapes such as cubes, columns, discs also show field distributions identical to the electric and magnetic dipoles as described by Mie theory.[64] In our investigations we look out for identical spectral features in the visible spectrum. In order to broaden the spectral characteristics of these degenerate points we perturb the resonant near field with a thin film dielectric via optical impedance matching.

The obtained structure is characterised optically for antireflection performance for both polarisations for all angles of incidence. The underlying implications of the measured spectra

are elaborated with the help of numerical simulations. We characterise the obtained structures for optoelectronic functionality with the aid of photoelectrochemical measurements. The resulting effect is characterised statistically and the structures are examined for morphology changes post measurement. Part of these results are based on those results presented in [86]. These results were obtained as a result of the acceptance of the user project proposal submitted by the author at Center for Integrated Nanotechnologies at Sandia National Labs and are included in a manuscript titled 'Enhanced hydrogen evolution reaction using an all dielectric metasurface'.

6.1 Designing metasurfaces consisting of nanostructured frustums for antireflection

Achieving spectrally and multidirectionally optimised antireflective properties in a high index material such as silicon has been a popular optics problem. Nanostructuring a material involves an elaborate increase in the fabrication effort in order to effectively harness specific optical resonances. This ideology of implementing nanostructured optical design in lossless dielectric materials is referred as metamaterial design.[53] The overall optical benefit that these nanostructures manifest in terms of antireflection therefore should substanially outperform planar equivalents to overcome the additional fabrication effort. This requires careful consideration of physical effects which arise as a result of nanostructuring a particular dielectric material. This approach is on the lines of metasurfaces and metamaterials which involve combining material benefits and optical resonances. We established about material supremacy of titanium dioxide by indicating good isolated scattering behavior on silicon in the previous chapter. Its dispersive optical constants are well suited to the visible frequency range in terms of controlling optical loss.[71] According to theoretical predictions, the ideal refractive index for establishing good anti-reflection performance between the air-silicon interface is around 2.3. This is close to the dispersive average of the titanium dioxide refractive index. Before getting into the details of the optical properties of nanostructuring titanium dioxide into metastructures, we explain the dispersive trend in the reflection properties of titanium dioxide thin films on silicon. Using transfer matrix calculations we quantify the reduction in the silicon reflection by mere planar layers of titanium dioxide. In these simulations, ellipsometrically measured optical constants of titanium dioxide are used. The exact dispersive spectra is found in 4.3.

In figure 6.1 we show the reflection spectrum of three different thicknesses of titanium dioxide on silicon. Since the thickness is less than 100 nm, we do not find pronounced interference fringes. For thicknesses higher than 100 nm, at short wavelengths, the reflection amplitude is fairly high, however at the long wavelengths the value is substantially lower as

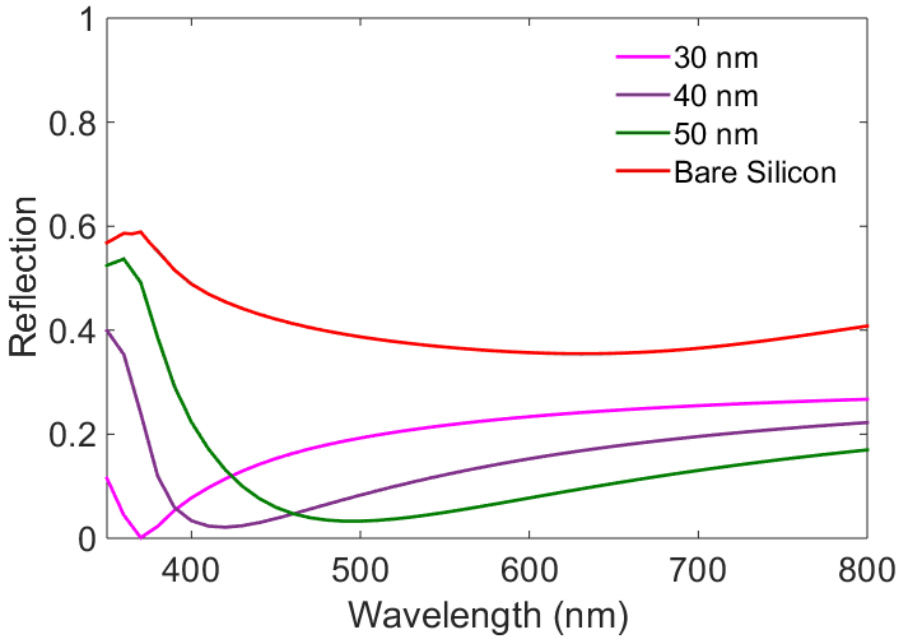

FIGURE 6.1: Simulated reflection of titanium dioxide thin films of different thickness on silicon

compared to bare silicon. This helps in introducing another degree of tunability to the optical design to aid to the overall antireflection envisioned through metastructure design. Such a film is particularly helpful at long wavelengths i.e. beyond 650 nm where the metastructured properties that are active for short wavelengths (400-650 nm) tend to weaken. The approach used at these long wavelengths (650-900 nm) is to engineer a graded index profile which allows slow variation of the refractive index and thereby reduces reflection.

At short wavelengths, we observe in figure 6.1 that the reflection is high for the 50 and 40 nm film but reduces gradually with wavelength and then increases again. In order to supress this increase in reflection, suitable design of nanostructures is required.[59] Nanostructures from dielectrics such as titanium dioxide possess tremendous tunability of optical resonances in the visible spectrum. In the preceeding chapter we have already described the scattering properties as a function of geometry and material interface. In a periodic arrangement, the individual resonances need to be well tuned in order to provide a high forward scattering in a high index medium such as silicon. Periodic arrangements of such structures can give rise to a variety of spectral properties in reflection and transmission unique to the type of lattice arrangements adopted.[67] Hexagonal and square lattices are two types of popular lattice arrangements.[25] Several investigations on the modal properties of such a lattice have been thoroughly investigated in literature. These investigations reveal that square lattices exhibit profound polarisation indifference.[131] For hexagonal lattices, polarisation strongly determines the propagation behavior of excitable modes.[9] A good antireflection behavior

requires strong reflection supression for both polarisations. Therefore the obvious choice for the arrangement of the system is a square lattice.

Such a periodic lattice of nanoresonators can result in increased reflection or increased transmission depending upon design. This increase in reflection or transmission can be attributed to the diffracted orders which arise in both directions as a result of the periodic variation of material constants. Our goal is to suppress reflection. This requires maintaining the arrangement of structures in a way that number and the magnitude of overall diffracted reflected modes is minimum and remains confined to the fundamental order of propagation. This requires careful consideration of selecting the periodicity of the overall arrangement. Modal calculations of periodic lattices reveal that subwavelength lattices of such structures result in the supression of higher orders of reflection and reduce the amplitude of the fundamental order.[122] For a perfect antireflective system, amplitude and strength of all orders should be zero or near zero. The periodic arrangement determines the propagating order. The magnitude of this order is influenced by the resonator design as well as interferences which occur at the interface. Partial interference control is exhibited by a very thin planar film of titanium dioxide. This can be further supported by adopting a resonator which in addition to providing excellent dielectric resonances also provides an excellent index profile at wavelengths where the resonant behavior is not so predominant.

In addition to controlling interferences, a peculiar shaped resonator results in a better mode confinement of the scattered response. We use a frustum like taper in order to excite degenerate dielectric resonances. These resonances are according to the resonances predicted by Mie theory for spherical and cylindrical particles. Due to the low aspect ratio of the frustum geometry, the resulting scattering properties of the system can be approximated to follow a Mie type resonant behavior. Owing to the frustum like geometry, the confinement of such modes within the material becomes much stronger resulting in increased forward cross sections especially for the higher angles of incidence (see chapter 5). Since the planar layer in contact with silicon is made from titanium dioxide we eliminate the need to include buffer layers. Exclusion of buffer layers from other materials such as popular oxides and nitrides also reduces fabrication process steps and does not hinder the intended optoelectronic functionality.[12] With a combination of the frustum arrangement and a planar thin layer broadband supression of reflection can be achieved.

The design problem therefore has following objectives: (1) strong forward scattering in the visible frequency range, (2) supressing higher order diffracted reflections and (3) controlling interferences. In chapter 5, we reported about the spectral dependancies of the scattering cross sections on the geometry of the structure. Holding on to the nanofrustum dimensions

derived in chapter 5, we now perform a sequence of investigations which result in identifying the final design of the the obtained nanostructure to arrive at a well defined antireflection system. We arrive at the ideal structure through conclusions derived from the following set of investigations consiting of computational analysis of:

- Different subwavelength pitches for the titanium dioxide nanofrustums in air
- Titanium dioxide nanofrustums on titanium dioxide
- Subwavelength pitches for the titanium dioxide nanofrustums on a hypothetically assumed lossless silicon
- Titanium dioxide nanofrustums on silicon
- Titanium dioxide nanofrustums on thin films of titanium dioxide on silicon

We now proceed to sequentially describe these investigations in the subsequent subsections. The simulations are performed with the help of the finite element software - JCMsuite using a periodic unit cell. The system is excited electromagentically by a plane wave. Spectral quantities such as reflection and transmission are evaluated with the help of the post processes of the software. These post processes involve integration of electric field fluxes over the input and ouput source port domains. In order to provide deeper implications of the measured spectra and to understand the scattering behavior which results in an effect typical for metasurfaces, we angularly resolve the calculated reflection and transmission. This is done by calculating the angular spread of the propagation vector $k(x, y, z)$ of the electric field strength in the domains which corresponds to reflection and transmission. This calculation gives a discrete set of angles in which the electromagnetic energy (S) is distributed as a result of the periodic arrangement of the nanostructures. Depending upon direction, these are referred to as transmitted or reflected orders. These directions are shown in figure 6.2. The following equations are used to calculate directional energy components. Here θ_n corresponds to the angle; the n^{th} diffraction order makes with the fundamental direction. In a given medium with refractive index m this is calculated from the total k vector, k_m and its z component k_z.

$$\theta_n = \arccos(k_z/k_m) \tag{6.1}$$

$$S(\theta, x, y, z) \propto cos(\theta_n) * \mid \vec{E}(\theta, x, y, z) \mid^2 . \frac{n}{2Z_0} . L_x L_y \tag{6.2}$$

Here k_z is the calculated propagation vector along the normal to the interface. Z_0 is the free space impedance (square root of the free space permittivity and permeability). The angle between these two vectors (k_z and k_m) is given by θ_n. This angle θ_n corresponds to the angle between the by the n^{th} diffraction order of the propagating k-vector (k_m in a medium

with the refractive index m) and the longitudinal direction This L_x and L_y represent the dimensions of the periodic unit cell in consideration. The total electric field as evaluated by rigorous simulations is attributed by $\vec{E}$. The spatial co-ordinates x, y, z define the domains across which reflection and transmission are calculated. From figure 6.2, modes which go into air are addressed as reflected diffracted modes. Modes which propagate in N_{sub} are the transmitted diffracted modes. As indicated in the equation, the calculation utilises the full electric field values to obtain the transmitted and reflected energy fraction along each direction.

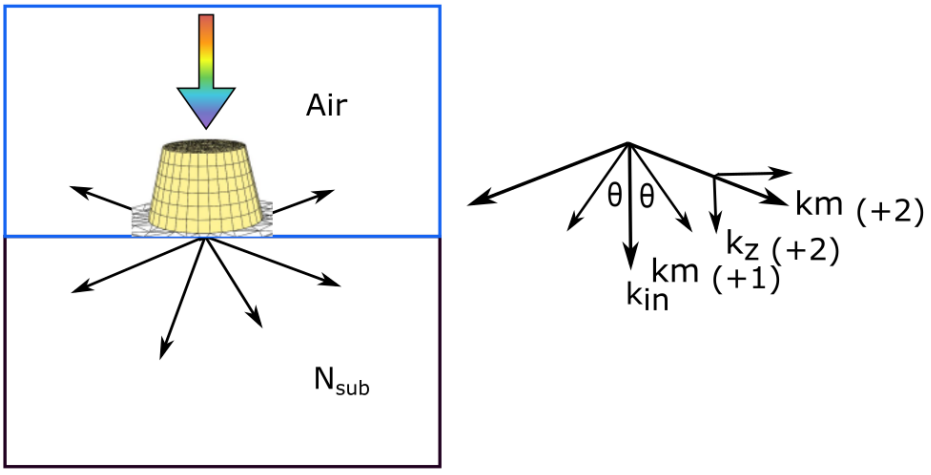

FIGURE 6.2: Illustration of reflected and transmitted diffraction orders. The graphic depicts the nanofrustum metasurface on a high index substrate with refractive index N_{sub}. It also shows the different angular directions in which the reflection or transmission of such a structure could be resolved into. k_z refers to the z component of a given diffraction order n = 0, +1 ... in the medium m with complete k vector k_m, where m could be either m or air or N_{sub}.

6.1.1 Different subwavelength pitches for the titanium dioxide nanofrustums in air

In this investigation, we start with the geometrical dimensions of the frustum as concluded in chapter 5. The nanofrustum under consideration has a top radius of 100 nm, bottom radius of 120 nm and height of 150 nm. With these dimensions we try and find a suitable periodic arrangement of the nanofrustum based metasurfaces in order to optimise the light transfer properties via the nanostructures. This investigation requires varying the pitch between the structures to arrive at the highest average transmission. The goal of this investigation is to show strong interaction of the structures with respect to visible light and find the inherent resonance positions of the periodic arrangement of the nanofrustums independent of an optical interface. This indicates the ability of the structures to preferentially couple light as a result of their resonant properties.[16] For this purpose, we set the structure environment to

be air. This eliminates index gradients from substrates. It also helps in preventing diffractive conditions arising as result of index gradients but rather focusses on intrisinc ability of the structures to interact with light. The envisioned strong interaction should be evident via either a strong value of reflection or transmission observed in the calculations. Any peaks observed in either spectra here, are solely due to the resonant properties of the structures and give an overview of the physical phenomenon occuring in the structure. Here we model a rectangular arrangement of nanofrustums (height = 150 nm, top radius = 100 nm, bottom radius = 120 nm) with two different pitches (360 and 450 nm) in air. This is done to understand the intrinsic behavior of such a system without the effect of an optical interface. From figure 6.3, We observe almost unity transmission for the entire wavelength range.

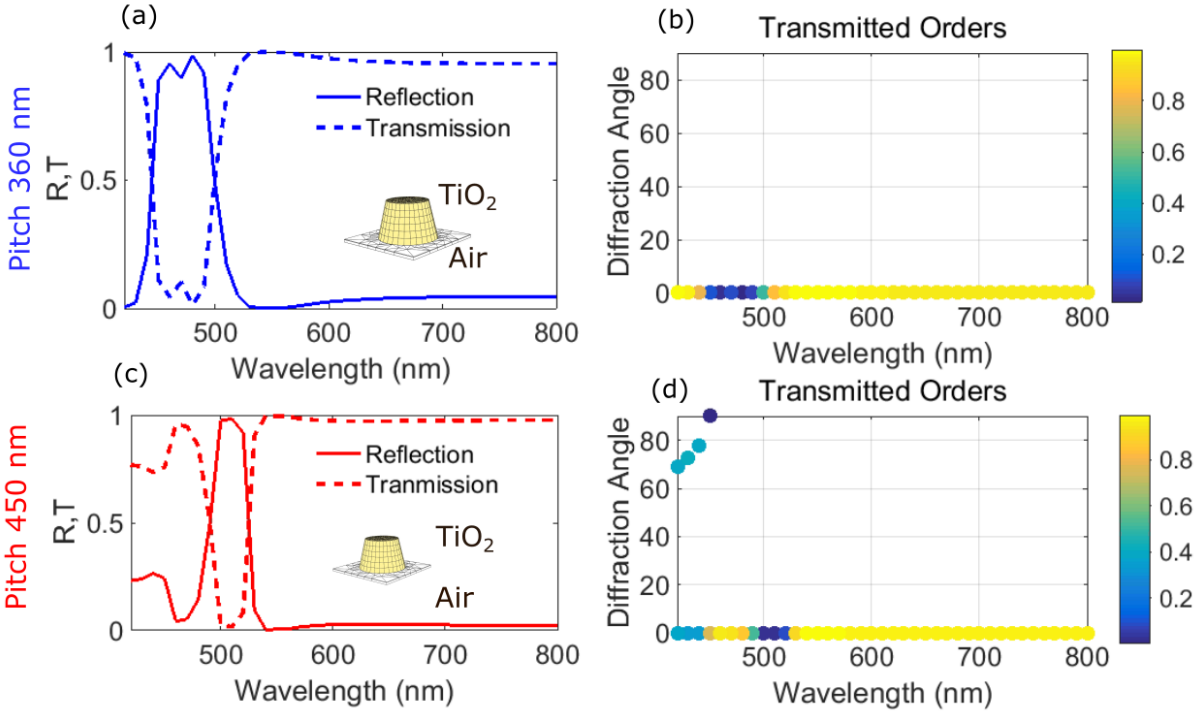

FIGURE 6.3: Reflection and transmission spectra of nanofrustum metasurfaces in air for the different pitches : (a) 360 and (c) 450 nm (center to center distance between the nanofrustums (height = 150 nm, $\text{radius}_{\text{top}}$ = 100 nm, $\text{radius}_{\text{bottom}}$ = 120 nm); Angle resolved transmission for aforementioned pitches(b) 360 and (d) 450 nm represented via circular markers along the resolved directions.

For the 360 nm pitch, at 460 nm and 480 nm, the transmission drops to almost zero in the form a very narrow dip as seen in figure 6.3. Such a narrow peak is often an indication of resonant behavior as a result of the light interaction arising in the material due to nanostructuring. If we look into the diffractive properties of the periodic structure, then we observe the presence of the fundamental order in diffraction in the transmitted spectra. The periodic arrangement maintained at 360 nm by itself does not result in additional higher order modes

for normal incidence. This proves that the periodic system simply propagates in the forward direction the resonant response of the individual nanostructures.

If we use the same conditions and maintain the pitch between the structures to be 450 nm, then we observe that the dip in the reflection spectrum red shifts with respect to the previous case. This is because the 450 nm pitch lies in the wavelength range and results in diffracted reflection. This is derived from the simulation where the electric field and propagation vector (E_i, k_i) indicated in section 2.4 contain 0^{th} and 1^{st} order componentsThe angle resolved transmission plots in 6.3 (b) and (d), indicate the presence of the first order diffraction in the transmission spectra. This first order diffraction order is present between wavelengths 400-450 nm. This explains the shift observed in the transmission spectra from the previous case. The transmission remains fairly constant above this wavelength. Moreover as a result of the first order of diffraction present in the reflection spectra, we observe that the reflection is significantly high between 400-450 nm. From this investigation, we can identify for the same nanofrustum geometry, the role the periodic arrangement plays in influencing the spectral response of the system. For the pitch with 450 nm, we observe co-existence of modes (fundamental order and first order reflection) arising on account of the periodic arrangement as well as the intrinsic scattering of the nanostructure. Our goal in designing the antireflective system is to take aid of the periodic arrangement and the resonant properties of the nanostructure to ensure maximum light coupling into silicon. This requires a design where at an interface of a high index material such as silicon no additional reflection is added on account of the periodic arrangement of nanofrustums. In the next step, we gradually move to a substrate material of titanium dioxide to observe the transmission behavior of the nanofrustum arrangement.

6.1.2 Titanium dioxide nanofrustums on titanium dioxide

This investigation is to check the propagation characteristics of the structure without an index gradient with respect to another medium with a higher refractive index than titanium dioxide. This helps in understanding the transmission characteristics excluding the influence of an index gradient. To calculate this, we maintain the same structure geometry and use it in the model along with a titanium dioxide substrate. In the previous section, we observed two reflection peaks in figure 6.3 (a). We now check in what form these peaks evolve and the overall optical performance of the system when having a titanium dioxide substrate. We take aid of the angle resolved transmitted energy spectrum in order to show the propagation aspects of the nanostructure. In figure 6.4 we see the distribution of the transmitted energy is divided into 4 diffraction orders which have their own characteristic direction of propagation. These angles are an effect of the scattering properties of the nanostructure into a medium of

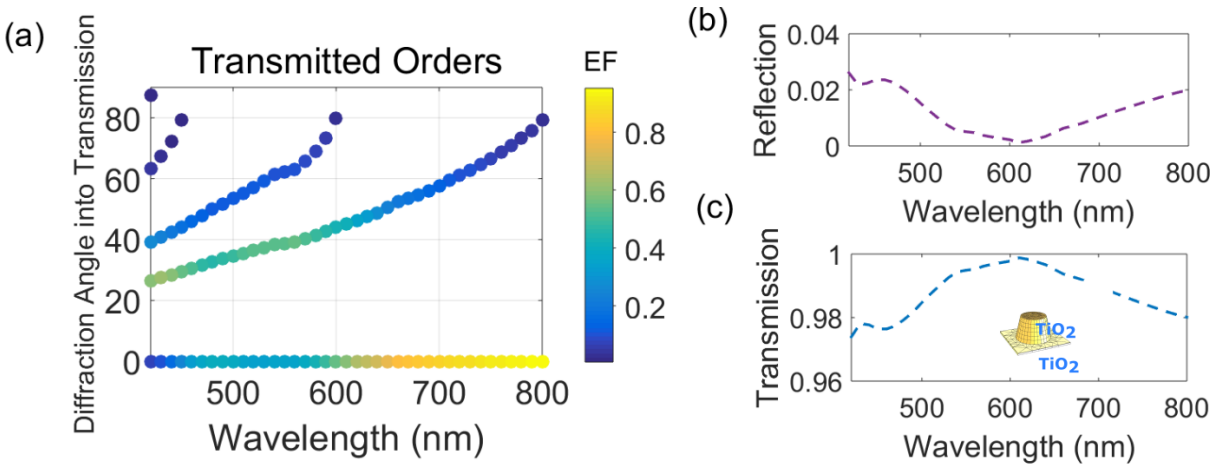

FIGURE 6.4: (a) Angle resolved transmitted spectrum of titanium dioxide nanofrustums(height = 150 nm, $\text{radius}_{\text{top}}$ = 100 nm, $\text{radius}_{\text{bottom}}$ = 120 nm) on titanium dioxide; indicating angular spread of transmitted diffracted energy. Each curve corresponds to the spectral trend of the transmitted energy fraction (EF) in different angular directions (b) total reflection and (c) total transmission of the nanofrustum spectrum on titanium dioxide.

higher refractive index arranged at a subwavelength pitch of 360 nm. Since the goal here is to just focus on the forward scattering without the presence of an index gradient, we perform this investigation for a single pitch value. The diffraction orders each have a peculiar spectral distribution in terms of amplitude. In the short wavelength range, the transmitted energy is distributed between the fundamental, first and second order. This energy distribution is clearly evident from figure 6.4(a). Transmitted energy distribution has considerable amplitude (0.4-0.6) in the short wavelength range. Sum of all the transmitted energy fraction in each of the resolved directions gives rise to the total transmission. This proves that at short wavelengths the nanostructure is fairly active in transmission of light. The combined amplitude of the first and second diffraction order amounts to almost 50 percent of the transmitted energy at these wavelengths. From the previous case, we do not observe higher orders in transmission. The higher order modes which are seen in the spectra are a result of the so called leakyness of the nanofrustum scattering behavior into a high index material. A high index medium enables an increased propagation constant. This eases the coupling tendencies of the scattered field into higher order modes. The electric and magnetic type of modes which are seen as reflection in air now are effectively coupled into titanium dioxide resulting in high transmission. In the long wavelength range the transmitted energy is mainly confined to the fundamental diffraction order. Only 20 percent of the transmitted energy goes into the first and second diffracted orders. The dominance of the fundamental diffraction order proves that at long wavelengths the structure majorly controls reflection (thereby transmission) on account of the tapered texture. The transmission characteristics of the structure thereby indicate immense light confining and directing tendencies. Since titanium dioxide is fairly lossless in the considered wavelength range, most of the light confined/directed by the

titanium dioxide nanostructures is directed into silicon. This is also evident by the very low '1 − reflection' calculated by simulation. This proves that the nanofrustum possess the full potential to direct light into silicon.

6.1.3 Two different subwavelength pitches for the titanium dioxide nanofrustums on a hypothetically assumed lossless silicon

The idea behind these investigations is to examine transmission into silicon as a result of the resonant and subwavelength properties of the metasurface. We expect to identify the Mie type resonances of the nanofrustum periodic arrangement on silicon. A high index material such as silicon will introduce a new boundary condition to the nanofrustum metasurface. This alters the ratio of the relative backward to forward scattering of the entire system. This influences the reflection behavior of the metasurface. This investigation is the real check of the enhanced ability of the designed system to ensure maximum transfer into silicon. Moreover comparing two different pitches helps in quantifying the effective light transfer into silicon as a result of the nanostructure metasurface.

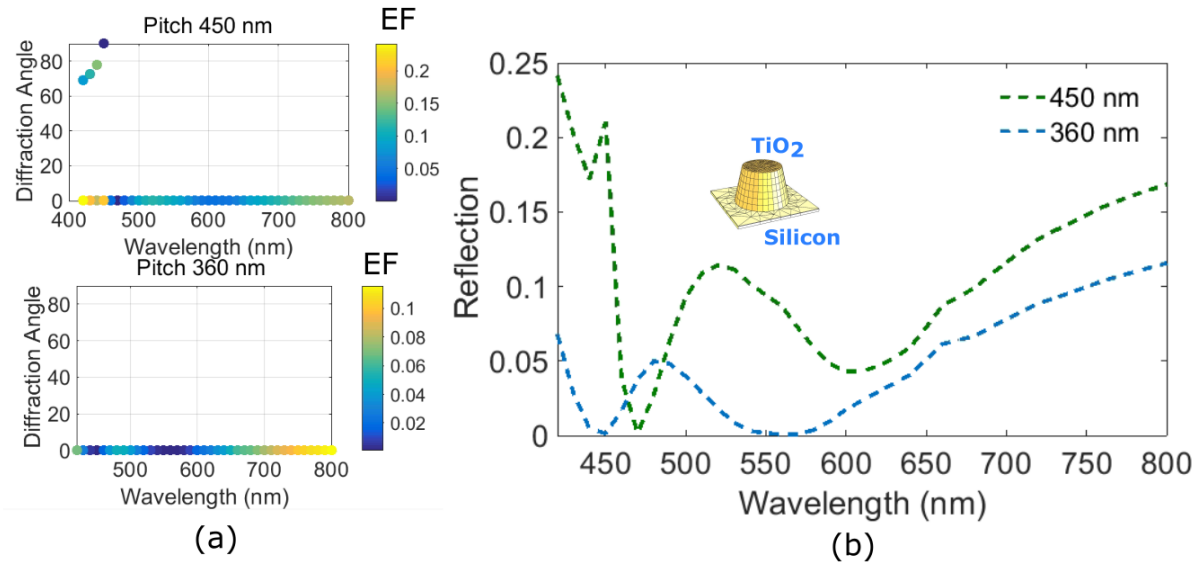

FIGURE 6.5: (a) Angle resolved reflection spectra of the two pitches -450 and 360 nm. (b) Reflection spectra of the two pitches 450 and 360 nm. The geometrical dimensions of the frustums are shown in table 4.2 (height = 150 nm, $\text{radius}_{\text{top}}$ = 100nm, $\text{radius}_{\text{bottom}}$ = 100nm, pitch = 360 nm are used in the simulation model

In figure 6.5, for the 450 nm arrangement, we observe the presence of the fundamental and the first diffraction order. The strength of the fundamental order is sufficiently large in the short wavelengths and amounts to 50 percent of bare silicon reflection (25 percent). While the green curve in figure 6.5 shows reflection supression, this definitely does not compete with the line of well designed antireflective structures. Moreover significant modulation is

observed in the spectra. The average reflection of the system is about 10 percent across the calculation bandwidth. The first order diffraction order is present only between 400-500 nm and is a result of the frustum pitch being in the wavelength range. The rather strong fluctuation observed between 450-500 nm is a result of the presence of the first order diffraction present in the spectrum. In the long wavelength range, we observe increased reflection as a result of the decrease in forward scattering tendancies of the metasurface. From the angle resolved energy calculations, shown in figure 6.5(a), the first order diffracted light is observed between angles $70° - 90°$ from the angle of incidence. This is effectively light lost in reflected diffraction which potentially can be coupled into silicon via a more effective design of the periodic arrangement. The previous discussion monitors transmission into titanium dioxide in order to examine transmittive behavior without an optical interface with a high index substrate. However in presence of silicon we specifically focus on reflection - to verify positions of degenerate resonances on silicon as well as specifically differentiate in presence of silicon, impact of the subwavelength pitch on silicon in comparison with a non subwavelength pitch. Degenerate zero reflection (360 nm pitch) is a pure metastructured response in comparison with a non zero reflection as observed for the 450 nm pitch.

If we look at the reflection spectra of the pitch with 360 nm, only the fundamental order of propagation is present. The maximum value of the peaks observed in the fundamental mode at short wavelength is around 10 percent. This value reduces to zero at particular wavelengths. This enables complete transfer of light into silicon as a result of the nanostructure's optical properties. The overall magnitude in this case much lower than what is observed for 450 nm. This proves the theoretical approach of the importance of subwavelength dimensionality in the nanostructure pitch. Such a pitch helps in restricting the reflection to the fundamental order. The amplitude of this fundamental order is also well in control and majorly influenced by the forward scattering tendencies of the titanium dioxide frustums.

Wavelengths, where we observe almost zero reflection correspond to those wavelengths at which all the light captured by the dielectric nanostructures is completely transfered into silicon. The fact that this action is localised to two wavelengths, i.e is 450 nm and 560 nm, indicates the presence of strong optical modes in the nanofrustums when present on silicon. We look into the near field images at these wavelengths in the plane of polarisation. These field distributions are identical to the field distributions of the electric and magnetic dipolar modes of a spherical particle as derived from Mie theory. From the arrow and vector field plots in figure 6.6, at 450 nm we observe the electric type resonance in the nanofrustum. The field distribution is exactly similar to the electric dipole of a sphere in the plane of polarisation. This is characterised by a centralised high intensity at the centre

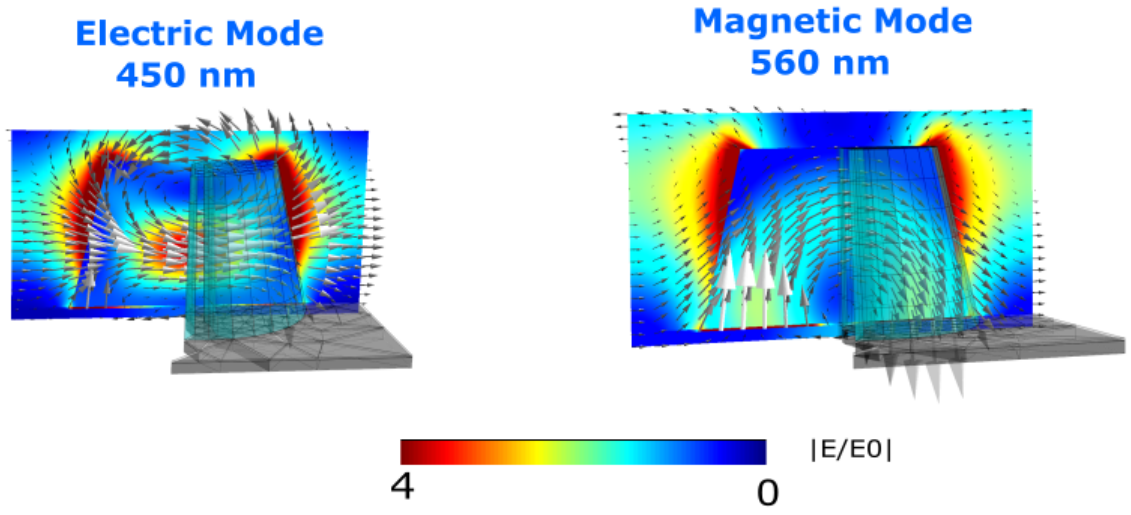

FIGURE 6.6: Electric field plots in the plane of polarisation for a nanoresonator on silicon at (a) the Mie type electric mode seen at 450 nm and (b) the Mie type magnetic mode seen at 560 nm. The geometrical dimensions of the frustums are shown in table 4.2 (height = 150 nm, $\text{radius}_{\text{top}}$ = 100nm, $\text{radius}_{\text{bottom}}$ = 120nm, pitch = 360 nm are used in the simulation model. These views are generated at angles and zoom which visually best show the field behavior associated with the described resonances.

of the nanofrustum. At 560 nm, the nanofrustums exhibit the resonance corresponding to that of a magnetic dipole. This is evident from the circulating electric field as observed in figure 6.6. These degenerate resonant points result in the complete transfer of light from the frustums into silicon. This action leads to localised zeroes in the reflection spectra. The lack of localised zeroes in the reflection spectra for the 450 nm pitch, confirms the fact that the presence of first order in the reflection spectra results in disrupting the perfect resonant flow of light from the nanofrustums into silicon. Therefore it makes sense to restrict the pitch to 360 nm for further improvements in the design of the antireflection. We further evaluate the complete transfer into silicon by resolving the light which is transmitted into silicon into different angular directions in figure 6.7. This helps in proving that transmitted light in angular directions apart from the fundamental one for the 360 nm has a higher intensity as compared to the 450 nm pitch. Additionally the high intensity in the transmitted first and second order is present in the short wavelengths. (400-600 nm) This further proves the effect of the forward scattering in the transmitted spectrum. The increased number of transmission of modes seen in figure 6.7 are physical evidence of the fact that the electric and dielectric type of resonances leak into the high index medium, increasing transmission. From figure 6.7 that even though the number of transmitted modes is more for the 450 nm pitch, their effective amplitude is much lower than for the pitch of 360 nm. Moreover for both cases, at long wavelengths, a high amplitude is observed in the fundamental order of propagation. This conclusion can be derived from the fact at long wavelengths, the nanofrustums do not exhibit any resonant behavior. The index profile helps in efficient non resonant scattering of

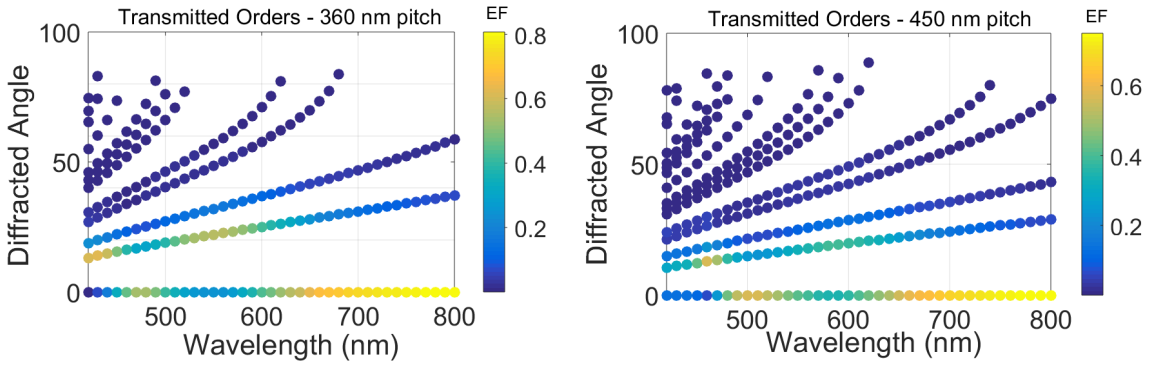

FIGURE 6.7: Angle resolved transmitted energy fraction (E.F) into silicon. Each curve represents the spectral trend of the angular spread of the energy: two different pitches are shown - (a) 360 and (b) 450 nm. The dimensions of the titanium dioxide nanofrustums are height = 150 nm, $\text{radius}_{\text{top}}$ = 100nm,$\text{radius}_{\text{bottom}}$ = 120nm

light into silicon. This is an evidence of the fact that the gradual variation of the index profile as a result of the taper of the frustum helps in more light coupling into silicon. Thus with a combination of nanostructured effects in the short wavelengths and a well tapered profile in the long wavelengths we are able to ensure maximum light transfer into silicon. Maintaining a subwavelength pitch thereby facilitates pure metastructured response instead of a diffractive response by restricting reflected light in the fundamental order. The focus is entirely on the engineered Mie type response. Theoretical investigations support that a subwavelength pitch helps in maintaining a metastructured response over a diffractive response.[106]

6.1.4 Titanium dioxide nanofrustums on absorbing silicon

In this investigation, we add the silicon absorption to the entire model and include the loss coefficient, to calculate the total silicon reflection. This provides how the periodic nanofrustum array behaves on a lossy material.[107] The two quantities of interest are the reflection of the total system and corresponding absorption observed. In figure 6.8 we show the total reflection and the resulting silicon absorption. We observe two localised peaks of unity absorption into silicon, as a result of the resonant properties of the system described in the previous investigations. We realise that the reflection observed here is almost more than three times lower than the bare silicon reflection. Moreover at the wavelengths of 450 nm and 560 nm, the reflection is zero. This effect is due to the perfect phase matching conditions locally observed at these wavelengths. This is a result of the fact that the backward scattering arising out of the Mie type resonances at these wavelengths is zero. In conclusion we achieve complete light transfer into silicon at these degenerate points. Beyond 600 nm, the reflection steeply rises. At these wavelengths, the resonant properties of the nanostructure are not predominant owing to the size restrictions. This results in silicon reflection to rise

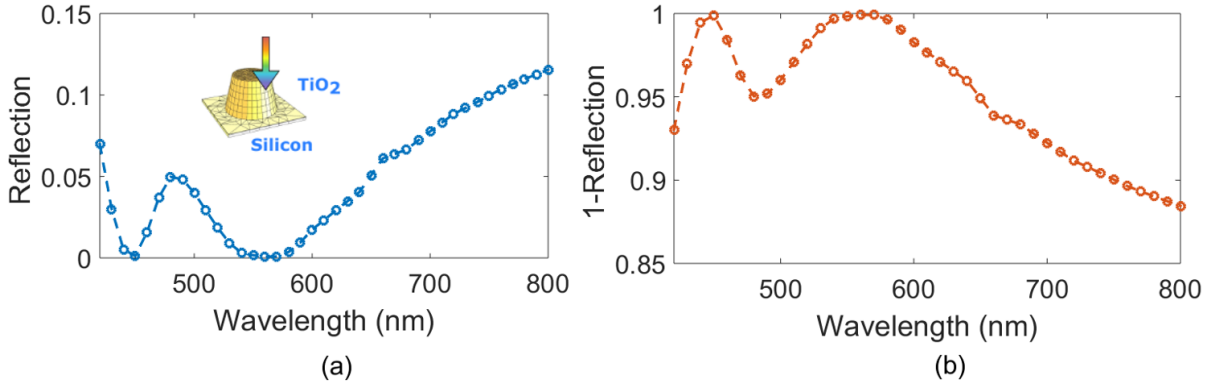

FIGURE 6.8: (a) Total reflection and (b) silicon absorption in presence of the entire nanostructure. These curves correspond to a metasurface pitch of 360 nm, where the nanofrustum dimensions are height = 150 nm, $\text{radius}_{\text{top}}$ = 100 nm, $\text{radius}_{\text{bottom}}$ = 120 nm.

well beyond 10 percent at normal incidence itself. This value needs to be optimised in order to prevent substantially higher reflections at higher angles of incidence.

6.1.5 Titanium dioxide nanofrustums on thin films of titanium dioxide on silicon

The idea of this investigation to show the role of a planar film of titanium dioxide on p-silicon and the TiO_2 frustums plays in further improving the antireflective properties of the nanostructure. We maintain the aforementioned described frustum geometry and a pitch of 360 nm between them. In figure 6.1, we observe the impact of titanium dioxide planar thin films on silicon reflection. In figure 6.8 we observe perfect conditions for optical impedance matching resulting in localised zeroes in reflection owing to the optical resonances of the nanofrustums. However the overall the magnitude of the reflection is still significantly high. We propose to combine the optical properties of the nanofrustum metasurface with the thin film to further optimise the behavior of the system. We perform numerical simulations to vary the thickness of the planar film. Fresnel theory provides solutions to the reflection and transmission of thin films on susbtrates.[5] According to this theory, a thin film having thickness in the range of the incident light wavelength will give rise to interferences.[63] Such interferences are undesirable in the design of a good antireflective structure. In the view of the visible light wavelength, we limit the thickness of the film to less than 100 nm. We already showed in figure 6.1 the trends in silicon reflection obtained by very thin films of titanium dioxide on silicon. The questions to answer via these simulations how exactly these thickness values play a role in influencing the silicon antireflection in combination with the nanostructures. The other question to answer is what is the ideal thickness which aids in improving the antireflection performance of the metasurfaces. The complete model and the obtained reflection spectra is shown in figure 6.9. We add the thin film in the layer stack between the structure and silicon and perform the rest of the calculations in a similar manner.

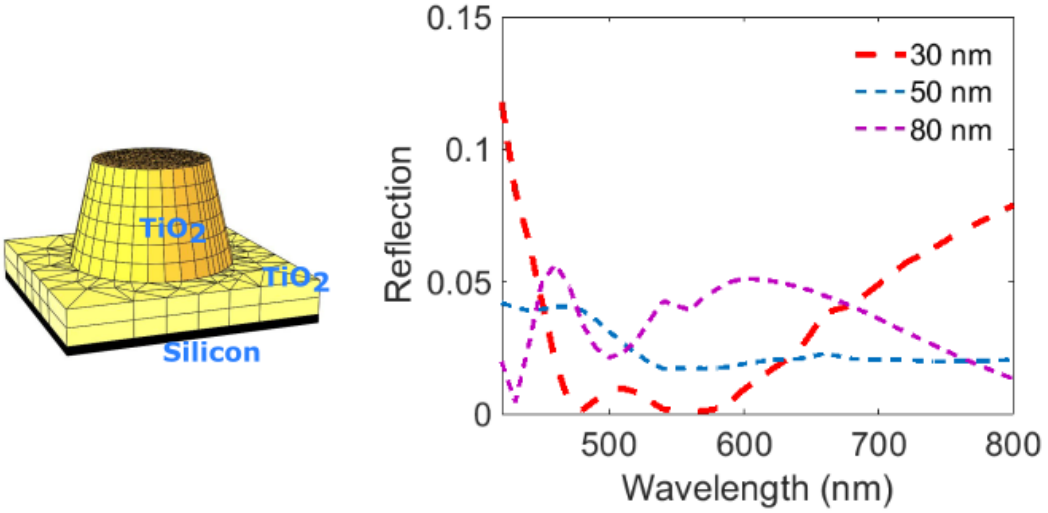

FIGURE 6.9: Reflection trend of the metasurface as a function of the intermediate film thickness between nanofrustum array and silicon. The metasurface pitch is 360 nm and the nanofrustum dimensions are height = 150 nm, $\text{radius}_{\text{top}} = 100$ nm, $\text{radius}_{\text{bottom}} = 120$ nm. The complete simulation model of the final design of the titanium dioxide nanofrustum, titanium dioxide thin film and silicon half space is illustrated. Reflection of the entire system is shown for three different film thicknesses

We vary the thickness of this film between 30-80 nm and record in each case the reflection obtained.

For the 50 nm film used in combination with the nanofrustums, the simulated reflection is much lower across the entire bandwidth in comparison with the simulated reflection for 30 nm. In the short wavelength range, the 30 nm film shows high reflection. However this is the wavelength where the optics of the nanofrustum periodic arrangement results in supressed reflection. In the wavelength range of 400-500 nm, without the planar film, the total reflection is around 8-10 percent. With this film, reflection shrinks down to 3.8 percent in average. The trend of reduced reflection also continues in the long wavelength range of 500-800 nm, where the average reflection reduces down to 2 percent in average. This proves the impact of having a planar film of an appropriate thickness in order to provide the correct index gradient to aid antireflective behavior at these wavelengths. This behavior shows a peculiar interaction of nanofrustums with the TiO_2 film on silicon. Adding a planar film of TiO_2 on silicon changes the index gradient with air. Moreover since this index gradient is of the same material as the nanostructures itself, the forward scattering leakyness into the substrate is not affected by the phase transitions which arises as a result of large index difference from titanium dioxide and silicon. Overall coupling between the nanostructure and silicon is enhanced via the

titanium dioxide film. The strength of the fundamental reflection order therefore decreases in amplitude and thereby ensures sufficient light absorption into the silicon.

If the thickness of this film is reduced to a mere 30 nm then we see an increase in reflection at both long and short wavelengths. At short wavelengths, for an intermediate thin film of 30 nm, peaks up to almost three times the average value seen for the 50 nm film. The overall trend of this curve is the same as that of the array of nanofrustums on silicon. Via simulation, for both cases we observe the fundamental mode of propagation. The described drastic change in reflection therefore implies that the thin intermediate film at short wavelengths results in a phase condition at the interface which results in preferentially backward scattering as a result of the nanostructure. This results in high reflection. It is important to note that in this case, the reflection between 500-600 nm drops drastically to almost zero. However the average value is significantly high for an effcient implementation as an antireflection layer. This is undesirable for the overall design goal to minimise reflection in the entire bandwidth range.

If we set the film thickness to be 80 nm, then across the spectrum, the reflection is lower than the 30 nm film but substantially higher than for the 50 nm. This observation via the simulation of dependence of different film thickness reveals that the titanium dioxide film thickness sets in a specific phase condition at the interface between titanium dioxide nanofrustums and silicon which decides the ratio of forward to backward scattering the nanostructures exhibit. This example also demonstrates the need to design and optimise nanostructures numerically. From figure 6.8 and figure 6.9, we identify the broadband optical impedance matching properties induced by the film in combination with the total system. The 50 nm titanium dioxide film results in a broadband supression of reflection although it disrupts the zero reflection condition. We therefore decide to have a target film thickness of 50 nm in the final design.

To exactly understand the light coupling between the nanofrustum arrangement and the intermediate planar film for the given thickness, we take aid of angle resolved transmitted and reflected energies. In order to be able to calculate the transmitted energy we set the silicon absorption to zero. The calculations as described in figure 6.2 provide the angular resolved energies in both directions. The important question to answer is what happens to electric and magnetic modes seen in figure 6.6 in presence of the 50 nm titanium oxide film. We observe in figure 6.10 that in the short wavelengths range, the transmitted energy is distributed between the fundamental, first and second order angular zones. We know from the figure 6.3 that the periodic nanostructure itself only the fundamental order of transmission. We show in figure 6.7 an increase in the trasmitted modes of the nanofrustum arrangement in the vicinity of a

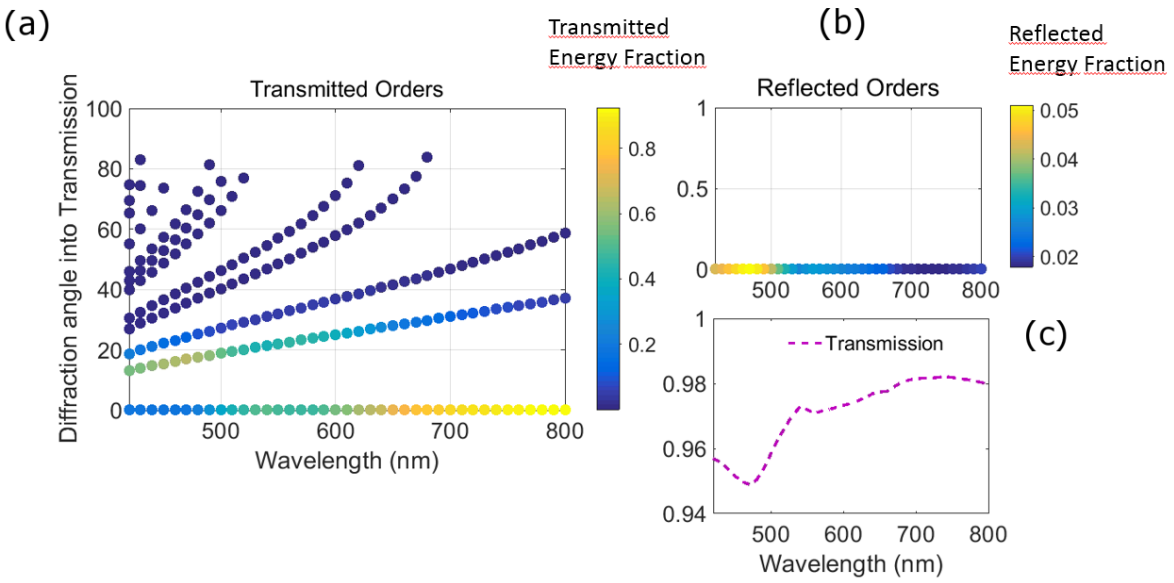

FIGURE 6.10: (a) Transmission and (b) reflection orders and (c) total transmission spectra for normal incidence as a result of intermediate film coupling. We model here, the nanofrustum arrangement on a 50 nm titanium dioxide thin film on hypothetically assumed lossless silicon.The metasurface pitch is 360 nm and the nanofrustum dimensions are height = 150 nm, $\text{radius}_{\text{top}}$ = 100 nm, $\text{radius}_{\text{bottom}}$ = 120 nm.

high index substrate. In presence of a film of an appropriate thickness, the relative amplitude of each of these modes increases due to improved coupling as a result of index matching. In figure 6.7 between 420-500 nm, the energy of the first order is quite strong as a result of the electric resonance observed at 460 nm. On introducing the 50 nm film, the energy in the first order is not as strong as before. This results in broadening of the resonance and more light being transmitted into silicon. Similarly the magnetic mode at 560 nm results in high energy distributed in the first order (figure 6.7). However in this case, the energy distribution along the fundamental and second angular order is almost equal in the wavelengths between 500-600 nm. Thus the magnetic mode is also broadened. In the long wavelength range, we observe that reflection reduces tremendously (0.02) maximising transmission to 0.98. This results from the implementation of an effective gradual index profile as previously described. Thus introduction of the film results in pertubation of the resonances which favorably couples more light into silicon. These investigations therefore conclude that localised resonances result in zero reflection. Perturbing these resonances [74] with the help of a planar thin film, helps in achieving enhanced broadband control of reflection. With this section we therefore conclude with final design parameters which are used as target parameters for the fabrication process described in chapter 2. They have been indicated in table 4.2.

6.2 Analysis of measured spectra: perpendicular incidence

We now proceed to characterise the optical spectra of the fabricated metasurfaces including the thin planar film with aid of optical measurements. The geometrical dimensions are shown in the fabrication section in table 4.2. In this section, we describe the measured reflection spectra and its significance between 420-800 nm of the metasurface. We measure the spectra with the help of a bright field microscope and spectrometer combination. The bright field microsope allows for the measurement of the total reflection of the structure on silicon. The system is also configured to measure the diffuse reflection of the structure. The ray diagram of the bright field microscope is shown in figure 6.11 Using this setup, we obtain

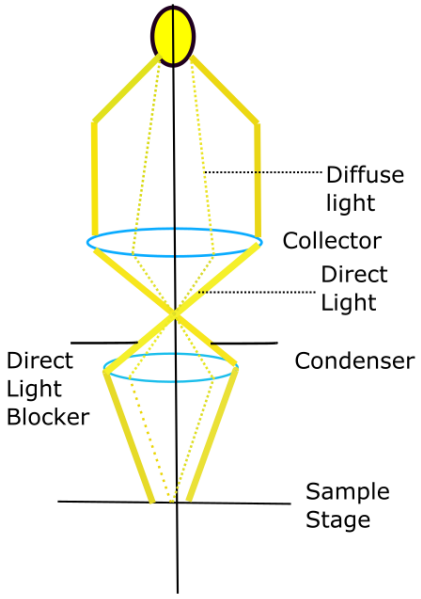

FIGURE 6.11: Ray diagram of the bright field microscope

the direct reflection from the sample. The spectral measurements of this sample are shown in figure 6.12. This reflection is similar to that predicted by the simulation in figure 6.10 for identical dimensions. This proves the accuracy of the the simulation model as well as the design process decribed in section 5.1. The experimental spectrum relates to the same physical scenario as depicted by simulations of perturbative broadening of Mie resonances in the short wavelengths and improved impedance matching. This is also evident in the measured spectra. The measured spectra however appears to be slightly blue shifted as compared to the simulated curve. This minor blue shift is a cumulative error present in all experimentally extracted inputs to the simulation along with systematic measurement error. Both spectra show the same physics and the corresponding reflection values obtained are in a good agreement with each other. If we compare this value to the bare silicon reflection,

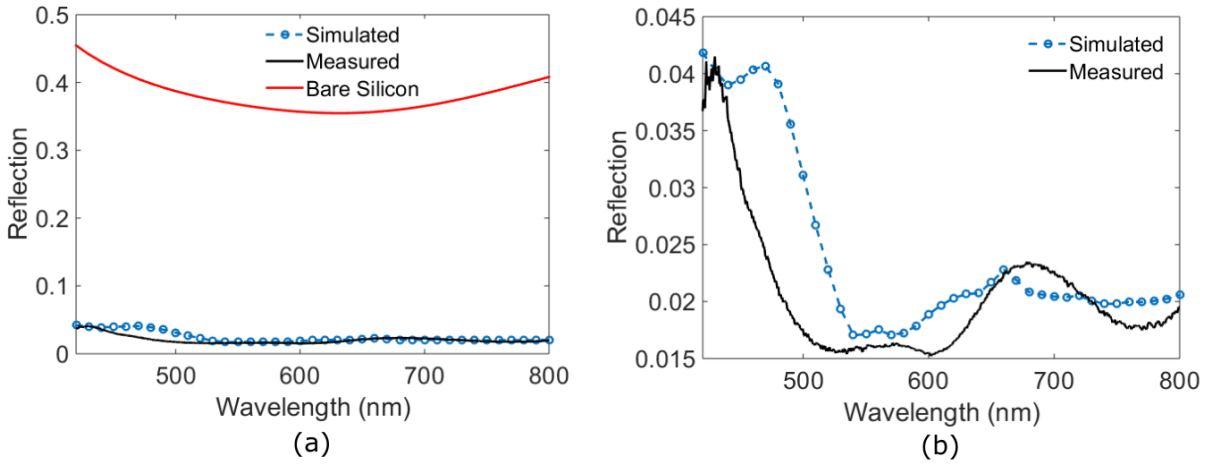

FIGURE 6.12: (a) Measured and simulated spectra compared against bare silicon reflection for normal incidence (b) Zoomed in reflection spectra indicating similar trend between simulated and measured spectra. The structure dimensions here correspond to the fabricated metasurface in the fabrication section 4.2

then we observe that the value shrinks down by a factor of 10 in the entire bandwith. This deems the structure design to be effective.

Owing to the subwavelength dimensions as well as the extremely smooth material texture, the measured diffuse reflection is almost negligible and lies beyond the noise floor of the spectrometer. This is in confirmation with the simulation result shown in figure 6.10, where the diffraction orders present in the reflected spectra are limited to the fundamental order. The obtained experimental result therefore is in reasonable agreement with the simulation prediction. The overall design strategy in arriving at the structure dimensions is therefore successful towards reflection supression.

6.3 Comparison of measured and simulation spectra: angular incidence

At normal incidence, we have observed significant supression of reflection across the bandwidth range. Given the effort of nanostructure design and fabrication of the metasurface, such reflection supressing properties should also be dominant for higher incident angles for both light polarisations. We measure such an angle dependent performance using a Woolam ellipsometer. The geometrical dimensions of the metasurface and the planar titanium dioxide planar film are shown in the fabrication section in table 4.2. For each incident angle, reflected light is separately measured for the two polarisations in the visible wavelengths of 420-800 nm. An ellipsometer consists of two goniometers which control the angle of incidence onto the sample as well as the detector angle which measures the reflection from the sample. The goniometer sets the detector angle to the direction of specular reflection for a given light incidence on the sample. The surface plots of these measurements and their

simulation counterparts are shown in figure 6.13. We show both measured and simulated

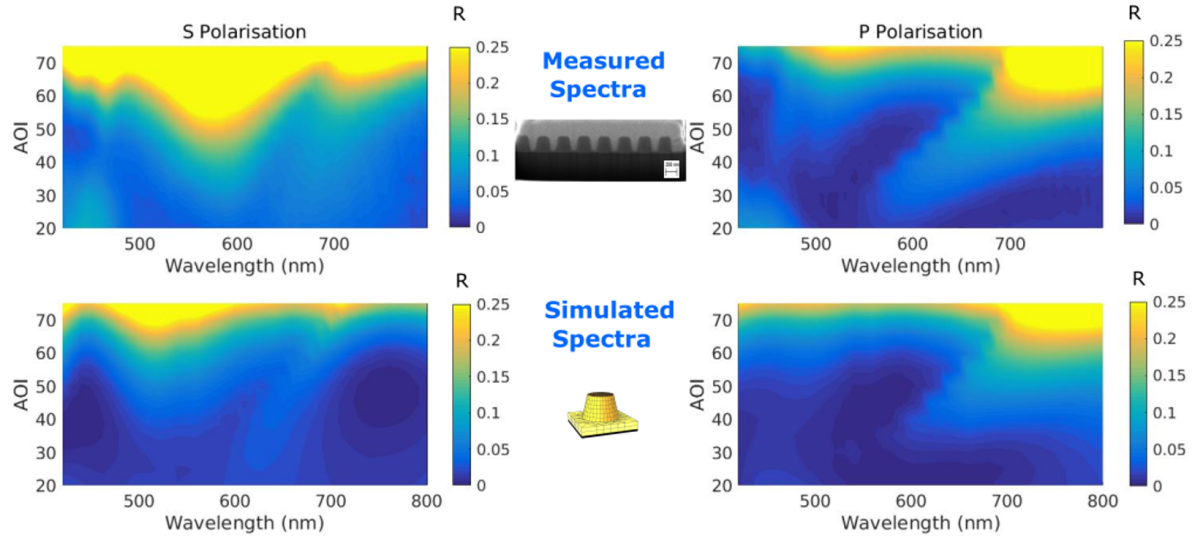

FIGURE 6.13: Measured and simulated specular reflection spectra for angular incident light for both polarisations. The geometrical dimensions are shown in table 4.2 (height = 150 nm, $\text{radius}_{\text{top}}$ = 100nm, $\text{radius}_{\text{bottom}}$ = 100nm, pitch = 360 nm, $\text{thickness}_{\text{film}}$ = 50nm are used in the simulation model)

spectral maps for the incident angles between 20° to 75°. We compare the measured spectra with the simulated spectra in order to evaluate the physical phenomenon due to which the structures effectively supress reflection even at higher angles of incidence. This calls for a good agreement between the experimental and simulation spectra. In such a case, the simulated spectra can be used to deduce details such as propagational diffraction orders and their polarisation dependancies for different angles of incidence. This can be used to verify the underlying physics which occurs for different incident conditions to give an overview of the functioning of the antireflection behavior. Both measured and simulated plots reveal that the reflection is significantly low for even higher angles of incidence in the entire spectral range. Experimental and simulated spectra show a similar physical trend in terms of the angular positions of the localised maximas observed. For incident angles upto 45° the reflection is well below 10 percent.

For *p*- polarized light, simulated and measured spectra for the short wavelength range show very low reflection (less than 5 percent) in the angles of incidence between 20°- 65°. We demonstrated in the design section 6.1 that in the short wavelength range, the pertubed electric and magnetic type Mie modes of the nanofrustum metasurfaces result in controlling the reflection value for perpendicular incidence. In this case, the angular spread of the total reflected energy was restricted to the fundamental order of propagation. These results prove that a good agreement is observed between the simulated and measured fundamental order reflection even at higher angles of incidence thereby further confirming the accuracy

and strategy of the design. An angular incidence results in more of the incident energy being coupled in the direction of the periodic arrangement. It is theoretically proved that depending upon incident direction, additional diffracton orders can get triggered.[27] To check the spectral dependence of the angular spread of these orders as a function of incident angles we take aid of the aforememtioned angle resolved energy plots.

For incident angles of 30° and 60°, we calculate the angular spectral energy distribution in reflected and transmitted orders. This analysis should provide a trend of higher order reflections which arise as a result of the nanostructure at higher incident angles. The amplitude and spectral dependancies of these higher order incident modes is of particular significance. This calculation also helps in identifying the polarisation dependance of the spectral distribution of the modes.

6.4 Diffractive analysis of the metasurface at angular incidence

In the previous section, we established a reasonable agreement between simulated and measured fundamental order reflection for different angles of incidence. In this section, we quantify with the aid of numerical simulations the magnitude and spectral spread of the diffractive components for two angles of incidence. This is to quantify the diffractive trend of the metasurface at an oblique angle of incidence. As explained in section 2.2.4, the first order reflection spectra is calculated by solely considering in equation 2.72, the corresponding first order electric field and propagation vector components. At wavelengths, where this spectra shows characteristic features like peaks and dips, we analyse the near field spectra. The goal of this section is to analyse with the help of computational investigations the added increase in reflection as a result of higher order reflection modes. We perform this analysis for two angles of incidence 30° and 60° to provide a quantitative spectral trend.

6.4.1 Properties for angular incidence of 30°

For s- and p-polarized light up to 540 nm, in addition to having the fundamental order, the reflection spectra also contains the first order. The amplitude of the first order reflection is not strong in comparison with the zero order reflection. At 30° presence of the first order only in the short wavelengths throws light on the peculiar modal response of the periodic system of nanoresonators. A peak is observed in the first order reflection spectra at the wavelength of 450 nm for s polarisation. We take aid of the near field image at 450 nm to analyse the significance of this peak in terms of field localisation at the interface. In this case, we observe that in the plane of polarisation, part of the electric field at the interface of the frustum and the titanium dioxide planar film is reflected away from the interface The

amplitudes of the obtained first orders and the corresponding near field features are shown in figure 6.14(a) and (b). This corresponds to the source of the first order reflection. For

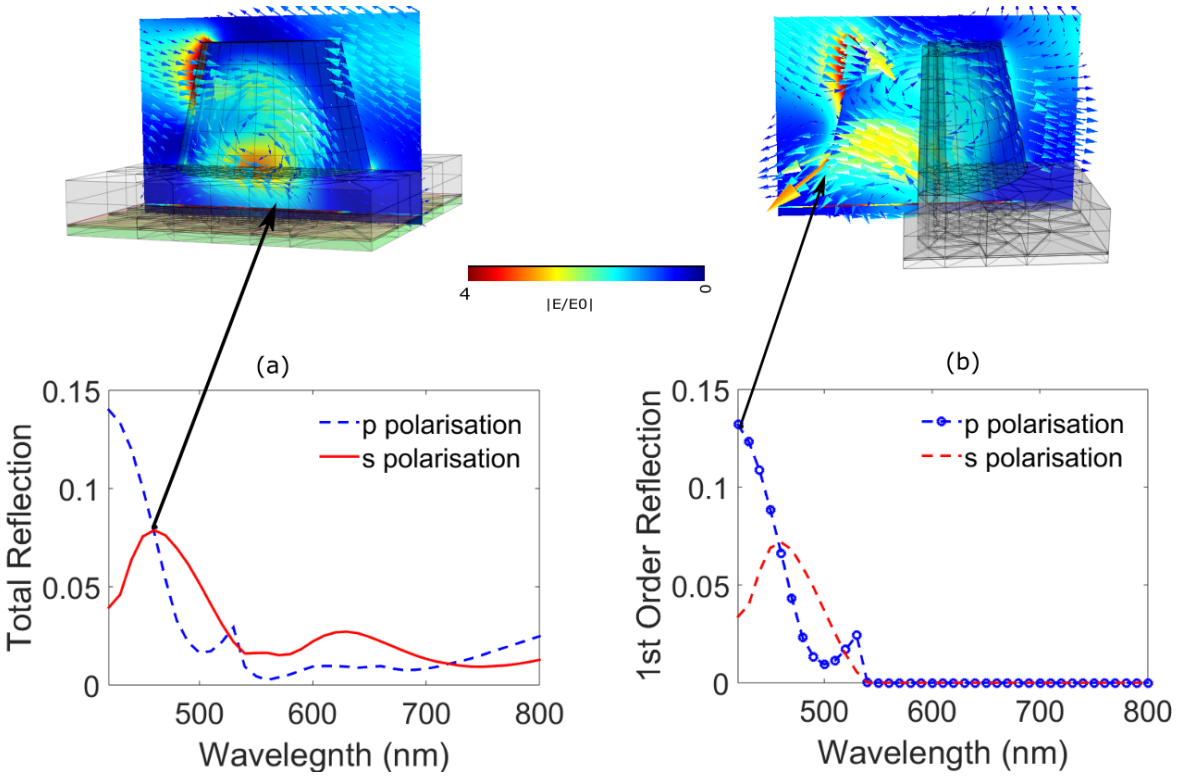

FIGURE 6.14: Numerical analysis of the obtained first order for an incident angle of 30° for the nanofrustum metasurface (a) Calculated total reflection spectrum for s and p polarisation indicating the near field electric field plot in the plane of polarisation at the light wavelength of 450 nm. (b) Calculated spectrum of the first order reflection for s and p polarisation and the near field electric field plot in the plane of polarisation at the light wavelength of 420 nm. The geometrical dimensions shown in table 4.2 (height = 150 nm, $\text{radius}_{\text{top}}$ = 100nm, $\text{radius}_{\text{bottom}}$ = 120nm, pitch = 360 nm, $\text{thickness}_{\text{film}}$ = 50nm are used in the simulation model)

p-polarisation, a strong peak in the first order is observed at 420 nm. In the near field image of this wavelength, in the plane of polarisation, the electric field propagates in a distinct loop like fashion. This loop results in part of the energy being coupled out as reflection giving rise to a high magnitude peak.

For p- polarisation, the amplitude of the observed peak is almost twice the amplitude of the s polarisation. This is because of the pronounced interaction of the incident field in the plane of incidence with the nanostructures. For the s- polarised light, the field is perpendicular to the structure geometry and the interaction is not as strong in comparison with p- polarised light. This is not seen in the measured data due to the fact that the ellipsometer only measures specular light. This makes it important to take the aid of simulations to characterise the amplitude of these orders for different angles of incidence. For perpendicular incidence, without the film, Mie type resonances give rise to zero reflection as seen in figure 6.8. This

behavior is made more broadband with the help of a film of appropriate thickness in figure 6.10. However at an angular incidence, the presence of additional components in the direction of the lattice vector increase the reflection via peculiar modes being observed for s- and p-polarised light in the nanofrustum. The first order reflection component therefore increases the reflection at the short wavelengths.

Between 540-800 nm, for both polarisations, the reflection is restricted to the fundamental order, as measured and in good agreement with the fundamental order simulated data. The subwavelength arrangement maintains a zero order in reflection. This, accompanied with the non-resonant scattering of the nanofrustums at these wavelengths results in the reflection being less than 1.5 percent for both s- and p- polarisation. This is really good performance in terms of angular incidence for both polarisations. It proves the effectiveness of the broadband optical impedance matching owing to nanostructuring. Beyond 650 nm, as described previously, the thin film helps in sustaining low reflection values for an off normal angle of incidence.

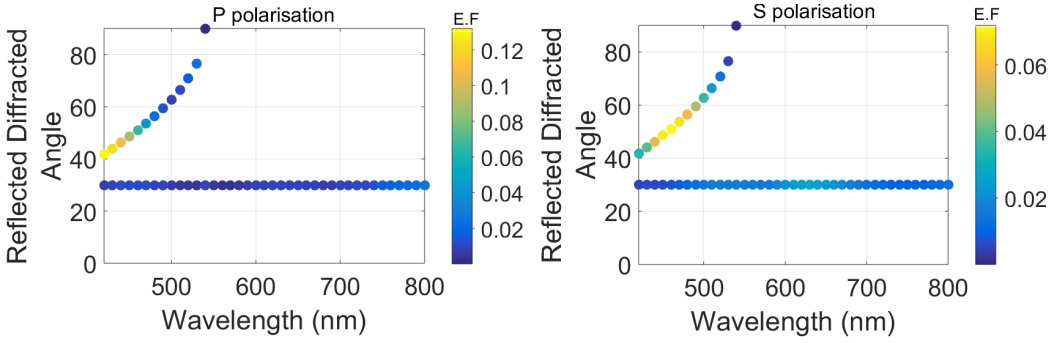

FIGURE 6.15: Angular spread of the reflected energy fraction for (a) p and (b) s polarised light at an angular incidence of 30°.The geometrical dimensions shown in table 4.2 (height = 150 nm, $\text{radius}_{\text{top}}$ = 100 nm, $\text{radius}_{\text{bottom}}$ = 100 nm, pitch = 360 nm, $\text{thickness}_{\text{film}}$ = 50 nm are used in the simulation model)

Figure 6.15 shows the angle resolved energy of the first and fundamental order reflection for an angle of incidence of 30°. For s polarised light, the first order reflection has a wider spread of high angular magnitude. This corresponds to a higher dominance of the periodic arrangement rather than localised interaction with the nanofrustum which is more dominant in case of p polarised light.[106]

6.4.2 Properties for angular incidence of 60°

We perform similar investigations for the incident angle of 60° to understand the trend of the high reflection seen in the measured and simulated spectra for the fundamental order. The curves of the total and first order reflection are seen in figure 6.16.

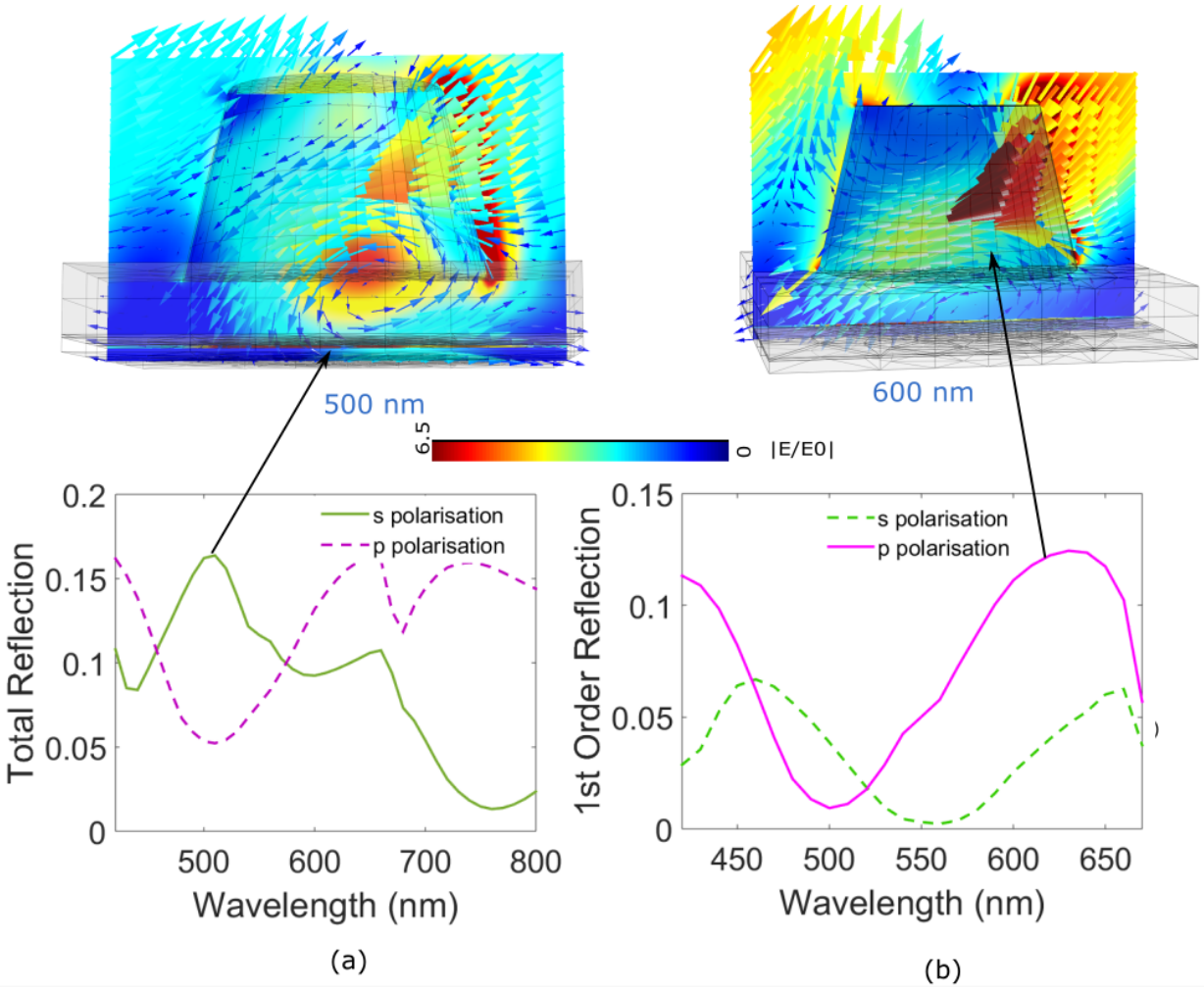

FIGURE 6.16: Numerical analysis of the obtained first order for an incident angle of 60° for the nanofrustum metasurface (a) Calculated total reflection spectrum for s and p polarisation indicating the near field plot in the plane of polarisation at the light wavelength of 500 nm. (b) Calculated first order reflection for s and p polarisation indicating the near field plot in the plane of polarisation at the light wavelength of 600 nm.The geometrical dimensions shown in table 4.2 (height = 150 nm, $\text{radius}_{\text{top}}$ = 100nm, $\text{radius}_{\text{bottom}}$ = 100nm, pitch = 360 nm, $\text{thickness}_{\text{film}}$ = 50nm are used in the simulation model)

For an incidence of 60°, the first order of reflection is present between 420-670 nm. Beyond 670 nm, reflection is restricted to the fundamental order. The amplitude of the first order reflection component increases in comparison with that seen at 30°. At the long wavelength range, at 650 nm we observe a pronounced amplitude of 0.08. This is evidence of pronounced diffractive trend at high incident angles onto the metasurface. These detailed investigations

for angular incidence, elaborate the fact that for off normal incidence, the first diffraction order gets triggered in the reflection spectra. The spectral presence of this order is dependent on the angle of incidence. Larger the angle of incidence, wider is the spectral presence of the first order. To provide an overview about this effect, we have shown through simulations, the presence of the first order for an incident angle for 30° is up to 540 nm. For 60°, the first order extends up to 670 nm. Beyond these wavelengths, in each case, reflection is solely due to the fundamental order. In both cases, the total reflection for both polarisations does not increase beyond 15 percent. The reflection spectra for both polarisations are dominated by the fundamental order resulting from the light propagation between the nanofrustum arrangement and the titanium dioxide thin film. This interaction is demonstrated with the help of the near field images at wavelengths where characteristic spectral performance is seen in the evaluated spectra. High amplitude of the first order in the reflected spectra can be linked to the increased field intensity which is seen to be coupled between the frustums from the near field images. The directional analysis of the angular spread of the reflection

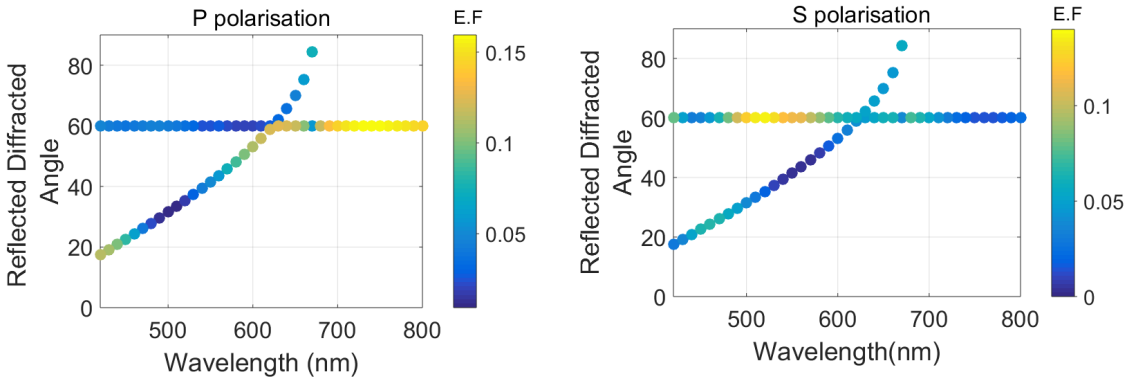

FIGURE 6.17: Angular spread of the reflected energy fraction for (a) p and (b) s polarised light 60°. The geometrical dimensions shown in table 4.2 (height = 150 nm, $\text{radius}_{\text{top}}$ = 100nm, $\text{radius}_{\text{bottom}}$ = 100nm, pitch = 360 nm, $\text{thickness}_{\text{film}}$ = 50nm are used in the simulation model)

components for both polarisations is shown in figure 6.17. For p- polarised light, the first order of reflection has a higher intensity in the short wavelength. The fundamental reflection is low at these wavelengths however strengthens at the long wavelengths. This proves that for p- polarised light, even at angular incidence there is predominant light interaction with the nanofrustums. At short wavelengths, the s-polarisation shows a weak response. For s polarised light, the first order does not have peculiar specular characteristics. Low reflection observed in the short wavelengths for both polarisations, indicates that the nanofrustum geometry scatters more light into silicon for even angular incidence. The angular spreads shown in figures 6.15 and 6.17 indicate the directional spread of the first order reflection which is not measured by the ellipsometer. This amplitude averages out to be 0.1 which in total is still less than the bare silicon reflection.

Despite of the presence of the first order in reflection, enough energy is coupled into silicon as a result of the effective broadband light directing properties of nanofrustum arrangement into silicon via the titanium dioxide. This broadband wide angle sustainance of the anti-reflection performance demonstrates the sancrosanctity of the step by step design approach taking aid of accurate rigorous simulation to arrive at metasurfaces.[114, 66] Realisation of such metasurfaces by state of the art fabrication methods helps in achieving complete understanding of ellipsometric optical measurements and their comparable numerically calculated counterparts.

6.5 Evaluation of photoelectrochemical properties of the metasurface on silicon

After comprehensively analysing on the antireflection properties resulting from effective design and fabrication strategies we demonstrate the intended application. The idea is to use the antireflective tendencies of the nanostructure to enhance the photoelectrochemical performance of a semiconductor-electrolyte pn- junction.[30] In this case the pn- junction is formed between p- type silicon and the hydrogen rich electrolyte. The J-V(current density-voltage) characteristics of this pn- junction shows photocurrent under illumination and an applied bias. This applied bias is necessary to have the photocurrent facilitate the water spitting reaction at the appropriate potenial value. The theory of the water splitting reaction as explained in chapter 2 shows the band energy characteristics of the water splitting reaction. The reaction needs two electrons to enable to water splitting into hydrogen ions and hydroxide ions. These two electrons are responsible to reduce the hydrogen ions to release hydrogen gas.[58] The hydroxide ions get oxidised to release oxygen gas.

To characterise this performance of the system, we perform a series of electrochemical measurements under illumination. For these measurements we use a patterned area of approximately 1 mm x 1 mm. In order to restrict the active sample area only to the nanostructured area, we seal the rest of the silicon sample with glue. This glue acts as insulator between the electrolyte and the silicon. The pn- junction therefore is only established in the patterned area. This helps in measuring the trend in J-V (current density-voltage) characteristics as a result of the light coupling by the nanostructures. In addition to controlling reflection, the nanostructures should allow the effective charge transfer between silicon and the electrolyte. This complements the light transfer function of the nanostructure. The measurements are compared with a planar silicon nanostructure for each measurement test case. The difference in the values obtained gives the quantitative benefit of the nanostructures on the J-V characteristics. All measured voltages are measured with reference to reversible hydrogen

electrode as indicated in figure 6.18. This electrode corresponds to the voltage of the reversible hydrogen reaction indicated in equation 2.78. The measured voltages are referred to as potenials vs RHE.

The first measurement is to evaluate the J-V curve under illumination and applied bias. The setup of the photoelectrochemical schematic is shown in figure 6.18. Under constant

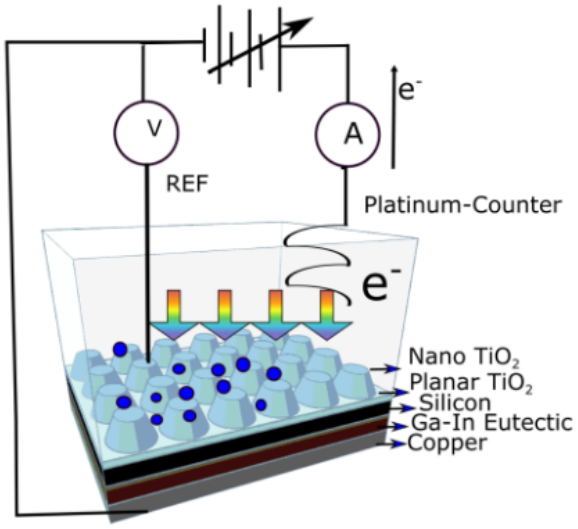

FIGURE 6.18: J-V characteristics of p-type silicon with and without the fabricated and optically analysed metasurfaces and planar titanium dioxide film.

illumination, the current voltage characteristics are measured for the applied bias between -0.1 to -3 V vs RHE. This applied bias depends on the electrical conductivities and doping values of the used p- type silicon wafer. With the help of this bias, we make up for the difference between the water splitting potenial and the bandgap of the silicon photocathode. The corresponding current measured for a voltage value gives out the total J-V performance. Figure 6.19 shows the measured characteristics of silicon with and without titanium dioxide nanostructures. The first important characteristics of this curve are the voltage value where the current changes from zero to non-zero. This is -1 V vs RHE. This value is referred to as the onset potential. We see in figure 6.19, that the potenial value for p- type silicon is -1.5 V vs RHE where the current saturates to a value of 15 mA/cm^2. This value more or less remains constant in the measured bandwidth. In addition to silicon reflection, this photocurrent is a function of the material properties of the utilised silicon wafer. These are enlisted in the table 6.1. The same curve for p- type silicon with the titanium dioxide metasurface starts off with the similar onset potential (-1 V vs RHE) The maximum current value in this case goes to an average value of 27 mA/cm^2. This average value is obtained by performing the measurement on three identical nanostructured samples. The close conformity of the

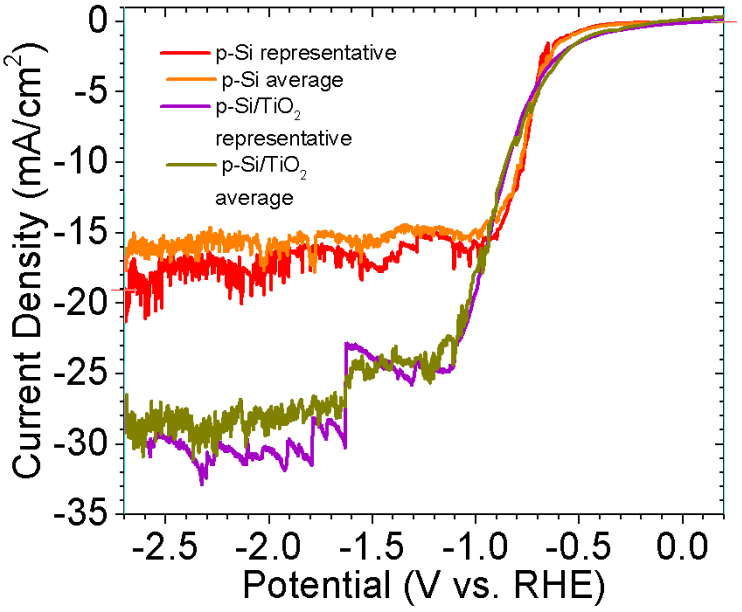

FIGURE 6.19: J-V characteristics of p- type silicon with and without nanostructres

Item Number 2611 PC Lot Number 31010							
Diameter	Material	Material type	Dopant	Orientation	Grade	Thickness (μm)	Resistivity (Ωcm)
3¨	CZ Silicon	P	B	<1-0-0>	Test	356-406	1-10

TABLE 6.1: Specifications of the used silicon substrates on which the metasurface stack was grown; information from the provider Quest International

average value with the representative sample indicates the reproducible nanostructure performance. Moreover as a result of the improved antireflection, we see a significant difference between the maximum current values with and without nanostructures. This effect stems from the theoretical relationship between the reflection(1-absorption) and the photocurrent density.[33] Since the reflection is drastically reduced, the difference in photocurrent values with and without nanostructures is substanial. Morever in the purple curve seen in figure 6.19, we see characteristic spikes. These spikes occur due to fall and rise of photocurrent. This rise and fall occurs as a result of the the generated hydrogen bubbles. These generated bubbles owing to high surface affinity of the hydrogen gas with titanium dioxide. This results in the light being partially blocked resulting in a dip in the current. After gaining significant volume, this bubble disintegrates from the surface, unblocking light, which again results in the rise in current. This proves that the titanium dioxide does not disturb the charge transfer dynamics across the semiconductor electrolyte pn- junction.

In order to further characterise this effect, in the next step, we change the illumination conditions. The illumination is periodically cut off every 2 secs and then again kept on for

2 secs. This investigation helps in determining the stability of the two layer system under dark illumination. Measuring the current under illumination right after a dark cycle helps in determining the current restoration of the system. This measurement is referred to as linear voltage sweep-'chop'. The curves for samples with and without structures are shown in figure 6.20. Also under this illumination condition, the silicon with nanostructures outperforms the

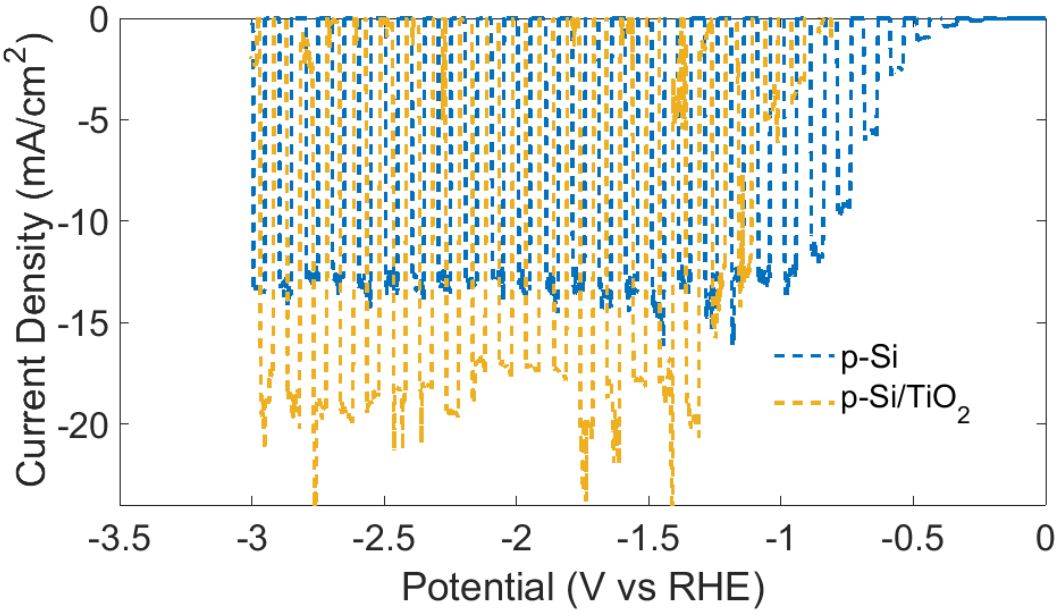

FIGURE 6.20: J-V characteristics of p- type silicon with and without the fabricated and optically characterised metasurface stack under chopped illumination

bare silicon structure. The two curves exactly overlap at the edges of the time interval sweeps. The photocurrent value for the no illumination time interval is almost zero and proves the stability of the system against a dark current value. Few localised dips seen in the curve with nanostructures correspond at exact intervals where spikes are also seen as a result of the bubble. On an average, these current values uniformly recover from the dark cycle. This proves good electronic stability in terms of charge carrier dynamics from the nanostructured material. The stability of the current proves the effectiveness of the photoelectrode in terms of constantly supplying current into the solution.

It also proves that the position of the band energy levels between the semiconductor bands and the electrolyte is independent of the change in illumination condition. If changing illumination introduces material changes in the semiconductor with nanostructure it would change the band alignment and thereby the current values. Accumulation of hydrogen bubbles does not change the band position but in addition to blocking light flow also changes the net impedance seen by the outflowing electrons.

In the last step, we analyse the steady state behavior of the system. This helps in evaluating the time dependent behavior of the improved photocurrent. This measurement is done at a constant voltage of -1.5 V vs RHE which is the onset voltage as seen in 6.19. These measurements are then performed both with and without illumination. Figure 6.21 shows that the measured current remains fairly constant for the silicon sample with the nanostructure. This proves that the nanostructure enhances the bare silicon performance for extended time intervals. Such an extended time interval measurement also provides an overview of dependence of current performance on the accumulation of bubbles. While these bubbles introduce fluctuations in the measured current, the average values and the trend of the curves during each on cycle remain constant. Most of these bubble introduced fluctuations are more pronounced in case of the nanostructures. This is a further confirmation of the increased hydrogen generation with and without such a nanostructured array of titanium dioxide.

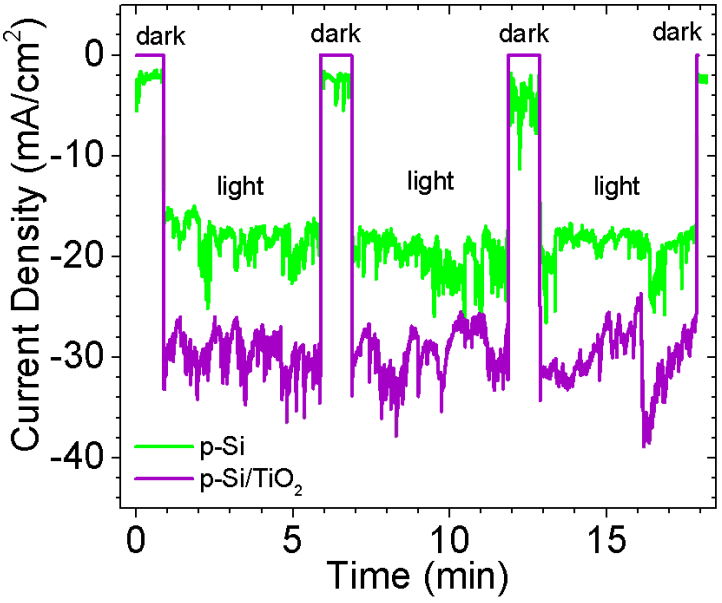

FIGURE 6.21: Time depedance of the photocurrent with (purple curve) and without (light green curve) the fabricated metasurface stack at a constant voltage of -1.5 V

In figure 6.21, it is apparent that for the dark illumination cycle the so-called dark current for the metasurfaced sample is not entirely zero as observed for the bare silicon sample. This difference can be attributed to the oxidation products which get developed on the surface of the contacts as a result of prolonged measurements. This minor dark current is not characteristic to the nanostructured sample but rather to the worn out contacts. It can equally occur at the contacts of both samples, structured and nonstructured. Although the light-limited photocurrent density is ultimately limited by the amount of photons absorbed, photocurrent density can also be limited by poor catalytic activity at a photoelectrode surface. To rule out any unanticipated catalytic influences by the TiO_2 nanofrustums, the photocurrent

density of the bare p-Si and p-Si/TiO_2 nanofrustum photocathodes were compared under different photon fluxes. The different photon flux spectra were obtained by inserting various neutral density filters between the solar simulator and photocathodes. The spectra for each measurment point is shown in figure 6.22.

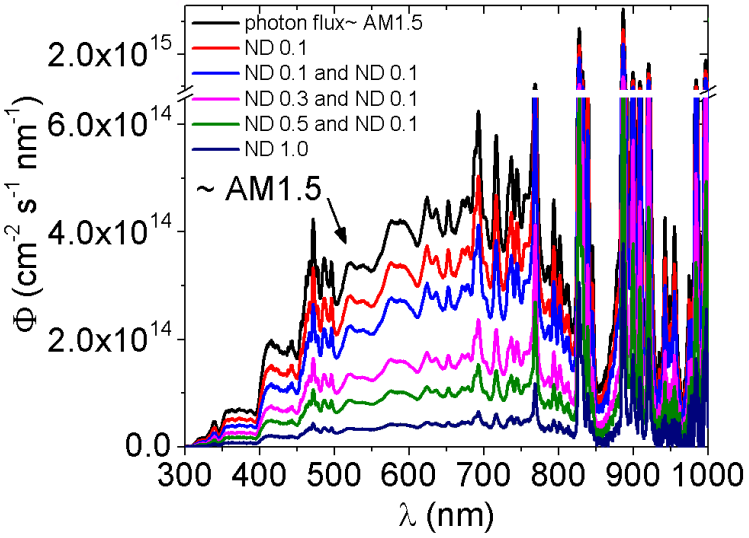

FIGURE 6.22: Photon flux (ϕ) with unit ($cm^{-2}s^{-1}$ nm^{-1}) spectra for the solar simulator under normal operation ($\sim$ AM1.5) and with various neutral density filters (ND) inserted between the solar simulator and photoelectrochemical cell. The graphs describe the corresponding solar spectrum for each case filter combination that attenuates the spectrum. These spectra were used to calculate J_{abs} from equation 6.3

In the absence of catalytic differences, the bare p-Si and p-Si/TiO_2 nanofrustum photocathodes should show photocurrent densities that are similarly proportional with respect to the number of absorbed photons absorbed by the underlying Si. The absorbed photocurrent density (J_{abs}) of the photocathodes were calculated using the reflectance for silicon from the literature and the measured reflectance for the p-Si/TiO_2 nanofrustrum photocathodes as follows

$$J_{abs} = \int_{430nm}^{900nm} e(1-R)(1-e^{-(\alpha)t})\phi d\lambda \tag{6.3}$$

where, e is the elementary charge (1.602×10^{-19}) C, R is the reflectance, α is the absorption coefficient (μm^{-1}), t is thickness of the Si substrates ($\sim$ 381 μm), ϕ is photon flux ($cm^{-2}s^{-1}nm^{-1}$) and λ is the wavelength (nm). The R spectra are shown in figure 6.13. Using the above equation, the absolute value of the light-limited photocurrent density ($|\ J_{ph}\ |$) was plotted as function of J_{abs} for the bare p-Si and p-Si/TiO_2 nanofrustum photocathodes. This is shown in figure 6.23. The points labeled $\sim$ AM1.5 are from measurements with the solar simulator under normal operation. In figure 6.23, the linear trends in $|\ J_{ph}\ |$ vs J_{abs} for bare p-Si and p-Si/TiO_2 nanofrustum photocathodes nearly overlap with identical slopes.

This is strong evidence that the improved photocurrent density after application of the TiO_2 nanofrustum layer is predominantly due to increased light absorption by the underlying p-Si.

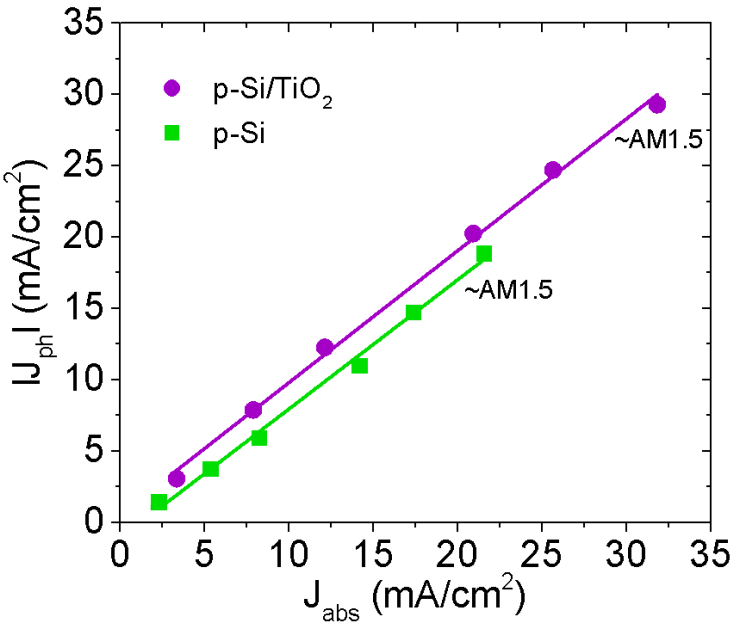

FIGURE 6.23: Measured photocurrent density (| J_{ph} |) for bare p-Si and p-Si/TiO_2 nanofrustrum photocathodes at a constant potential -1.79 V vs . RHE (right hand side electrode) in 1 N H_2SO_4 with 1 mM Triton X-100 vs. the absorbed photocurrent density (J_{abs}). J_{abs} is the calculated photocurrent density for a given wavelength and spectral reflection value as shown in equation in 6.3

The hydrogen evolution reaction involves continous high currents being passed through the semiconductor electrolyte interface across the nanofrustums. Since the nanofrustums are made out of amorphous titanium dioxide, it might result in morphology changes, as a result of the high charge transfer and established potential gradients. In order to investigate this behavior, we compare the morphology of a structure measured for several hours with a pristine sample of the nanofrustum metasurface. The direct comparison of this structure is shown in figure 6.24. The post measurement images indicate areas where the entire nanostructure stack seems to have lost its integrity. This can be attributed to the poor stability of titanium dioxide in a high charge transfer zone owing to its amorphous nature. [39] It is important to note that this change in morphology occurs after obtaining several consistent measurements indicating enhancement in the observed photocurrent. This highlights that the structures do have potential for optically improving photocathode performance but need to be optimised in terms of their long term material stability in electrochemical environments.

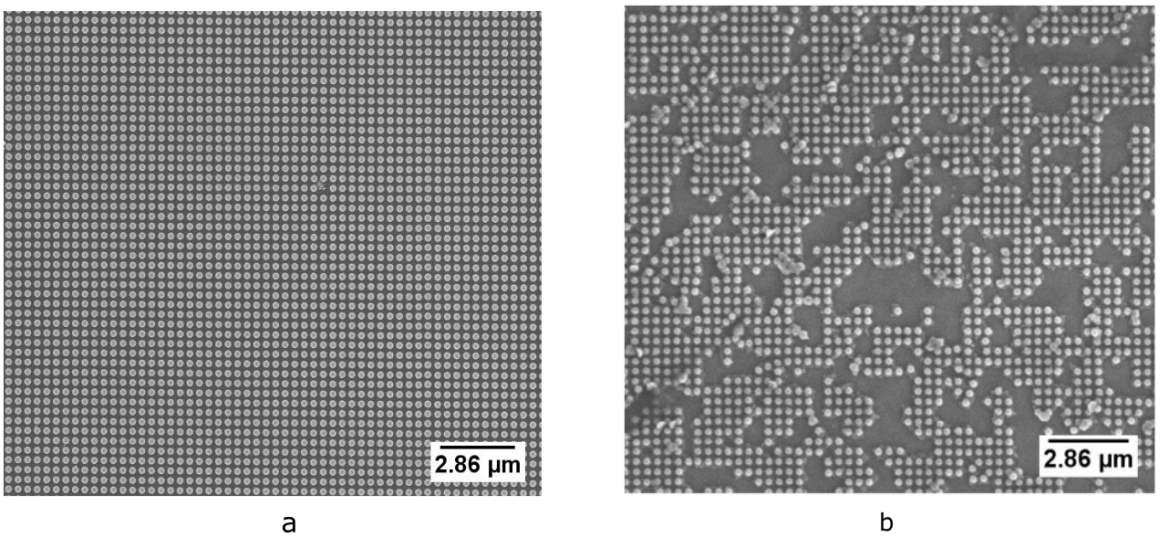

FIGURE 6.24: SEM images of (a) a pristine $p-Si/TiO_2$ nanofrustum photoelectrode and (b) a $p-Si/TiO_2$ nanofrustum photoelectrode that has undergone photoelectrochemical testing for several hours

6.6 Discussions from the comprehensive analysis of metasurfaces

In the design section 6.1, with the aid of computational analysis we have determined the influence of the refractive index gradient across the metasurface. Gradually varying the index gradient across the nanostructure helped in distinguishing inherent optical properties of the complete array. We identified from these investigations conditions which result in degenerate wavelength points where the nanofrustum resonances result in complete transfer of light into silicon. In order to broaden this effect, perturbed the resonance with a very thin titanium dioxide film in order to improve the coupling between silicon and titanium dioxide near the resonant wavelengths. This helped in improving light transfer at long wavelengths to account of the gradual variation of refractive index.

The optical characterisation of this structure reveals good agreement with simulated values for normal and angular incidence. On account of the subwavelength design, most of the reflection is confined to the fundamental order however at oblique angle of incidence, first order diffraction has a significant amplitude and spectral spread, which increases with increase in the incident angle. To quantify this effect we provided simulation results of the total, fundamental and first order reflection. Additionally we also provide the angular spread of these orders to highlight the peculiar diffractive features of the metasurface at incident angles.

We finally establish the optoelectronic benefit of the nanostructures by demonstrating an improvement in the photoelectrochemical current responsible for hydrogen generation.

In conclusion, we derived the parameters of the metasurfaces, discussed their optical operation in terms of pertubed Mie resonances and demonstrated consistent optoelectronic enhancement for optically improving the photocurrent responsible for hydrogen generation.

Chapter 7

Comprehensive Analysis of Spherical Bowls

This chapter focusses on the optical and electrochemical characterisation of the titanium dioxide soupbowl nanostructure. It is fabricated to achieve significant antireflection behavior in silicon wafers as well as to be a potential candidate for large scale fabrication. Large area fabrication is envisioned by the demonstrated implementation of the nanosphere lithography in the adopted process sequence as shown in chapter 4. The obtained nanostructure is systematically characterised with the help of spectral optical measurements. These optical measurements especially focus on the performance of the structure as an anireflection layer for large angles of incidence. A systematic analysis of these measurements is provided by elaborating their physical implications.

Computational analysis of the obtained geometry is also described with the help of 3D electromagentic FEM simulations in order to evaluate the role of the hexagonal periodic lattice towards the antireflection behavior. In order to demonstrate usability of the structure for effectively coupling light into an optoelectronic device without impairing device characterisitics, we characterise the nanostructure for photoelectrochemical performance. For this we show, the comparison between the photoelectrochemical performance of a bare silicon wafer with and without nanostructures. This comparison also includes a thorough statistical analysis of the relative benefit of the structure. Additionally we provide a morphological study of the nanostructure after being used for light coupling in a photoelectrochemical cell.

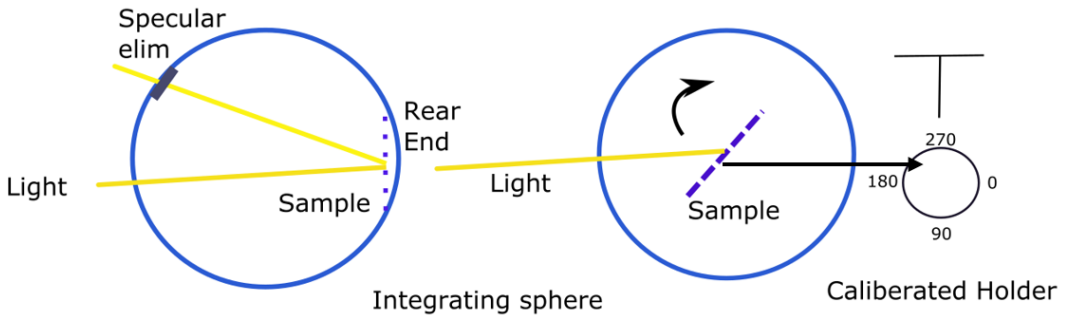

FIGURE 7.1: Schematic of the integrating sphere showing sample measurements first for near perependicular light incidence. The sample is placed at the rear end of the sphere to measure total reflection for perpendicular incidence. (left) The sample is mounted on a rotable calibrated holder at the center of the integrating sphere in order to change the direction of light incidence with the rotation of the holder. (right) A caliberated angular holder is used to rotate the sample to measure total reection under angular light incidence.

7.1 Experimental characterisation of optical spectra

The first step in evaluating the optical performance of the soupbowl structure is to measure the total reflection spectra for different incident angles for both s- and p- polarisations. These spectra are measured by an integrating sphere combined with a spectrometer.

The light collection component from the sample measurements is an integrating sphere. With the help of detectors inside the integrating sphere, this light is processed with a spectrometer to obtain reflection spectra. In order to measure for near normal or higher angles of incidence, the sample is placed at the rear end or the centre of the integrating sphere, respectively. This holder, for the latter measurements has a well calibrated circular angular scale and it enables rotating the sample under a predefined angle. The integrating sphere has a well calibrated specular elimination port to measure the diffuse reflection of a sample for normal incidence. The orientation of the sample during measurements for rear end (normal incidence) and central holder (angular incidence) is shown in figure 7.1.

With the help of an external polariser which alternates between the two polarisations, we systematically measure the total reflection for different angles of incidence. A non-normal angle of incidence breaks the symmetry of the structure which would result in different optical properties for both s- and p- polarised light. Such measurements help in indentifying the underlying effects which give rise to reflection in different directions. The specular reflection accounts for the light reflected in the direction of the fundamental propagation order. Specularly reflected light is purely a function of geometrical dimensions of the structure, i.e. in this case due to coherent nanostructure light interaction.[84] Diffuse reflection, if present in the nanostructure accounts for, higher orders of directional propogation. Other effects

which give rise to high reflection being measured at the diffuse port include aperiodic effects such as scattering as a result of material and surface imperfections across the nanostructure profile. The resulting light interaction due to these effects is incoherent. Such diffuse reflection corresponds to the light which gets reflected from the titanium dioxide-silicon interface into random multiple directions. The total reflection is the net sum of both of these effects. In this section we investigate the spherical soupbowl like structure fabricated with the 600 nm colloidal mask, whose dimensions are shown in table 4.3.

Having introduced the measured quantities of interest, we now describe their measured spectra. We first describe the total, diffuse and specular reflection of the sample for a normal incidence, measured with the aid of an integrating sphere. The sample is placed at the rear end of the integrating sphere such that it is inclined at an 8° angle with respect to the incoming light. This inclination angle is essential in order to prevent the light collected by the sample from escaping out of the sphere. Light is incident on the sample and all the reflected light from the sample is collected by the detectors present inside the integrating sphere. This detector signal is fed to a spectrometer which analyses the spectra for different wavelengths. The obtained spectra are shown in figure 7.2 between 420 - 750 nm. The overall reflection

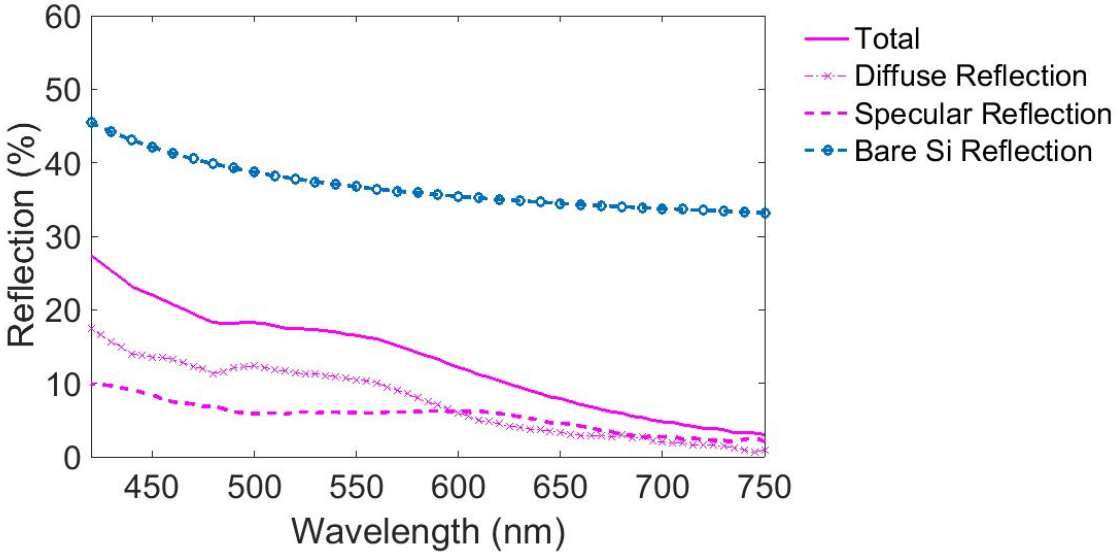

FIGURE 7.2: Measured reflection spectra of the nanostructured soupbowl obtained for an incidence angle of 8° obtained using an integrating sphere. The curves indicate total, specular and diffuse reflection measured in comparison with the bare silicon reflection.The geometrical details of the sample investigated here are as follows : height = 240 nm, $\text{diameter}_{\text{hole}}$ = 480 nm, lattice length = 290 nm.

of the investigated nanostructured sample is substanially lower than the reflection of bare silicon. The reflection peaks at the short wavelengths, decreases thereafter to a constant value of 15 percent at 500 nm. In the long wavelengths, the reflection drastically drops over

the wavelength range to as low as 5 percent. The overall reflection drops from 30 percent to 5 percent across the entire wavelength range.

This indicates that the structure operates like an effective medium in the presence of an index gradient between air, titanium dioxide and silicon. Other effects influencing this spectra consist of aperiodic sample defects and varying thicknesses obtained out of material growth. In the next step, we measure the diffuse reflection. This reflection is measured by eliminating the specular reflection by opening the window present in the integration sphere in the direction of the specular component. The spectral trend seen in the diffuse reflection contributes substanially to the spectral trend of the total reflection. The diffuse reflection is only lower than the total reflection with exactly the same trend.[69] The difference between the total reflection and diffuse reflection forms the specular reflection. The spectral trend of the specular reflection in up to a wavelength of a 500 nm closely resembles the observed trend in reflection of the total reflection. Beyond 500 nm, the reflection remains constant up to 650 nm and then decreases with wavelength. Between 500-650 nm, the specular reflection has a characteristic spectra quite different from the total and diffuse reflection spectra. In the long wavelength range, the specular reflection is very low, as the structures can be approximated to an effective medium. The goal of these optical measurements and subsequent analysis is to seek for characteristic optical behavior of the soupbowls which can be mapped to their antireflection function. Measurements at perpendicular incidence thus do not reveal presence of optical behavior typical to nanostructures. To seek further insight into the optical behavior, we perform total reflection measurements for different angles of incidence with the aid of an integrating sphere. Figure 7.3 show these spectra for p- and s-polarised light.

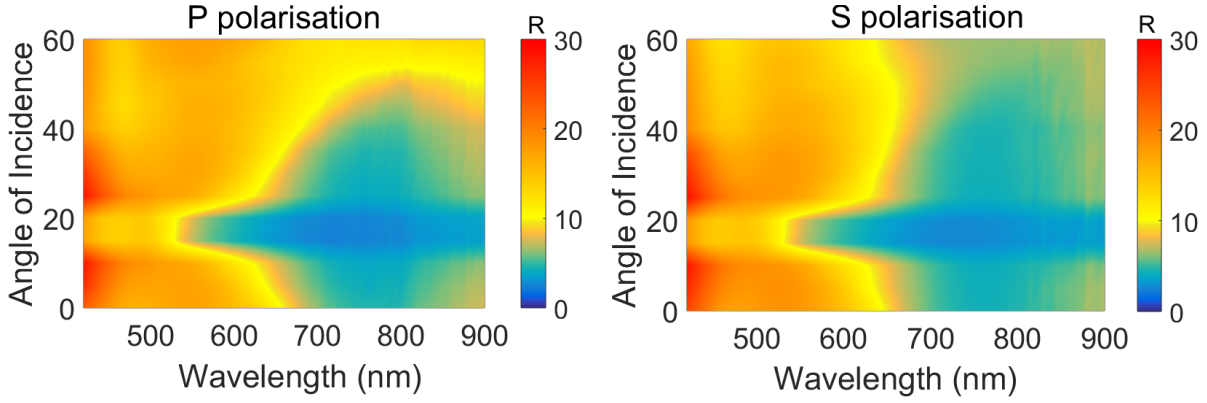

FIGURE 7.3: Total reflection of the soupbowl structure measured for angular incidence for p- and s- polarised light performed using an integrating sphere. The geometrical details of the sample investigated here are as follows : height = 240 nm, $\text{diameter}_{\text{hole}}$ = 480 nm, lattice length = 290 nm.

For p- polarised light, at wavelengths of 420-550 nm and angles of incidence (aoi) $0 - 20°$, the total reflection is significantly high. At these angles, the index constrast is maximum between the material interface of air and silicon as light is incident. A high index constrast naturally results in increased reflection. However this is still significantly lower than that of a bare silicon wafer as a result of the characteristic shape of the nanostructure. This wavelength and angular band is not the most dominant band of strong anti-reflection as a result of the nanostructure. It is also of importance to state the fact that across $15° - 20°$ light incidence, the reflection decreases. It again peaks between 20° and 40°. This alternating increase in reflection as a function of the incident angle across a peculiar wavelength range resembles resembles the angular variation in reflection spectra often observed for a periodic hexagonal lattice. The exact correlation needs to be confirmed by rigorous simulations. Between incident angles $(40 - 60°)$, the incident light tends to follow the gradual spherical contour of the nanostructure resulting in a predominant reduction in reflection.

In the wavelength range from 500-650 nm, for angles of incidence up to 15°, the reflection is moderately high but no pronounced regions with high intensities are present. For the angle of incidence between 15° to 25° the reflection is remarkably low. Such a characteristic drop in reflection in a given wavelength range indicates functionalities of an optical lattice. Reflection largely remains constant between $25° - 60°$ around $10 - 15$ percent which is a drastic reduction in silicon reflection. In the long wavelength range from 650-900 nm, the structure dimensions are small as compared to the incident light wavelength. This results in the suppression of reflection for most of the angles of incidence upto 55°. At higher angles of incidence, moderate reflection bands are observed.

The total reflection for s- polarised light more or less follows identical properties to that of p-polarised light up to the wavelength of 650 nm for angles of incidence up to 25°. For angles up to 60°, the reflection value is around $10 - 15$ percent till 650 nm. A peculiar horizontal widening in the reflection band is observed which is quite different from the observed reflection spectra for p polarisation. For the long wavelengths between $650 - 900$ nm, the reflection is low for all angles of incidence right up to 25° which is different from the values obtained for p- polarised light. The structure shows significant polarisation symmetry for the total reflection for all angles of incidence till 650 nm. Bands of moderate reflection are observed for high angles of incidence at long wavelengths only for p- polarised and not for s- polarised light. The polarisation symmetry observed in reflection for the two layer structure can be deduced to be an effect of the circular contour present in the nanostructure.

We have described that the integrating sphere measures the diffuse reflection for close to normal incidence by eliminating the specular component. It is not possible to measure diffuse

reflection for different angles of incidence because it has only one fixed position opening to eliminate specular light. It is therefore not possible to measure solely measure diffuse reflection as a function of the incident angles.

In order to get a more detailed overview of the implications of the measured angular reflection, we measure the specular reflection with an automated reflection analyser. The reflection obtained via this measurement is limited only to the specular reflection for each angle of incidence. The measurement setup is shown in 7.4. It consists of a spherical chamber.

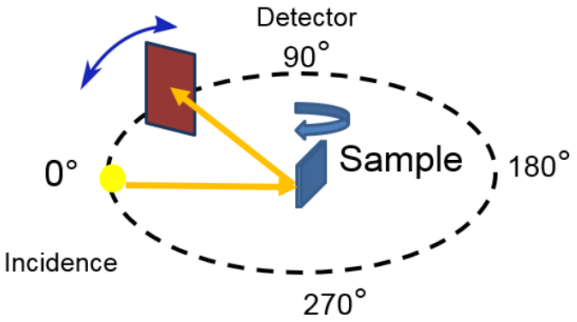

FIGURE 7.4: Setup to measure specular reflectance as a function of incident angle.The geometrical details of the sample investigated here are as follows : height = 240 nm, $\text{diameter}_{\text{hole}}$ = 480 nm, lattice length = 290 nm.

The detector moves along the circumference of the spherical chamber in order to capture light at various angular positions. The angular span of reflection measurements therefore starts from 6°. The direction of the incoming light remains constant along the diameter of the spherical chamber. The sample is placed on a goniometer stage which rotates to change the angle of incidence. For a given angle of incidence, the detector moves to a position which corresponds to the direction of the specular reflection for the set sample goniometer angle. This results in an angular light incidence on the sample. The measurements are performed for both s- and p- polarised light. Figure 7.5 shows the reflection spectra for p- and s- polarised light.

For p- polarised light, in the short wavelength range, up to 450 nm, we observe localised reflection maximas for angles up to 20°. These reflection bands are a direct function of the nanostructure geometry. Since they are observed in the specular reflection spectra, they correspond to the fundamental order diffraction. Between 20 to 50° angles of incidence, the specular reflection is absent. For larger angles of incidence, specular reflection increases again. For s- polarised light, the specular reflection maximas occur at small angles of incidence. These bands are a direct function of the nanostructuring which result in light being reflected in the fundamental order. They are not observed for large angles of incidence for any of the wavelengths. This is further proof of the fact that at these wavelengths, the structure acts

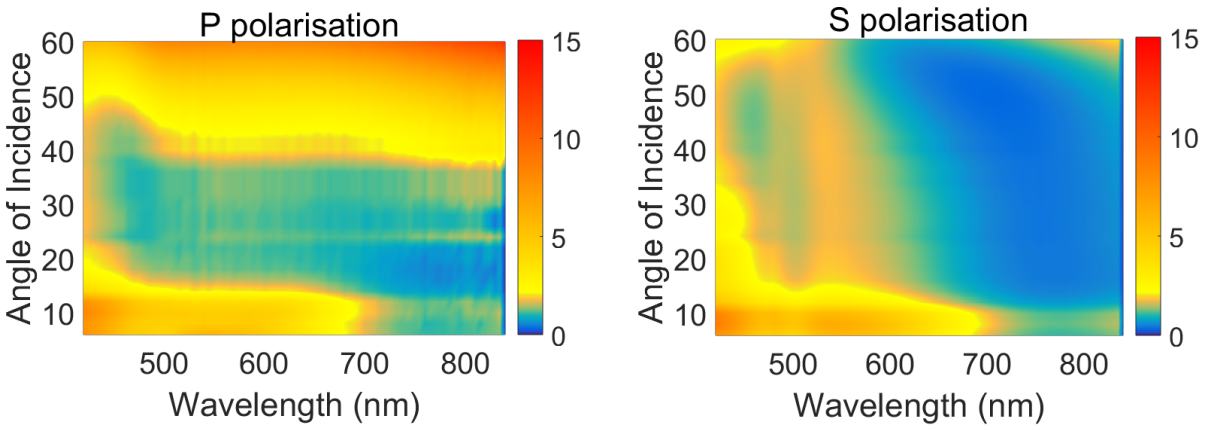

FIGURE 7.5: Specular reflection measured for angular incidence for p- and s- polarised light.The geometrical details of the sample investigated here are as follows : height = 240 nm, $\text{diameter}_{\text{hole}}$ = 480 nm, lattice length = 290 nm.

as an effective medium. Now for a simple bilayer system consisting of a dielectric thin film on silicon, for p- polarised light, reflection decreases with increasing the angle of incidence according to Fresnel theory. This trend is also observed here. After comparing these specular reflection maps to that of the total reflection, we observe that most of the bright bands seen in the total reflection are not related to the specular reflection. Most of these reflection bands are a function of the diffuse reflection. It highlights the fact that the process sequence results in structures which have a very low specular reflection even for higher angles of incidence. The diffuse reflection is significant. The source of diffuse reflection can be attributed to the material quality of the sputtered material including varying thickness, as well as the line defects present in the pattern. A part of this reflection may also be due to the non fundamental diffraction orders. The presence of these higher diffraction orders needs to be confirmed by numerical simulations. Line defects result in relatively high amount of titanium dioxide being deposited between the the patterened areas. However the sum of these two components which results in the total reflection is substanially lower than the total reflection of silicon. This makes the process reliable and highly simple to fabricate nanostructures which sustain anti-reflective behavior for even higher angles of incidence.

7.2 Simulations for a TiO_2 soupbowl like structure and comparison with experimental spectra

The goal of this section is to simulate the optical spectral performance of the system as a function of geometry. The geometrical details of the soupbowl structure of interest are as follows - height = 240 nm, $\text{hole}_{\text{diameter}} = 480$nm, lattice length = 290 nm. To describe the effect of the lattice length, on the hexagonal lattice of spherical holes, we maintain the hole parameters constant and use the lattice length corresponding to one generated a colloidal mask size of 900 nm. This investigation is of particular importance at off normal incidence. At off normal incidence, the propagation vector of the incident light consists of additional components in the direction of the lattice periodicity. These components give rise to the reflected and transmitted diffracted modes. A good anti-reflection structure should control the reflected diffracted modes even at higher angles of incidence.[22] These modes are primarly a function of the pitch of the lattice.[19] The other factors such as hole geometry and thickness also play a role but the contribution of these factors is largely limited to controlling optical interferences for a given pitch.

The idea of this exercise is to identify the exact correlation between the reflection spectra and the mask size. A representative model of the obtained structure is a hexagonal lattice of spherical soupbowls. The radius of the colloidal mask determines the unit cell length of the hexagonal model. This is set up with the help of a hexagonal unit cell with periodic boundaries in all six directions of the hexagon. The model consists of a layer of air, nanostructured titanium dioxide and silicon. Perfectly matched boundary conditions are set at the top and bottom of the structure. The source input to the simulation is a plane wave. Tetrahedral meshes are dened across the volume of the three computational layers. The simulation cell for the two cases is shown in figure 7.6. The titanium dioxide optical material constants which go into the model as simulation inputs are obtained via ellipsometeric modelling from planar layer stacks. The geometrical dimensions of the spherical hole such as the nanostructure thickness and the diameter of the spherical opening are obtained with the help of electron microscope images and focussed ion beam cross sections shown in figure 4.12. We perform two simulations in accordance with the dimensions obtained and establish a simulation trend between the contributing geometric parameters and the specular reflection of the pitch of the unit cell. The angle of incidence is set to 20° to derive differences in light coupling for the two geometries. By comparing pitches corresponding to the two mask sizes, we can determine which is the most beneficial. Numerical simulations of a periodic lattice give values of all reflection components pertaining to the nanostructured material.[14] These consist of the fundamental order of propagation and if present in the structure also higher orders. The reflection is evaluated with the help of electromagentic field energy flux integrals

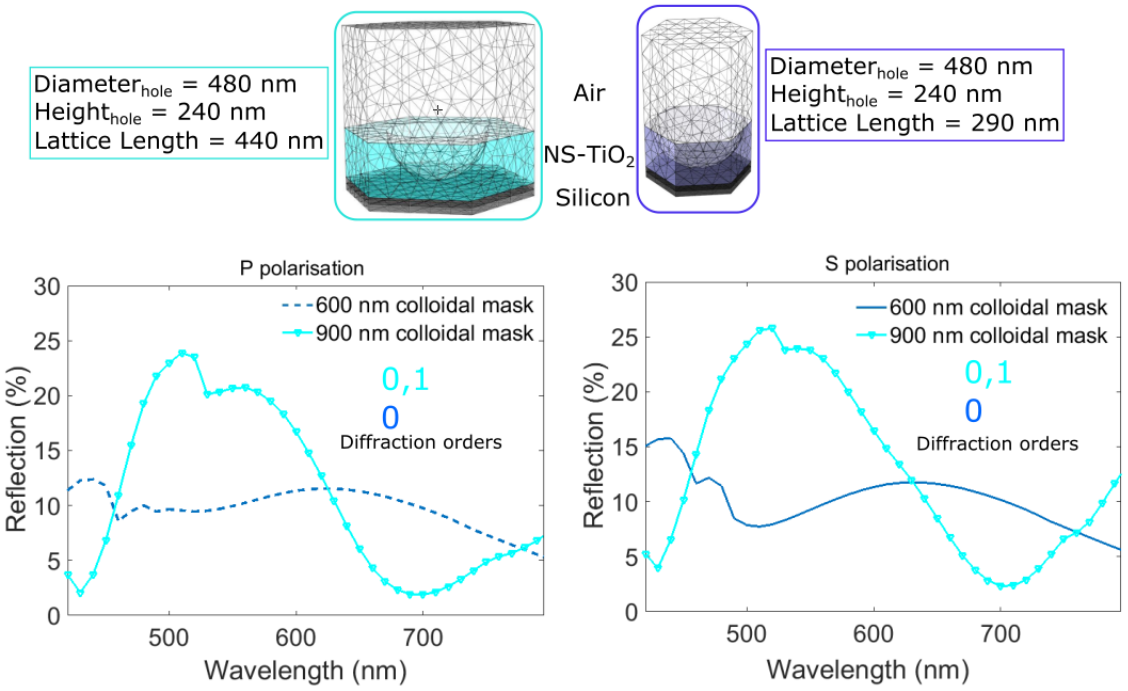

FIGURE 7.6: Simulation overview showing the effect of unit cell constant and indicating spectral tendencies of the simulated refletion for dimensions corresponding to the two colloidal masks under an incident angle of 20°. The lattice length in each case is calculated from the diagonal length of the unit cell. This length is calculated from the SEM top view as shown in figure 4.14. For both cases, we simulate the toal reflection and indicate that for the colloidal mask of 900 nm, the 0th and 1st order diffraction order is present in contrast for the colloidal mask of 600 nm where the reflection is confined to the fundamental reflection order

of the incident field on the plane of incidence. This flux integral is calculated on the plane of the input source port. Normalising this flux integral to the input power, the characteristic air impedance as well as the port area gives the reflection of the system. From these calculations, we systematically show the number of reflected diffracted modes present in each case.[14] We also compare the total reflection values of both structures and provide a short overview. Figure 7.6 shows the simulation unit cells with their respective dimensions. We also see for s- and p- polarised light the magnitudes of reflection for both unit cells. In the insets we also provide information about the calculated values of the diffraction orders for both unit cells. For the 900 nm colloidal mask with higher lattice length (440 nm), we calculate the existance of the fundamental and first order reflected diffracted order. The presence of this extra order contributes to increased reflection in the short wavelength ranges.

For the 600 nm colloidal mask (lattice length = 290 nm) with a proportionately lower pitch, the calculation reveals only the presence of the fundamental diffraction order. This explains why the reflection is much lower in the short wavelength ranges. In the long wavelength range, interferences due to the refractive index gradients at different material interfaces play

a stronger influence. These interferences are governed by the spherical profile of the structure. For the larger pitch, this profile is more gradual. A gradual profile leads to slow variation of refractive index which helps in supressing reflection. This explains why at long wavelengths, reflection is reduced for the higher lattice length. In case of the smaller mask this effect is not as pronounced at long wavelengths due to the less gradual nature of the spherical profile. The effect of this gradual effect of the spherical profile aids in predominant reflection supression in the long wavelength (650 -900 nm) range. In the rest of the visible wavelength range, the reflection is significantly higher than the smaller lattice length. Overall, the 600 nm colloidal mask proves to be effective in supressing reflection in a strong broadband effect. This establishes the importance of using the 600 nm colloidal mask.

In the next step, we compare experimental and simulated reflection of the experimentally optimised sample shown in figure 4.12. A high contribution of the diffuse reflection was identified in the total reflection of the structure. It is therefore challenging to verify the measured total reflection with the help of a periodic lattice in numerical electromagnetic simulations. The goal of these simulations is to compare the simulated spectra with the measured specular reflection. Such a comparison is essential to obtain a qualitative and quantitative relation between the spectral properties of the obtained structure and a regular periodic hexagonal lattice with the same dimensions. The measured specular reflection is obtained by subtracting the diffuse reflection from the total reflection. This diffuse reflection is measured by eliminating the specular light resulting in a small amount of the diffuse light being eliminated too and results in a systematic error in the measurement. The calculation bandwidth is set between 420 and 900 nm. An input angle of 8° is set in order to model the light incidence as seen in the experiment.

In order to verify the numerical calculation, we check the sum of all flux integrals over the ports and the total absorption for convergence to unity. The obtained simulation results satisfy this condition across the calculation bandwidth. The propagating Fourier coefficients as explained in section 2.4 reveal the sole existence of the fundamental order of propagation. This is obtained by calculating the diffraction orders as defined by the reciprocal grid vectors of the hexagonal unit cell.[61] The nanostructures therefore function as subwavelength structures which supress reflection by limiting it only to the zeroth order of propagation. Figure 7.7 shows the simulated spectrum of the structure for s- and p- polarised light, overlaid with the corresponding experimental counterparts. For the simulated spectra for both polarisations, we observe in the short wavelengths, between $400 - 550$ nm, distinct reflection features, where the reflection peaks first and then remains constant.

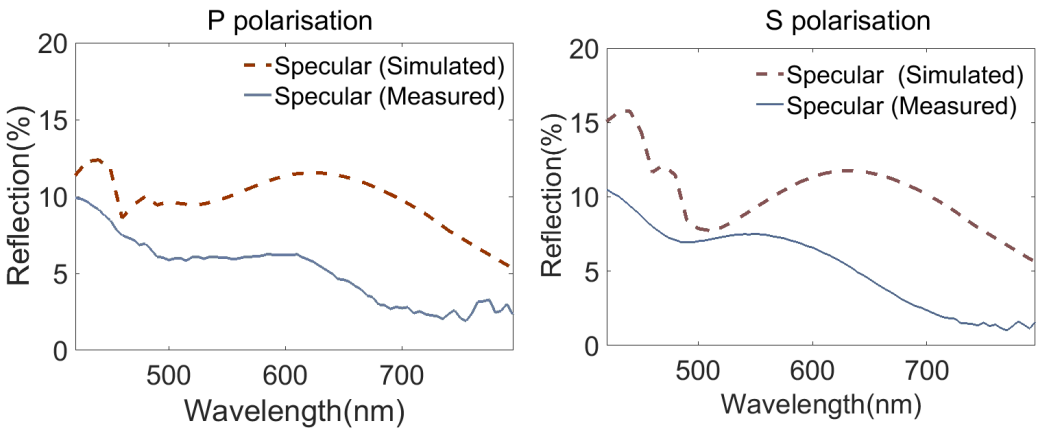

FIGURE 7.7: Simulated and experimental specular reflection spectra for an incident angle of 8°

The reflection drops down to a value of 10 percent and remains more or less constant between $470-570$ nm. This is an indication of the strong light interaction with the geometry of the structure for the given bandwidth. These characteristics are often seen in the case of regular periodic arrangements of nanostructures having dimensions in the same order of the light wavelength. In this case, the mode propagation order is decided by the periodicity of the nanostructure, i.e the size of the unit cell. The intensity of this order is influenced by the interferences which arise due to the stack of structured titanium dioxide on silicon. A controlling factor for these interferences is the spherical profile of the soupbowls. The spherical profile is a function of the spherical hole radius and the overall thickness of the titanium dioxide nanostructure. These interferences are also governed by the thickness of the nanostructure and play a decisive role in determining the reflection spectra.[1] Here, between $480-560$ nm, the reflection is more or less constant which corresponds to the presence of a narrow reflection supression band owing to the fundamental order of light propagation. In the long wavelength range, the reflection continously reduces with increasing wavelengths. In the long wavelength ranges, therefore the structures act as an effective medium owing to the increased size difference between the structure dimension and wavelength. The specular reflection therefore is supressed to as low as 2 percent amounting to significant reduction in comparison with the ease with which the structure is fabricated. In hindsight, such an operative optical feature can be considered to be analogous to the moth eye structures based on graded index nanostructures as described in chapter 2. We thereby demonstrate that such spherical soupbowls also are an effective way of being able to demonstrate a moth eye like effect adding another potential for design.

We compare in the next step, the simulated spectra for p- polarised light to the corresponding measured specular reflection. In the short wavelength range, the measured and simulated

reflection show a decreasing trend from 10 and 12 percent respectively. These reflection spectra then monotonously decreases till 500 nm. The measured spectra decreases monotonously at a lower rate as compared to simulated spectra. In the wavelength range between 450 - 560 nm, both the measured and the simulated spectra show a more or less flat reflection curve. The magnitude of the simulated spectra is on an average 3.5 percent higher than the measured spectra. In the long wavelength range around 610 - 620 nm, the simulated and measured spectra respectively both show a gradual decrease in reflection. The overall magnitude of the simulated curve is on anzgf average 5 percent higher than that of the measured curve. This proves in principle that the nanostructure derieves its optical properties from a hexagonal lattice of spherical voids. The absence of the peaks in the measured spectra are a result of the fact that the simulation takes into account an ideal perfectly ordered hexagonal lattice.

For s- polarised light, the overall trend in the simulated curve is the same as the simulated p- polarised light except in the short wavelengths where we observe two pronounced peaks. These peaks can be attributed to the interaction of the s- polarised light with the nanostructure which is different from p-polarised light. The overall magnitude of the reflection in this case is slightly higher than that of the p- polarised light, especially in the short wavelengths. This can be accounted by the fact that, the field in this case is perpendicular to the plane of propagation and the spherical profile of the structure. However it is parallel to the titanium dioxide silicon interface, therefore the spherical profile of the structure influences the optical interferences at the material interface. In the long wavelength range, both simulated and measured spectra monotonously decrease in a similar qualitative fashion.

In the actual sample, patterned via nanosphere lithography, several domains lay the framework of the hexagonal pattern and come together to form a closed pack structure. The lattice directionality in the actual structure therefore is not exactly aligned with the directions of the hexagonal periodicity. This plays a big role in influencing light propagation properties which are dependent on the directions of hexagonal symmetry. These directions are referred to in theory as Γ_M and Γ_K which relate to the two dimensional symmetry of the hexagonal structure in terms of incident light.[19] These directions are 30° apart from each other. In an ideal hexagonal lattice, these axis of symmetry are responsible for characteristic spectral response for s- and p- polarised light. In in an ideal lattice, rotating the sample by 30° therefore results in a different spectral response for the same polarisation under angular incidence. Another way of exploiting this symmetry is to change the direction of the azimuthal angle of the incident propagation light vector such that it lies along one or the other symmetry line. As shown in figure 7.8, since the periodicity of the given soupbowl structure is formed out of the combination of lattices in different directions, therefore no such symmetry directions

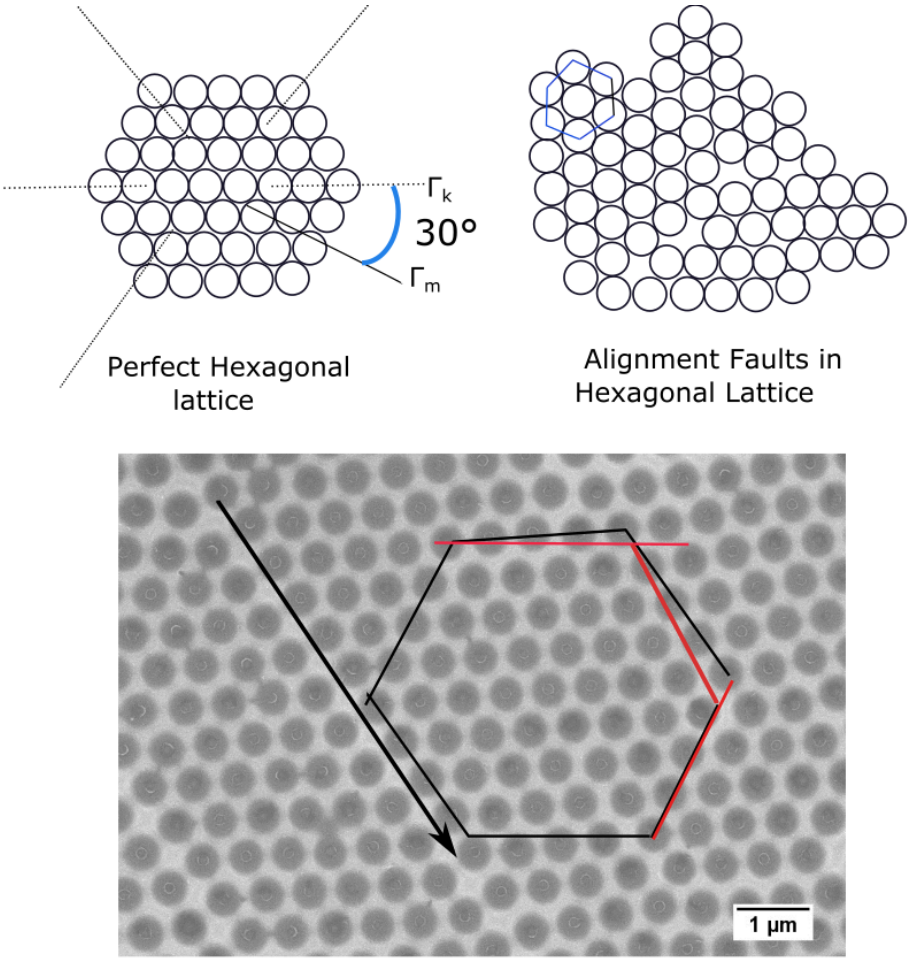

FIGURE 7.8: Comparison of an ideal hexagonal lattice with the one with alignment faults as observed in the fabricated sample shown in chapter 4. The geometrical details of the sample investigated here are as follows : height = 240 nm, $\text{diameter}_{\text{hole}}$ = 480 nm, lattice length = 290 nm. The SEM image of the actual sample shows an example of the lattice misalignment indicating line defects as well as tilts (displacement between red and black lines) from a perfect hexagonal lattice

exist. These differently oriented domains result in the disturbing the perfect symmetry of the periodic lattice. This can be identified as a contributing factor to the difference between experimental and simulated reflection spectra. Furthermore, rotating such a sample does not indicate any change in spectral properties.

Additionally, the simulation assumes a perfectly smooth material texture which overapproximates the reflection contribution of the nanostructure. Experimentally we measure a high diffuse reflection which confirms the presence of scattering due to aperiodic contributions. This also stems from the height fluctuations seen in figure 4.13. Since in the simulation we only find the existence of the fundamental diffracted order, it is safe to conclude that the experimentally measured diffuse reflection is a result of aperiodic scattering features and material roughness.

The morphological cross section images also indicate occasional aperiodic dents and sharpness in an aperiodic fashion which results in deviations from the behavior of a perfect periodic lattice. The average magnitude of the measured diffuse spectra in the wavelength range is 6.5 percent. The average difference between the measured and reflected spectra across the bandwidth is 5 percent. This reasonably explains the difference between the magnitudes of the measured and simulated spectra. Another defect is the tilt of the lattice direction and the effective deviation from the hexagonal lattice structure. This is evident from figure 7.8, following any given line of spherical holes, tracing a hexagon doesnt't yield the full symmetry of an ideal hexagon with lattice angles 120°. The misalignments from the directionality of a regular hexagonal lattice, explains why some small peaks are observed in the simulated spectra but not in the measured spectra. The important point to note is the fact that despite the alignment issues in the lattice and barring a few small peaks, the overall trend of the simulated reflection is similar to that of the measured specular reflection for p- polarised light and for an incident angle of 8°.

These misalignments do not play a significant role for close to normal incidence owing to the overall symmetry of the hexagonal structure with respect to the incoming light. However at higher angles of incidence, depending upon polarisation, the azimuthal angle value is determined by the symmetry direction. The absence of a unique symmetry direction results in uncertainty in the azimuthal angle. At a near normal incident angle of 8° itself, we observe localised peaks in the simulated spectra as a result of the hexagonal lattice modes. These are absent in the measured spectra. It therefore is exponentially challenging to get a fair comparison of the angle dependent incident properties of the fabricated structure with a hexagonal lattice simulation.

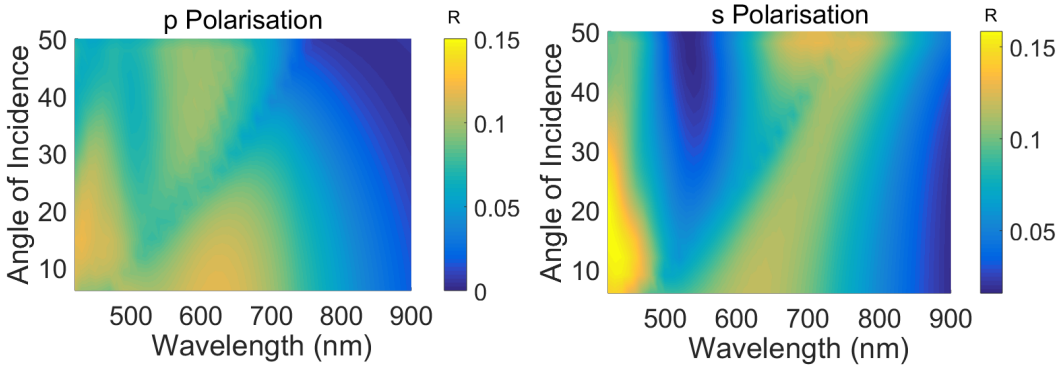

FIGURE 7.9: Simulated reflection spectra as a function of the incident angle of an ideal hexagonal lattice with same dimensions of the experimentally fabricated sample. The geometrical details of the sample investigated here are as follows : height = 240 nm, $\text{diameter}_{\text{hole}}$ = 480 nm, lattice length = 290 nm.

Barring the presence of diffuse reflection resulting from fabrication limits, the structure geometry does bring down the high reflection value of silicon to substanially low values by confining light to the fundamental order of propagation. In figure 7.9, we therefore show the simulated representative spectra of an ideal hexagonal lattice with the same dimensions of the soupbowl structure to highlight the fact that the soupbowl lattice geometry is capable of restricting simulation to substanially low values even for higher angles of incidence. The fabrication sequence needs to be optimised systematically in a way to obtain smooth nanotextures such that the diffuse aperiodic reflection is supressed to low values. The model of the hexagonal lattice can then be elaborately used for optimising the structure for even increased reflection supression at higher angles of incidence. These optimised values obtained out of such simulations can be used as target ranges for the fabrication process.

7.3 Evaluation of photoelectrochemical properties of the TiO_2 soupbowl nanostructure on silicon

In this section, we evaluate the optoelectronic functionality of the titanium dioxide soupbowl nanostructure on silicon. We demonstrate this by forming a pn- junction between the titanium dioxide nanostrutures on silicon and a hydrogen rich aqueous electrolyte.[108] This is done in a photoelectrochemical cell, whose functioning is described in section 2.3. The idea here as described in the case of the nanofrustum metasurfaces is to demonstrate an enhancement in the current voltage characteristics of the pn- junction upon light incidence. The proposal here is to exploit the antireflective properties of the titanium dioxide nanostructure on a large scale such that maximum light is transferred into silicon. The important check for optoelectronic functionality is the extent to which the structures allow charge transfer between silicon and titanium dioxide. An important point to check in this direction is the stability of the titanium dioxide nanostructure after long term measurements. The two layer stack consisting of the nanostructure and silicon forms the active working photoelectrode, i.e. in this case is the photocathode. Owing to the large size of the patterned area we use a teflon cell without using the previously described sealed tubes. The actual experimental setup of such a system is shown in figure 7.10. The working electrode is placed in the spherical hole. The platinum (Pt) wire seen in the cell is the counter - electrode. The reference electrode (REF) of such a cell is the standard (silver-silver chloride in saturated KCl) electrode. All voltages are measured against this reference electrode and indicated in conventional formulation as "x V vs RHE (reversible hydrogen electrode)". Light is incident on the system through the nanostructure and guided into silicon. Since more light is incident into silicon, it facilitates, increased photogeneration of electron hole pairs. The photogenerated electrons need to travel into the solution across the nanostructure to allow for reduction of the H^+ ions from the electrolyte. This reduction of the H^+ ions results in generation of

hydrogen gas which appears as bubbles on the surface of the photoelectrode. In order to

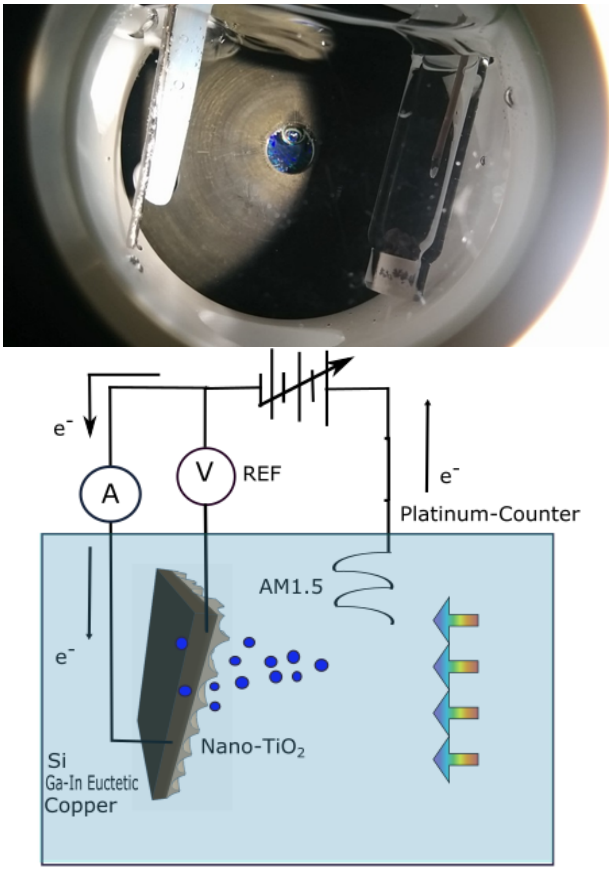

FIGURE 7.10: Photograph of the photoelectrochemical demonstrator cell along with the schematic showing charge transfer under illumination. All voltages are measured with reference to the reference electrode which serves at the reversible hydrogen electrode.

fully quantify the performance of this pn- junction on account of the antireflective properties of the nanostructure, we provide a systematic overview on the current voltage curves of the system obtained for different light illumination conditions. We also evaluate the long term stability, with the aid of measurements carried out with a constant applied potential in presence of a chopped illumination cycle. These measurements quantify the photogeneration of electron-hole pairs within the semiconductor and the charge transfer process between the semiconductor and electrolyte in accordance with the photoelectrochemical behavior.[72] In order to arrive at a significant measure of confidence on the obtained trend, we perform the measurement three times with the nanostructure and demonstrate the J-V characteristics for the obtained structures.

The normal trend of a forward bias pn- junction in presence of a light source, results in increased negative current for an increase in negative voltage. The oneset potential for bare p-silicon is -0.5 V vs RHE but for p-silicon with the soupbowls is -1 V. This offset in the onset potenial can be attributed to the charge transfer dynamics between silicon and the solution

via the nanostructures. After a certain voltage, the current reaches a maximum value and remains constant within a range of fluctuation. The voltage at which the current remains more or less constant is an important quantity to characterise the junction. We sweep the negative voltage between 0 to -2 V vs RHE and record the current for the each voltage under constant illumination exactly according to the solar spectrum. We first measure the characteristics of a bare silicon wafer and indicate those in figure 7.11. Such a measurement is called linear voltage sweep under constant illumination. We observe that the onset potential

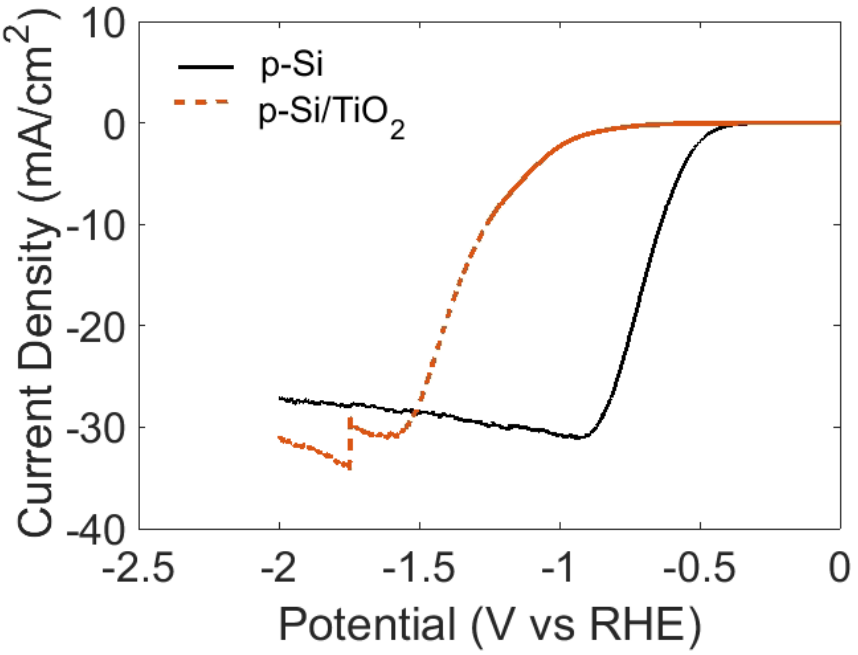

FIGURE 7.11: J-V characteristics of the photoelectrochemical demonstration with and without nanostructures on silicon. The geometrical details of the sample investigated here are as follows : height = 240 nm, $\text{diameter}_{\text{hole}}$ = 480 nm, lattice length = 290 nm.

for silicon is exactly -0.5 V vs RHE. The silicon current at the onset potential is 30 mA. These values are a function of the intrinsic material properties of the p-type silicon used. These are enlisted in table 7.1. With increasing negative voltage, the current decreases by

PO Lot Number 4081587							
Diameter	Material	Material type	Dopant	Orientation	Grade	Thickness (μm)	Resistivity (Ω-cm)
100 mm	CZ Silicon	P	B	<1-0-0>	Test	525±125 μm	1-5

TABLE 7.1: Specifications of the silicon information from the provider Silicon Materials

a slight fraction. The maximum current value is within the limits of the theoritical model of silicon taking into account the equation for photocurrent considering silicon conductivity, bandgap and the maximum reflectivity and internal power conversion efficiency. In the next step, we measure three samples of identically processed nanostructures. As shown in figure

7.11, the curves, show an onset potential of -1 V. The more negative onset potential of the p-Si/TiO2 sample would be an indication that the p-Si/TiO2 sample has a slower charge transfer rate to the electrolyte.

The photogenerated hole pairs travel into the silicon substrate, thereby into the current measuring device and the electrons into the solution. These electrons enable the reduction of hydrogen ions to hydrogen. These bubbles are seen in the setup of figure 7.10. Careful observation of the system during measurements reveals that these generated hydrogen bubbles have increased surface affinity towards the titanium dioxide nanostructure. This phenomenon can be seen as a jump in the J-V curve. The light coupling due to the nanostructure results in an increased photocurrent value as compared to bare silicon. This in turn results in more hydrogen generation. The maximum current in case of silicon with the nanostructure stack is observed in the voltage range between -1.7 to -2 V vs RHE. The average maximum current value obtained out of three samples is -33.9 mA/cm^2. The average value of the silicon is -27 mA/cm^2. This effectively amounts to a relative increase of 22 percent in the photocurrent in the maximum voltage range. Such an increase demonstrates good charge carrier dynamics despite of the traditionally established poor charge transfer ability of amorphous titanium dioxide. [100]

A supplementary measurement to such a current voltage measurement under constant illumination is to change the illumination conditions in a periodic fashion. This is done by exposing the sample with light illumination for a defined time interval of two seconds and chopping off the illumination for the following two seconds. The current voltage characteristics are continously measured during this entire cycle. Such a measurement is often referred to as linear voltage sweep under chopped illumination. In figure 7.12, the J-V characteristics under periodically chopped illumination is shown for silicon with and without nanostructures. We observe a similar trend in the onset voltages of the nanostructures as well as in the voltage region where the nanostructures show a higher photocurrent as compared to the bare silicon wafer. It appears in this case, that the silicon photocurrent is of the same magnitude of the nanostructures. Chemical phenomena which instantaneously occurs when the illumination source is cut off from the pn- junction is responsible for such anamalous behavior. Chemical stability of the silicon with the nanostructures at the electrochemical interface under dark illumination therefore plays an important role for proper migration of charge carriers across the electrochemical interface.[26] A reduced photocurrent after dark exposure could be attributed to several electrochemical phenomenona, which are beyond the scope of this thesis. This investigation reveals minor chemical stability issues of the system under dark illumination. Nonetheless the system functions reasonably well as evident by the revival in the photocurrent value as observed in figure 7.12 once the illumination is

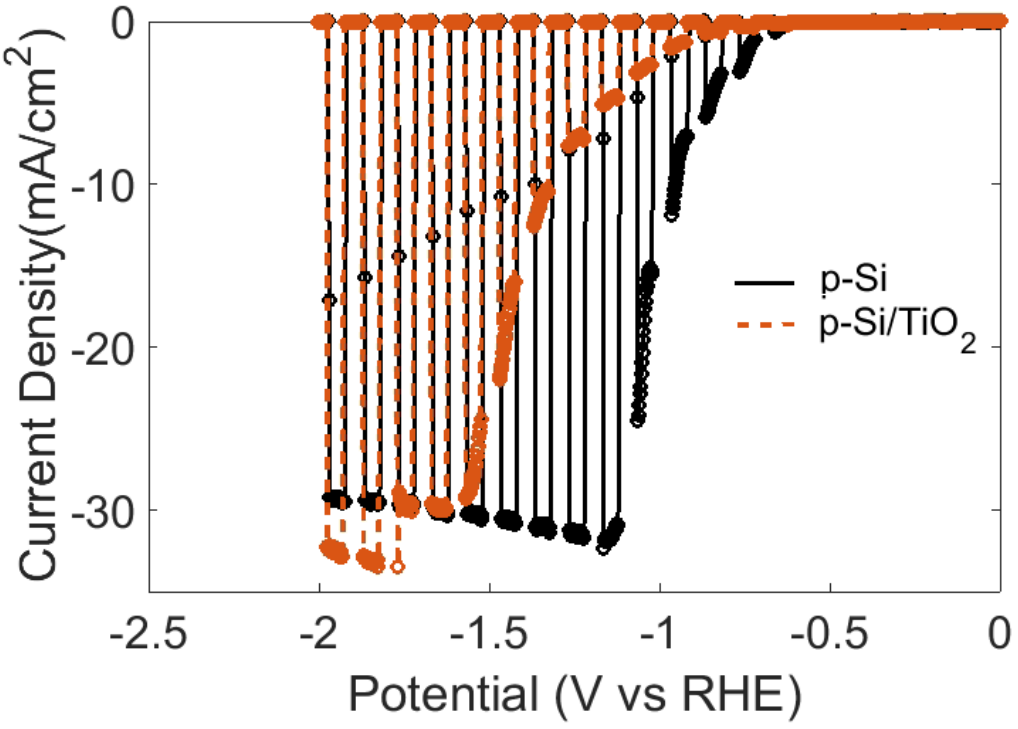

FIGURE 7.12: J-V characteristics with and without nanostructures on silicon with periodically chopped illumination. The geometrical details of the sample investigated here are as follows : height = 240 nm, diameter$_{\text{hole}}$ = 480 nm, lattice length = 290 nm.

restored back. The last check is demonstrating the stability of this increased photocurrent over extended periods of time. This is done via a so called potentiostatic measurement. The applied potenial is set to a constant value of -1.5 V vs RHE. The illumination is chopped to maintain an on cycle for 300 seconds and an off cycle for 60 seconds. This repetition of the on and off cycles is carried out for 1800 seconds. The resulting representative curve is shown in figure 7.13. We observe that for the entire time duration the increased photocurrent has a similar maximum value. This long term cycle does elaborate more clearly on the increased accumulation of bubbles on the nanostructure surface. The dip and rise of current forming minor current zig-zags is evidence of the accumulation and release of hydrogen bubbles at the interface. After performing such measurements multiple times, we visually observe that the nanostructure sample appears to have thinned down. To check for other morphological changes, we observe the sample post measurement under an electron microscope. As shown in figure 7.14, we observe that bowls lose their spherical contour and appear more like flat textures. However, the overall pattern of the hexagonal array remains intact. This is an indication of the fact that the charge transfer still takes places between silicon and electrolyte interface. This charge needs to travel through the titanium dioxide layer. The titanium dioxide layer being amorphous does not withstand the transfer of charge carriers across its nanoscale thickness. A work around this is to use crystalline titanium dioxide. However, nanostructuring of crystalline titanium dioxide is not straightforward. Efforts need to be

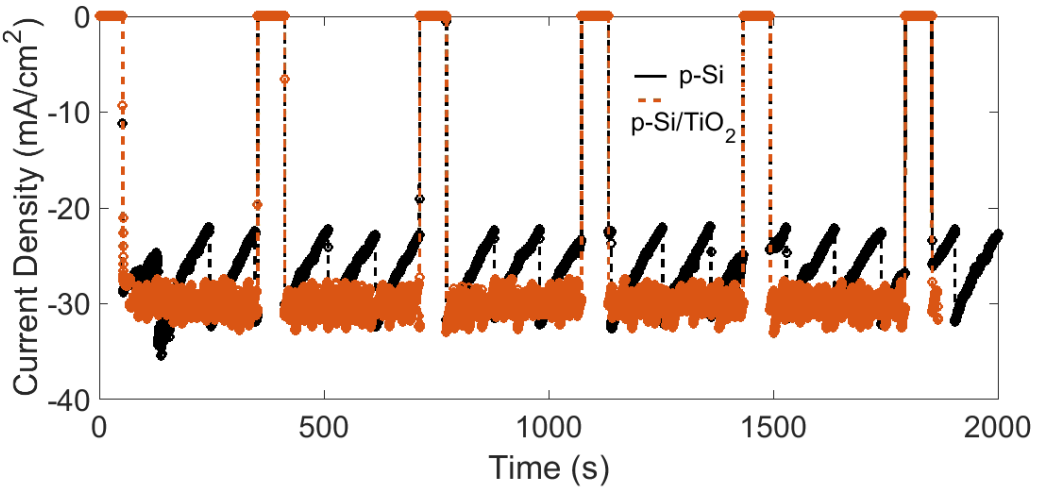

FIGURE 7.13: Steady state characteristics of the system with and without nanostructures for a constant potenial of -1.5 V vs RHE. These curves are obtained by periodically eliminating the illumination to measure the dark and light response in a cyclic manner to record the steady state response of the system.

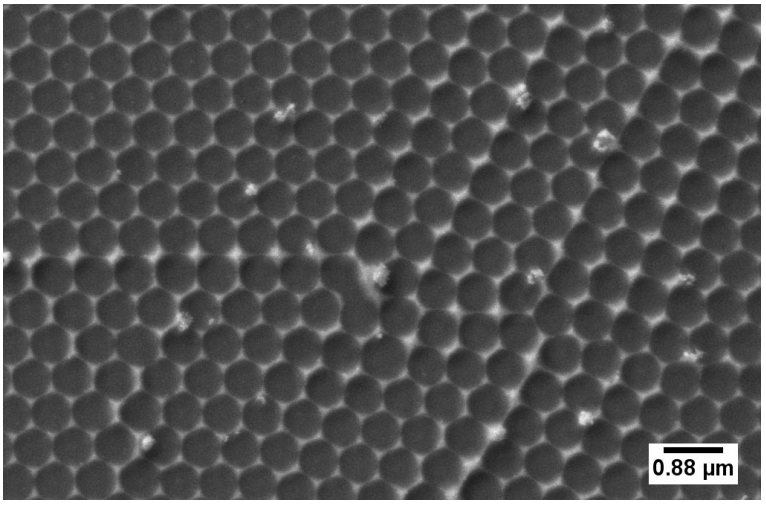

FIGURE 7.14: Morphology of the nanostructure post photoelectrochemical measurements

invested in the direction of nanostructuring amorphous titanium dioxide as described above and then anneal it over its crystalline temperature in order to achieve crystalline phases. This can be an outlook for future work.

7.4 Discussions from the comprehensive analysis of the soupbowls

In summary, the optical properties of the iteratively fabricated soupbowl nanostructure were extensively characterised. Spectral trends of the diffuse, specular and total reflection were

indicated. Overall the structure helps in achieving significant reflection supression as compared to the bare silicon. In the wavelength range between (420 - 600 nm) the value of this reflection is supressed to an average value of 50 percent and to an average value of 80 percent in the wavelength range 600 nm and beyond. Numerical simulations affirm the importance of the selected mask size. We have compared the specular reflection of the obtained structures with the simulated spectra. Presence of lattice misalignments and uneven layer thicknesses are revealed to be important reasons of the deviation of the optical properties of the obtained structure and a regular hexagonal lattice.

In the end, the optoelectronic functionality via the optical benefit of the structures were elaborated via measurements of a photoelectrochemical cell. These measurements are quantified for different illumination and current voltage conditions. A comparison was made between the current characteristics with and without nanostructures.

Chapter 8

Evaluation of Nanostructure Functionality

In this chapter, we provide a quantitative comparison of the two investigated structures in this thesis. Both these structures are then compared with planar titanium dioxide layers of the same thickness as the nanostructures. Additionally we compare the structures to a highly cited state of the art reflection spectra of titanium dioxide nanodisks reported in literature.[111] This comparison helps in quantifying the antireflection properties manifested via the elaborate nanostructuring efforts - experimental and computational as described in this thesis. We also compare the photoelectrochemical performance of the two structures. Comparisons of optical and photoelectrochemical performance help in establishing that nanostructuring is beneficial in effectively rendering spectral properties which are otherwise hard to engineer with unstructured materials.

8.1 Providing an overview of the geometrical features

We first bring together the morphological images and the corresponding dimensions of the two structures.

Dimensions of the Titanium Dioxide Nanofrustums				
Frustum Height	Radius Top	Radius Bottom	Height of Planar Film	Pitch
150 nm	100 nm	120 nm	50 nm	360 nm

TABLE 8.1: Dimensions of the frustums obtained out of the process sequence

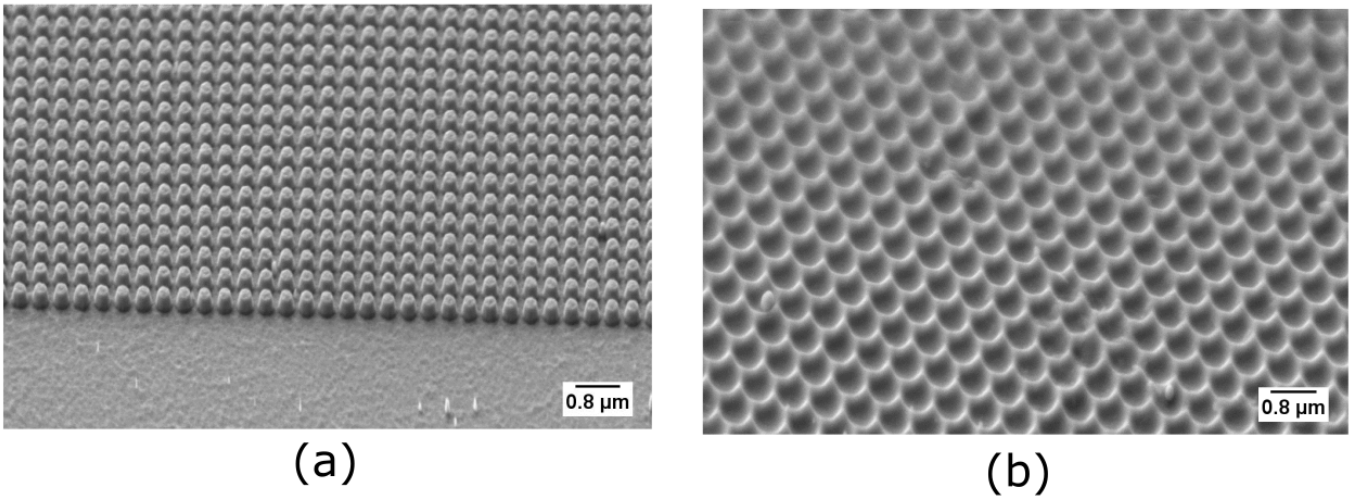

FIGURE 8.1: Morphology of the two structures (a)nanofrustum metasurfaces and (b)soupbowls as observed under a tilt of 54°.

Dimensions of the Titanium Dioxide soupbowls		
Height	Lattice Length	Diameter hole
240 nm	290 nm	480 nm

TABLE 8.2: Dimensions of the spherical soupbowl obtained out of the iterative fabrication process. The lattice length is calculated from the lattice length of the hexagonal unit cell.

8.2 Antireflection: Comparing the nanofrustum metasurface and the soupbowl nanostructure

The goal of this section is to compare systematically, the spectral properties of two the investigated nanostructures. We begin with comparing the simulated reflection spectra of both the top down (nanofrustum metasurface) and bottom up structure (soupbowls) for normal incidence. Both spectra indicate the total reflection of the sample which have been described in detail in chapter 5 and chapter 6. The average reflection of the bottom up - soupbowls on silicon is 12.04 % in the measured bandwidth between 400-900 nm. The average reflection of the top down structure is 2.5 %. This difference in reflection confirms the superiority of the metasurface design parameters.

In the next step, we compare the simulated reflection for the structures for different incident angles. For both cases, the maps for reflections are shown in figure 8.3. At an angular incidence, reflection in a periodic nanostructure tends to increase due to propagational components which increase in the direction of periodicity. Since this discussion revolves around the benefits of nanostructuring and the optical properties imparted by it, we restrict ourselves in comparing the simulated total reflection of the top down and bottom up structure. This comparison is aimed to give an overview of the antireflection performance precisely due to

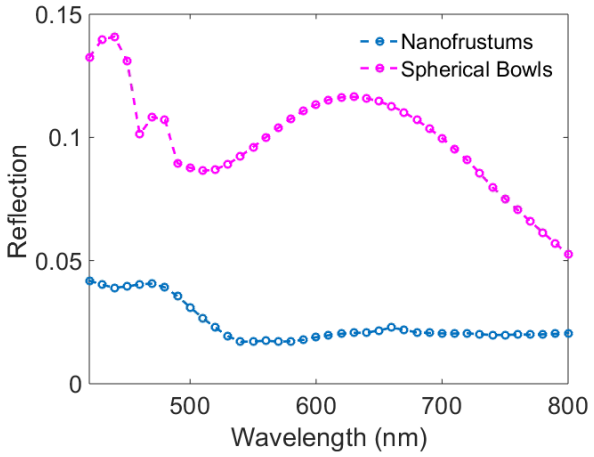

FIGURE 8.2: Simulated reflection spectra of the nanofrustum metasurface compared with the soupbowls

structuring titanium dioxide. The comparison of the simulated angular reflection also helps in eliminating that the experimental setup used for the top down structure only measures specular reflection. It also helps in overcoming the problem of experimentally measured diffuse reflection for the soupbowl structure. Comparing the simulated total reflection therefore helps in establishing the design supremacy of one nanostructure against the other in terms of antireflective properties.

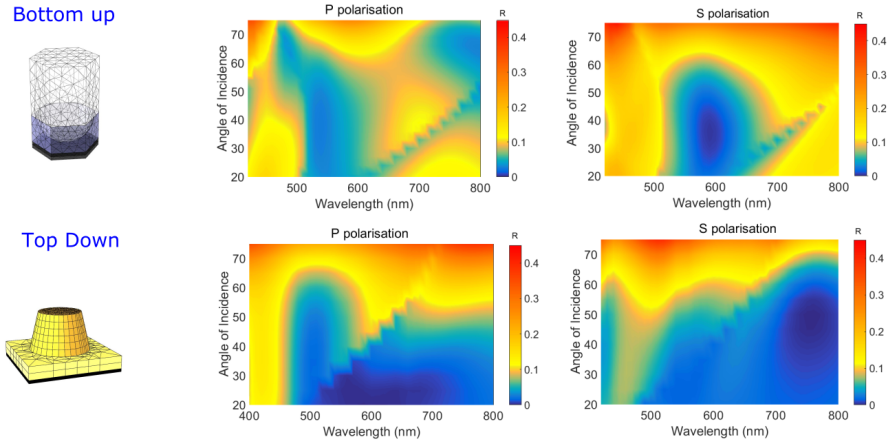

FIGURE 8.3: Simulated total reflection for the metasuruface developed via the top down process and the soupbowl structure developed via the bottom up process for both polarisations

It is clear that for off normal incidence, the nanofrustum metasurface has lower total reflection in comparison with the spherical soupbowl lattice. This can be attributed to the subwavelength arrangement of the frustums and their preferrential forward scattering into silicon. Moreover the frustum design parameters are obtained with the aid of computational

simulations. However in case of the bottom up spherical soupbowl structure, the structure is obtained by an iterative experimental parameter verification. Scaling down the periodicity of the soupbowl nanostructure and obtaining a viable requires several trials. This makes it difficult to easily arrive at optimised geometry. These structures can be fabricated on a large spatial order, however are not able to substantially contribute towards reducing reflection. This proves that geometry of the nanostructure made from the same material plays a big influence in the optical performance of the nanostructure. The nanofrustrum metasurface has a good geometry to control antireflection but the accompanying lithographic implementation is feasible only on a small range patterning.

8.2.1 Comparison with bare silicon and planar TiO_2/Si

In order to provide an overview about the bare silicon reflection for angular incidence, we first show the reflection spectra for both s- and p- polarisation. As shown in figure 8.4, both polarisations show distinct behavior with respect to angular incidence. For p- polarisation, reflection is maximum for near normal incidence and then decreases for higher incident angles. For s- polarisation, reflection increases from a moderate to high value with increase in angle of incidence. To demonstrate the benefit of nanostructuring for antireflection, we compare

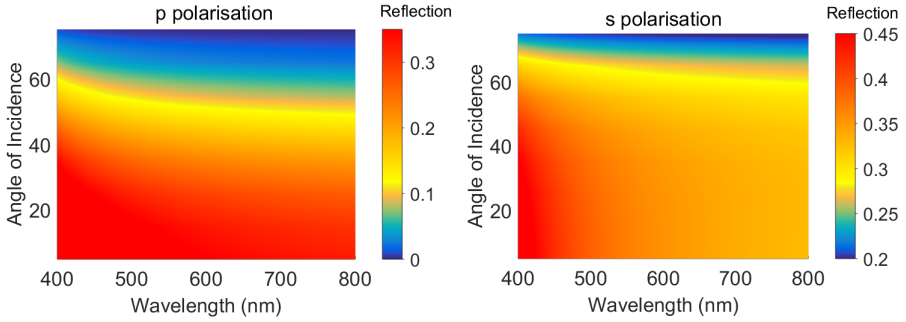

FIGURE 8.4: Reflection spectra of bare silicon as a function of angle of incidence for both p and s polarisation

the variation of reflection for angular incidence for planar layers of different thicknesses. This calculation is performed by using the thickness values of the two nanostructures - 240 nm (spherical soupbowl structure) and 150 nm (nanofrustum structure). Both these values are compared to the angle dependent reflection properties of the nanostructures and a relative overview is obtained. Such a comparison helps in further demonstrating the spectral advantages of the nanostructures against planar layers. Figure 8.5 shows the reflection for angular incidence on a 150 nm planar layer of titanium dioxide on silicon. This 150 nm thickness is identical to the height of the nanofrustums. It clearly demonstrates that the reflection shrinks to low values only for a really short wavelength band and is high across most of the spectrum. The tolerance is also low for higher angles of incidence. This narrow band minima

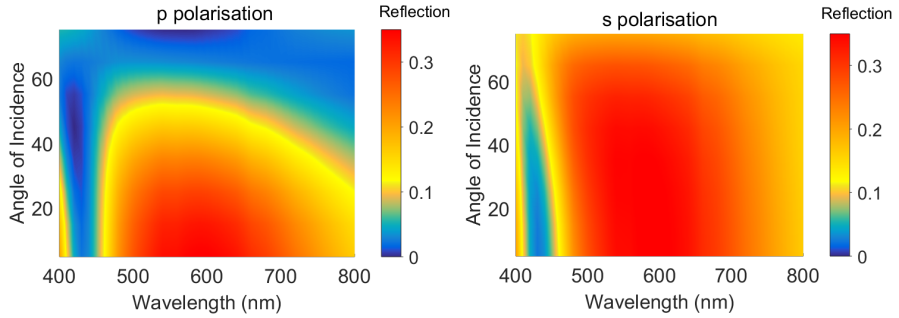

FIGURE 8.5: Reflection spectra of a 150 nm titanium dioxide film on silicon as a function of angle of incidence for both p and s polarisation

in reflection can be attributed to the destructive interference of reflected waves only at one wavelength. For the nanostructured systems, reflection is supressed on a broader scale owing to specially induced optical phenomenon. To further elaborate the dependance of thickness, we perform the calculation for a thickness of 240 nm. This thickness is indentical to the vertical thickness of the spherical bowl like structures. Figure 8.6 indicates the reflection for a planar layer of titanium dioxide on silicon. We observe in this case that on account of in-

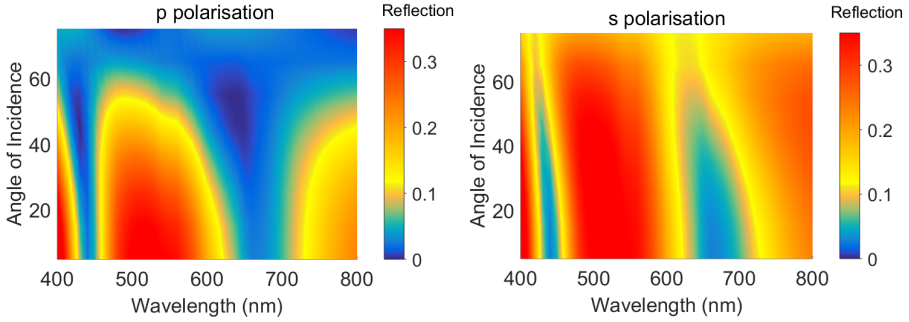

FIGURE 8.6: Reflection spectra of a 240 nm titanium dioxide film on silicon as a function of angle of incidence for both p and s polarisation

creased thickness, the number of interferences increase. Whereas in case of the the spherical bowl structures, the simulated spectra showed in figure 8.3 and the experimental spectra in figure 7.12 show much lower reflection across the different angles of incidence.

The idea of this investigation is to quantify the angle dependent benefits of the nanostructure against planar equivalents. This directly is in line with the theory of Fresnel coefficients which decides the reflection across a material interface.[5] For a bare silicon wafer for p- polarised light, this reflection is maximum for normal incidence and decreases with an increase in angle of incidence. For s- polarised light this trend is reversed. For a planar layer of titanium dioxide on silicon, total reflection is governed by the film thickness and the resulting interferences. These interferences give rise to peaks in the reflection spectra. Due to the peculiar broadband optical properties comprising of perturbed Mie resonances, these interferences are

absent in the nanofrustum metasurface. These interferences result in an increased reflection at angular incidences for a planar bi-layer of a thin flim of titanium dioxde on silicon. The nanostructured samples have a better tolerance with respect to controlling reflection at angular incidences for both light polarisations. This can be seen from the plots for angular incidence in case of the top down nanofrustums for both polarisations. While the effective reflection for the spherical soupbowl structures is more than the frustums, it is still less than the planar reflection layer. This effect arises due to the fundamental order of propagation in the nanostructures due to subwavelength pitch. The spherical profile also helps in providing slow variation of refractive index.

8.2.2 Comparison with a highly cited state of the art structure

We now compare the results described in this thesis with those described in literature. In chapter two, we elaborated upon other examples where both nanostructured resonances as well as effective medium profiles are used to engineer antireflection. We compare our approach of the nanofrustum metasurface to the antireflection system consisting of titanium dioxide. Mie coatings on a multilayer stack of a planar stack of titanium dioxde on aluminium oxide on p-type silicon.[111] In addition to pattern generation and material deposition, this work uses an additional stage of depositing aluminium oxide via ALD. Aluminium oxide deposition is an additional material processing step in comparison with the work deposited in this thesis. For normal incidence, the nanofrustum metasurfaces on a planar interlayer shows slightly lower reflection values as compared to the work by Pinelli et al. in the wavelength range between 400-650 nm. However in the long wavelength (650-800 nm), the reflection spectra of reported nanofrustums in this thesis show a much better performance due to enhanced impedance matching. The work doesn't record spectra for angular incidence, however owing to a non subwavelength pitch of 500 nm, we expect profound presence of the first diffraction order especially for higher angles of incidence.

While the nanofrustum metasurfaces show good antireflection performance for both normal and angular incidence, the drawback lies in the patterning method. In this thesis, we have used e-beam patterning to fabricate and characterise the samples. However this method is not feasible for large order patterning which is often desired in solar energy systems. Our alternative demonstration for a large order antireflection system is indicated with the aid of nanosphere lithography patterning. As reported, we get a novel structure, but not significant improvements in the antireflection properties in comparison with the nanofrustum metasurface as well as other antireflection systems reported in literature.

8.3 Photoelectrochemical Properties

We now compare the current density versus voltage sweeps of the pn- junction established between silicon and electrolyte for the top down and bottom nanostructures. This helps in providing an overview of how the antireflective benefits arising from the two structures translate to improvement in the optoelectronic benefit. It is to be noted that due to logistical experimental limitations, the two structures are fabricated on p-type silicon wafers of different resistivity and thicknesses and lots. This information has been indicated in table 6.1 and 7.1. This results in different measured current densities of the bare silicon values. Different lots also imply fundamentally different defect centres. We therefore limit the comparison to the relative increase in photocurrent in case of each nanostructure. Moreover owing to the size limitation of the metasurface, the photoelectrochemical measurements are performed using two different methods of electrically contacting the sample. This results in slightly different impedances across the sample and the electrolyte in the two cases.

However it is to be noted that both measurements result in ultimately describing the relative increase with and without the antireflective nanostructure on silicon. It is important to note that even in presence of the two nanostructures, in each case, the pn- junction is formed between silicon and the electrolyte. The increased surface area of the nanostructure therefore does not play a role in the photocurrent enhancement. The figure 8.7 indicates the trend in the J-V curves of the two structures. For the soupbowl structure we observe an offset from the bare silcion value in terms of the voltage where the current starts saturating. This can be attributed to the charge transfer dynamics through the titanium dioxide layer of the nanostructure. Since this offset is not observed for the nanofrustum metasurface, we conclude that annealing the titanium dioxide as explained in chapter 4 helps in improving the dynamics. The onset potenial is a function of charge carrier dynamics while the measured maximum photocurrent density is a function of the optical properties as well as the charge carrier dynamics. We therefore illustrate the improvement in terms of peak current density as measured at the maximum voltage. These figures imply that the nanofrustum metasurface outperforms the soupbowl nanostructure in terms of the peak current density observed at maximum voltage. This proves the overall benefit of the metasurface is higher than that of soupbowl.

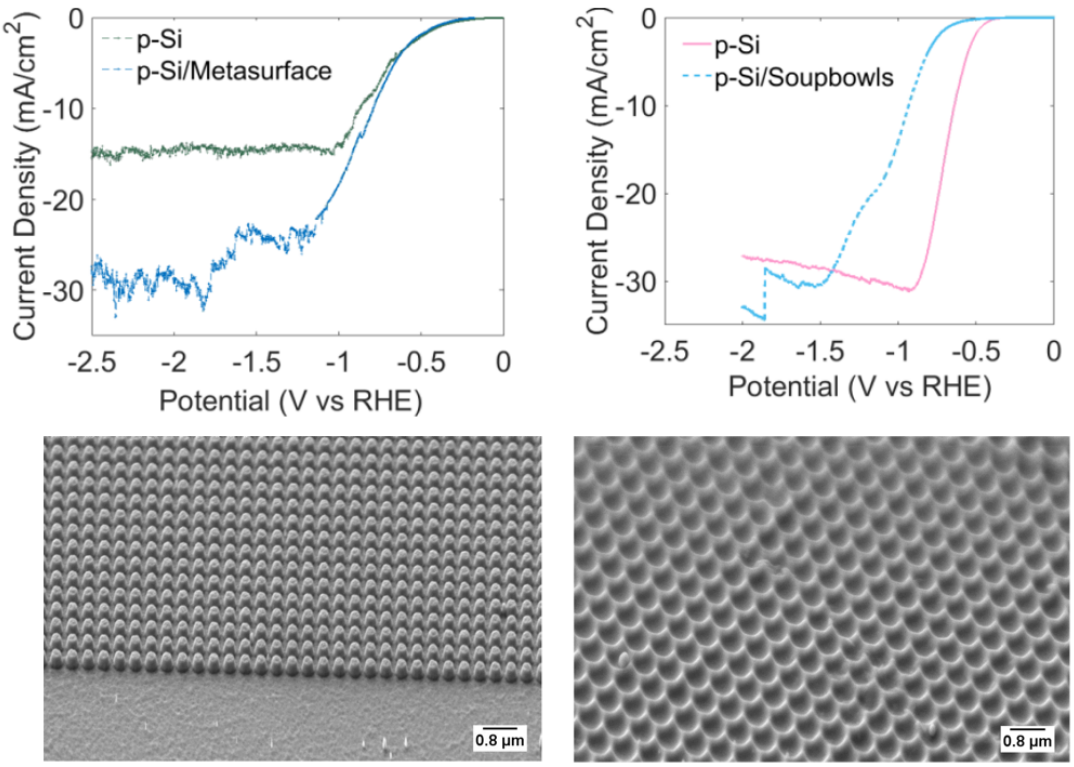

FIGURE 8.7: Comparison of the photoelectrochemical performance of the metasurface and the soupbowl nanostructure. The current versus voltage characteristics of the both structures is indicated along with the morphological image. The optical effects implemented in the metasurface via design assisted fabrication result in a larger relative increase in the measured photocurrent.

8.4 Discussions

In this chapter we bring the two fabricated structures together on the same graphical scale and compare their spectral performance. The superiority of the metasurfaces over the soupbowl nanostructure is a result of the efficiency of the fabrication process in implementing the designed physics calculated by the simulation trend. While the soup bowl structures offer better potential towards a realistic large area deployement, their exisiting antireflection spectra call for improvement in the fabrication methodology.

The direct influence of the superiority in antireflection can be observed in the differences in photoelectrochemical performance. The metasurfaces show better enhancement in the photocurrent obtained. The material stability of both these structures needs to be improved in order to have sustainable performance in the antireflection beahvior on a long term basis.

Chapter 9

Conclusion and Outlook

In this thesis we investigated nanostructures fabricated via two different lithographic processes implementing two different kinds of physics - perturbed Mie resonances and gradually varying periodic nanostructures, respectively. We describe the outcome of these processes with aid of thorough experimental and computational characterisation. We summarise the main findings here of the details described in chapters 4, 5, 6 and 7.

- **Nanofrustum Metasurfaces**

  In chapter 4, the fabrication process sequence which provides flesh, bone and life to the optical spectra of the nanostructure and helps in correlating it with computational efforts is elaborated in terms of significance of associated physical parameters. The closed network of nanofrustum metasurfaces is obtained via highly precise structuring through electron beam lithography. The subsequent inductively coupled reactive ion etching helps in giving the perfect shape to the resonator. Physical process parameters govern the final outcome of the structure. These so called soupbowl structures were obtained via iterative optimisation of the process in order to get material growth around the mask. This resulted in large areas of nanostructures with patterned structures with a spherical contour. We thus show our efforts in determining these parameters and in iterative process development

  In chapter 5, with the aid of numerical simulations, we investigated the scattering properties of nanofrustums into silicon. This helps in establishing spectral dependencies of scattering tendencies in terms of the incident angle for both s and p polarised light in relation with the overall geometry of the structure.

In chapter 6, we elaborate upon the system design and implications of subwavelength arrays of nanofrustum metasurfaces in the visible spectrum. Owing to the excellent material properties of titanium dioxde,an all dielectric behavior in the visible spectrum is observed due to perturbed Mie resonances. Numerical simulations help in understanding the role of each parameter of the metasurface in lowering the reflection.

These numerical investigations model the parallel interplay of phenomemon such as substrate influenced Kerker effect as well as Mie resonances of nanostructures. They also highlight the aspect ratio dependence of the nanostructures in terms of scattering light into silicon for different angles of incidence.

In the subsequent step we have characterised the optical performance to indicate tremendous reflection supression for normal and angular incidence. Under normal incidence, spectral measurements revealed that the silicon reflection reduced to an average value of 2.5 percent for normal incidence as a result of the metasurface light coupling. For angular incidence, the specular reflection remains below 10 percent up to angles as high as 60°. We also have given a numerical account of the unmeasured non-specular coherent reflection in terms of amplitude and spectral spread. This helped in establishing both superiority of the metasurfaces in terms of controlling reflection for controlling angular incidence. It also provided an overview in understanding the subwavelength optics of metasurfaces under angular incidence.

In order to demonstrate the optoelectronic benefit of antireflection, we elaborate upon current density versus voltage curves with and without nanostructures. These measurements showed a strong improvement in the measured current as a result of the increase in light absorption in silicon.

- **Spherical bowls**

The second class of the nanostructures is the so-called soupbowl structure. On account of these structures, the reflection reduced to an average value of 12 percent. However these structures also indicate high measured diffuse reflection. This diffuse reflection can be attributed to rough surfaces and point defects and varying structure thickness as observed in the SEM images. An additional design drawback of this structure is the lack of long range hexagonal symmetry of the structure which thereby results in different properties as predicted by simulation. While the asymmerty offers design potential for polarisation independent antireflection, it makes it difficult to computationally optimise the structures for optical performance due to invalid periodicity. This results in an increase in computational effort. Line and area defects of the pattern

in the fabricated sample also result in significant differences in terms of the observed properties. While these structures have the potential to reduce the silicon reflection, the underlying fabrication process needs to be improved for potentially optically optimising the structure via simulation to improve the measured reflection values. Once such improvements in fabrication result in a structure give strong supression in reflection, the simulation space can be extended to include computationally expensive features such as line defects and tilts with the aid of a supercell.

We also investigate the benefit of these structures to improving the current voltage characteristics of the pn- junction between silicon and electrolyte. There is a relative increase of 20 percent as a result of the antireflective properties of the nanostructure. This helps in further establishing the optoelectronic functionality of the structures. We also analyse the stability of the structures post photoelectrochemical measurements to observe that the titanium dioxide layer degrades away as a result of the high charge flow. This effect occurs after several hours of measurements.

The superiority of the metasurfaces in comparison with the spherical bowls in terms of optical performance is evidence of the effectiveness of the close coordination of the design ideology via computational simulations and its precise implementation through fabrication. This is further translated to the enhancement in the photocurrent observed in the two cases. This proves that all factors involved in the integration of structured materials to optically improve fuel generation devices are important to exploit the full potenial which nano and metastructured optics offer.

Outlook

- **Nanofrustum Metasurface** The nanofrustum metasurface on a planar layer of titanium dioxide significantly reduces silicon reflection for normal and angular illumination. The demonstrated method of patterning is via the relatively slow electron beam patterning. In order to make these structures on a large scale, the patterning methods needs to be efficient in terms of scalability. This can be improved by adopting methods such as photolithography using light sources in the deep ultraviolet regime to reach the resolution required to obtain densily packed features with spacings of the order of 120 nm. An alternative approach is to use organic block copolymers which have mask dimensions corresponding to the nanostructure pattern [119]. Once an optimised method to fabricate the structures is obtained, power of numerical optimisation can be utilised to minimise reflection and obtain the geoemtric dimensions.

- **Nano soupbowls** The principal outlook to improve the optical performance of the spherical bowls is to reduce the diffuse reflection. The problem of asymmerty arising due to long range patterning can be improved by using a more compact and precise way of patterning as compared to a colloidal mask. An example of this case, is using annodised alumina templates or block copolymers[75].

- **Titanium dioxide material properties** Nanostructures investigated in the thesis are fabricated out of amorphous titanium dioxide. Amorphous titanium dioxide is not stable under a high charge carrier environment. A potential improvement is utilising crystalline titanium dioxide. However crystalline titanium dioxide is not easy to nanostructure in terms of etching. A work around in this direction is to first nanostructure amorphous titanium dioxide and then anneal the fabricated nanostructure after. Annealing beyond its crystallisation temperature helps in increasing stability against high currents.

Appendix A

Literature

Bibliography

[1] Adachi, M. M., Labelle, A. J., Thon, S. M., Lan, X., Hoogland, S., and Sargent, E. H. (2013). Broadband solar absorption enhancement via periodic nanostructuring of electrodes. *Scientific Reports*, 3:2928.

[2] Adzhri, R., Arshad, M. K. M., Fathil, M. F. M., Hashim, U., Ruslinda, A. R., Ayub, R. M., Gopinath, S. C. B., Voon, C. H., Foo, K. L., Nuzaihan, M., Azman, A. H., and Zaki, M. (2016). Optimization of time on cf4/o2 etchant for inductive couple plasma reactive ion etching of tio2 thin film. *AIP Conference Proceedings*, 1733(1):020069.

[3] Alaee, R., Filter, R., Lehr, D., Lederer, F., and Rockstuhl, C. (2015). A generalized kerker condition for highly directive nanoantennas. *Opt. Lett.*, 40(11):2645–2648.

[4] Asakura, K. (1999). *Dispersion, Complex Analysis and Optical Spectroscopy*. Springer.

[5] Azzam, R. M. A. (1979). Transformation of fresnel's interface reflection and transmission coefficients between normal and oblique incidence. *Journal of the Optical Society of America*, 69(4):590–596.

[6] Azzam, R. M. A. (1986). Relationship between the p and s fresnel reflection coefficients of an interface independent of angle of incidence. *J. Opt. Soc. Am. A*, 3(7):928–929.

[7] Babicheva, V. E. and Evlyukhin, A. B. (2017). Resonant lattice kerker effect in metasurfaces with electric and magnetic optical responses. *Laser & Photonics Reviews*, 11(6):1700132.

[8] Bardosova, M., Hodge, P., Pach, L., Pemble, M., Smatko, V., Tredgold, R., and Whitehead, D. (2003). Synthetic opals made by the langmuir–blodgett method. *Thin Solid Films*, 437(1):276–279.

[9] Barth, C., Burger, S., and Becker, C. (2016). Symmetry-dependency of anticrossing phenomena in slab-type photonic crystals. *Opt. Express*, 24(10):10931–10938.

[10] Baryshnikova, K. V., Petrov, M. I., Babicheva, V. E., and Belov, P. A. (2016). Plasmonic and silicon spherical nanoparticle antireflective coatings. *Scientific Reports*, 6:22136.

[11] Bereza, A. S., Nemykin, A. V., Perminov, S. V., Frumin, L. L., and Shapiro, D. A. (2017). Light scattering by dielectric bodies in the born approximation. *Phys. Rev. A*, 95:063839.

[12] Berglund, S. P., He, H., Chemelewski, W. D., Celio, H., Dolocan, A., and Mullins, C. B. (2014). p-si/w2c and p-si/w2c/pt photocathodes for the hydrogen evolution reaction. *Journal of the American Chemical Society*, 136(4):1535–1544.

[13] Bernhard, C. G. and Ottoson, D. (1964). Quantitative studies on pigment migration and light sensitivity in the compound eye at different light intensities. *The Journal of General Physiology*, 47(3):465–478.

[14] Bezus, E. A., Bykov, D. A., Doskolovich, L. L., and Kadomin, I. I. (2008). Diffraction gratings for generating varying-period interference patterns of surface plasmons. *Journal of Optics A: Pure and Applied Optics*, 10(9):095204.

[15] Bohren, C. F. and Huffman, D. R. (1983). *Absorption and scattering of light by small particles*. Wiley, New York.

[16] Brongersma, M. L., Cui, Y., and Fan, S. (2014). Light management for photovoltaics using high-index nanostructures. *Nature Materials*, 13:451.

[17] Buencuerpo, J., Llorens, J. M., Dotor, M. L., and Ripalda, J. M. (2015). Broadband antireflective nano-cones for tandem solar cells. *Opt. Express*, 23(7):A322–A336.

[18] Busch, K., König, M., and Niegemann, J. Discontinuous galerkin methods in nanophotonics. *Laser & Photonics Reviews*, 5(6):773–809.

[19] Busch, K., von Freymann, G., Linden, S., Mingaleev, S. F., Tkeshelashvili, L., and Wegener, M. (2007). Periodic nanostructures for photonics. *Physics Reports*, 444(3):101–202.

[20] Busch, P. K. (2016). Lecture notes in computational photonics.

[21] Butakov, N. A. and Schuller, J. A. (2016). Designing multipolar resonances in dielectric metamaterials. *Scientific Reports*, 6:38487.

[22] Chao, Y.-C., Chen, C.-Y., Lin, C.-A., and He, J.-H. (2011). Light scattering by nanostructured anti-reflection coatings. *Energy Environ. Sci.*, 4:3436–3441.

[23] Christiansen, A. B., Caringal, G. P., Clausen, J. S., Grajower, M., Taha, H., Levy, U., Asger Mortensen, N., and Kristensen, A. (2015). Black metal thin films by deposition on dielectric antireflective moth-eye nanostructures. *Scientific Reports*, 5:10563.

[24] Colson, P., Henrist, C., and Cloots, R. (2013). Nanosphere lithography a powerful method for the controlled manufacturing of nanomaterials. *Journal of Nanomaterials*, 2013:19.

[25] Dabas, B. and Sinha, R. (2010). Dispersion characteristic of hexagonal and square lattice chalcogenide as2se3 glass photonic crystal fiber. *Optics Communications*, 283(7):1331 – 1337.

[26] de Krol, R. V. (2011). *Photoelectrochemical Hydrogen Prouction*. Wiley.

[27] De Leon, I., Horton, M. J., Schulz, S. A., Upham, J., Banzer, P., and Boyd, R. W. (2015). Strong, spectrally-tunable chirality in diffractive metasurfaces. *Scientific Reports*, 5:13034.

[28] Demiryont, H. and Sites, J. R. (1984). Effects of oxygen in ion-beam sputter deposition of titanium oxides. *Journal of Vacuum Science & Technology A*, 2(4):1457–1460.

[29] Ellinas, K., Smyrnakis, A., Malainou, A., Tserepi, A., and Gogolides, E. (2011). "mesh-assisted" colloidal lithography and plasma etching: A route to large-area, uniform, ordered nano-pillar and nanopost fabrication on versatile substrates. *Microelectronic Engineering*, 88(8):2547–2551.

[30] Fan, R., Mao, J., Yin, Z., Jie, J., Dong, W., Fang, L., Zheng, F., and Shen, M. (2017a). Efficient and stable silicon photocathodes coated with vertically standing nano-mos2 films for solar hydrogen production. *ACS Applied Materials & Interfaces*, 9(7):6123–6129.

[31] Fan, W., Li, Q., Hu, L., Yan, S., Wen, W., Chai, Z., and Liu, H. (2017b). Polystyrene-based hollow microsphere synthesized by γ ray irradiation-assisted polymerization and self-assembly and its application in detection of ionizing radiation. *Scientific Reports*, 7:41876.

[32] Fantone, S. D. (1983). Refractive index and spectral models for gradient-index materials. *Appl. Opt.*, 22(3):432–440.

[33] Foroutan, S., Dizaji, H. Z., and Riahi, A. (2017). Plasmon resonance-enhanced photocathode by light trapping in periodic concentric circular nanocavities on gold surface. *Optik-International Journal for Light and Electron Optics*, 138:223 – 228.

[34] Fountaine, K. T., Cheng, W.-H., Bukowsky, C. R., and Atwater, H. A. (2016). Near-unity unselective absorption in sparse inp nanowire arrays. *ACS Photonics*, 3(10):1826–1832.

[35] Franta, D., Nečas, D., and Ohlídal, I. (2015). Universal dispersion model for characterization of optical thin films over a wide spectral range: application to hafnia. *Appl. Opt.*, 54(31):9108–9119.

[36] Frey, H. (2015). *Cathode Sputtering*, pages 133–165. Springer Berlin Heidelberg, Berlin, Heidelberg.

[37] Fujiwara, H. (2007a). *Data Analysis*, pages 147–207. John Wiley & Sons, Ltd.

[38] Fujiwara, H. (2007b). *Spectroscopic Ellipsometry*. John Wiley and Sons.

[39] Fukuhara, M., Kuroda, T., and Hasegawa, F. (2016). Amorphous titanium-oxide supercapacitors. *Scientific Reports*, 6:35870.

[40] Garnett, E. and Yang, P. (2010). Light trapping in silicon nanowire solar cells. *Nano Letters*, 10(3):1082–1087. PMID: 20108969.

[41] Ginn, J. C., Brener, I., Peters, D. W., Wendt, J. R., Stevens, J. O., Hines, P. F., Basilio, L. I., Warne, L. K., Ihlefeld, J. F., Clem, P. G., and Sinclair, M. B. (2012). Realizing optical magnetism from dielectric metamaterials. *Phys. Rev. Lett.*, 108:097402.

[42] Goldstein, D. H. (2011). *Polarised Light*. CRC Press.

[43] Harland G Tompkins, E. A. (2005). *Handbook of Ellipsometry*. William Andrew Publishing,NY,2005.

[44] Haynes, C. L. and Van Duyne, R. P. (2001). Nanosphere lithography, a versatile nanofabrication tool for studies of size-dependent nanoparticle optics. *The Journal of Physical Chemistry B*, 105(24):5599–5611.

[45] Heikal, A. M. and Obayya, S. S. (2016). New trends in computational photonics. In *Latin America Optics and Photonics Conference*, page LTu5D.3. Optical Society of America.

[46] Himcinschi, C., Friedrich, M., Murray, C., Streiter, I., Schulz, S. E., Gessner, T., and Zahn, D. (2001). Characterization of silica xerogel films by variable-angle spectroscopic ellipsometry and infrared spectroscopy. *Semiconductor Science and Technology*, 16(9):806.

[47] Holl, H. B. (1967). Specular reflection and characteristics of reflected light∗. *J. Opt. Soc. Am.*, 57(5):683–690.

[48] Hulteen, J. C. and Duyne, R. P. (1995). Nanosphere lithography: A materials general fabrication process for periodic particle array surfaces. *Journal of Vacuum Science & Technology A: Vacuum, Surfaces, and Films*, 13(3):1553–1558.

[49] Hung, Y.-J., Lee, S.-L., Wu, K.-C., Tai, Y., and Pan, Y. (2011). Antireflective silicon surface with vertical-aligned silicon nanowires realized by simple wet chemical etching processes. *Opt. Express*, 19(17):15792–15802.

[50] Hussain, B. and Ebong, A. (2015). Specifications of zno growth for heterostructure solar cell and pc1d based simulations. *Data Brief*, 5:516–21. 2352-3409 Hussain, Babar Ebong, Abasifreke Data Brief. 2015 Dec;5:516-21. doi:10.1016/j.dib.2015.09.050.

[51] Jackson, J. D. (1998). *Classical Electrodynamics*. Springer.

[52] Jahani, S. and Jacob, Z. (2016a). All-dielectric metamaterials. *Nature Nanotechnology*, 11:23.

[53] Jahani, S. and Jacob, Z. (2016b). All-dielectric metamaterials. *Nature Nanotechnology*, 11:23.

[54] Jang, H. K., Whangbo, S. W., Choi, Y. K., Chung, Y. D., Jeong, K., Whang, C. N., Lee, Y. S., Lee, H.-S., Choi, J. Y., Kim, G. H., and Kim, T. K. (2000). Titanium oxide films on si(100) deposited by e-beam evaporation. *Journal of Vacuum Science & Technology A*, 18(6):2932–2936.

[55] Jeon, J., Bhattarai, K., Kim, D. K., Kim, J. O., Urbas, A., Lee, S. J., Ku, Z., and Zhou, J. (2016). A low-loss metasurface antireflection coating on dispersive surface plasmon structure. *Sci Rep*, 6. 2045-2322 Jeon, Jiyeon Bhattarai, Khagendra Kim, Deok-Kee Kim, Jun Oh Urbas, Augustine Lee, Sang Jun Ku, Zahyun Zhou, Jiangfeng Sci Rep. 2016;6:36190. doi:10.1038/srep36190.

[56] Ji, L., McDaniel, M. D., Wang, S., Posadas, A. B., Li, X., Huang, H., Lee, J. C., Demkov, A. A., Bard, A. J., Ekerdt, J. G., and Yu, E. T. (2014a). A silicon-based photocathode for water reduction with an epitaxial srtio3 protection layer and a nanostructured catalyst. *Nature Nanotechnology*, 10:84.

[57] Ji, L., McDaniel, M. D., Wang, S., Posadas, A. B., Li, X., Huang, H., Lee, J. C., Demkov, A. A., Bard, A. J., Ekerdt, J. G., and Yu, E. T. (2014b). A silicon-based photocathode for water reduction with an epitaxial srtio3 protection layer and a nanostructured catalyst. *Nature Nanotechnology*, 10:84.

[58] Jia, J., Seitz, L. C., Benck, J. D., Huo, Y., Chen, Y., Ng, J. W. D., Bilir, T., Harris, J. S., and Jaramillo, T. F. (2016). Solar water splitting by photovoltaic-electrolysis with a solar-to-hydrogen efficiency over 30 *Nature Communications*, 7:13237.

[59] Jiang, X., Liang, B., Yang, J., Yang, J., and chun Cheng, J. (2018). Acoustic planar antireflective focusing lens with sub-diffraction-limit resolution based on metamaterials. *Journal of Applied Physics*, 123(9):091717.

[60] Jin, J.-M. (2014). *The Finite Element Method in Electromagnetics*. Wiley.

[61] Joannopoulos, J., Meade, R., and Winn, J. (1995). *Photonic Crystals: Molding the Flow of Light*. Princeton University Press.

[62] Jonathan Grandidier, Michael G. Deceglie, D. M. C. H. A. (2012). Simulations of solar cell absorption enhancement using resonant modes of a nanosphere array. *Proc.SPIE*, 8256:8256–8256–9.

[63] Kang, H. C., Stephenson, G. B., Liu, C., Conley, R., Khachatryan, R., Wieczorek, M., Macrander, A. T., Yan, H., Maser, J., Hiller, J., and Koritala, R. (2007). Sectioning of multilayers to make a multilayer laue lens. *Review of Scientific Instruments*, 78(4):046103.

[64] Khorasaninejad, M. and Capasso, F. (2017). Metalenses: Versatile multifunctional photonic components. *Science*.

[65] Kim, K.-H. and Park, Q. H. (2013). Perfect anti-reflection from first principles. *Scientific Reports*, 3:1062.

[66] Kim, W., Guo, J., and Hendrickson, J. (2015). Subwavelength metal grating metamaterial for polarization-selective optical antireflection coating. *J. Opt. Soc. Am. B*, 32(7):1392–1398.

[67] Kluge, C., Adam, J., Barié, N., Jakobs, P.-J., Guttmann, M., and Gerken, M. (2014). Multi-periodic nanostructures for photon control. *Opt. Express*, 22(S5):A1363–A1371.

[68] Koppel, G., Rech, B., and Becker, C. (2016). Sinusoidal nanotextures for light management in silicon thin-film solar cells. *Nanoscale*, 8:8722–8728.

[69] Kortüm, G., Braun, W., and Herzog, G. (1963). Principles and techniques of diffuse-reflectance spectroscopy. *Angewandte Chemie International Edition in English*, 2(7):333–341.

[70] Koynov, S., Brandt, M. S., and Stutzmann, M. (2006). Black nonreflecting silicon surfaces for solar cells. *Applied Physics Letters*, 88(20):203107.

[71] Kuo-Tong, L. and Jenn-Ming, W. (2004). Rf-magnetron sputtering of titanium dioxide for microelectronic applications. *Japanese Journal of Applied Physics*, 43(1R):232.

[72] Lai, W. C., Ma, M. H., Lin, B. K., Hsieh, B. H., Wu, Y. R., and Sheu, J. K. (2014). Photoelectrochemical hydrogen generation with linear gradient al composition dodecagon faceted AlGaN/n-GaN electrode. *Opt. Express*, 22(S7):A1853–A1861.

[73] Lalanne, P. and Morris, G. M. (1997). Antireflection behavior of silicon subwavelength periodic structures for visible light. *Nanotechnology*, 8(2):53.

[74] Lee, E., Seo, I. C., Jeong, H. Y., An, S.-C., and Jun, Y. C. (2017). Theoretical investigations on microwave fano resonances in 3d-printable hollow dielectric resonators. *Scientific Reports*, 7(1):16186.

[75] Lee, W. and Park, S.-J. (2014). Porous anodic aluminum oxide: Anodization and templated synthesis of functional nanostructures. *Chemical Reviews*, 114(15):7487–7556. PMID: 24926524.

[76] Levi, A. F. J. (2016). The lorentz oscillator model. In *Essential Classical Mechanics for Device Physics*, 2053-2571, pages 5–1 to 5–21. Morgan Claypool Publishers.

[77] Lewis, N. S. and Nocera, D. G. (2006). Powering the planet: Chemical challenges in solar energy utilization. *Proceedings of the National Academy of Sciences*, 103(43):15729–15735.

[78] Liu, S., Sinclair, M. B., Saravi, S., Keeler, G. A., Yang, Y., Reno, J., Peake, G. M., Setzpfandt, F., Staude, I., Pertsch, T., and Brener, I. (2016). Resonantly enhanced second-harmonic generation using iii–v semiconductor all-dielectric metasurfaces. *Nano Letters*, 16(9):5426–5432.

[79] Liu, S., Vaskin, A., Campione, S., Wolf, O., Sinclair, M. B., Reno, J., Keeler, G. A., Staude, I., and Brener, I. (2017). Huygens' metasurfaces enabled by magnetic dipole resonance tuning in split dielectric nanoresonators. *Nano Letters*, 17(7):4297–4303. PMID: 28590748.

[80] Liu, X., Coxon, P. R., Peters, M., Hoex, B., Cole, J. M., and Fray, D. J. (2014). Black silicon: fabrication methods, properties and solar energy applications. *Energy and Environmental Science*, 7(10):3223–3263.

[81] Ludwig, W., Ohm, W., Correa-Hoyos, J., Zhao, Y., Lux-Steiner, M. C., and Gledhill, S. (2013). Electrodeposition parameters for zno nanorod arrays for photovoltaic applications. *physica status solidi (a)*, 210(8):1557–1563.

[82] Macleod, H. (2010a). *Optical Interferometry*. CRC Press.

[83] Macleod, H. (2010b). *Thin-Film Optical Filters*. CRC Press.

[84] Maia, R., D'Alba, L., and Shawkey, M. D. (2011). What makes a feather shine? a nanostructural basis for glossy black colours in feathers. *Proc Biol Sci*, 278(1714):1973–80. 1471-2954 Maia, Rafael D'Alba, Liliana Shawkey, Matthew D Proc Biol Sci. 2011 Jul 7;278(1714):1973-80. Epub 2010 Dec 1 doi:10.1098/rspb.2010.1637.

[85] Mangalgiri, G., Manley, P., Riedel, W., and Schmid, M. (2016). Optical investigations of nanorod-substrate interaction for light management. In *Conference on Lasers and Electro-Optics*, page JTh2A.15. Optical Society of America.

[86] Mangalgiri, G. M., Manley, P., Riedel, W., and Schmid, M. (2017). Dielectric nanorod scattering and its influence on material interfaces. *Scientific Reports*, 7(1):4311.

[87] Manley, P. (2016). *Simulation of Plasmonic Nanoparticles in Thin Film Solar Cells*. PhD thesis, Freie Universität Berlin.

[88] Manley, P., Schmidt, F., and Schmid, M. (2013). Light extraction from plasmonic particles with dielectric shells and overcoatings. In *Renewable Energy and the Environment*, page PW3B.7.

[89] Mie, G. (1908). Beiträge zur optik trüber medien, speziell kolloidaler metallösungen. *Annalen der Physik*, 330(3):377–445.

[90] Miller, F., Vandome, A., and John, M. (2010). *Fresnel Equations*. VDM Publishing.

[91] Mokkapati, S. and Catchpole, K. R. (2012). Nanophotonic light trapping in solar cells. *Journal of Applied Physics*, 112(10):101101.

[92] Mokkapati, S., Saxena, D., Tan, H. H., and Jagadish, C. (2015). Optical design of nanowire absorbers for wavelength selective photodetectors. *Scientific Reports*, 5:15339.

[93] Mueller, J., Rech, B., Springer, J., and Vanecek, M. (2004). Tco and light trapping in silicon thin film solar cells. *Solar Energy*, 77(6):917–930.

[94] N.Kaiser, H. (2010). *Optical Interference Coatings*. Springer.

[95] Nozik, A. J. and Memming, R. (1996). Physical chemistry of semiconductor liquid interfaces. *The Journal of Physical Chemistry*, 100(31):13061–13078.

[96] Oskooi, A. F., Roundy, D., Ibanescu, M., Bermel, P., Joannopoulos, J., and Johnson, S. G. (2010). Meep: A flexible free-software package for electromagnetic simulations by the fdtd method. *Computer Physics Communications*, 181(3):687 – 702.

[97] Otto, M., Algasinger, M., Branz, H., Gesemann, B., Gimpel, T., Füchsel, K., Käsebier, T., Kontermann, S., Koynov, S., Li, X., Naumann, V., Oh, J., Sprafke, A. N., Ziegler, J., Zilk, M., and Wehrspohn, R. B. (2014). Black silicon photovoltaics. *Advanced Optical Materials*, 3(2):147–164.

[98] Patoka, P. and Giersig, M. (2011). Self-assembly of latex particles for the creation of nanostructures with tunable plasmonic properties. *J. Mater. Chem.*, 21:16783–16796.

[99] Petrov, E. Y. and Kudrin, A. V. (2012). Electromagnetic oscillations in a driven nonlinear resonator: A description of complex nonlinear dynamics. *Phys. Rev. E*, 85:055202.

[100] Pham, H. H. and Wang, L.-W. (2015). Electronic structures and current conductivities of b, c, n and f defects in amorphous titanium dioxide. *Phys. Chem. Chem. Phys.*, 17:11908–11913.

[101] Piprek., J. (2017). *Handbook of Optoelectronic Device Modeling and Simulation (Two-Volume Set)*. CRC Press, Boston.

[102] Pleskov, Y. (1986). *Semiconductor Photoelectrochemistry*. Wiley.

[103] Poitras, D. and Dobrowolski, J. A. (2004). Toward perfect antireflection coatings. 2. theory. *Appl. Opt.*, 43(6):1286–1295.

[104] Pomplun, J., Burger, S., Zschiedrich, L., and Schmidt, F. (2007). Adaptive finite element method for simulation of optical nano structures. *physica status solidi (b)*, 244(10):3419–3434.

[105] Raut, H. K., Dinachali, S. S., Loke, Y. C., Ganesan, R., Ansah-Antwi, K. K., Góra, A., Khoo, E. H., Ganesh, V. A., Saifullah, M. S. M., and Ramakrishna, S. (2015). Multiscale ommatidial arrays with broadband and omnidirectional antireflection and antifogging properties by sacrificial layer mediated nanoimprinting. *ACS Nano*, 9(2):1305–1314. PMID: 25634665.

[106] Rybin, M. V., Filonov, D. S., Samusev, K. B., Belov, P. A., Kivshar, Y. S., and Limonov, M. F. (2015). Phase diagram for the transition from photonic crystals to dielectric metamaterials. *Nature Communications*, 6:10102.

[107] Sai, H., Mizuno, H., Makita, K., and Matsubara, K. (2017). Light absorption enhancement in thin-film gaas solar cells with flattened light scattering substrates. *Journal of Applied Physics*, 122(12):123103.

[108] Sartori, A., Orlandi, M., Berardi, S., Mazzi, A., Bazzanella, N., Caramori, S., Boaretto, R., Natali, M., Fernandes, R., Patel, N., Bignozzi, C. A., and Miotello, A. (2018). Functionalized p-silicon photocathodes for solar fuels applications: Insights from electrochemical impedance spectroscopy. *Electrochimica Acta*, 271:472 – 480.

[109] Sersic, I., Tuambilangana, C., Kampfrath, T., and Koenderink, A. F. (2011). Magnetoelectric point scattering theory for metamaterial scatterers. *Phys. Rev. B*, 83:245102.

[110] Southwell, W. H. (1983). Gradient-index antireflection coatings. *Opt. Lett.*, 8(11):584–586.

[111] Spinelli, P., Macco, B., Verschuuren, M. A., Kessels, W. M. M., and Polman, A. (2013). Al2o3/tio2 nano-pattern antireflection coating with ultralow surface recombination. *Applied Physics Letters*, 102(23):233902.

[112] Spinelli, P., Verschuuren, M. A., and Polman, A. (2012). Broadband omnidirectional antireflection coating based on subwavelength surface mie resonators. *Nature Communications*, 3.

[113] Starowicz, Z., Lipiński, M., Berent, K., Socha, R., Szczepanowicz, K., and Kruk, T. (2013). Antireflection tio(x) coating with plasmonic metal nanoparticles for silicon solar cells. *Plasmonics*, 8(1):41–3. 1557-1963 Starowicz, Z Lipiński, M Berent, K Socha, R Szczepanowicz, K Kruk, T Boston Plasmonics. 2013 Mar;8(1):41-3. Epub 2012 Jul 7 doi:10.1007/s11468-012-9412-y.

[114] Staude, I. and Schilling, J. (2017). Metamaterial-inspired silicon nanophotonics. *Nature Photonics*, 11:274.

[115] Stratton, J. A. (1998). *Electromagnetic Waves*. Chapman and Hall.

[116] Stratton, J. A. (2007). *Electromagnetic Theory*. Wiley.

[117] Su, Z., Zhao, Q., Song, K., Zhao, X., and Yin, J. (2017). Electrically tunable metasurface based on mie-type dielectric resonators. *Scientific Reports*, 7:43026.

[118] Suri, M. (2001). The p and hp finite element method for problems on thin domains. *Journal of Computational and Applied Mathematics*, 128(1):235 – 260. Numerical Analysis 2000. Vol. VII: Partial Differential Equations.

[119] Tang, C., Lennon, E. M., Fredrickson, G. H., Kramer, E. J., and Hawker, C. J. (2008). Evolution of block copolymer lithography to highly ordered square arrays. *Science*, 322(5900):429–432.

[120] Tang, Y.-H., Huang, M.-J., Su, J.-Y., and Shiao, M.-H. (2012). Fabrication of nanocone subwavelength antireflection structures on quartz substrates. *Japanese Journal of Applied Physics*, 51(6S):06FF06.

[121] Toccafondi, C., Uttiya, S., Cavalleri, O., Gemme, G., Barborini, E., Bisio, F., and Canepa, M. (2014). Optical properties of nanogranular and highly porous tio 2 thin films. *Journal of Physics D: Applied Physics*, 47(48):485301.

[122] Tuccio, S., Centini, M., Benedetti, A., and Sibilia, C. (2013). Subwavelength coherent control and coupling of light in plasmonic nanoresonators on dielectric waveguides. *J. Opt. Soc. Am. B*, 30(2):450–455.

[123] Vabishchevich, P. P., Liu, S., Sinclair, M. B., Keeler, G. A., Peake, G. M., and Brener, I. (2018). Enhanced second-harmonic generation using broken symmetry iii–v semiconductor fano metasurfaces. *ACS Photonics*, 5(5):1685–1690.

[124] van de Groep, J. and Polman, A. (2013). Designing dielectric resonators on substrates: Combining magnetic and electric resonances. *Opt. Express*, 21(22):26285–26302.

[125] van de Haar, M. A., van de Groep, J., Brenny, B. J., and Polman, A. (2016). Controlling magnetic and electric dipole modes in hollow silicon nanocylinders. *Opt. Express*, 24(3):2047–2064.

[126] von Freymann, G., Koch, W., Meisel, D. C., Wegener, M., Diem, M., Garcia-Martin, A., Pereira, S., Busch, K., Schilling, J., Wehrspohn, R. B., and Gösele, U. (2003). Diffraction properties of two-dimensional photonic crystals. *Applied Physics Letters*, 83(4):614–616.

[127] Walter, M. G., Warren, E. L., McKone, J. R., Boettcher, S. W., Mi, Q., Santori, E. A., and Lewis, N. S. (2010). Solar water splitting cells. *Chemical Reviews*, 110(11):6446–6473. PMID: 21062097.

[128] Wang, X., Fujimaki, M., and Awazu, K. (2005). Photonic crystal structures in titanium dioxide (tio2) and their optimal design. *Opt. Express*, 13(5):1486–1497.

[129] Xi, J. Q., Schubert, M. F., Kim, J. K., Schubert, E. F., Chen, M., Lin, S. Y., Liu, W., and Smart, J. A. (2007). Optical thin-film materials with low refractive index for broadband elimination of Fresnel reflection.

[130] Xiong, Z., Chen, W., Wang, P., and Chen, Y. (2017). Classification of symmetry properties of waveguide modes in presence of gain/losses, anisotropy/bianisotropy, or continuous/discrete rotational symmetry. *Opt. Express*, 25(24):29822–29834.

[131] Yasa, U. G., Giden, I. H., Turduev, M., and Kurt, H. (2017). Polarization splitting phenomenon of photonic crystals constructed by two-fold rotationally symmetric unit-cells. *Journal of Optics*, 19(9):095005.

[132] Yin, G., Manley, P., and Schmid, M. (2016). Light absorption enhancement for ultra-thin chalcopyrite solar cells using closely packed 2-d sio2 nanosphere arrays. *Solar Energy Materials and Solar Cells*, 153:124–130.

[133] Yu, Z., Gao, H., Wu, W., Ge, H., and Chou, S. Y. (2003). Fabrication of large area subwavelength antireflection structures on si using trilayer resist nanoimprint lithography and liftoff. *Journal of Vacuum Science & Technology B: Microelectronics and Nanometer Structures Processing, Measurement, and Phenomena*, 21(6):2874–2877.

[134] Yuan, G. B., Le, Y., and (David), L. X. W. (2017). Formation of single-holed cobalt/n-doped carbon hollow particles with enhanced electrocatalytic activity toward oxygen reduction reaction in alkaline media. *Advanced Science*, 4(10):1700247.

[135] Zschiedrich, L. (2009). *Transparent boundary conditions for Maxwell's equations: Numerical concepts beyond the PML method.* PhD thesis, FU-Berlin.

Appendix B

List of Publications

1. Gauri. M. Mangalgiri, Sean P. Berglund, Martin Hammerschmidt, Ting S. Luk, Tristan Kohler, John Nogan, Doug Pete, Anthony James, Lilian Stan, Igal Brener, Roel van de Krol, Sven Burger, Oliver Benson, Martina Schmid 'Enhanced hydrogen evolution reaction using all dielectric Titanium Dioxide metasurfaces ' in final internal review

2. Gauri. M. Mangalgiri, Phillip Manley, Wiebke Riedel and Martina Schmid, Dielectric nanorod scattering and its influence on material interfaces. Scientific Reports, 7(1): 4311,2017.

3. G. Mangalgiri, M. Šiškins, A. Arslanova, M. Hammerschmidt, P. Manley, W. Riedel, and M. Schmid, "Highly Transmittive Broadband Dielectric Nanoholes," in Conference on Lasers and Electro-Optics, OSA Technical Digest (online) (Optical Society of America, 2017), paper JTu5A.117.

4. G. Mangalgiri, P. Manley, W. Riedel, and M. Schmid, "Optical Investigations of Nanorod-Substrate Interaction for Light Management," in Conference on Lasers and Electro-Optics, OSA Technical Digest (online) (Optical Society of America, 2016), paper JTh2A.15.

5. Water-resistant surfaces using zinc oxide structured nanorod arrays with switchable wetting property Houda Ennaceri, Lan Wang, Darja Erfurt, Wiebke Riedel, Gauri Mangalgiri, Asmae Khaldoun, Abdallah El Kenz, Abdelilah Benyoussef, Ahmed Ennaoui, Volume 299, 2016,Pages 169-176,ISSN 0257-8972

Appendix C

Acknowledgement

I am grateful to have been a part of the Helmholtz Zentrum berlin für Materialien und Energie and the Humboldt Universität Zu Berlin's joint programme Hybrid4Energy under the primary supervision of Prof. Martina Schmid. I sincerely acknowledge that extended friday afternoon discussions with Martina improved me in being systematic. Thanks Martina for the handwritten corrections on everything I have written. Dr. Phillip Manley played an important role in familiarising me with nanooptical scattering. I thank Phill for the countless disucssions and many tips in matlab and inkscape. I thank Dr. Wiebke Riedel and my summer students for all the ZnO work. I thank Tristan Köhler who got me started on vaccuum based sputter deposition systems and for the many quick fixes in many fixes. I would also like to thank Micheal Kirsch for countless discussions on the physical functioning of the sputter machine. I would also like to thank Holger, Katja, Daniel and Karolina Mack for help in morphological and optical measurements at HZB. The silicon photocathode enhancement demonstration was possible only due to Dr. Sean Berglund's enthusiasm and I express my sincere gratitude for him introducing me into photoelectrochemical hydrogen generation. I thank Sean for patiently answering all my questions and for all his help in the photoelectrochemistry lab, calculations and in writing the manuscript.

Over time I also became a member of the Zuse Institute at computational nanooptics. I am profoundly indebted to Dr Sven Burger and Prof Frank Schmidt for integrating me into the group. Dr. Martin Hammerschmidt played a pivotal role in getting me started with jcmwave and educating me in diffracted optics. Working with Martin has immensely educated me on scripting, analysing optical spectra and optical properties of nanostructures. I sincerely acknowledge valueable discussions with Martin and Sven on simulations and their experimental comparison. I am also thankful to Dr. Lin Zscheidrich for discussions on optical phenomenona and enquiring about my progress with interest on a regular basis. I thank Theresa, Felix and Dr. Phillip Schneider for helping me with latex. I thank Theresa and Phill for reading certain chapters of this thesis and giving me their inputs. I also acknowledge Xavi, Phillip Gutsche, Sven Hermann and Dr. Klaus Jäger for motivating me at various points. I sincerely owe a lot of my thesis progress to the educating and encouraging atmosphere at ZIB. I sincerely acknowledge JCMSuite for all computational results, beautiful vector plots and maps and for the regular supply of good coffee.

I would like to thank Dr. Igal Brener at Center for Integrated Nanotechnologies at Sandia National Labs for getting me into cleanroom fabrication. I am sincerely greatful for equipment introductions and regular discussions with John, Antony, Doug and Will at CINT for helping me get frustums out of the cleanroom. I also thank Liliana Stan from Argonne for titanium dioxide growth and discusssions. I am very greatful to Willie for help with various ellipsometeric measurements. I am also thankful to Polina, Sheng, Yuanmu and Alex for various discussions as well as for a nice time in Albuquerque. I would like to thank Dr. Gabi Lampert for help with my application to the PhD research abroad programme at the Helmholtz Zentrum Berlin which ensured I had a comfortable stay in Albuquerque.

I also thank Prof. Dr. Oliver Benson at the Humboldt Univeristy for being my secondary supervisor for this thesis. I am grateful to him for monitoring my progress, encouraging remarks on graduate school progress reports and regular motivating interaction. I thank him for reading my thesis and for his valued feedback.

I would also like to thank my friends for their support especially - Burcu, Harry, Heike and Ana in Berlin. I am thankful to Mercury toastmasters for the many fun speechy wednesdays and the FU Wassersport zentrum for tolerating my slow rowing and SKF Zehlendorf for encouraging me with chess. I acknowledge Urveen, Tanmaya, Sathe, Neha, Harsh, Palak, Khayali, Christine, and Anupam being so encouraging and influencing me to grow on all fronts. Last but not certainly not the least, I express my sincere heartfelt gratitude to my parents and family. Their unreserved support, encouragement in my work and my progress motivated me to improve. I am thankful that mummy and daddy's love for their only daughter only transformed into wings of freedom to explore new opportunties.

I formally acknowledge the support of the following funding and organisational units for this thesis. The Helmholtz Association for support from the Initiative and Networking Fund for the Young Investigator Group VH-NG-928. The Hybrid4Energy graduate school programme of the Helmholtz Zentrum Berlin and the Humboldt Universitaet Zu Berlin. The computational results were obtained at the Berlin Joint Lab for Optical Simulations for Energy Research (BerOSE) of Helmholtz-Zentrum Berlin fuer Materialien und Energie GmbH, Zuse Institute Berlin and Freie Universitaet Berlin. This work was performed, in part, at the Center for Integrated Nanotechnologies and Center for Nanoscale Materials, two office of Science User Facilities operated for the U.S. Department of Energy (DOE) Office of Science under contract No.DE-AC02-06CH11357. Sandia National Laboratories is a multi-mission laboratory managed and operated by National Technology and Engineering Solutions of Sandia, LLC., a wholly owned subsidiary of Honeywell International, Inc., for the U.S. Department of Energy's National Nuclear Security Administration under contract DE-NA-0003525.

Appendix D

Selbstständigkeitserklärung

Ich erkläre hiermit, die vorliegende Arbeit selbständig und nur unter verwendung der angegebenen Quellen und Hilfsmittel angefertigt zu haben. Ich habe mich nicht anderweitig um einen Doktorgrad beworben und besitze einen solchen auch nicht. Die dem Verfahren zugrunde liegende Promotionsordnung der Mathematisch-Naturwissenschaftlichen Fakultät der Humboldt-Universität zu Berlin habe ich zur Kenntnis genommen.

Berlin, den

Gauri Mangalgiri